Development of Quantum Cascade Lasers for Gas Sensing Applications

Deivis Vaitiekus

Department of Physics and Astronomy

University of Sheffield

Submitted for the degree of Doctor of Philosophy

December 2015

Abstract

Quantum cascade lasers ($QCLs$) are capable of high power, tunable wavelength and single mode emission at room temperature in the mid-infrared wavelength region. These capabilities make them perfect light sources for laser based gas spectroscopy. The work described in this thesis focuses on development of QCLs suitable for selective gas sensing applications.

The thesis starts with the description of different changes to the QCL active region design. These changes were studied in order to improve laser performance while keeping the emission wavelength fixed. The proposed modifications were performed on short mid-infrared wavelength ($\lambda = 3 - 4\ \mu m$) quantum cascade lasers based on $InGaAs/AlAsSb$ and $InAs/AlSb$ material systems.

The focus of this work is then moved to the description of a single mode quantum cascade laser with a third order unilateral grating. The previously unreported grating architecture that was used to achieve distributed feedback (DFB) in a QCL, as well as grating design and laser characterization are detailed in Chapter 5. The reported laser generates single mode emission with 30 dB side mode suppression ratio and a linewidth of 0.4 cm^{-1}. The simplified fabrication process for a third order DFB grating is developed for $\lambda = 3.3 - 3.6\ \mu m$ emission wavelength.

A different approach to achieve single mode emission in a QCL is described in Chapter 6. An external cavity QCL setup combined with the Fabry-Pérot (FP) reflector is re-

ported for the first time. The FP reflector is used to provide selective feedback that is controlled by the separation distance between two FP reflector mirrors. This external cavity arrangement allows generation of a wide spectral range and the rapid wavelength tuning capability.

Finally, the thesis is concluded with sensitive gas detection experiments. The direct absorption technique is utilized to demonstrate the 160 *ppmv* detection of methane with the ro-vibrational absorption line located at $\lambda \sim 3.3\ \mu m$ and 1 *ppmv* detection of nitric oxide with the absorption line located at $\lambda \sim 5.3\ \mu m$. The experiments were performed using single mode lasers that were designed and fabricated in Sheffield.

Contents

List of Publications **ix**

List of Conferences **xi**

Acknowledgement **xiii**

1 Introduction **1**

1.1 General principles of a semiconductor laser 1

1.2 Intersubband transitions 5

1.3 Mid-infrared sources 6

1.4 Quantum cascade laser 8

1.4.1 Historical development of QCL 9

1.4.2 Active region design 13

1.4.3 Different designs 15

1.4.4 The waveguide 19

1.4.5 Material consideration for laser growth 20

1.4.6 Short wavelength heterostructures 23

1.5 Applications 28

1.5.1 Gas sensing 28

1.5.2 Telecommunications 29

References 31

2 Theory **41**

2.1 Intersubband gain 41

2.2 Rate equations 42

2.2.1 Population inversion 44

2.2.2 Threshold current density 47

2.3 Fabry-Pérot lasers 50

2.4 Distributed feedback lasers 52

2.4.1 Coupling coefficient 55

References 57

3 Device Growth, Fabrication and Characterization **59**

3.1 Introduction 59

3.2 Epitaxy 60

3.2.1 Molecular beam epitaxy 60

3.2.2 Metal organic vapour phase epitaxy 62

3.3 Standard laser fabrication 64

3.4 Laser characterization 67

3.4.1 Experimental setup 67

3.4.2 Fourier transform infrared spectroscopy 70

3.4.3 IV and LI curve measurements 71

3.4.4 Characteristic temperature T_0 72

References 73

4 The Development of Fabry-Pérot Quantum Cascade Lasers for Gas Detection in $\lambda \sim 3-4\ \mu m$ Wavelength Region **75**

4.1 Introduction 75

4.2 InP based lasers 77

4.2.1 Laser design: 1^{st} growth 80

4.2.2 Results 82

4.2.3 Laser design: 2^{nd} growth . . . 85
4.2.4 Results . . . 87
4.2.5 Laser design: 3^{rd} growth . . . 89
4.2.6 Results . . . 91
4.3 InAs based lasers . . . 93
4.4 Results . . . 96
4.5 Conclusion . . . 97
References . . . 98

5 Quantum Cascade Laser with Unilateral Grating 99
5.1 Introduction . . . 99
5.2 Working principles of distributed feedback . . . 102
5.2.1 Grating calculation . . . 103
5.3 Computer modeling and sample fabrication . . . 104
5.3.1 Computer modeling . . . 105
5.3.2 Sample fabrication . . . 109
5.4 Device characterization . . . 113
5.4.1 Results . . . 114
5.5 Unilateral grating for 3.37 μm wavelength generation . . . 116
5.5.1 Results . . . 120
5.6 Conclusion . . . 121
References . . . 124

6 External Cavity Wavelength Modulation Based on Fabry-Pérot Reflector 129
6.1 Introduction . . . 129
6.2 Fabry-Pérot reflector . . . 131
6.2.1 Theoretical analysis of the Fabry-Pérot reflector . . . 132
6.2.2 Free spectral range . . . 135

6.2.3 Minimum resolvable bandwidth . . . 136
6.2.4 Finesse . . . 136
6.2.5 Contrast factor . . . 138
6.3 FP reflector with plain secondary mirror . . . 139
6.3.1 Secondary mirror characteristics . . . 140
6.3.2 FP reflector alignment . . . 141
6.3.3 Results . . . 142
6.3.4 Triangular external cavity setup . . . 147
6.4 FP reflector with wedged secondary mirror . . . 151
6.4.1 Thin film deposition . . . 153
6.4.2 Interferometer alignment . . . 155
6.4.3 Results . . . 158
6.5 Rapid wavelength modulation via tunable FP reflector . . . 159
6.6 Conclusion . . . 163
References . . . 166

7 Quantum Cascade Lasers in Gas Sensing Setups 169

7.1 Introduction . . . 169
7.2 Gas absorption in mid-infrared region . . . 170
7.2.1 Direct absorption spectroscopy . . . 171
7.2.2 Wavelength modulation spectroscopy . . . 173
7.2.3 Farraday rotation spectroscopy . . . 175
7.3 Detection of the methane (CH_4) gas using $\lambda \sim 3.3\ \mu m$ QCL . . . 176
7.3.1 Motivation and laser design . . . 176
7.3.2 Pressure dependence . . . 180
7.3.3 Experimental setup . . . 181
7.3.4 Signal analysis . . . 182
7.3.5 Wavelength tuning by current injection scan . . . 183
7.3.6 Multi-pass cell . . . 185

7.4 Nitric oxide (NO) detection . . . 186
7.4.1 NO absorption bands for FRS . . . 186
7.4.2 Experimental setup . . . 188
7.4.3 Laser wavelength determination and discussion . . . 189
7.5 Summary . . . 193
References . . . 195

8 Conclusion **203**

9 Future Work **205**
References . . . 207

Appendices **209**

A Short wavelength QCL Designs **209**
A.1 M4054 laser design for $\lambda \sim 3.3 - 3.5\ \mu m$ emission wavelength . . . 209
A.2 MBE grown short wavelength QCL designs . . . 210
A.2.1 The control QCL design $SF0657$ . . . 210
A.2.2 Raised injector design . . . 211
A.2.3 Longer injector, narrower barriers design . . . 211
A.2.4 Even more lowered injector design . . . 212
A.2.5 Laser design to improve T_0 . . . 212
A.2.6 Vertical transition design . . . 212
A.2.7 $InGaAs$ laser design for $\lambda \sim 3.37\ \mu m$ . . . 213

List of Publications

[1] Deivis Vaitiekus, Dmitry G. Revin, Kenneth L. Kennedy, Shiyong Y. Zhang, and John W. Cockburn. Quantum cascade laser with unilateral grating. *IEEE Photonics Technology Letters*, 24(23):2112–2114, 2012.

[2] Dmitry G. Revin, Michael Hemingway, Deivis Vaitiekus, John W. Cockburn, Nils Hempler, Gareth T. Maker, and Graeme P.A. Malcolm. Continuous wave room temperature external ring cavity quantum cascade laser. *Applied Physics Letters*, 106(26), 2015.

[3] Deivis Vaitiekus, Michael Hemingway, Andrey Krysa, John Cockburn, and Dmitry G. Revin. Exernal cavity quantum cascade laser based on fabry-perot reflector. In *CLEO: 2015*, page JTh2A.15. Optical Society of America, 2015.

[4] Michael Hemingway, Deivis Vaitiekus, John Cockburn, Nils Hempler, Gareth Maker, Graeme Malcolm, and Dmitry G. Revin. Continuous wave room temperature external ring cavity quantum cascade laser. In *CLEO: 2015*, page STu4G.6. Optical Society of America, 2015.

[5] Deivis Vaitiekus, Dmitry G. Revin, Michael Hemingway, and John W. Cockburn. External cavity laser based on Fabry-Pérot reflector. *Manuscript in preparation*, 2016.

List of Conferences

[1] Deivis Vaitiekus, Dmitry G. Revin, Kenneth L. Kennedy, Shiyong Y. Zhang, and John W. Cockburn. Quantum cascade laser with uni-lateral grating. In *UK Semiconductors*, The Edge Conference Complex, Sheffield, UK, July 2012.

[2] Dmitry G. Revin, Michael Hemingway, Deivis Vaitiekus, John W. Cockburn, Nils Hempler, Gareth T. Maker, and Graeme P.A. Malcolm. Continuous wave room temperature external ring cavity quantum cascade laser. In *2015 Conference on Lasers and Electro-Optics (CLEO)*, San Jose Convention Center, San Jose, CA, USA, May 2015.

[3] Deivis Vaitiekus, Michael Hemingway, Andrey B. Krysa, John W. Cockburn, and Dmitry G. Revin. External cavity quantum cascade laser based on fabry-pérot reflector. In *2015 Conference on Lasers and Electro-Optics (CLEO)*, San Jose Convention Center, San Jose, CA, USA, May 2015.

Acknowledgment

First and foremost I would like to thank my supervisor prof. John Cockburn, for providing me with the opportunity to do this PhD.

I am also grateful to my colleagues, surrounding me throughout my PhD. My fellow PhD students – Chris and Michael. A big thanks goes to the staff members at III-V National centre facilities, Ken Kennedy and Saurabh Kumar for their advice and assistance during the numerous hours spent in clean room facilities. A big shout-out goes to the people responsible for material growth – Jan Devenson, for introducing me to the MBE reactor and for putting a huge amount of extra hours just to make sure we get the samples, Andrey Krysa for a consistent, incredible quality sample growth, and Shyong Zhang for Short wavelength QCL growth.

I would also like to thank the Life Science Trace Gas Facility group at Radboud University in Nijmegen, Netherlands supervised by Frans Harren for taking time to demonstrate the concept of trace gas detection using quantum cascade lasers. A big thank you goes to postdoc and fellow students for making my time in Netherlands unforgettable. And most of all I would like to say big thank you to the person who contributed to my academic development the most – Dr. Dmitry Revin. The person who taught me critical thinking, and made me see a wider picture and always question my results. I am incredibly thankful for his constant support and advice throughout my PhD.

Taipogi norėčiau padėkoti žmonėms kurie padarė mano praleistą laiką Sheffield'e daug smagesniu. Įpatinga padėka Andreikai, už jo ištikimybę ir besąligišką pagalbą. Esu dėkingas jam už jo tikrą draugystę, nesibaigiančius pokalbius telefonu, nuoširdų žingeidumą bei palaikimą. Taipogi dėkoju Pauliui ir Beatai už jų be galo linksmą kompaniją, milijoną projektų, judančias spalvas (if you know what I mean) bei pastovias nesąmones (#TRRKT). Ačiū Emiliui ir Verai už jūsų palaikymą, bei įveiktas viršūnes padėjusias man prasiblaškyti bei atsipalaiduoti. Labiausiai norėčiau padėkoti savo broliui, Dariui, kuris niekada manimi neabėjojo ir nedvejojo.

А также хочу поблагодарить свою семью за огромную поддержку и безусловную любовь. Огромное спасибо семье Карпинских, за веру в меня и постоянное напоминание что *Британские учёные - самые лучшие*. Так же спасибо семье Никитиных, за их мотивацию и поддержку, которая меня подталкивала в перед. И больше всего я хотел поблагодарить своих родителей, особенно свою маму, Ларису, которая желала мне успеха независимо от моего выбора. Огромное ей спасибо за то, что дала мне понять что независимо где я буду и чем я буду заниматься - я всегда желанный гость дома. А также я хочу поблагодарить свою бабушку Шуру, которой я и посвящаю эту работу.

Chapter 1

Introduction

1.1 General principles of a semiconductor laser

The acronym "*LASER*" stands for "*Light Amplification by Stimulated Emission of Radiation*". The phenomenon is based on the quantum mechanical process of stimulated emission. Stimulated emission is different from spontaneous emission - the process that produces luminescence in light emitting diodes. Stimulated emission is responsible for the photon density increase inside a laser cavity, which leads to optical amplification. In contrast, absorption is the reason the photon density reduces, causing optical attenuation.

A simplified version of the processes inside a semiconductor laser cavity is shown in Figure 1.1. The photon can be created with energy $h\nu$ traveling inside the cavity through the spontaneous emission process. It can be absorbed by the reverse process causing light attenuation or it can stimulate another electron transition through the stimulated emission process causing light amplification. In the normal condition of thermal equilibrium, the energy level E_1 will be more populated than the upper level E_2, as given by the Boltzmann factor in Equation 1.1.

$$\frac{N_2}{N_1} = \exp(-\frac{\Delta h\nu}{k_B T}) \tag{1.1}$$

where N_1 and N_2 are carrier populations at the respective energy levels; h - Planck constant; ν - frequency; k_B - Boltzmann constant and T - temperature.

The $N_1 > N_2$ condition means that the absorption process is dominant causing light attenuation. If the condition is reversed, the opposite will be true, resulting in net light amplification. This condition is called population inversion and in the intersubband semiconductor lasers is typically achieved by careful energy level design.

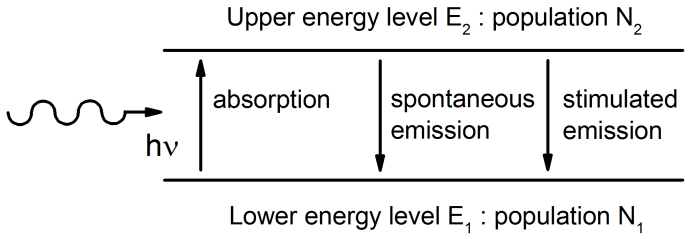

Figure 1.1: Simplified diagram of the transition processes inside a laser cavity. Absorption and spontaneous emission are the dominating processes when population N_1 of the lower energy level E_1, is higher than population N_2 of the upper energy level E_2. The stimulated emission process starts to dominate when the condition is reversed.

If the population inversion criterion is met, the stimulated emission process starts to dominate over the absorption process provided that an appropriate laser cavity is available. The schematic diagram of a semiconductor laser cavity is shown in Figure 1.2. The light is kept inside the cavity through the reflections caused by the difference in the refractive indices between the semiconductor material ($n \sim 3.2$) and air ($n = 1$). The reflectivity at the semiconductor-air boundary is typically about 27% and often is sufficient to obtain lasing without the need for reflectivity enhancement through high reflectivity coatings or external mirrors.

The injected charge into the upper energy level can produce a photon through radiative

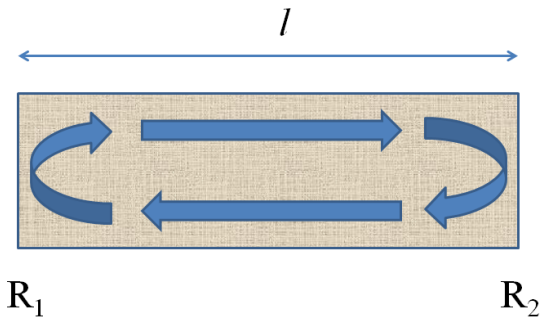

Figure 1.2: Schematic diagram of laser cavity

transition with frequency corresponding to the transition energy $\sim E_g/h$ for interband lasers and $\sim E_{sub}/h$ for intersubband lasers. The produced light is reflected back and forth generating more photons of the same frequency through the combination of spontaneous and stimulated emission processes. At some particular injection current value (for the electrically pumped laser), called the threshold current (I_{th}), the optical gain produced inside the laser cavity becomes equal to the losses thus creating the conditions for laser emission. Further increase in the current converts the excess of the charge carriers into photons increasing the output power.

The oscillating light inside the cavity forms longitudinal standing waves that can be described by Equation 1.2:

$$l = M \times \frac{\lambda'}{2} \tag{1.2}$$

where l is the length of the laser cavity; M is an integer; λ' is the wavelength inside the optical cavity, and is equal to λ/n with n equal to the refractive index of the cavity and λ is the free space wavelength. From here it can be shown that the oscillating frequencies inside this cavity must satisfy Equation 1.3.

$$\nu = M \times \frac{c}{2nl} \tag{1.3}$$

where c is the speed of light. As a result only frequencies that are covered by the laser gain bandwidth and that satisfy Equation 1.3 can exist inside the laser cavity.

The gain coefficient G is a characteristic property of a laser describing its ability to increase optical power. When the condition for the light oscillation inside the cavity is met, the threshold gain, G_{th}, is at its maximum and can be expressed using Equation 1.4.

$$G_{th} = \alpha - \frac{1}{2l}\ln(R_1 R_2) \tag{1.4}$$

where α is the attenuation coefficient accounting for scattering losses and absorption due to processes other than interband transitions and R is the mirror reflectivity.

Assuming that the gain coefficient increases linearly with the injection current (I_{in}), as shown in Figure 1.3a, G_{th} will be reached when $I_{in} = I_{th}$. At this point, the gain coefficient is equal to the losses experienced by the optical cavity and cannot increase any further, otherwise the stability condition required for oscillation to occur would be broken. As a result, the excess of input current will be converted into electron-hole recombination for interband lasers and $\Delta E = E_{upper} - E_{lower}$ electron transition for intersubband lasers, causing linear power increase as shown in Figure 1.3b.

The power output can therefore be written as:

$$P_{out} = \eta\frac{h\nu}{e}(I_{in} - I_{th}) \tag{1.5}$$

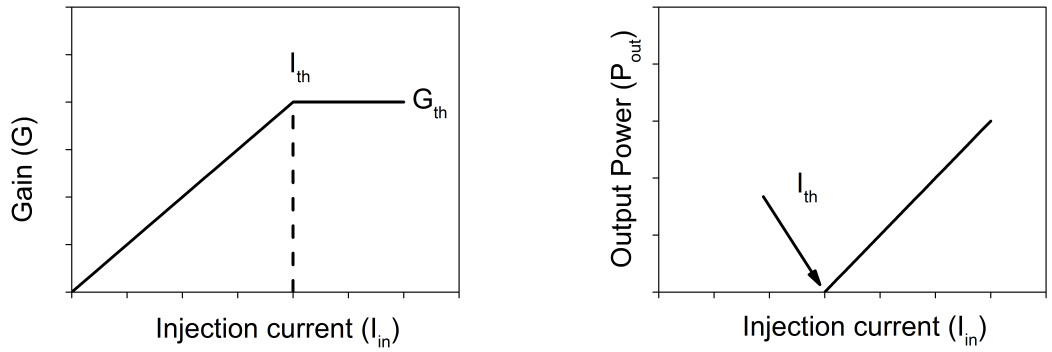

(a) Gain coefficient vs injection current (b) Power output vs injection current

Figure 1.3: Power output (a) and gain coefficient G (b) as a function of injection current I_{in}. I_{th} is the threshold injection current and G_{th} is the threshold gain coefficient required for laser emission.

where η defines the electron to photon conversion ratio, also known as the quantum efficiency and e is the electron charge. Careful active region design and defect-free samples can bring this quantity close to unity. Lasers with cascaded active region designs can have quantum efficiencies of $\eta > 1$.

1.2 Intersubband transitions

An intersubband transition is the type of transition where the electron changes its energy state inside the subband of the valence or conduction band. This is unlike the interband transition, where the electron has to recombine with the hole between two bands - conduction and valence. The schematic diagram of an intersubband transition inside a quantum well is shown in Figure 1.4.

The energy difference ΔE_{sub}, between the intersubband levels is usually smaller than the energy difference of the interband transitions, resulting in a longer wavelength photon generation. A typical 8.5 nm $GaAs/Al_{0.3}Ga_{0.7}As$ quantum well will have two levels spaced at ~ 0.1 eV, producing a photon with the mid-infrared wavelength of ~ 12 μm. The mid-infrared spectral region plays an important technological role in industrial applications

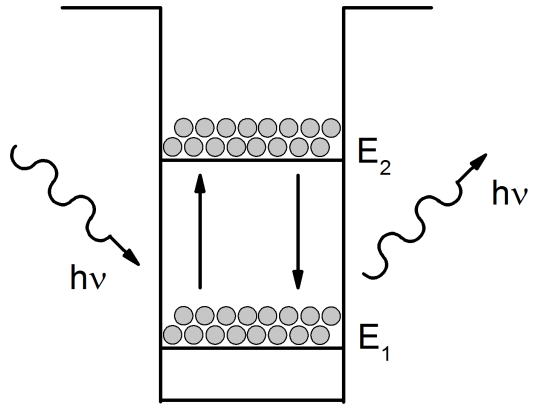

Figure 1.4: Radiative electron transition producing (absorbing) a photon of energy $\Delta E = E_2 - E_1$ where E_1 and E_2 are confined energy levels within the subband.

such as atmospheric sensing and pollution monitoring. The system used for trace gas detection utilizing laser spectroscopy is described in more detail in Chapter 7.

The intersubband transition is excited by light polarized along z axis according to the selection rules for intersubband transitions, where z is defined to be along the growth direction of the heterostructure. The matrix element for a transition from the m_{th} to the m'_{th} subband can be written as $\langle m|z|m'\rangle$. The transition also has to obey the selection rule described by $\Delta m = (m - m')$, where Δm is an odd number.

1.3 Mid-infrared sources

Most of the mid-infrared spectral region can be accessed by lasers emitting light through intersubband transitions. The main reason intersubband laser emission is limited to the mid- and far-infrared regions is the immature growth technology preventing the growth of high quality quantum wells with large conduction band discontinuity, such as those found in $InGaN/AlN$ heterostructures.

A schematic comparison of different laser sources emitting in the mid-infrared region is shown in Figure 1.5. CO and CO_2 lasers can produce high output powers but are lim-

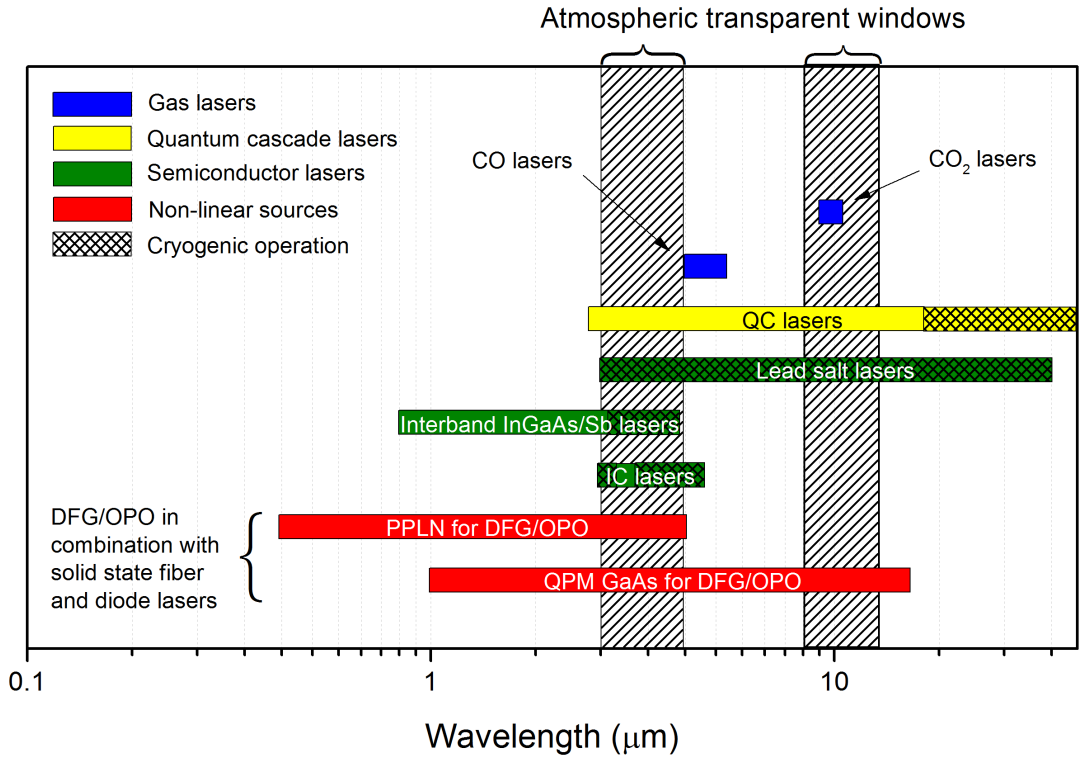

Figure 1.5: Comparison of different mid-infrared and near-infrared laser sources. Wide coverage can be achieved with non-linear frequency doubling devices with the help of near-infrared based fiber lasers. Lead salt lasers are capable of large wavelength coverage at the expense of stability. Semiconductor lasers cover the whole mid-infrared region. (*PPLN* - Periodically Poled Lithium Niobate; *QPM* - Quasi-phase matching; *DFG* - Difference frequency generation; *OPO* - Optical parametric oscillator)

ited in terms of wavelength tuning. It can be noticed that the large wavelength region is covered with sources based on down-conversion from near-infrared fiber lasers, where operation in the mid-infrared region is achieved through non-linear processes. These systems are usually bulky and expensive to operate, making them less attractive for commercial use despite their high output powers and wide wavelength coverage. The $IV - VI$ lead salt semiconductor lasers are capable of wide frequency coverage but suffer from limited reliability, low output powers and need of cryogenic cooling.

The interband cascade laser (*ICL*) is a hybrid of a regular diode laser, where the radiative transition occurs between conduction and valence bands, and a quantum cascade laser

(QCL), where charge carriers are recycled between the active stages. The first demonstration of luminescence obtained from interband cascade quantum wells was in 1995 by Yang [1] with the first laser demonstrated by Meyer *et al* in 1996 [2]. ICLs are most efficient in the $3-4\ \mu m$ wavelength region with reported wavelengths of up to $5.4\ \mu m$ [3]. Continuous wave (CW) operation at room temperatures has been achieved at $3.5-3.7\ \mu m$ [4, 5]. Quantum cascade lasers, on the other hand, can produce wavelength coverage ranging from $2.6\ \mu m$ up to $250\ \mu m$ [6, 7] with high power outputs and CW room temperature operation in certain wavelength ranges.

1.4 Quantum cascade laser

Unlike diode lasers, where photon production is only possible through electron and hole recombination, quantum cascade lasers are unipolar devices. In a unipolar device the electron transition occurs between the localized states within a single band, the conduction band in QCLs.

Unipolar and bipolar devices also exhibit differently shaped dispersion curves. Intersubband transitions occur between subband states with the same in-plane dispersion curve. As a result any elastic or inelastic transition that provides the required momentum exchange allows the scattering of the electron from the upper to the lower states, reducing the lifetime of the electron typically to the order of picoseconds, thus favoring non-radiative recombination. By contrast, the recombination in interband devices is dominated by radiative transitions. Different curvatures in k space for unipolar and bipolar devices are shown in Figure 1.6.

Another unique property of the unipolar device, such as QCL, is that the transition energies are defined by the confinement of the energy levels inside the quantum well, allowing energy level tailoring by changing the width of the quantum well. This can be achieved over a wide wavelength range throughout the mid-infrared and far-infrared regions.

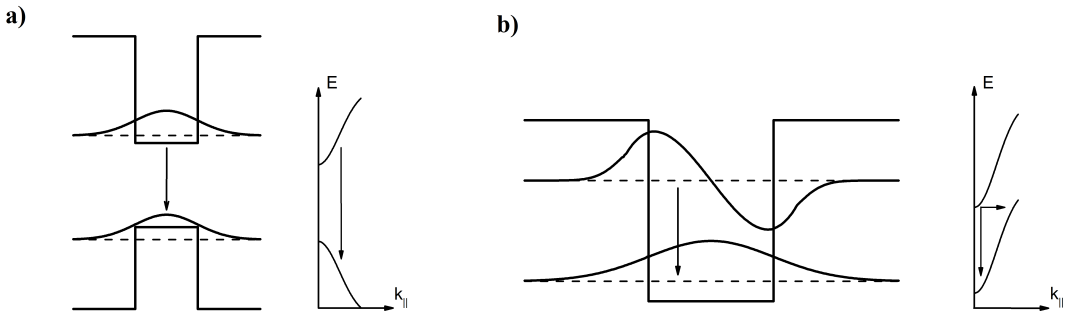

Figure 1.6: Interband transition (a) occurs between conduction and valence bands that have opposite curvature in k space. The recombination process is dominated by radiative transitions. Intersubband transition (b) occurs inside the same band (the conduction band for QCLs) and therefore has the same curvature of in-plane dispersion. The recombination process is dominated by interface roughness or optical phonon emission reducing the lifetime of the upper energy levels.

Quantum cascade lasers consist of a number of linked periods (typically $\sim 30 - 50$) that can recycle the electrons from one period to another for multiple photon generation. This property results in QCLs having high quantum efficiencies η (proportional to the number of stages).

1.4.1 Historical development of QCL

The first documented design of a unipolar laser based on the intersubband transition in a semiconductor heterostructure goes back to the seminal work of R. Kazarinov and R. Suris [8, 9]. In their papers, a superlattice under an applied electric field is considered. The heterostructure is aligned in such a way that the ground state of one quantum well (E_1) is located just below the second excited energy state (E_3) of the next quantum well (see Figure 1.7). The photon is emitted during the electron transition from the ground state to the first excited state (E_2) of the downstream well. The population inversion is achieved by different scattering times, where the transition time between $E_1 \rightarrow E_2$, τ_{12}, is longer than the intra-well scattering times, τ_{21}.

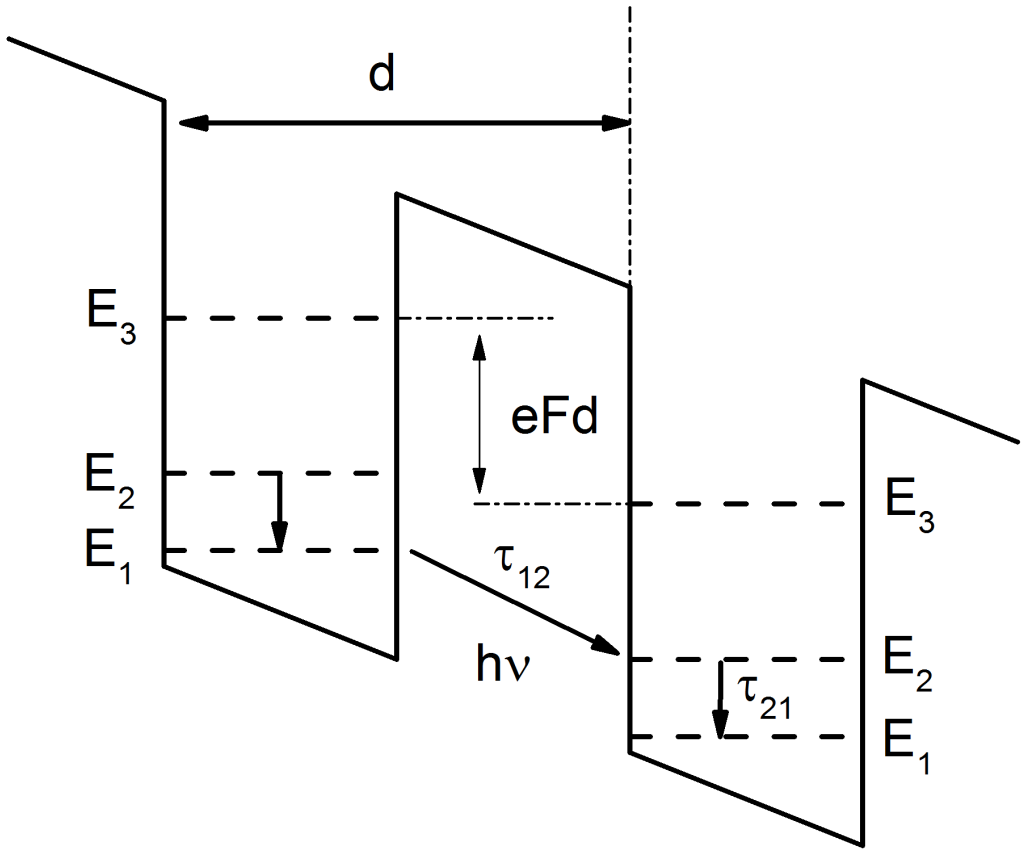

Figure 1.7: Schematic diagram of proposed intersubband transition in a superlattice under electric field F by assisted photon tunneling. eFd is equal to the energy acquired by an electron in an electric field F in a distance equal to the superlattice period d.

This prediction, however, could not be observed experimentally due to low spontaneous emission efficiencies of grown samples, making it difficult to be detected. The advent of molecular beam epitaxy (MBE) in the 1970's allowed for the first time of very sharp interface and excellent layer selectivity growth creating the interest for multi-quantum-well structure studies [10]. The first intersubband absorption in $GaAs/AlGaAs$ superlattice grown by MBE was observed in 1985 by West and Eglash [11]. A number of attempts were made to implement Kazarinov's proposal experimentally in $GaAs/AlGaAs$ superlattices. This led to the first demonstration of the sequential resonant tunneling in a superlattice

by Capasso *et al.* in 1986 [12] and the observation of intersubband luminescence pumped by resonant tunneling by M. Helm *et al.* in 1989 [13]. Kazarinov's work stimulated a lot of theoretical interest that led to the proposals of intersubband lasers, mostly based on resonant tunneling in superlattices [12], superlattices with two quantum well periods [14] and the carrier injection into either the first excited state of superlattice or the miniband [15–18].

The breakthrough came in 1994 when Faist *et al.* working at AT&T Bell Laboratories demonstrated the first intersubband laser naming it *"The Quantum Cascade Laser"* [19]. The first intersubband laser device was grown by MBE and used the $In_{0.53}Ga_{0.47}As/Al_{0.48}In_{0.52}As$ material system lattice matched to InP. The device was operational only at cryogenic temperatures with the emission wavelength of $\sim 4.2\ \mu m$. $12\ \mu m$ wide and $0.5\ mm$ long devices demonstrated laser emission at a driving current of $I = 850\ mA$, corresponding to the threshold current density $J_{th} = 15\ kA/cm^2$. Despite the limited collection efficiency (40 %) and the beam divergence ($\pm 40°$), peak powers above $8\ mW$ were observed.

The high threshold current density prevented laser emission at higher temperatures. It was not until the original three-quantum-well design with the diagonal radiative transition was improved with the vertical transition three-well design (see Section 1.4.3), that the first room temperature pulsed operation in 1996 [20] was observed. Later on it was discovered that this design suffers from thermal backfilling, where the electrons start to re-occupy lower laser levels as the temperature of the device increases, reducing its performance.

The poor operation of QCLs at higher temperatures led to the development of improved active region designs, namely bound-to-continuum [21] and double phonon resonance [22], described in more details in Section 1.4.3. These designs increased the operating temperatures, allowing the first observation of continuous wave room temperature operation by Beck *et al.* in 2002 [23]. These two designs are still used for high temperature, high power CW QCLs.

Another important milestone in QCL development has been achieved with the demonstration of the first laser device grown by metal organic vapour phase epitaxy (MOVPE) at the University of Sheffield in 2003 [24, 25]. The main advantages of MOVPE are much shorter baking cycles, accelerating the atmospheric contamination recovery, higher growth rates and also the ability to facilitate larger numbers of wafers inside its chamber for higher commercial production yield.

Short wavelength QCLs were always of interest due to the need of emission wavelengths spectroscopically suitable for commercial applications. The pioneering work on short wavelength QC lasers was done in 2004 in Baranov's group at the University of Montpellier using the $InAs/AlSb$ material system [26]. The group at the University of Sheffield, using $InGaAs/AlAsSb$ material system with lattice matched on InP substrate also demonstrated short wavelength operation in the same year [27], with room temperature operation achieved in 2009 [28]. The first QC laser device with the emission wavelength $\lambda \sim 3\ \mu m$ was demonstrated at the University of Montpellier by Devenson *et al.* in 2006 [29]. The same group also hold the record for the shortest wavelength QCL, demonstrated in 2010, at $\lambda \sim 2.6\ \mu m$ wavelength [6].

Distributed feedback gratings, due to their ability to produce single mode wavelengths, especially useful for spectroscopic applications, were implemented into quantum cascade laser fabrication with the first single mode laser achieved in 1997 by Faist *et al.* [30]. Room temperature and single mode CW operation has been demonstrated since, over the wavelength region of 3.0 μm [31] to 10 μm [32].

Laser efficiency is often described by the quantity known as a wall plug efficiency (WPE). WPE shows how efficiently the electric power injected into a device is converted into optical power. The first QCL device producing more light than heat (*i.e.* WPE > 50 %) was reported by Y. Bai in M. Razeghi's group [33] with reported wall plug efficiency of 53 %. The same group also managed to demonstrate the highest CW power at room temperature peaking at 5.1 W [34] and pulsed devices with peak powers up to 190 W also

at room temperature [35].

1.4.2 Active region design

The fundamental concepts needed for the successful active region design in intersubband lasers are electrically stable structure at the operating point, population inversion and sufficient gain to compensate for the losses experienced inside the waveguide. The architecture of the active region, responsible for efficient light generation and current transport consists of the periodic arrangements of the active periods each one made of varying thickness quantum wells and barriers. A schematic diagram of such an arrangement is shown in Figure 1.8.

This periodic structure can be divided into two main sections - active and bridging regions. The active region is where the light is generated and therefore must be designed to create the conditions required for a population inversion to occur. The population inversion can be achieved in a number of ways of electronic level arrangement and will be discussed in more detail later in this chapter. In general, an active region consists of at least three energetic levels, with electrons being injected into upper energy level E_3 (see Figure 1.8b) to initiate the population inversion with respect to level E_2. Assuming 100% injection efficiency into level E_3, the population inversion is created when $\tau_{32} > \tau_2$, where τ_{32} is the scattering time for $E_3 \rightarrow E_2$ energy levels and τ_2 is the total carrier lifetime in level E_2. The non-radiative transition from $E_3 \rightarrow E_1$ in the coupled-well structures is not negligible so that the more general lifetime requirement is defined as $\tau_3 > \tau_2$, where τ_3 and τ_2 are the total carrier lifetimes of states E_3 and E_2 respectively.

It is good practice to design the laser active region so that under the applied electric field the structure aligns its lower electronic levels to be equal to the longitudinal optical phonon energy (34 meV in $In_{0.53}Ga_{0.47}As$, 36 meV in $GaAs$) to further enhance carrier extraction from E_2 by resonant scattering. This decreases the lifetime of the E_2 level down to sub-picosecond values, while the optical phonon scattering lifetime τ_{32}^{OP} between

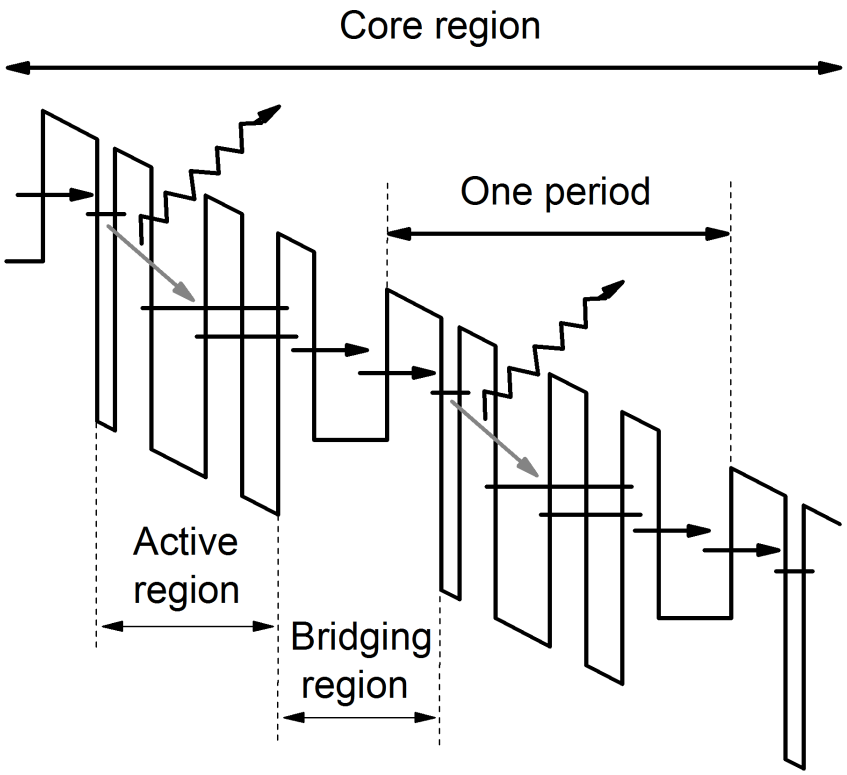

(a)

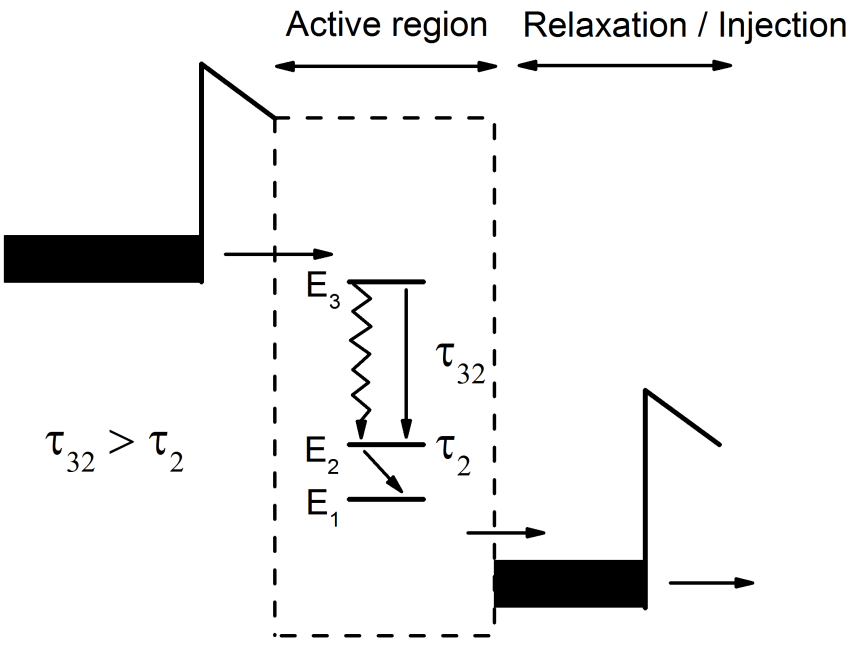

(b)

Figure 1.8: a) Schematic diagram of a quantum cascade laser conduction band [37]. The cascaded structure is made of a number of repeats of the active and injection/relaxation (bridging) regions. The electron transitions from one level to another emitting a photon and moving to the next active region where the same electron is reused and the process is repeated. b) Schematic diagram of the energy levels and associated lifetimes inside the active region.

E_3 and E_2 levels remains high due to it being associated with much larger wavevector transfer [36].

The bridging region, also known as injection/relaxation region follows the active region. The function of this region is to cool down carriers to the lattice temperature prior to injecting them into the next period. It is usually achieved by alternating quantum wells and barriers with a changing duty cycle, creating step-like electronic levels that become aligned under the electric field to enhance the electron tunneling through resonance effects [38]. The bridging region, unlike the active region, is doped, providing the electron charge needed for transport. The active region is left undoped to avoid the laser transition broadening [39] and scattering increase due to ionized impurities.

The active region can have two different types of transitions - vertical and diagonal. Vertical transitions occur in the heterostructures with upper and lower energy level wavefunctions being localized in the same quantum well. As a result the spatial wavefunction overlap is increased, enhancing the gain. The transition is termed as being diagonal if the wavefunctions are spatially localized in different wells, thus experiencing reduced overlap. Despite smaller overlap, the diagonal transitions have larger dipole matrix elements contributing towards the gain increase.

1.4.3 Different designs

After the successful demonstration of the first working laser many studies were aimed at maximizing the efficiency of light production using different active region designs. Several strategies have been combined based on tunneling, optical phonon resonance and manipulation of phase space to produce, what are now the most commonly used designs in quantum cascade lasers.

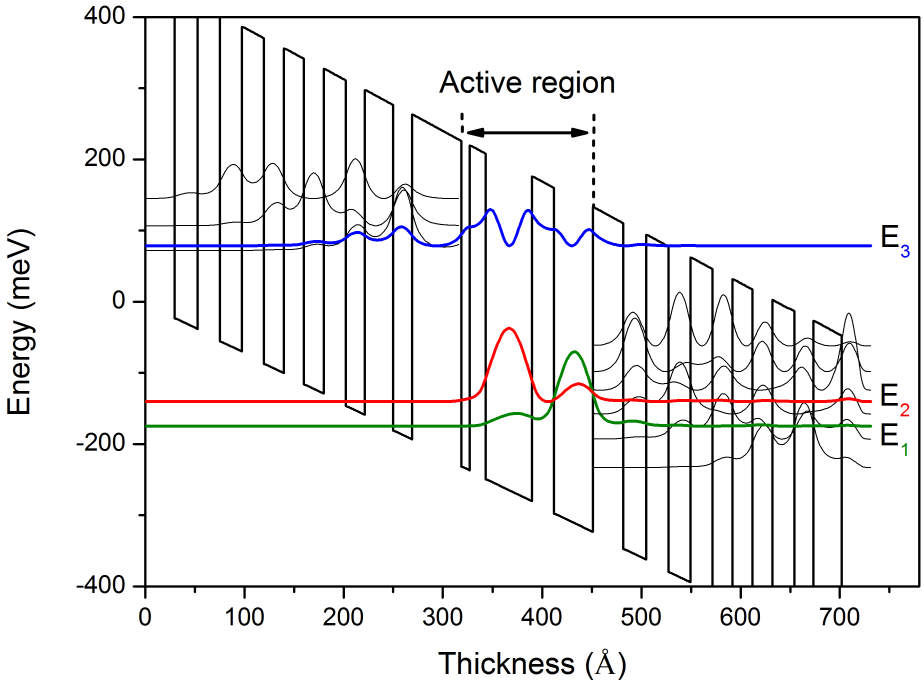

Figure 1.9: Three quantum well design. The radiative energy transition occurs between level E_3 and E_2. The separation between E_2 and E_1 equals to the optical phonon energy in order to enhance carrier depopulation [20]. The radiative transition can be either vertical or diagonal, depending on the wavelength coupling strength and barrier thickness.

Three-quantum-well active region

The active region of the three-quantum-well design, as shown in Figure 1.9, consists of three coupled quantum wells. The thickness of the middle well is adjusted so as to provide the energy separation between energy level E_3 and energy level E_2 equal to the designed wavelength emission energy. The second quantum well is then added downstream. The thickness of the 2^{nd} well is adjusted so that the lower energy level of this well is in resonance with the lower energy level of the middle QW under the applied electric field. The splitting, which arises as a result of two levels being in resonance, is designed to correspond to the phonon resonance energy, to enhance depopulation of the lower laser level. A third thin

quantum well is added upstream to increase injection efficiency due to its wavefunction extension into the injection region. The thin QW is adjusted so that its ground state level is in line with the upper energy level of the middle quantum well to produce the diagonal radiative transition from the first quantum well into the middle QW.

Double phonon resonance active region

The double phonon resonance design (also known as a four-quantum-well design) improves the electron extraction from the ground state compared with the three-quantum-well design. Studies of the diagonal three-quantum-well design showed that the carrier extraction lifetimes from the ground state to the miniband is of the order of 2 ps. This lifetime is comparable to the electron scattering time associated with the thermal backfilling of the lower laser energy level, thus reducing the population inversion and the laser performance at higher temperatures.

Beck *et al.* [23] demonstrated that introducing an additional ground state level into the system by the addition of an extra quantum well and thus forming three states separated by the energies equal to the optical phonon transition energy decreases the population of the lower state significantly. The schematic diagram of this design is shown in Figure 1.10.

The active region consists of four quantum wells which result in three coupled lower states. The middle state (E_2) is spaced from its neighboring states (E_1 and E_3) by the energy separation equal to the optical phonon energy. This separation yields much faster electron extraction from lower laser energy level E_3 that is a crucial requirement to achieve population inversion. The wavefunction leakage into the injector region also boosts efficient carrier extraction. This design resulted in devices with high output powers and high temperature operation [22].

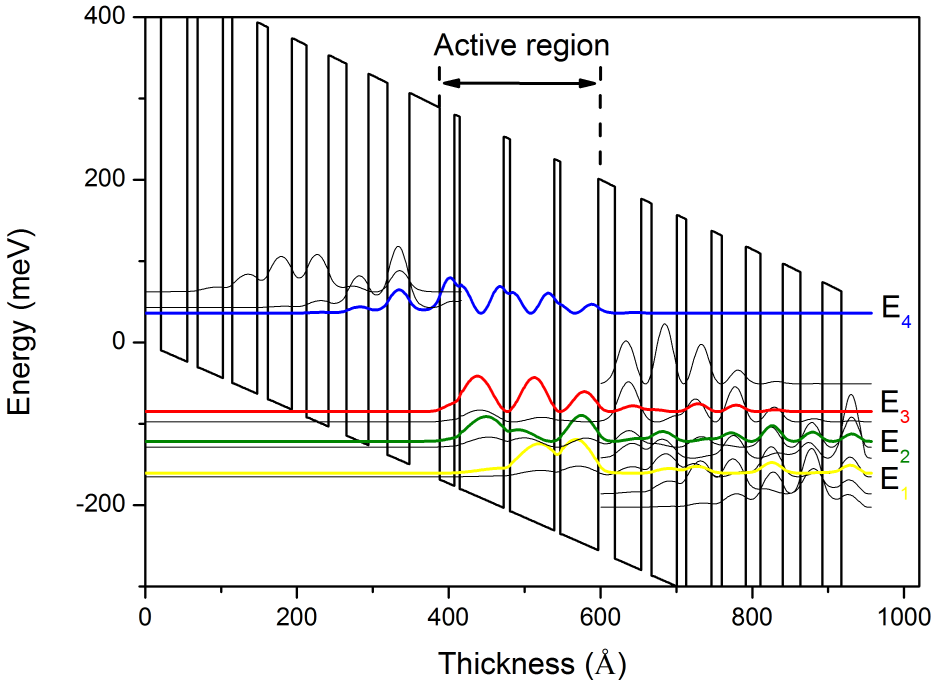

Figure 1.10: Double phonon resonance design. The radiative transition occurs between energy level E_4 and energy level E_3. Energy level E_2 is separated from energy levels E_3 and E_1 by the optical phonon energy to enhance carrier depopulation. Similarly to the three-quantum-well design, the radiative transition can be both vertical or diagonal. The design is taken from Appendix A.2.1 in Ref. [37].

Bound-to-Continuum active region

The bound-to-continuum active region, in general, is very similar to the double phonon resonance design with the main difference being a thinner exit barrier (see Figure 1.11). This results in stronger coupling between the lower coupled states and the bridging region, thus forming a continuum of states and increasing the extraction efficiency even further. The bound-to-continuum active region design can be seen as an evolution of the active region based on superlattices. The upper level of this design is similar to the four-quantum-well design with efficient carrier injection through the barrier into the upper laser level.

As a result bound-to-continuum design provides an efficient approach for maintaining high

population inversion and low threshold current densities even at high temperatures. Most of the devices with good temperature dissipation are made utilizing this active region design [21, 31, 33, 40], capable of maintaining emission at temperatures as high as $400K$ [41]. Additionally, due to efficient wavefunction penetration into the bridging region, the charge carriers have reduced probability to thermally backfill the lower laser energy level, thus maintaining population inversion in the active region.

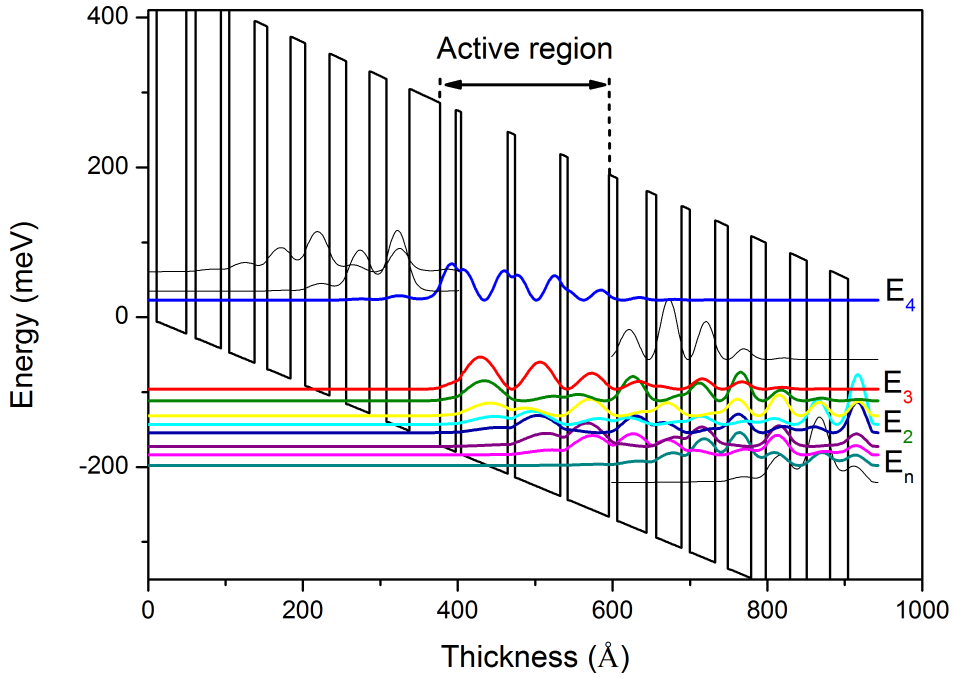

Figure 1.11: Bound to continuum design. The radiative transition occurs between energy level E_4 and E_3, following by the non-radiative transitions into the continuum of the lower energy states (E_n).

1.4.4 The waveguide

In order for laser action to occur, the light has to be guided inside the optical cavity. This is usually achieved with the help of waveguides, confining the light in the required region. The light confinement is attained through the phenomenon known as total internal

reflection according to *Snell's law*. This is achieved by making waveguide claddings from optically less-dense medium compared to that of the laser core region. Optical waveguides of mid-infrared lasers usually exhibit higher internal cavity losses and have thicker cladding layers compared to near-infrared lasers [42–44].

For devices emitting in a far-infrared spectral region the cladding thickness is the limiting factor for efficient performance. Thicker claddings create growth problems due to the defect introduction [42, 43]. Also, due to the very short upper-level lifetime for the intersubband transition, the optical gain is achieved at the cost of very large power dissipation. As a result, thinner cladding layers are preferred due to better thermal extraction.

The optimum quantum cascade laser waveguide would need to fulfill the requirements of minimal optical losses arising from the transverse-magnetic (TM) polarized mode, originating from the intersubband transitions according to the selection rules.

The material choice for the waveguides is dictated by the material used in the core region. For example, a core region made of $InGaAs/AlInAs$ material grown on InP substrate can use InP cladding, due to its lower refractive index. A laser core grown on $GaAs$ substrates cannot use low-doped $GaAs$ material to clad this core region thus alternative approaches have to be developed.

The main purpose of the claddings is to confine the light in the vertical direction. The horizontal confinement is usually achieved through the ridge definition. The vertical confinement is typically less lossy due to the gradual transition of the refractive indexes in the epitaxial layers as opposed to the confinement achieved through the abrupt refractive index drop at the ridge/air interface.

1.4.5 Material consideration for laser growth

The reason that the intersubband transition devices are so spectrally versatile is that the wavelength can be tuned using bandgap engineering techniques, unlike the interband

transitions in bulk materials, where the radiative transition is determined by the band gap. As a result, a large range of wavelengths can be achieved covering all of the mid-infrared spectral region. However, not all materials behave the same way, some perform better and are easier to grow than the others. The main characteristic properties of the material considered for growth are its conduction band offset (ΔE_c), the electron effective mass (m^*) and its thermo-electrical properties. The conduction band offset determines the shortest achievable wavelength, approximated empirically by $E_{\lambda_{max}} \approx \Delta E_c/2$. The reason for this limitation arises from the fact that the electrons from the upper laser level can be thermally excited into the continuum states at the Γ point or states in the lateral X and L valleys. Smaller m^* increases the dipole matrix element as well as providing longer non-radiative transition times, creating higher optical gain as described in Section 2.1. Thermal conductivity, especially that of the cladding material, enhances heat extraction from the laser core thus improving the performance.

InGaAs/AlInAs/InP

The first QCL was grown using a $In_{0.53}Ga_{0.47}As/Al_{0.48}In_{0.52}As$ heterostructure on a InP substrate. This type of material system is the most commonly used due to its relatively high conduction band offset ($\sim 0.52\ eV$), low electron effective mass ($m^* = 0.043m_0$ in $In_{0.53}Ga_{0.47}As$) and good thermal conductivity properties as well as low refractive index of the InP substrate, allowing it to be used for the waveguide cladding. The strain balanced techniques (see Section 1.4.6) allows higher intersubband energy separation to be achieved while keeping the overall strain across the superlattice close to zero. Room temperature CW operation has been demonstrated between 3.0 μm [31] and $\sim 9\ \mu m$ [23] with pulsed operations reaching the wavelengths as long as $\sim 80\ \mu m$ [45] showing the versatility of this material system.

GaAs/AlGaAs

The first laser based on $GaAs/AlGaAs$, operating in pulsed mode up to 140 K, was demonstrated by Sirtori *et al.* working at Thomson-CSF (now Thales) in collaboration with the University of Neuchâtel [46]. This material system has a lot of advantages, one of the most important being that lattice constant of $Al_{(x)}Ga_{(1-x)}As$ for any mole concentration of Al $(0 > x > 1)$ is almost identical of that of $GaAs$ (see Figure 1.12), allowing a wide flexibility in wavelength design without the consequence of creating strained systems. Also, the complexity of epitaxial growth is minimized by reducing the number of varying materials (only Al is varied) during the growth, potentially reducing the number of defects and dislocations. The larger diameter of available wafers (4" and 6") makes this material system more attractive for commercialization purposes.

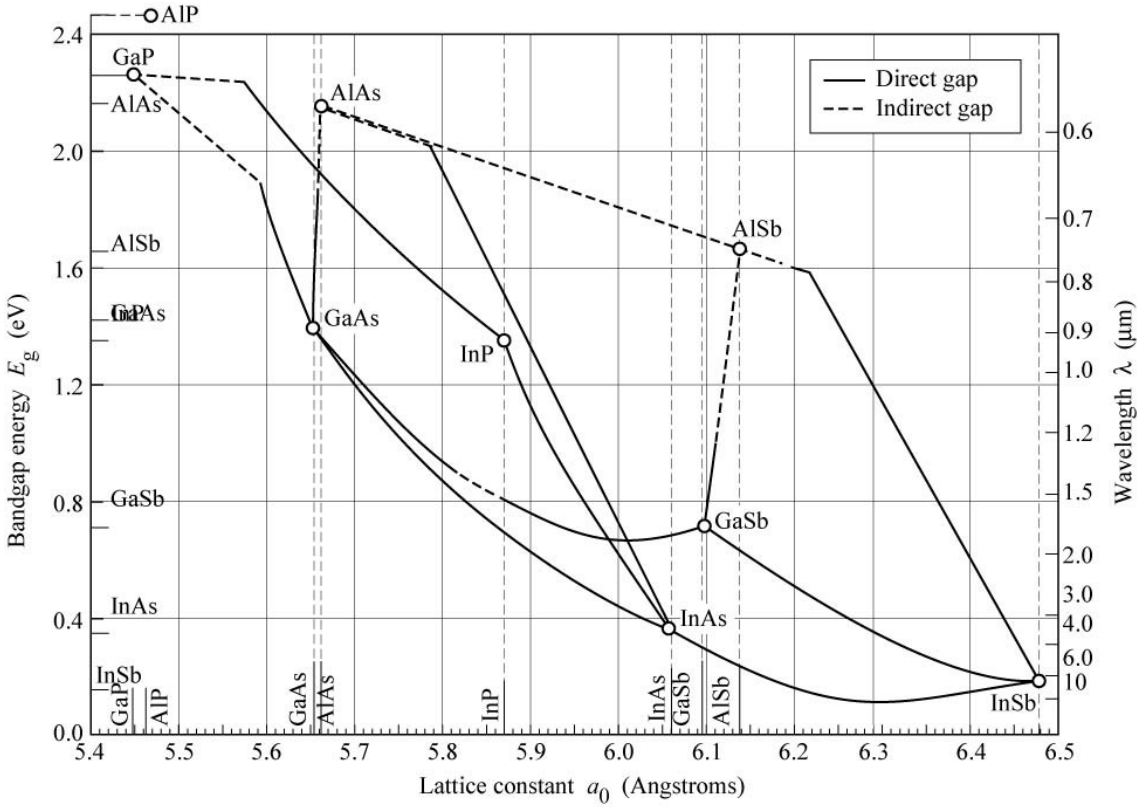

Figure 1.12: Bandgap energy and lattice constant of various III-V semiconductors at room temperature (adopted from Tien, 1988).

However, much heavier electron mass ($m^* = 0.067m_0$ in $GaAs$) makes devices grown with this type of material inferior to previously described $InGaAs/AlInAs$ lasers. The first room temperature pulsed operation was demonstrated in 2001 by Page *et al.* [47], higher temperatures were achieved at longer wavelengths of $\lambda \sim 10.8\ \mu m$ [48]. The small conduction band offset of $GaAs/Al_{(x)}Ga_{(1-x)}As$ heterostructure ($\Delta E_c \approx 0.4\ eV$ for $x = 0.45$) limits the shortest achievable wavelength to 7.5 μm at low temperature [49] and $\sim 8.5\ \mu m$ at room temperature [50]. For larger Al concentrations (for $x > 0.45$) the alloy becomes an indirect gap semiconductor, inhibiting the lasing due to the upper laser level state at Γ point being placed higher than the lowest X state in the injection barrier. It has been demonstrated in Ref. [51] that structures with the upper laser energy level placed above the injection barrier X state showed no lasing due to carrier leakage arising from intervalley ($\Gamma - X$) electron transfer.

Another major inconvenience of this material system is the unsuitability of $GaAs$ substrate to be used for cladding layers. Unlike InP material, that allows it to be used as a substrate and an upper cladding, $GaAs$ has higher refractive index than $GaAs/AlGaAs$ core, making it unsuitable for vertical confinement of the optical mode inside the core region. Conventionally, highly doped n-$GaAs$ or metallic surface plasmon layers are used for the cladding formation.

1.4.6 Short wavelength heterostructures

The $In_{0.53}Ga_{0.47}As/Al_{0.48}In_{0.52}As$ material systems is lattice matched to InP substrate allowing wide variation in band engineering for different wavelength generation. However, most of the reported devices performed in a longer mid-infrared region at the wavelengths $\lambda > 5.5\ \mu m$. This is mainly because the conduction band offset of $E_c = 520\ meV$ of lattice matched $In_{0.53}Ga_{0.47}As/Al_{0.48}In_{0.52}As$ is too small to accommodate shorter wavelength transitions without electron leakage into the superlattice continuum. An increase in the conduction band discontinuity would improve the chances of short wavelength genera-

tion.

Another important consideration that has to be taken into account for the choice of short wavelength material is the position of lateral valleys (L and X). Lateral valleys are known to have large electron effective mass and therefore large density of states in *III-V* semiconductors. Correspondingly, the upper laser intersubband level must be placed energetically far enough below the lateral valley to prevent current leakage and performance degradation. Adverse effects of the current leakage into the lateral valleys have been demonstrated in high-pressure experiments by Jin *et al.* [52].

This section discusses different types of materials that can be used for short mid-infrared wavelength generation.

Strain compensated InGaAs/AlInAs

The concept of strain compensation in a QCL device was first demonstrated by Faist *et al.* in 1998 [53] observing emission of $\sim 3.4\ \mu m$. This group used compressively strained $In_{(x)}Ga_{(1-x)}As$ wells with $x > 0.53$ and tensile strained $Al_{(y)}In_{(1-y)}As$ barriers with $y < 0.52$ to achieve higher conduction band discontinuity. The concept relies on the fact that the cumulative strain in the system is kept close to zero, since the compressive and tensile strains are equal in magnitude and act in the opposite directions. This technique allowed heterostructure material to be grown carefully lattice matched to the substrate so that bulk layers would not develop dislocations due to the strain between the epitaxial layers.

The benefit of using strain compensated $InGaAs/AlInAs$ includes the increase of conduction band discontinuity by about $200-250\ meV$ as compared to the unstrained lattice matched system, the lateral valleys discontinuity shifts to higher energies, reducing potential current leakage. Since the strained system is lattice matched on InP substrate, it allows InP to be used as a waveguide, benefiting from its good optical and thermal properties.

Continuous wave operation with output powers as high as 5.1 W emitting at $\lambda \sim 4.9\ \mu m$ with the threshold current density of $J_{th} = 1.37\ kA/cm^2$ at room temperature [34] has been demonstrated in 2011. Emission wavelengths as short as $\lambda \sim 3.0\ \mu m$ with the threshold current density at room temperature as low as $J_{th} = 1.97\ kA/cm^2$ [31] has also been established using this material system in 2012.

InAs/AlSb

Another promising material system for short wavelength generation is $InAs/AlSb$ grown on $InAs$ substrate. This heterostructure possess large band discontinuity of $\Delta E_c = 2.1\ eV$ [54] suitable for short wavelength generation. $InAs$ quantum wells also have lighter electron effective mass of $m^* = 0.023m_0$ compared to $m^* = 0.043m_0$ in $InGaAs$ enabling larger optical gain and potentially smaller current threshold values [55]. In addition, satellite L and X valleys are placed about $\sim 0.8\ eV$ above the Γ valley minimum in $InAs$ [56].

While this heterostructure has a lot of potential for short wavelength QCLs, it has a few complications associated with its properties and growth techniques. $InAs$ substrate has low band gap energy ($E_{gap} = 350\ meV$), making it susceptible to interband absorption exceeding these energies. Slightly mismatched lattice constant and the fact that $InAs/AlSb$ interface do not share a common atom creates a condition where either $In-Sb$ or $Al-As$ interface bonds can be favored, introducing additional strain to the material system.

Low doped $InAs$ alloy, similarly to previously described low doped $GaAs$, has high refractive index, preventing it being used as a waveguide cladding. In 2002 and 2003, Ohtani and Ohno working at Tohoku university in Japan overcame this problem by using a combination of high-doped ($3 \times 10^{18} cm^{-3}$) and low-doped ($2 \times 10^{16} cm^{-3}$) $InAs$ layers as a cladding layer to surround the laser core. The carrier plasma in the heavily doped layers provides the refractive index reduction required for light confinement. This plasmon enhanced waveguide enabled the first quantum cascade laser based on $InAs/AlSb$ het-

erostructure at $\sim 10\ \mu m$ [57, 58]. The same technique was adopted by Baranov's group at the University of Montpellier demonstrating shorter wavelength emissions at 6.7 μm [59] and 4.6 μm [26] with devices operating up to 220 K and 300 K respectivelly. But, as mentioned above, shorter wavelength generation could not be observed, due to interband absorption of $InAs$. The shortest wavelength, using plasmon enhanced waveguide layers was demonstrated to stand at $3.5 - 3.65\ \mu m$ at low temperatures [60]. In 2006, Devenson *et al.* working at the University of Montpellier, demonstrated a different waveguide approach, achieving $\lambda \sim 3\ \mu m$ emission with $InAs/AlSb$ system [29] where $InAs$ spacer layers were replaced with $InAs/AlSb$ superlattice with lower refractive index. The interband absorption of $InAs$ cladding layers was avoided by high doping ($N_d = 3 \times 10^{19}\ cm^{-3}$) shifting the absorption edge by conduction band filling. The absorption within the superlattice was avoided by ensuring that it did not contain any energy levels separated close to the designed laser emission frequency. Since the discovery, this group has demonstrated short wavelength emission of 2.75 μm at 80 K [61] and sub - 3 μm radiation at room temperature [62]. High emission powers of over 1 W at $\lambda \sim 3.3\ \mu m$ at 300 K were shown a year later [63].

Despite some impressive results, this material systems still has shortcomings. The thermal conductivity of InP cladding layers (65 $WK^{-1}m^{-1}$) for short wavelength QCLs are twice as good as those found in the $InAs$ based cladding layers (27 $WK^{-1}m^{-1}$) and many times higher than superlattice layers (2 $WK^{-1}m^{-1}$) used as spacers between the core region and the cladding [64], resulting in a typically higher threshold current densities ($10 - 20\ kW/cm^2$) for devices emitting below $\lambda = 4\ \mu m$. As a result, the first continuous wave emission has been demonstrated at longer, $\lambda = 10\ \mu m$ wavelength at $T = 255\ K$ with the output power of 0.8 W [64]. In conclusion, this material system can successfully emit wide range mid-infrared wavelengths, with reported values from 2.63 μm [6] up to 21 μm at room temperature [65]. The successful integration into external cavity system has also allowed pulsed, room temperature single mode operation at short mid-infrared wavelength range [66].

InGaAs/AlAsSb

From Figure 1.12 one can notice that substituting $Al_{0.48}In_{0.52}As$ barriers with $Al_{0.56}AsSb_{0.44}$ creates large lattice matched conduction band offset. The conduction band discontinuity of $\Delta E_c \sim 1.6\ eV$ [67] is very well suited for short wavelength generation. The group led by J.W. Cockburn at the University of Sheffield was the first one to try this new heterostructure in quantum cascade laser design. The benefit of the larger band gap, however, comes with associated drawbacks primarily related to the crystal growth. The epitaxial growth of alloys dominated by group V materials, such as $AlAsSb$ is much more challenging than that consisting mainly of group III materials like $InGaAs$ and $AlInAs$. Higher level of precision and growth parameter optimization are required due to more sensitive growth conditions induced by group V atoms [68]. Furthermore, $AlAsSb$ possesses large miscibility gap [69, 70], resulting in atoms tending to form energetically more favorable binary compounds over the intended ternary alloys. Careful control of temperature and deposition rate allow MBE growth within this gap [67]. The growth of high purity wells is also compromised by the tendency of Sb to diffuse into the neighboring quantum well layers. This problem has been countered by growth interruption and ensuring As termination between $InGaAs$ and $AlAsSb$ layers [67, 71].

Despite these growth problems and difficulties associated with the intersubband physics of this material system, the first electroluminescence [72, 73] and then lasing at $\lambda \sim 4.3\ \mu m$ [74] was demonstrated by Revin *et al.* at the University of Sheffield in 2004 using $In_{0.53}Ga_{0.47}As/AlAs_{0.56}Sb_{0.44}$ heterostructure lattice matched to InP substrate. A year later, Yang *et al.* at the Fraunhofer Institute demonstrated high temperature operation at $\lambda \sim 4.6\ \mu m$ [75] and at $\sim 3.7-3.9\ \mu m$ up to 310 K [76]. In 2007, Sheffield university group demonstrated laser emission at $\sim 3.5\ \mu m$ and $\sim 3.05\ \mu m$ at liquid nitrogen temperatures [74]. This work led to the strain compensated approach ($In_{0.67}Ga_{0.33}As/AlAs_{0.8}Sb_{0.2}$) realizing better laser performance at wavelength of $\lambda \sim 3.1\ \mu m$ [28]. The same group demonstrated devices operating up to $T = 400\ K$ at $\lambda = 3.3\ \mu m$ [40] a year later, with

peak output powers exceeding 20 W at $T = 285$ K [77].

1.5 Applications

The unique emission wavelength, wide tuning capabilities, high output powers and high temperature tolerances have made QC lasers very desirable for industrial applications. The possibility of making a mid-infrared free space optical link has raised interest in high frequency modulation of these devices. Gas sensing spectroscopy still remains the main application for mid-infrared laser sources. The brief overview of possible and existing utilization of the quantum cascade lasers is described in this section.

1.5.1 Gas sensing

Laser based spectroscopic techniques have a great potential for sensitive, non-invasive trace gas measurements. The ability to operate at a range of wavelengths in the important mid-infrared spectral region makes quantum cascade laser spectroscopy a very important and useful technique. Rotational-vibrational modes of the gas molecules tend to cover a wide range of frequencies, with the fundamental modes covering the significant portion of the mid-infrared and far-infrared spectrum. The advantage of using fundamental modes for spectroscopy, over its overtones is the increased oscillator strength, making the transitions stronger from 100 times for methane (CH_4) to $25,000$ times for nitric oxide (NO) compared to the absorption strengths at the near-infrared and visible wavelength regions.

The general principle of the laser based spectroscopy consists of the emission intensity monitoring as the beam passes through a gas. The laser emission is frequency tuned and the emission signal is recorded. The intensity at the emission frequency corresponding to the ro-vibrational absorption modes of the gas is reduced according to the concentration of the measurable compound.

1.5.2 Telecommunications

Another attractive use of quantum cascade lasers is to create free space optical link between two points for the telecommunication signal transmission where optical fibers are not available or difficult to implement. The optical link could be established through the atmosphere in a direct line of sight with minimal atmospheric absorption losses. Fast free-space data links would be particularly useful to momentarily increase the bandwidth, create high-bandwidth connections where fiber optics is inaccessible, difficult to implement (urban areas) or economically not viable. The choice of light emitter and its wavelength has to meet certain criteria for the idea to be feasible:

- The atmosphere has to be transparent at the emission wavelength
- Safe for eye exposure
- High frequency modulation hardware availability at the operating wavelength
- Resistance to solar scintillation and weather conditions (eg. fog, rain, etc.)

The atmosphere has a few spectral regions where the optical absorption is very close to zero, called atmospheric windows. An electromagnetic spectral transmission windows are found at 800 nm, 1.5 μm, $3-4$ μm and $8-10$ μm spectral range. The telecommunication wavelength, $\lambda = 1.55$ μm, has a clear advantage owing to the available modulation hardware, potential coherent integration with the readily available fiber optic technology and semi eye-safe operation. The 800 nm wavelength offers broader range of sensitive detectors based on Si avalanche photodiodes, however both of these near-infrared wavelengths lie close to the peak of the solar spectrum, making the free-space optical link vulnerable to the scintillation from the objects in the atmosphere, such as dust particles.

The mid-infrared channels at $3-4$ μm and $8-10$ μm are placed further away from solar peak, making the transmitted signal less susceptible to solar glare. The huge advantage of free space data transmission at these wavelengths is the reduced scattering from the fog and rain particles due to the Rayleigh scattering dependence of λ^{-4}. Computational

simulations show that the mid-infrared range is more advantageous over near-infrared in extending link distance by the factor of 3 to 10 [78]. Quantum cascade lasers can produce such wavelengths as well as respond to high frequency modulation [79] producing high powers required for data transfer [80, 81].

References

[1] R. Yang. Infrared laser based on intersubband transitions in quantum wells. *Superlattice Microstructures*, 17:77, 1995.

[2] J.R. Meyer, I. Vurgaftman, R.Q. Yang, and L.R. Ram-Mohan. Type-II and type-I interband cascade lasers. *Electronic letters*, 32:45–46, 1996.

[3] C.J. Hill, C.M. Wong, B. Yang, and R.Q. Yang. Type-II interband cascade lasers emitting at wavelengths beyond 5.1 μm. *Electronic letters*, 40(14):878–879, 2004.

[4] C.L. Canedy, J. Abell, C.D. Merritt, W.W. Bewley, C.S. Kim, M. Kim, I. Vurgaftman, and J.R. Meyer. Pulsed and CW performance of 7-stage interband cascade lasers. *Optics Express*, 22:7:7702–7710, 2014.

[5] C. S. Kim, M. Kim, J. Abell, W. W. Bewley, C. D. Merritt, C.L. Canedy, I. Vurgaftman, and J.R. Meyer. Mid-infrared distributed-feedback interband cascade lasers with continuous-wave single-mode emission to 80^oC. *Appl. Phys. Lett.*, 101:061104–061104–3, 2012.

[6] O. Cathabard, R. Teissier, J. Devenson, J. C. Moreno, and A. N. Baranov. Quantum cascade lasers emitting near 2.6 μm. *Appl. Phys. Lett.*, 96:141110, 2010.

[7] C. Walther, M. Fischer, G. Scalari, R. Terazzi, N. Hoyler, and J. Faist. Quantum cascade lasers operating from 1.2 to 1.6 THz. *Applied Physics Letters*, 91:131122, 2007.

[8] R.F. Kazarinov and R.A. Suris. Possibility of amplification of electromagnetic waves in a semiconductor with a superlattice. *Sov. Phys. Semicond.*, 5:707, 1971.

[9] R.F. Kazarinov and R.A. Suris. Electric and electromagnetic properties of semiconductors with a superlattice. *Sov. Phys. Semicond.*, 6:120, 1972.

[10] A. Cho. *Molecular beam epitaxy.* AIP Press, Woodbury, 1994.

[11] L. C. West and S. J. Eglash. First observation of an extremely large-dipole infrared transition within the conduction band of GaAs quantum well. *Appl. Phys. Lett.*, 46: 1156, 1985.

[12] F. Capasso, K. Mohammed, and A.Y. Cho. Resonant tunneling through double barriers, perpendicular quantum transport phenomena in superlattices, and their device applications. *IEEE Journal of Quantum Electronics*, 22:1853, 1986.

[13] M. Helm, P. England, E. Colas, F. DeRosa, and S. Allen Jr. Intersubband emission from semiconductor superlattices excited by sequential resonant tunneling. *Phys. Rev. Lett.*, 63:74, 1989.

[14] H.C Liu. A novel superlattice infrared source. *J. Appl. Phys.*, 63:2856, 1988.

[15] A. Kastalsky, V.J. Goldman, and J.H. Abeles. Possibility of infrared laser in a resonant tunneling structure. *appl. Phys. Lett.*, 59:2636, 1991.

[16] S.I. Borenstain and J.Katz. Evaluation of the feasibility of a far-infrared laser based on intersubband transitions in $GaAs$ quantum wells. *Appl. Phys. Lett.*, 55:654, 1989.

[17] Q. Hu and S. Feng. Feasibility of far-infrared lasers using multiple semiconductor quantum wells. *Appl. Phys. Lett.*, 59:2923, 1991.

[18] P. Yuh and K.L. Wang. Novel infrared band-aligned superlattice laser. *Appl. Phys. Lett.*, 51:1404, 1987.

[19] J. Faist, F. Capasso, D. L. Sivco, C. Sirtori, A. L. Hutchinson, and A. Y. Cho. Quantum cascade laser. *Science*, 264:553, 1994.

[20] J. Faist, F. Capasso, C. Sirtori, D. L. Sivco, J. N. Baillargeon, A. L. Hutchinson, Sung-Nee G. Chu, and A. Y. Cho. High power mid-infrared ($\lambda \sim 5$ μm) quantum cascade lasers operating above room temperature. *Appl. Phys. Lett.*, 68:3680, 1996.

[21] J. Faist, M. Beck, T. Aellen, and E. Gini. Quantum cascade laser based on a bound-to-continuum transition. *Appl. Phys. Lett.*, 78:147, 2001.

[22] D. Hofstetter, M. Beck, T. Aellen, and J. Faist. High temperature operation of distributed feedback quantum-cascade lasers at 5.3 μm. *Appl. Phys. Lett.*, 78:396, 2001.

[23] M. Beck, D. Hofstetter, T. Aellen, J. Faist, U. Oesterle, M. Ilegems, E. Gini, and H. Melchior. Continuous wave operation of a mid-infrared semiconductor laser at room temperature. *Science*, 295:301, 2002.

[24] J.S. Roberts, R. P. Green, L. R. Wilson, E. A. Zibik, D. G. Revin, J. W. Cockburn, and R.J. Airey. Quantum cascade lasers grown by metalorganic vapour phase epitaxy. *Appl. Phys. Lett.*, 82:4221, 2003.

[25] R. P. Green, A. Krysa, J.S. Roberts, D. G. Revin, L. R. Wilson, E. A. Zibik, W.H. Ng, and J. W. Cockburn. Room-temperature operation of $ingaas/alinas$ quantum cascade lasers grown by metalorganic vapor phase epitaxy. *Appl. Phys. Lett.*, 83:1921, 2003.

[26] R. Teissier, D. Barate, A. Vicet, C. Alibert, A. N. Baranov, X. Marcadet, C. Renard, M. Garcia, C. Sirtori, D. Revin, and J. Cockburn. Room temperature operation of $InAs/AlSb$ quantum cascade lasers. *Appl. Phys. Lett.*, 85:167, 2004.

[27] D. G. Revin, L.R. Wilson, E.A. Zibik, R.P. Green, J.W. Cockburn, M.J. Steer, R.J. Airey, and M. Hopkinson. $InGaAs/AlAsSb$ quantum cascade lasers. *Appl. Phys. Lett.*, 85:3992, 2004.

[28] S. Y. Zhang, D. G. Revin, J. W. Cockburn, K. Kennedy, A. B. Krysa, and M. Hopkinson. $\lambda \sim 3.1\,\mu m$ room temperature $InGaAs/AlAsSb/InP$ quantum cascade lasers. *Appl. Phys. Lett.*, 94:031106, 2009.

[29] J. Devenson, D. Barate, O. Cathabard, R. Teissier, and A. N. Baranov. Very short wavelength ($\lambda = 3.1 - 3.3\,\mu m$) quantum cascade lasers. *Appl. Phys. Lett.*, 89:191115, 2006.

[30] J. Faist, C. Gmachl, F. Capasso, C Sirtori, D. L. Sivco, J. N. Baillargeon, and Al-

fred Y. Cho. Distributed feedback quantum cascade lasers. *Appl. Phys. Lett.*, 70: 2670, 1997.

[31] N. Bandyopadhyay, Y. Bai, S. Tsao, S. Nida, S. Slivken, and M. Razeghi. Room temperature continuous wave operation of $\lambda \sim 3 - 3.2$ μm quantum cascade lasers. *Appl. Phys. Lett.*, 101:241110, 2012.

[32] R. Darvish, S. Slivken, A. Evans, J.S. Yu, and M. Razeghi. Room-temperature, high-power, and continuous-wave operation of distributed-feedback quantum-cascade lasers at $\lambda \sim 9.6$ μm. *Appl. Phys. Lett.*, 88:201114, 2006.

[33] Y. Bai, S. Slivken, S. Kuboya, S.R. Darvish, and M. Razeghi. Quantum cascade lasers that emit more light than heat. *Nature Photonics*, 4:99–102, 2010.

[34] Y. Bai, N. Bandyopadhyay, S. Tsao, S. Slivken, and M. Razeghi. Room temperature quantum cascade lasers with 27% wall plug efficiency. *Appl. Phys. Lett*, 98:181102, 2011.

[35] Y. Bai, S. Slivken, S.R. Darvish, A. Haddadi, B. Gokden, and M. Razeghi. High power broad area quantum cascade lasers. *Appl. Phys. Lett*, 95:221104, 2009.

[36] C. Sirtori, J. Faist, F. Capasso, D. L. Sivco, A. L. Hutchinson, and A. Y. Cho. Long wavelength infrared $\lambda \sim 11$ μm quantum cascade lasers. *Appl. Phys. Lett.*, 69:2810, 1996.

[37] J. Faist. *Quantum Cascade Lasers*. Oxford University Press, 2013.

[38] K. Choi, B. Levine, R. Malik, and J. Walker ad C. Bethea. Periodic negative conductance by sequential resonant tunneling through an expanding high-field superlattice domain. *Phys. Re. B*, 35(8):4172–4175, 1987.

[39] J. Faist, F. Capasso, C. Sirtori, D. L. Sivco, A. L. Hutchinson, S. Chu, and A. Y. Cho. Narrowing of the intersubband electroluminescent spectrum in coupled-quantum well heterostructures. *Appl. Phys. Lett.*, 65, 1994.

[40] J. P. Commin, D. G. Revin, S. Y. Zhang, A. B. Krysa, K. Kennedy, and J. W. Cockburn. High peak power $\lambda \sim 3.3$ and $3.5\,\mu m$ InGaAs/AlAs(Sb) quantum cascade lasers operating up to 400 K. *Appl. Phys. Lett.*, 97:031108, 2010.

[41] J. P. Commin, D. G. Revin, S. Y. Zhang, A. B. Krysa, and J. W. Cockburn. High performance, high temperature $\lambda \sim 3.7\,\mu m$ InGaAs/AlAs(Sb) quantum cascade lasers. *Appl. Phys. Lett.*, 95:111113, 2009.

[42] A. Tredicucci, C. Gmachl, F. Capasso, D.L. Sivco, A.L. Hutchinson, and A.Y. Cho. Long wavelength superlattice quantum cascade lasers at $\lambda = 17\ \mu m$. *Appl. Phys. Lett.*, 74:638, 1999.

[43] C. Sirtori, C. Gmachl, F. Capasso, J. Faist, D. L. Sivco, A. L. Hutchinson, and A. Y. Cho. Long wavelength ($\lambda = 8-11.5\ \mu m$) semiconductor lasers with waveguides based on surface plasmons. *Opt. Lett.*, 23:1366, 1998.

[44] W.W. Bewley, C. L. Felix, E. H. Aifer, I. Vurgaftman, L. J. Olafsen, J. R. Meyer, H. Lee, R.U. Martinelli, J.C. Connolly, A.R. Sugg, G.H. Olsen, M. Yang, B.R. Bennett, and B.V. Shanabrook. Above-room-temperature optically pumped mid-infrared W lasers. *Appl. Phys. Lett.*, 73:3833, 1998.

[45] M. Fischer, G. Scalari, C. Walther, and J. Faist. Terahertz quantum cascade lasers based on $In_{0.53}Ga_{0.47}As/In_{0.52}Al_{0.48}As/InP$. *Journal of Crystal Growth*, 311:1939, 2009.

[46] C. Sirtori, P. Kruck, S. Barbieri, P. Collot, J. Nagle, M. Beck, J. Faist, and U. Oesterle. $GaAs/al_xga_{1-x}as$ quantum cascade lasers. *Appl. Phys. Lett.*, 73(24):3486, 1998.

[47] H. Page, C. Becker, A. Robertson, G. Glastre, V. Ortiz, and C. Sirtori. 300 K operation of a $GaAs$ - based quantum-cascade lasers at $\lambda \sim 9\ \mu m$. *Appl. Phys. Lett.*, 78:3529, 2001.

[48] C. Pflugl, W. Schrenk, S. Anders, G. Strasser, C. Becker, C. Sirtori, Y. Bonetti,

and A. Muller. High-temperature performance of $GaAs$ - based bound-to-continuum quantum-cascade lasers. *Appl. Phys. Lett.*, 83:4698, 2003.

[49] L.R. Wilson, J.W. Cockburn, M.J. Steer, D.A. Carder, M.S. Skolnick, M. Hopkinson, and G. Hill. Decreasing the emission wavelength of $GaAs-AlGaAs$ quantum cascade lasers by the incorporation of ultrathin $InGaAs$ layers. *Appl. Phys. Lett.*, 78:413, 2001.

[50] D.A. Carder, L.R. Wilson, R.P. Green, J.W. Cockburn, M. Hopkinson, M.J. Steer, R. Airey, and G. Hill. Room temperature operation of an $InAs-GaAs-AlAs$ quantum-cascade laser. *Appl. Phys. Lett.*, 82:3409, 2003.

[51] L.R. Wilson, D.A. Carder, J.W. Cockburn, R.P. Green, D.G. Revin, M.J. Steer, M. Hopkinson, G. Hill, and R. Airey. Intervalley scattering in GaAsAlAs quantum cascade lasers. *Appl. Phys. Lett.*, 81:1378, 2002.

[52] S.R. Jin, C.N. Ahmad, S.J. Sweeney, A.R. Adams, B.N. Murdin, H. Page, X. Marcadet, C. Sirtori, and S. Tomic. Spectroscopy of $GaAs/AlGaAs$ quantum-cascade lasers using hydrostatic pressure. *Applied Physics Letters*, 82(22):221105, 2006.

[53] J. Faist, F. Capasso, D. L. Sivco, A. L. Hutchinson, S-N. G. Chu, and A. Y. Cho. Short wavelength ($\lambda \sim 3.4\,\mu m$) quantum cascade laser based on strained compensated $InGaAs/AlInAs$. *Appl. Phys. Lett.*, 72:680, 1998.

[54] C. Gauer, J. Scriba, A. Wixforth, J.P. Kotthaus, C.R. Bolognesi, C. Nguyen, B. Brar, and H. Kroemer. Energy-dependent cyclotron mass in $InAs/AlSb$ quantum-wells. *Semiconductor Science and Technology*, 9:1580, 1994.

[55] I. Vurgaftman, J.R. Meyer, F.H. Julien, and L.R. Ram-Mohan. Design and simulation of low-threshold antimonide intersubband lasers. *Applied Physics Letters*, 73:711, 1998.

[56] I. Vurgaftman, J.R. Meyer, and L.R. Ram-Mohan. Band parameters for $III-V$

compound semiconductors and their alloys. *Journal of Applied Physics*, 89:5815, 2001.

[57] K. Ohtani and H. Ohno. An $InAs$-based intersubband quantum cascade laser. *Japanese Journal of Applied Physics Part-2 Letters*, 41:L1279, 2002.

[58] K. Ohtani and H. Ohno. $InAs/AlSb$ quantum cascade lasers operating at 10 μm. *Appl. Phys. Lett.*, 82:1003, 2003.

[59] R. Teissier, D. Barate, A. Vicet, D.A. Yarekha, C. Alibert, A. N. Baranov, X. Marcadet, M. Garcia, and C. Sirtori. $InAs/AlSb$ quantum cascade lasers operating at 6.7 μm. *Electronics Letters*, 39:1252, 2003.

[60] J. Devenson, D. Barate, R. Teissier, and A. N. Baranov. Short wavelength ($\lambda = 3.5 - 3.65$ μm) $InAs/AlSb$ quantum cascade lasers. *Electronics Letters*, 42:1284, 2006.

[61] J. Devenson, R. Teissier, O. Cathabard, and A. N. Baranov. $InAs/AlSb$ quantum cascade lasers emitting below 3 μm. *Appl. Phys. Lett.*, 90:111118, 2007.

[62] J. Devenson, O. Cathabard, R. Teissier, and A. N. Baranov. $InAs/AlSb$ quantum cascade lasers emitting at $2.75 - 2.97$ μm. *Appl. Phys. Lett.*, 91:251102, 2007.

[63] J. Devenson, O. Cathabard, R. Teissier, and A. N. Baranov. High temperature operation of 3.3 μm quantum cascade lasers. *Appl. Phys. Lett.*, 91:141106, 2007.

[64] A.N. Baranov and R. Teissier. Quantum Cascade Lasers in the $InAs/AlSb$ Material System. *IEEE Journal of Selected Topics in Quantum Electronics*, 21(6):85–96, 2015.

[65] M. Bahriz, G. Lollia, P. Laffaille, A.N. Baranov, and R. Teissier. $InAs/AlSb$ quantum cascade lasers operating near 20 μm. *Electronics Letters*, 49(19):1238–1240, 2013.

[66] T. Kruczek, K.A. Fedorova, G.S. Sokolovskii, R. Teissier, A.N. Baranov, and E.U. Rafailov. InAs/AlSb widely tunable external cavity quantum cascade laser around 3.2 μm. *Applied Physics Letters*, 102(1):011124, 2013.

[67] N. Georgiev and T. Mozume. Photoluminescence study of $InGaAs/AlAsSb$ heterostructure. *Journal of Applied Physics*, 89:1064, 2001.

[68] S. Nemeth, B. Grietens, and G. Borghs. Compositional dependence of $AlAs_ySb_{1-y}$ ternaries on the ratio of sb/as fluxes and on the substrate-temperature. *Journal of Applied Physics*, 77:3552, 1995.

[69] J.R. Pessetto and G.B. Stringfellow. $Al_xGa_{1-x}As_ySb_{1-y}$ phase-diagram. *Journal of Crystal Growth*, 62:1, 1983.

[70] V.S. Sorokin, S.V. Sorokin, A.N. Semenov, B.Y. Meltser, and S.V. Ivanov. Novel approach to the calculation of instability regions in $GaInAsSb$ alloys. *Journal of Crystal Growth*, 216:97, 2000.

[71] N. Georgiev and T. Mozume. Effect of growth interruptions on the interfaces of $InGaAs/AlAsSb$ superlattice. *Applied Physics Letters*, 75:2371, 1999.

[72] D. G. Revin, L.R. Wilson, E.A. Zibik, R.P. Green, J.W. Cockburn, M.J. Steer, R.J. Airey, and M. Hopkinson. $\lambda \sim 4 - 5.3\ \mu m$ intersubband emission from $InGaAs - AlAsSb$ quantum cascade structures. *Appl. Phys. Lett.*, 84:1447, 2004.

[73] D. G. Revin, M.J. Steer, L.R. Wilson, R.J. Airey, J.W. Cockburn, E.A. Zibik, and R.P. Green. $InGaAs - AlAsSb$ quantum cascade structures emitting at 3.1 μm. *Electronics Letters*, 4:874, 2004.

[74] D. G. Revin, J. W. Cockburn, M.J. Steer, R. J. Airey, M. Hopkinson, A. B. Krysa, L. R. Wilson, and S. Menzel. $InGaAs/AlAsSb/InP$ quantum cascade lasers operating at wavelengths close to $3\,\mu m$. *Appl. Phys. Lett.*, 90:021108, 2007.

[75] Q. Yang, C. Manz, W. Bronner, C. Mann, L. Kirste, K. Kohler, and J. Wagner. $GaInAs/AlAsSb$ quantum-cascade lasers operating up to 400 K. *Appl. Phys. Lett.*, 86:131107, 2005.

[76] Q.K. Yang, C. Manz, W. Bronner, K. Kohler, and J. Wagner. Room-temperature

short-wavelength ($\lambda \sim 3.7 - 3.9\ \mu m$) $GaInAs/AlAsSb$ quantum-cascade lasers. *Appl. Phys. Lett.*, 88:121127, 2006.

[77] D.G. Revin, J.P. Commin, S.Y. Zhang, A.B. Krysa, K. Kennedy, and J.W. Cockburn. InP-Based Midinfrared Quantum Cascade Lasers for Wavelengths Below 4 μm. *IEEE Journal of Selected Topics in Quantum Electronics*, 17(5):1417–1425, 2011.

[78] M. Achour. Free-space optics wavelength selection: 10 μm versus shorter wavelengths. *Journal of Optical Networking*, 2(6):127, 2003.

[79] R. Martini, C. Gmachl, J. Falciglia, F.G. Curti, C.G. Bethea, F. Capasso, E.A. Whittaker, R. Paiella, A. Tredicucci, A.L. Hutchinson, D.L. Sivco, and A.Y. Cho. High-speed modulation and free-space optical audio/video transmission using quantum cascade lasers. *Electronics Letters*, 37(3):191–193, 2001.

[80] R. Martini, C.G. Bethea, F. Capasso, C. Gmachl, R. Paiella, E.A. Whittaker, H.Y. Hwang, D.L. Sivco, J.N. Baillargeon, and A.Y. Cho. Free-space optical transmission of multimedia satellite data streams using mid-infrared quantum cascade lasers. *Electronics Letters*, 38(4):181–183, 2002.

[81] S. Blaser, D. Hofstetter, M. Beck, and J. Faist. Free-space optical data link using peltier-cooled quantum cascade laser. *Electronics Letters*, 37(12):778–780, 2001.

Chapter 2

Theory

This chapter describes general working principles behind the intersubband semiconductor laser. Firstly, the theoretical treatment of the intersubband gain is studied to understand the process behind the high photon density production inside the optical cavity. The simplified three level intersubband model is then considered to construct conditions required to achieve high gain and population inversion inside the active region. The focus is then shifted to the two cavity types - the more common Fabry-Pérot optical cavity, typically used for multi-mode light generation, and the distributed feedback cavity that is used for efficient single mode production.

2.1 Intersubband gain

The optical gain is an important property of any laser. It describes the efficiency of photon generation inside the laser cavity. In a QCL, the peak material gain G_P, between two subbands - i and j is expressed by [1]:

$$G_P = \frac{4\pi e^2}{\varepsilon_0 n_{ref} \lambda} \frac{z_{ij}^2}{2\gamma_{ij} L_P} (N_j - N_i) \tag{2.1}$$

where e is the electron charge; λ - emission wavelength; n_{ref} is the mode refractive index; z_{ij} - transition dipole matrix element; $2\gamma_{ij}$ is the FWHM of the emission determined from the spontaneous radiation spectrum; N_j and N_i are the sheet electron densities in subbands i and j respectively; and L_P is the single active region period length as described in Reference [2]. The term on the left of the population inversion $(N_j - N_i)$ in Equation 2.1 is often referred to as the gain cross section g_c and is defined as:

$$g_c = \Gamma \frac{4\pi e^2}{\varepsilon_0 n_{ref} \lambda} \frac{z_{ij}^2}{2\gamma_{ij} L_P} \tag{2.2}$$

where Γ is the waveguide confinement factor, specifying the fraction of the optical mode confined inside the core of a QCL. Equation 2.1 demonstrates the quadratic relationship between the optical gain and dipole matrix element z_{ij}. This quadratic dependence influences the material choice in order to maximize the gain.

The quantized energy levels inside the quantum well are inversely proportional to both the particle effective mass m^* and the square of the well width. The electron effective mass for $GaAs$ heterostructure is $m^* = 0.067m_0$, which is larger than that found in the $InGaAs$ heterostructure, meaning that for the same energy level separation, the width of the $GaAs$ wells has to be narrower than those found in the heterostructures grown on InP substrates.

2.2 Rate equations

A simplified three-level active region model can be used to describe the processes inside the gain region of a quantum cascade laser through the analysis of the rate equations. By examining all electronic transitions and the transition rates associated with them, it is possible to describe the conditions required to achieve the population inversion and to define the threshold current density. A schematic diagram of a simplified three-level system is shown in Figure 2.1.

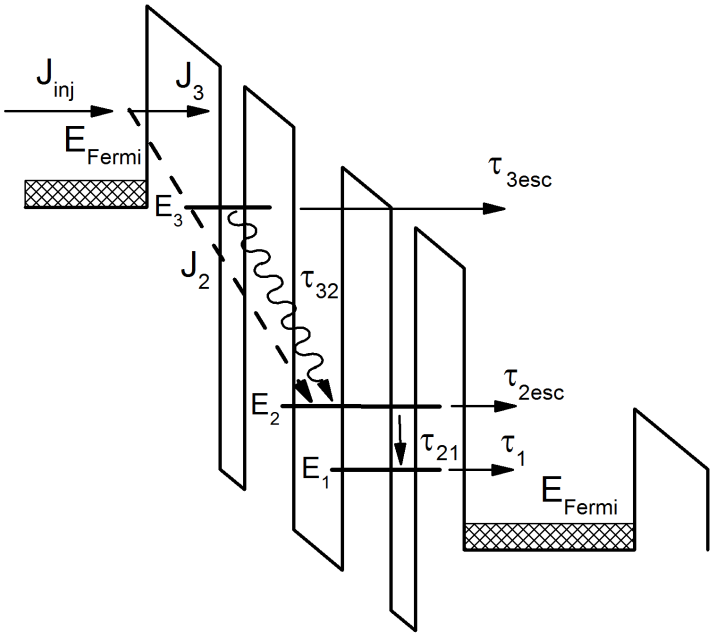

Figure 2.1: Schematic diagram of the simplified three-level active region and all electronic transitions occurring within the active region. Electrons injected into the upper laser energy state E_3 can undergo either radiative transition ($E_3 \rightarrow E_2$) with lifetimes of $\sim 2-3\ ps$ or non-radiative transition with shorter lifetimes ($\sim 200-500\ fs$). The non-radiative transition may include an electron escape process into the continuum, or a phonon assisted recombination.

From the perspective of maximizing the population inversion between the upper and the lower energy states (E_3 and E_2 respectively), the current injection into the upper energy level E_3 is considered to be lossless, hence 100 % injection efficiency. In reality, however, the parasitic current path J_2, might be formed from injector level straight to the lower energy state E_2, reducing the population inversion. The parasitic path J_2 occurs due to current leakage. J_2 is prevalent at small bias, due to electron tunneling into energy level E_2. The leakage current becomes negligible near and above the threshold, since $E_{Fermi} \rightarrow E_3$ route becomes energetically more favorable.

Each potential transition has the associated transition rate τ^{-1}, where τ is the lifetime for which the charge carrier will remain at its initial energy level before making transition to the next level. The carrier injected into E_3 energy level has the possibility to undergo radiative $E_3 \rightarrow E_2$ transition at a rate τ_{32}^{-1}, followed by $E_2 \rightarrow E_1$ transition with associated transition rate τ_{21}^{-1} before exiting the active region into the adjacent injector level described by the transition rate τ_1^{-1}. Non-radiative transitions can also occur and will reduce the efficiency of the device. Such transitions can occur between the upper and the lower energy levels ($E_3 \rightarrow E_1$), with associated transition times τ_{31}^{-1} (not shown on the diagram), or escape E_3 level into the continuum states above the injector miniband with the escape rate τ_{3esc}^{-1}. The escape into the miniband from energy level E_2 is also possible with the associated lifetime τ_{2esc}.

2.2.1 Population inversion

The population inversion can be described by considering the relative electron sheet densities N_3 and N_2 of levels E_3 and E_2 respectively, and the lifetimes associated with the transitions described above. Additionally, N_2^{therm} term describes the equilibrium charge carrier population that can be thermally excited back to the lower energy state E_2 through the thermal backfilling process.The rate of change (dN/dt), of electron population N_3 at level E_3 is given by:

$$\frac{dN_3}{dt} = \frac{J_3}{e} - \frac{N_3}{\tau_{32}} - \frac{N_3}{\tau_{31}} - \frac{N_3}{\tau_{3esc}} \tag{2.3}$$

where J_3 is the current injected into energy level E_3. The same approach can be applied to electron population N_2 at level E_2:

$$\frac{dN_2}{dt} = \frac{J_2}{e} + \frac{N_3}{\tau_{32}} - \frac{N_2}{\tau_{21}} - \frac{N_2}{\tau_{2esc}} + \frac{N_2^{therm}}{\tau_2^{therm}} \tag{2.4}$$

The system, below threshold, can be considered in a steady state when:

$$\frac{dN_3}{dt} = \frac{dN_2}{dt} = 0 \tag{2.5}$$

by substituting Equation 2.3 and 2.4 into Equation 2.5 and setting them to zero it can be shown that:

$$N_3 = \frac{J_3}{e}\left(\frac{1}{\tau_{32}} + \frac{1}{\tau_{31}} + \frac{1}{\tau_{3esc}}\right)^{-1} \tag{2.6}$$

and

$$\frac{N_2}{N_3} = \frac{J_2}{N_3 e}\left(\frac{1}{\tau_{21}} + \frac{1}{\tau_{2esc}} - \frac{1}{\tau_2^{therm}}\right)^{-1} + \frac{1}{\tau_{32}}\left(\frac{1}{\tau_{21}} + \frac{1}{\tau_{2esc}} - \frac{1}{\tau_2^{therm}}\right)^{-1} + \frac{N_2^{therm}}{N_3} \tag{2.7}$$

Substituting Equation 2.6 into Equation 2.7 and assuming that the current density injected into energy level E_3 is much greater compared to the leakage current density J_2, *i.e.* $J_2/J_3 \Rightarrow 0$, we can simplify Equation 2.7 into:

$$\frac{N_2 - N_2^{therm}}{N_3} \approx \frac{1}{\tau_{32}}\left(\frac{1}{\tau_{21}} + \frac{1}{\tau_{2esc}} - \frac{1}{\tau_2^{therm}}\right)^{-1} \tag{2.8}$$

the electron lifetimes τ_{21}, τ_{2esc} and τ_2^{therm}, corresponding to transitions from $E_2 \rightarrow E_1$, E_2 to the miniband and $E_1 \rightarrow E_2$, can be combined into lifetime τ_2, that describe the total lifetime of the electrons spent on level E_2 before undergoing any transition. As a result we arrive at the conclusion that the ratio between electron population N_3 and N_2 is directly proportional to the representative lifetimes of these levels described as:

$$\frac{N_3}{N_2 - N_2^{therm}} \approx \frac{\tau_{32}}{\tau_2} \tag{2.9}$$

As a result, in order to achieve population inversion between levels E_3 and E_2, the corresponding transition lifetime τ_{32} has to be larger than the lifetime τ_2 for which the electrons occupy energy level E_2.

Similarly, the population inversion $\Delta N = N_3 - N_2$ can be calculated applying the steady state condition $dN/dt = 0$ and assuming that the escape rate of the electrons from E_3 directly into the continuum and the current leakage into level E_2 is very small (τ_{3esc}^{-1} and $J_2 \approx 0$), population N_3 and N_2 can be expressed as:

$$N_3 = \frac{J_3}{e}\tau_3 \tag{2.10}$$

and

$$N_2 = \frac{\tau_2}{\tau_{32}}N_3 + N_2^{therm} \tag{2.11}$$

where τ_3 is the total lifetime for which the electrons populate energy level E_3. The population difference ΔN can then be expressed as :

$$\Delta N = \frac{J_3}{e}\tau_3\left(1 - \frac{\tau_2}{\tau_{32}}\right) - N_2^{therm} \tag{2.12}$$

As seen from Equation 2.12, in order to maximize the difference in electron population between two levels, the ratio of two lifetimes corresponding to two energy levels has to approach zero ($\tau_2/\tau_{32} \Rightarrow 0$). The ratio τ_2/τ_{32} approaching zero will result in the increased optical gain, as demonstrated in Equation 2.1, where the direct proportionality ($G_P \propto (N_j - N_i)$ between the population difference of two energy levels is observed.

Commonly, the lifetime of the upper energy level can be increased by reducing the wavefunction overlap in any particular active region design (e.g. the diagonal transition). However, the decreased wavefunction overlap also causes reduction in the matrix element, in turn reducing the gain. A fine balance has to be reached in order to optimize any particular QCL design.

2.2.2 Threshold current density

The expression for the threshold current density J_{th} can be derived similarly to the process described above. The population of the thermally backfilled electrons is temperature dependent according to Equation 2.13:

$$N_2^{therm} = N_g \exp(-\Delta/kT) \tag{2.13}$$

where N_g is the sheet doping density and Δ is the energy difference between the Fermi energy and the lower laser level E_2. Assuming the current leakage is non existent ($J_2 = 0$), previous rate equation 2.4 can be solved for N_2 and N_3, giving:

$$\frac{dN_3}{dt} = \frac{J}{e} - \frac{N_3}{\tau_3} \tag{2.14}$$

where $J = J_3 + J_2 = J_3$ since $J_2 = 0$, and

$$\frac{dN_2}{dt} = \frac{N_3}{\tau_{32}} - \frac{N_2 - N_2^{therm}}{\tau_2} \tag{2.15}$$

similarly, the steady state condition can be considered by setting Equations 2.14 and 2.15 to zero, to obtain:

$$N_3 = \frac{J\tau_3}{e} \tag{2.16}$$

and

$$N_2 = N_3\frac{\tau_2}{\tau_{32}} + N_2^{therm} \tag{2.17}$$

hence the population difference $\Delta N = N_3 - N_2$ can be written as:

$$\Delta N = \frac{J\tau_{eff}}{e} - N_2^{therm} \tag{2.18}$$

where the total electron transition lifetime τ_{eff} is defined as $\tau_{eff} = \tau_3(1 - \tau_2/\tau_{32})$. The current threshold, by definition, is reached when the modal gain equals to the total losses (α_{tot}) experienced by the laser cavity, such as:

$$G_M = \Gamma G_P = \alpha_{tot} \tag{2.19}$$

G_P and Γ, taken from Equations 2.1 and 2.2, can be substituted into Equation 2.19 to obtain:

$$g_c\Delta N = \alpha_{tot} \tag{2.20}$$

substituting population difference ΔN, we obtain:

$$g_c\left(\frac{J\tau_{eff}}{e} - N_2^{therm}\right) = \alpha_{tot} \tag{2.21}$$

Lastly, rearranging for J_{th}, the expression for the current threshold density can be obtained:

$$J_{th} = \frac{\alpha_{tot}/g_c + N_2^{therm}}{\tau_{eff}} e \tag{2.22}$$

The importance of a larger upper state lifetime is apparent. The threshold current density is reduced with large τ_{eff}, where $\tau_{eff} \rightarrow \tau_3$, when $\tau_{32} \gg \tau_2$. Another important term in Equation 2.22 is the total losses α_{tot} experienced by the laser cavity. The threshold is reduced when the losses are lowered. Total losses α_{tot} are typically made of the combination of mirror losses α_m, waveguide losses α_w and losses arising from light reabsorption α_{abs}. High reflectivity coating, careful material consideration and efficient active region design will lower threshold current densities. For example, the first reported QCL was operating at $T = 88\ K$ with the threshold current density as high as $J_{th} = 15\ kA/cm^2$, while the lowest threshold current density for the same material system was demonstrated in 2004, where $J_{th} = 0.5\ kA/cm^2$ was achieved [3]. The operational voltage for these devices varies depending on the emission wavelength. Devices emitting at the higher end of the mid-infrared region ($\lambda \sim 10\ \mu m$) operate at $V = 8 - 12\ V$ bias, while short wavelength mid-infrared emitters ($\lambda \sim 3\ \mu m$) require bias as high as $V - 15 - 25\ V$. The difference in operational voltage comes from the difference of the energy levels inside the active region. Short mid-infrared emitters require higher voltages to achieve the same energy level alignment.

2.3 Fabry-Pérot lasers

The Fabry-Pérot laser cavity is the simplest type of the cavity that provides required feedback for light oscillation to occur. The feedback is received from the two as-cleaved mirrors at each end of the cavity. An uncoated facet will experience reflectivity of about 27 % in InP and $GaAs$ semiconductor devices due to the difference in the semiconductor and the air refractive indexes. Additional coatings can alter the mirror reflectivity anywhere from $\sim 0 - 100$ % depending on the type and purpose of the coating.

As mentioned previously, the light inside the cavity will experience losses α_{tot}, consisting of mirror (α_m), waveguide (α_w) and light re-absorption (α_{abs}) losses. The waveguide losses are typically dominated by free carrier losses but also has a contribution from scattering at the ridge side walls and from material imperfections caused by the growth or fabrication. Since, for an optimum active region design, the losses arising from light re-absorption are much smaller than the losses experienced by the waveguide ($\alpha_{abs} \ll \alpha_w$), they can be ignored for simplicity purposes. The intensity of passing planar wave W in the propagation direction will change exponentially according to:

$$W(z) = W_0 \exp[z(G_m - \alpha_w)] \tag{2.23}$$

where W_0 is the initial intensity of the passing planar wave; α_w is the waveguide associated losses; and G_M is the modal gain expressed as $G_M = \Gamma G_p$. The optical mode intensity after one round trip in a cavity with length L and mirror reflectivity R_1 and R_2 is expressed as:

$$W_{rt} = W_0 R_1 R_2 \exp\big(2L[G_M - \alpha_w]\big) \tag{2.24}$$

The gain threshold is reached when the gain compensates the losses. At this point the round trip intensity of the optical mode is equal to its initial value W_0, i.e.

$$W_{rt} = W_0 \tag{2.25}$$

substituting Equation 2.24 into 2.25, we arrive at:

$$1 = W_0 R_1 R_2 \exp\big(2L(G_{M,th}\Gamma - \alpha_w)\big) \tag{2.26}$$

and the expression for the threshold gain can be expressed as:

$$G_{M,th} = \alpha_w + \frac{1}{2L} ln\left(\frac{1}{R_1 R_2}\right) = \alpha_w + \alpha_m \tag{2.27}$$

Two parallel mirrors at each end of the Fabry-Pérot cavity provide the conditions for the standing wave formation. The standing waves are formed according to:

$$2k_0 n_{eff} L = M \cdot 2\pi \tag{2.28}$$

where k_0 is the wave number, defined as $k_0 = 2\pi/\lambda$. The possible wavelengths of these modes are given by:

$$\lambda = \frac{2n_{eff}L}{M} \tag{2.29}$$

where $M \in \mathbb{N}$, representing the number of nodes of the standing wave. The spacing between two subsequent nodes (M and $M-1$) expressed in wavenumber units cm^{-1}, is:

$$\Delta k = \frac{1}{2Ln_g} \tag{2.30}$$

where $\Delta k = \Delta(\lambda^{-1})$; and n_g is the effective group index $n_g = n_{eff} + dn_{eff}/dk \cdot k$.

A typical semiconductor laser cavity is a few millimeters long, producing modes spaced between $\sim 0.3 - 2\ cm^{-1}$ apart. A typical pulsed QCL has its emission spectra with Full Width at Half Maximum ($FWHM$) $\sim 100 - 300\ cm^{-1}$, depending on the emission wavelength. The emission broadening occurs due to multiple factors including broad gain, temperature gradient during the pulse, the variation in quantum well widths throughout the period, Stark shift and the variation of the position of the lower laser energy levels in Bound to Continuum QCL design. As a result the produced spectra typically consists of the symmetric lines centered around the transition energy separated by the cavity modes. Multimode emission, in many cases, is unsuitable for spectroscopic applications, where single mode is desired.

2.4 Distributed feedback lasers

The main advantage of the distributed feedback laser is its ability to produce single mode emission that can be tailored through different optical feedback techniques. The single mode emission is particularly useful for spectroscopic applications. This section focuses on coupled mode theory that is used to design and evaluate DFB designs.

Kogelnik and Shank were the first to use coupled wave analysis of distributed feedback lasers [4] that is presented in this section. The model is based on the scalar wave equation for the electric field:

$$\frac{\delta^2 E_F}{\delta z^2} + k^2 \cdot E_F = 0 \tag{2.31}$$

where E_F is the complex amplitude of the electric field. The medium constants (n and α), in a DFB structure vary periodically along propagation axis z. This variation can be expressed as the spatial modulation of the refractive index and losses according to:

$$n(z) = n_{eff} + \frac{\Delta n}{2}\cos(2\beta_0 z) \tag{2.32}$$

$$\alpha(z) = \alpha + \frac{\Delta \alpha}{2}\cos(2\beta_0 z) \tag{2.33}$$

where n_{eff} and α are the average refractive and loss indexes of the cavity; values $\Delta n/2$ and $\Delta\alpha/2$ are the amplitudes of variation of these values from their average. Δn and $\Delta\alpha$ can be calculated by determining the maximum values of n_{eff} and α between the grating peaks and troughs. β_0 is the Bragg propagation constant that is tied to the wavelength through:

$$\beta_0 = \frac{m\pi}{\Lambda} = \frac{2\pi n_{av}}{\lambda_b} = k_0(\lambda_b)n_{av} \tag{2.34}$$

where λ_b is the Bragg wavelength. Equation 2.34 can be used to determine the required grating period Λ, for a chosen wavelength amplification, where

$$\Lambda = \frac{m\lambda_b}{2n_{eff}} \tag{2.35}$$

It can be noticed that the grating period is directly proportional to the order of the grating m. Higher order gratings can be fabricated containing larger features that are easier accessible through the standard optical lithography. Chapter 5 describes the process and results used to fabricate the third order grating on a QCL chip. Wave propagation constant k, for a wave propagating in a complex dielectric is defined in Reference [4] as:

$$k^2 = k_0^2 n^2(z)\left(1 + i\frac{2\alpha(z)}{k_0 n(z)}\right) \tag{2.36}$$

where $k_0 = 2\pi/\lambda_0$ is the free space propagation constant. Assuming the variation ampli-

tudes of the refractive index and losses are much smaller than their average values (*i.e.* $\Delta n \ll n_{av}$ and $\Delta\alpha \ll \alpha_{av}$) we can substitute Equation 2.32 and 2.33 into 2.36 to get:

$$k^2 = \beta^2 + i2\beta\alpha(z) + 4\beta\kappa\cos(2\beta_0 z) \tag{2.37}$$

where $\beta = k_0 n(z)$. Rearranging this, we can obtain the coupling coefficient κ. The coupling coefficient indicates the amount of coupling per unit length and plays very important role in the DFB laser design. κ is defined as:

$$\kappa = \frac{\pi\Delta n_{eff}}{2\lambda_0} + i\frac{\Delta\alpha}{4} \tag{2.38}$$

The DFB waveguide will host two counter-propagating waves with respective amplitudes of $R(z)$ and $S(z)$. As a result the total electric field $F(z)$, is expressed as the sum of these two amplitudes:

$$F(z) = R(z)\exp(-i\beta_0 z) + S(z)\exp(-i\beta_0 z) \tag{2.39}$$

Under the assumption that the amplitude variation of these two propagating waves is very small, so that the second derivatives of the wave equation 2.31 can be ignored, we substitute Equation 2.39 and 2.37 into Equation 2.31 to obtain:

$$\frac{-\delta R}{\delta z} + (\alpha - i\delta)R = i\kappa S \tag{2.40}$$

and

$$\frac{-\delta S}{\delta z} + (\alpha - i\delta)S = i\kappa R \tag{2.41}$$

where normalized detuning is given by $\delta \approx \beta - \beta_0 = n(\omega - \omega_0)/c$. In the previously

referenced paper by Kogelnik and Shank, these equations were solved for a device with no mirror reflectivity, creating the boundary conditions as $R(-\frac{1}{2}L) = S(\frac{1}{2}L) = 0$, with the cavity length L. As a result, the field amplitudes can be expressed as:

$$R(z) = \sinh\left(\gamma(z + \frac{1}{2}L)\right) \tag{2.42}$$

$$S(z) = \sinh\left(\gamma(z - \frac{1}{2}L)\right) \tag{2.43}$$

with $\gamma^2 = \kappa^2 + (\alpha - i\delta)^2$ denominating the dispersion relation of the complex propagation constant γ.

While this simplification allows for the easier theoretical treatment, it is difficult to achieve in practice. Even the best anti-reflective coatings can retain small reflectivities, compromising the above assumption. The more complete analysis, taking into account the facet reflectivity and the phase difference, has been made by Streifer *et al.* in Reference [5]. Despite this incomplete treatment, the effect of κL product on the internal electric field can still be studied and is used in Chapter 5 to determine optimal laser length.

2.4.1 Coupling coefficient

As mentioned previously, the coupling coefficient κ, is an important quantity that is used to model and evaluate the performance of a distributed feedback laser. The coupling coefficient depends on the periodic change in losses $\Delta\alpha$ and the modal overlap with the laser core $\Delta\Gamma$ inside the DFB laser structure between the peaks and grooves created by the diffraction grating. The modal overlap will also provide periodic modal gain change ΓG_{th}, where G_{th} is the threshold gain. The coupling coefficient also depends on the shape, order and the *mark:space* ratio of the grating. The coupling is maximized for a rectangular, first order ($m = 1$) grating with 50 % *mark:space* ratio. Any other variation from this will

result in the efficiency reduction by a factor ζ, where $0 \leqslant \zeta \leqslant 1$. The coupling coefficient can be expressed as:

$$\kappa = \left[\frac{\pi \Delta n}{2\lambda_0} + i \frac{\Delta\alpha + (\Delta\Gamma G_{th})}{4} \right] \zeta \tag{2.44}$$

For a non-sinusoidal grating shape, the reduction factor ζ can be estimated from the fundamental Fourier coefficient of the grating shape described in Reference [6]. The grating shape used to fabricate single mode device described in Chapter 5 is rectangular, as a result the reduction factor for the rectangular shape can be calculated using:

$$\zeta(m) = \frac{1}{m} |\sin(\pi m R_{M:S})| \tag{2.45}$$

where $R_{M:S}$ is *mark:space* ratio. The coupling coefficient for different shapes has been derived in Reference [6]. It is important to note that the irregular shape grating will have the reduced coupling coefficient affecting the performance of the device [7]. Misshapen gratings are common during the fabrication process.

References

[1] J. Faist, F. Capasso, C. Sirtori, D.L. Sivco, and A.Y. Cho. *Quantum Cascade Lasers. Intersubband Transitions in Quantum Wells: Physics and Device Applications II.* Academic Press, 1999.

[2] J. Faist, H.C. Liu, and F. Capasso. *Quantum Cascade Lasers, Intersubband Transitions in Quantum Wells: Physics and Device Applications II.* Academic Press, 1999.

[3] S. Slivken, J.S. Yu, A. Evans, J. David, L. Doris, and M. Razeghi. Ridge-width dependence on high-temperature continuous-wave quantum-cascade laser operation. *IEEE Photonics Technology Letters*, 16(3), 2004.

[4] H. Kogelnik and C. Shank. Coupled-wave theory of distributed feedback lasers. *J. Appl. Phys.*, 43:2327, 1972.

[5] W. Streifer, R.D. Burnham, and D.R. Scifres. Effect of external reflectors on longitudinal modes of distributed feedback lasers. *IEEE Journal of Quantum Electronics*, QE11:154–161, 1975.

[6] W. Streifer, D.R. Scifres, and R.D. Burnham. Coupling coefficients for distributed feedback single-heterostructure diode lasers. *IEEE Journal of Quantum Electronics*, 24:867, 1975.

[7] P. Correc. Coupling-coefficients for trapezoidal gratings. *IEEE Journal of Quantum Electronics*, 24:8, 1988.

Chapter 3

Device Growth, Fabrication and Characterization

3.1 Introduction

The transformation of a raw semiconductor material into a working quantum cascade laser is a lengthy, multi stage process typically carried out in a highly controlled clean-room environment. This chapter describes the techniques used to grow the multi-layered wafers from the combination of group *III-V* semiconductors. All short wavelength ($\lambda < 4\ \mu m$) lasers described in this thesis have been grown using *MBE* on InP substrate with the InP cladding overgrown by the *MOVPE* (with the exception of $InAs$ based lasers described in Section 4.3). Lasers used for external cavity experiments ($\lambda > 5\ \mu m$) were exclusively grown in the *MOVPE* reactor here in Sheffield.

The laser fabrication section describes the standard wafer processing steps that were carried out here in the National Centre for $III-V$ Technologies clean rooms to transform a raw wafer into a working laser device. The focus of this chapter is then moved to the laser characterization section where experimental techniques used to measure laser performance

are described.

3.2 Epitaxy

The current semiconductor wafer growth is typically done using two main epitaxial techniques - molecular beam epitaxy (*MBE*) and metal organic vapour phase epitaxy (*MOVPE*). The brief explanation of both systems is given below.

3.2.1 Molecular beam epitaxy

Molecular beam epitaxy (*MBE*) is a high precision and high purity deposition technique used in the semiconductor growth process. *MBE* is very similar to the ultra high vacuum (*UHV*) based evaporation method mainly used for single crystal deposition.

Molecular beam epitaxy has the capability of delivering extremely thin layer films, quite often as low as 1 angstrom thick with high precision. When performing growth at such small scales the defects play an important role. The *MBE* is capable of keeping impurity levels as low as 10 parts per billion [1] providing the chamber is kept at ultra high vacuum conditions (10^{-8} Pa).

A typical *MBE* reactor consists of three chambers that are kept at high vacuum and separated by high vacuum gate valves - a growth chamber, a buffer chamber and a load lock chamber.

The load lock chamber is used to provide an intermediate area between *UHV* growth chamber and the atmosphere. The wafers are being loaded into the lock chamber while keeping the integrity of the vacuum of the growth chamber. This chamber is equipped with a turbomolecular pump, a bake-out heater and a vacuum ion gauge - all required to monitor and reduce the pressure of the loading chamber.

The buffer chamber is used to store loaded wafers under the vacuum condition in order

to prevent atmospheric contamination. The schematic diagram of the growth chamber is shown in Figure 3.1. The growth chamber consists of *UHV* ion pump, a closed-cycle cryogenic helium pump, liquid nitrogen cryogenic panels, effusion cells, substrate heaters, a rotating holder and an electron gun with fluorescent screen mounted at the opposite end. An optical pyrometer is used to measure and control the temperature of the substrate. The gas composition and check for leaks is performed using a quadrupole mass analyzer.

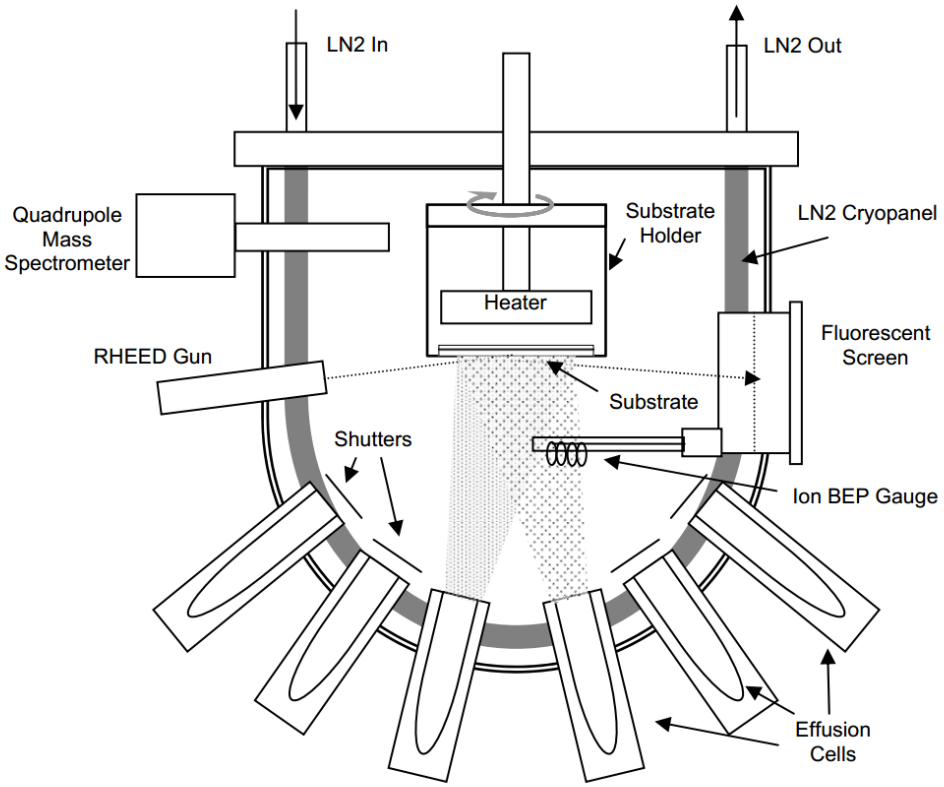

Figure 3.1: Schematic diagram of MBE growth chamber. Reprinted from Reference [2]

The wafer is typically mounted on molybdenum substrate holder blocks (molyblocks) and is rotated during the growth process. The elements, used for the growth, are located in the effusion cells where they typically are in either solid or liquid form. The elements are being heated until they begin to undergo the sublimation process. These elements, now in the gaseous form, mix forming dual, triple or even quadruple compounds before condensing

on the surface of the wafer. The wafer has to be kept at high enough temperatures in order to provide sufficient energy for the molecules to settle into the lattice. However, very high temperatures will provide too much energy preventing the particles to settle. Due to the time required for the elements to form a uniform morphology on the surface of the substrate, the deposition rate is typically anywhere from 1 to 10 angstroms per second.

The flux is usually controlled with the cracker valves or by mechanically blocking the molecular beam using a computer controlled shutter system. Reflection high energy electron diffraction (*RHEED*) technique is utilized to monitor morphology of the surface in-situ. High energy electrons emitted from the electron gun scatter from the surface of the substrate towards the fluorescent screen creating complex diffraction patterns. These patterns are analyzed and used to monitor the quality and periodicity of the grown structure.

The typical growth time required to form the epitaxial layers of the QCL ranges from 6 to 10 hours, depending on the actual device design. The active region is typically deposited with the rate of 1 Å/s with the 2 s pause between the layers to prevent cross-contamination and to increase interface sharpness. Additional 1.5 hours are required for temperature and source flux stabilization. Depending on the particular *MBE* configuration, additional $2-3$ hours might be needed to allow for wafer transfer to the $MOVPE$ reactor and top cladding overgrowth.

Since the creation of the first *MBE* system in early 1970s the technology has been improved dramatically and provides superior results compared to vapor phase or liquid phase epitaxy.

3.2.2 Metal organic vapour phase epitaxy

Unlike the *MBE* where mostly solid sources are used for wafer formation, the *MOVPE* employs gases flowing over the hot substrate forming required compounds through chemical reactions (see Figure 3.2). The growth of *III-V* semiconductor materials is typically

achieved using precursor compound gases of the required elements. $GaAs$, for example, is typically formed via flow of trimethylgallium ($Ga(CH_3)_3$)) and arsine (AsH_3). These compounds are transported using carrier gas, usually hydrogen (H_2), over a substrate held at high temperatures ($\sim 700°C$) to provide required energy for chemical reactions to occur. These substances decompose into their constituent components forming *III-V* compounds on the surface of the substrate. The organic compounds are removed from the chamber as waste gases [3].

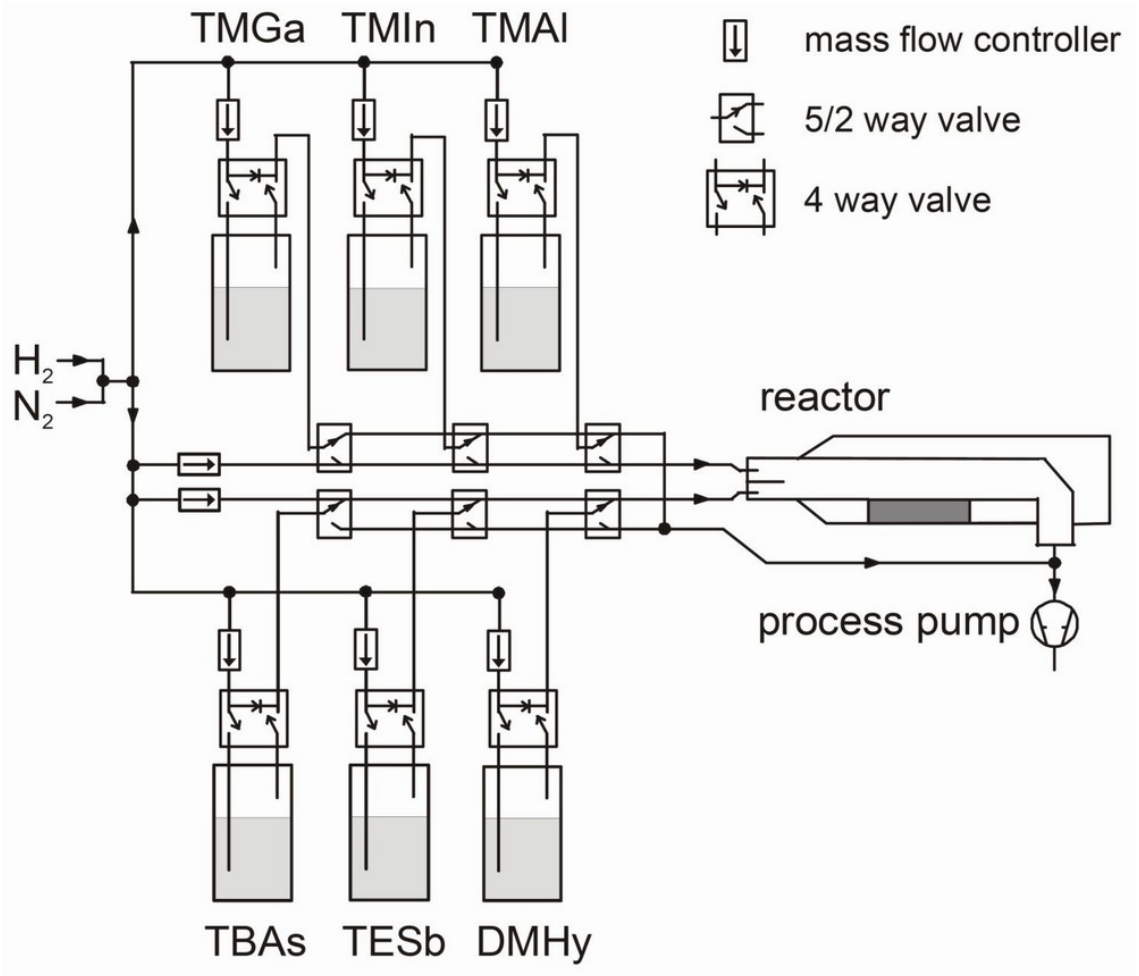

Figure 3.2: Schematic diagram of MOVPE growth chamber. Precursor compound gases are used to form *III-V* semiconductor layers. Hydrogen gas is used to transport compounds towards the reactor.

QCL growth using *MOVPE* is typically advantageous for a few reasons. Firstly, the

growth chamber of *MOVPE* can be operated at less demanding atmosphere pressures than *MBE* systems. The typical growth inside *MOVPE* chamber can occur at low-pressure ($\sim 150\ Torr$) or close to the atmospheric pressure ($\sim 750\ Torr$) without compromising on the quality. The growth rate is also typically 10 times larger in *MOVPE* systems ($5\ \mu m/hr$ compared to $0.5\ \mu m/hr$ for *MBE*). This combined with its ability to grow larger number of wafers (60×2" or 15×4") makes *MOVPE* very attractive choice for the scaled optoelectronics device production.

Furthermore, *MOVPE* has the capability to form heterostructures from the phosphide group, such as InP, with its precursor gas phosphine (PH_3). Phosphide growth in *MBE* is much more problematic due to unstable and potentially dangerous nature of solid-state phosphorus.

3.3 Standard laser fabrication

Different types of lasers are processed using different techniques, however the brief description of a standard "dry" etching process, used for most of the lasers mentioned in the thesis, is given in this section with the reference to the Figure 3.3.

The overgrown 2" wafer is cleaved into smaller, typically $1\ cm \times 0.6\ cm$ rectangle, and cleaned using the three solvent clean method. The three solvent clean method involves placing the sample into an n-butyl acetate then replacing it into an acetone and then into an isopropyl alcohol solution. The sample is then blasted with a compressed nitrogen to blow-dry remaining solvent particles. This cleaning method is also applied after most of the subsequent processing stages to prevent contamination.

Once the sample is sufficiently cleaned it is covered with the 800 nm layer of silicon dioxide (SiO_2) using plasma enhanced chemical vapour deposition (*PECVD*) creating the basis for the hard mask that is used for ridge definition by *dry* etching the wafer. The sample is then spin coated with $\sim 1\ \mu m$ thick photoresist. The thickness and the type of the

resist can be adjusted according to the size of the exposed laser features. Since most of the laser features are larger than 5 μm, standard optical lithography can be used to define it [4]. The wafer is placed in a mask-aligner (*Karl Suss UV300*) positioned underneath the quartz mask with chrome patterned ridge structure ready to be transfered onto the sample. Exposed photoresist undergoes chemical reaction depending on the resist properties. Positive photoresist contains a stabilizer that breaks down when exposed to light. The stabilizer slows down the rate at which the resist dissolves in the developer, therefore etching light exposed area from the sample, while unexposed area remains unmodified. Negative photoresist works in a reverse order, creating polymer where the light strikes. Formed polymer remains on the sample, while unexposed resist is developed [5].

The formed photoresist pattern is then transferred onto SiO_2 layer (Figure 3.3a) by the inductively-coupled plasma (ICP) etching. To ensure that oxide layer is etched faster than the resist, a combination of argon (Ar) and trifluoromethane (CHF_3) is used, selectively targeting silicone dioxide layer. Once SiO_2 is etched all the way down to the underlying semiconductor surface, the etch is terminated and the resist is stripped forming the oxide *hard-mask*. The ridges are formed by second ICP etch that selectively removes the semiconductor material over the silicone dioxide *hard-mask* (Figure 3.3b). A combination of argon (Ar) and silicone tetrachloride ($SiCl_4$) gases is used to create an anisotropic etch responsible for vertical ridge wall formation. In order to prevent either under- or over-etching, the directed light from a $\lambda = 960\ nm$ laser source reflected from the sample is monitored by comparing the intensity change to the calculated model. The process is typically stopped after the depth exceeds the thickness of the core region located about $\sim 5\ \mu m$ underneath the cladding surface. The formed ridges are stripped from the remaining silicone dioxide residue in the ICP etch with the same gas composition used for the *hard-mask* formation (Figure 3.3c).

The formed ridges are then electrically isolated with a 400 nm layer of SiO_2 deposited using a $PECVD$ reactor (Figure 3.3d). Contact windows are formed along the whole

length of the ridge to direct the current towards the laser core. The process is created by spin-coating the sample with photoresist and placing the sample in the mask-aligner. The alignment and exposure process is similar to the one described above. The sample with the opened resist windows is placed back into the *ICP* for SiO_2 removal (Figure 3.3e). Again, the process is selective only targeting exposed insulator inside the opened windows. Once the etching is completed, the sample is cleaned and prepared for the deposition of the top electrical contact.

The top contact is typically formed by the metal deposition either through the thermal evaporation or sputtering. Deposited thin titanium layer (20 nm) is followed by thicker (200 nm) layer of gold (Figure 3.3f). Titanium acts as an adhesive medium at the semiconductor-gold interface. In order to improve heat extraction, the substrate is mechanically thinned from 350 μm to $\sim$ 200 μm using a mechanical polisher with a combination of fine diamond pastes (Figure 3.3h). Thiner substrate also alleviate the sample cleaving process. The electrical back contact is formed with 20 nm layer of In/Ge and 200 nm layer of gold (Figure 3.3i). At this fabrication stage, the device, in principle, is ready to be cleaved, mounted and wire-bonded in order to be tested. However, an additional thick layer of electroplated gold can be used to improve the heat extraction from the laser core. Electroplating is achieved by immersing the sample into a gold solution and applying a small electrical current to create the potential difference between the sample and the platinum wire mesh positioned across the sample (Figure 3.3g).

Once, the electroplating is finished, device is cleaved into desirable length and indium soldered onto either gold-coated nickel $T05$ headers or aluminium-nitride tiles for individual use. The electrical contact is provided with the addition of gold wiring between the device and the connection pins of the mount, enabling the laser to be tested and characterized.

Any deviation from the standard processing steps are described in the relevant chapters.

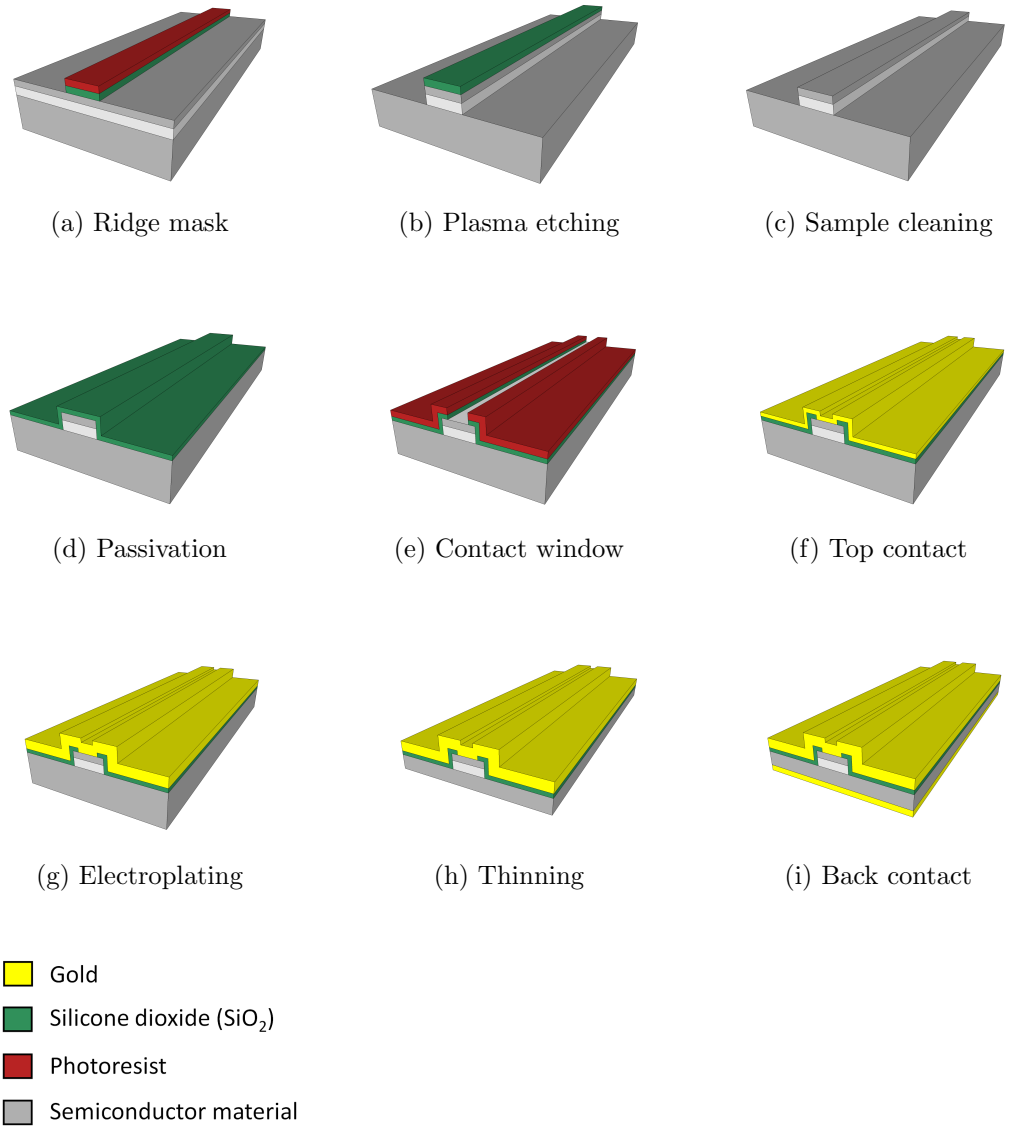

(a) Ridge mask (b) Plasma etching (c) Sample cleaning

(d) Passivation (e) Contact window (f) Top contact

(g) Electroplating (h) Thinning (i) Back contact

Figure 3.3: Schematic diagram of different semiconductor laser fabrication stages. The sample is coated with hard mask (SiO_2) and desired ridge is formed (a). Chemical plasma etching is used to define vertical walls (b), after the etching all masks are removed and the sample is thoroughly cleaned using chemical or oxygen plasma cleaning (c). The sample is then insulated (d) and the contact window is opened (e). The top contact is formed using gold evaporation (f) and then thickened by electroplating (g). The sample is thinned (h) and back contact is added (i).

3.4 Laser characterization

The fabricated lasers are tested and characterized in order to determine its performance and possible application. This section presents the description of the experimental setup used for the laser characterization. The brief explanation of importance of other laser characteristics, such as $L-I$, $I-V$ curves and the temperature T_0, is also mentioned.

3.4.1 Experimental setup

The fabricated QCL, is characterized by the set of parameters, such as its emission spectra, light-current and voltage-current dependencies. The schematic diagram of the setup used to measure these properties is shown in Figure 3.4.

The sample, depending on its performance and experimental requirements can be sealed inside a continuous-flow cryostat (*Janis Research Co.*) allowing temperature variations ranging from 10 K up to > 400 K. The window used to decouple light from the inside of the cryostat is made out of CaF_2 with the cut-off wavelength of ~ 9 μm. Devices operating at room temperature can also be mounted on a simple translation stage.

The lasers were driven with a power supply capable of different pulse length and amplitude generation depending on the model (*Avtech AVL-2-C/Av-1101-C and TTi PL330P*). The choice between these power supplies is made depending on whether the lasers are driven in pulse or continuous wave mode. The pulsed laser systems were typically driven with very low duty cycle ($\sim 0.025\%$) with the frequency of 5 kHz. The frequencies as high as 100 MHz were also accessible.

The spectra presented in this thesis were measured using Bruker IFS66V vacuum spectrometer with KBr beam splitter (the cut-off wavelength $\lambda \approx 27\mu m$). The signal, passing through the interferometer was collected using a deuterated tri-glycene sulfate ($DTGS$) or a liquid nitrogen cooled mercury cadmium telluride ($HgCaTe$) detector (the cut-off wavelength $\lambda \approx 13\mu m$). The MCT detector has a sensitivity $\sim$ 100x better than that of $DTGS$

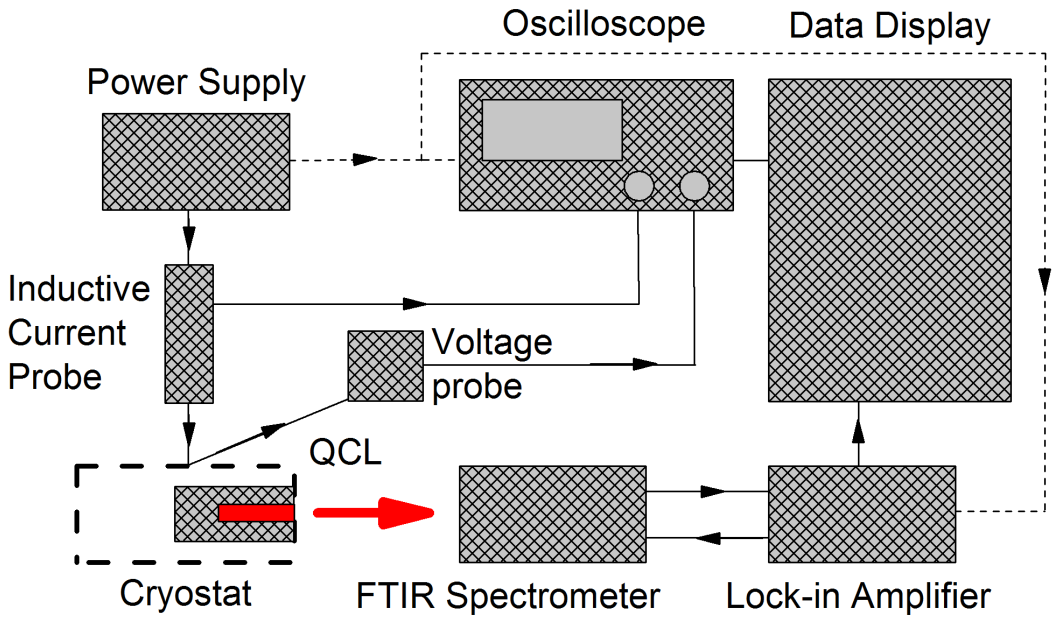

Figure 3.4: Schematic diagram of the experimental setup used to characterize QCL devices. The QCL is positioned inside the cryostat for the temperature control. The current is supplied from the power supply with its reference signal sent to the lock-in amplifier. The current and the voltage are measured using an inductive current probe and a voltage probe respectively. The emission spectrum is measured with the *FTIR* spectrometer. The signal is then sent to the lock-in amplifier. The data is stored and displayed using a data display (computer).

making it more suitable for electro-luminescence and low duty cycle pulsed laser detection. The spectrometer signal is passed to a lock-in amplifier (*EG&G Instruments*) where it is combined with the reference signal obtained from the power supply to be converted into *D.C.* signal.

3.4.2 Fourier transform infrared spectroscopy

The working principle of Fourier transform infrared (*FTIR*) spectrometer used for emission spectra measurements throughout this thesis is based on Michelson interferometer shown in figure 3.5.

The collimated beam of light is incident on to the transparent 50:50 beam splitter. Part of this monochromatic light goes towards mirror M_1 and the other is split towards mirror M_2. The reflected light is passed back towards the beam splitting plate where it recombines with the incident beam producing interferogram depending on the path length $M_1 - B$ and $M_2 - B$. If the mirrors M_1 and M_2 are positioned equidistantly from the splitting plate, the amplitude of recombined signal will be at its maximum. The same will be observed if mirror M_1 is $M\lambda$ away from the beam splitter, where M is integer number. For the half number of the wavelength the produced interference will be destructive producing no signal. By moving one of the mirrors (the other one remains stationary) the detector will detect signal modulation - the interferogram. This interferogram is then converted into the frequency domain by applying the Fourier transformation.

In the case of light consisting of multiple frequencies, the detected interferogram won't be a simple periodic sequence of minima and maxima, but instead a combination of multiple waves creating a beating that consists of multiple frequencies which can be extracted using Fourier analysis. *FTIR* spectrometry is a much quicker technique compared to the conventionally used dispersive techniques, especially in the mid-infrared. The ability to measure multiple wavelengths during one scan reduces the total measurement time, compared to the optical spectrometers utilizing a diffraction technique. Also, the signal to noise ratio (S/N) can be increased by measuring multiple interference patterns at the same mirror step ($S/N \propto \sqrt{N}$). *FTIR* system is capable of more sensitive detection, since the signal passing through does not require the use of an optical slit that severely deteriorates the intensity of the signal.

Unlike regular optical spectrometers, the maximum achievable resolution of FTIR spectrometer doesn't depend on the number of grooves in the grating nor the refraction properties of the prism, but the total length between two mirrors. The maximum resolution achievable with Bruker IFS66V spectrometer is 0.25 cm^{-1}

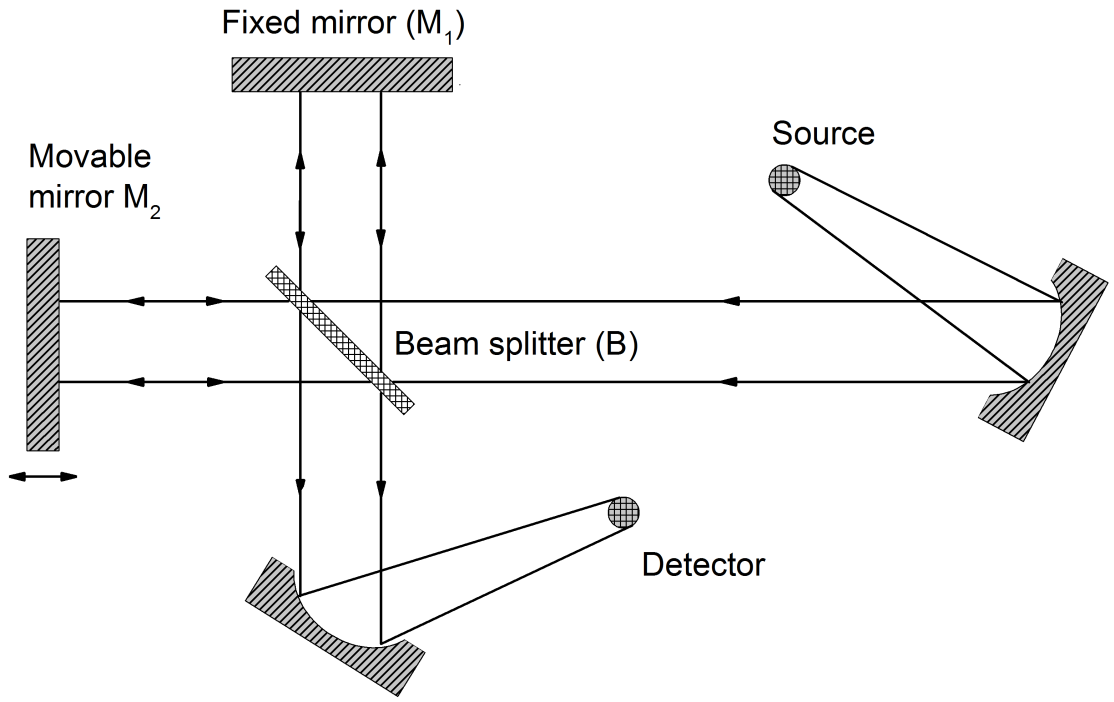

Figure 3.5: Schematic diagram of Fourier transform spectrometer based on Michelson interferometer.

3.4.3 IV and LI curve measurements

The current-voltage ($I-V$) characteristics of the fabricated devices were measured using a high impedance voltage probe across the QC laser. The current passing through the device was measured by an inductive current probe calibrated to output 1 V on the oscilloscope per 1 A of current passing through the probe. $I-V$ dependence was measured either at liquid nitrogen (77 K) or room (300 K) temperatures.

The light output power versus the injection current ($L-I$) characteristics were measured using a calibrated thermopile detector (*Molectron EPM1000*). The output powers were calibrated against the lock-in signal received from MCT detector for production of accurate $L-I$ plots. The power-current characteristics were measured in a wide temperature range from 10 K up to 420 K, depending on the performance of the laser. The flexibility of the output power measurements at different temperatures also allows the calculations of

a device's characteristic temperature T_0.

3.4.4 Characteristic temperature T_0

The exponential increase in the device's threshold current density at the increased temperatures can be described by the empirical parameter T_0 - the characteristic temperature. The relationship between threshold current density and the temperature is shown in Equation 3.1 [6].

$$J_{th} = J_0 \exp\Big(\frac{T}{T_0}\Big) \tag{3.1}$$

It is clear that T_0 can be extracted from the linear fit of the natural logarithm of the threshold current density versus the temperature at wich this J_{th} is measured. Higher T_0 values indicate smaller threshold current density fluctuation as the temperature changes. In contrast, smaller T_0 value indicate much quicker threshold current density increase as the temperature progresses. Small T_0, is typically associated with the worse performing devices.

References

[1] A.Y. Cho and J.R. Arthur. Molecular beam epitaxy. *Progress in solid state chemistry*, 10:157–191, 1975.

[2] Jan Devenson. *InAs/AlSb Short wavelength quantum cascade lasers*. PhD thesis, Vilnius University, Semiconductor institute of center for physical sciences and technology, 2010.

[3] G.B. Stringfellow. A critical appraisal of growth mechanisms in $MOVPE$. *Journal of Crystal Growth*, 68:111–122, 1984.

[4] K. Ronse. Optical lithography - a historical perspective. *Comptes Rendus Physique*, 7 (8):844–857, 2006.

[5] S. Franssila. *Introduction to Microfabrication*. Wiley, 2010.

[6] C. Gmachl, F. Capasso, D.L. Sivco, and A.Y. Cho. Recent progress in quantum cascade lasers and applications. *Reports on Progress in Physics*, 64:1533–1601, 2001.

Chapter 4

The Development of Fabry-Pérot Quantum Cascade Lasers for Gas Detection in $\lambda \sim 3 - 4\ \mu m$ Wavelength Region

4.1 Introduction

The technologically important $\lambda \sim 3-4\ \mu m$ wavelength window harbors a lot of hydrocarbon absorption lines, used for sensitive gas concentration measurements and qualitative gas detection. Quite often, the precise concentration of the particular analyte is not required, thus less sensitive laser based detection systems can be employed. Such systems can utilize broadband laser emission spectra typically produced in *FP* cavities in a mid-infrared spectral region, for the detection of specimens with the broadband absorption features, such as butane found at $3.35 - 3.4\ \mu m$ wavelength region. Despite the fact that qualitative gas detection can be achieved without the need for single mode devices, the

wavelength realization at this spectral region is still somewhat challenging.

The design and realization of QC laser sources in short mid-infrared wavelength region ($\lambda < 4\ \mu m$) is much more difficult using conventional material systems (non-stress compensated $InGaAs/AlInAs$), since the conduction band offset is too small to sustain short wavelength transitions. Furthermore, the laser performance made out of the material with the large conduction band offset can become compromised by the carrier leakage to the neighboring X and L valleys. It was suggested by multiple sources that the laser action is suppressed once the upper laser energy level at Γ point is positioned above the energy level of the lowest X or L lateral valley minimum in the $InGaAs$ quantum wells, limiting the shortest achievable wavelength to $\sim 3.7\ \mu m$ [1–3].

In 2007, Revin *et al.* demonstrated that much shorter wavelength lasing is achievable even when the calculated upper laser energy level is placed above the lateral valley minimum [4]. These devices demonstrated low output powers and low maximum operating temperatures compared to the device performance at longer wavelengths achievable at the time. In 2010, Commin *et al.* demonstrated short wavelength QCL emission in $InGaAs/AlAs(Sb)$ heterostructure with watt level peak powers and the operating temperatures exceeding 400 K [5]. The demonstrated characteristics of these devices opened up the possibility for laser commercialization, at this spectroscopically important wavelength region.

However, the reproducibility of QCL devices with the specified wavelength is very poor, with emission variation as high as $\pm 0.5\ \mu m$ between different wafer growths. Additionally, the yield of electrically stable devices emitting at the right wavelength is very low, typically not exceeding 10 %, due to growth defects caused by poor epitaxial system calibration and not optimized growth conditions.

In this chapter a description of different laser core region designs used to improve electrical stability and optical performance of $InGaAs/AlAsSb$ and $InAs/AlSb$ laser heterostructures is given. The energy separation of the active region is kept unaffected throughout the optimization of the laser core region, in order to improve laser performance while keeping

the emission wavelength fixed. The chapter starts with the description of the observed systematic wavelength shift occurring as a result of new, improved *MBE* growth conditions that were employed in order to stabilize the emission wavelength across the multiple growth runs. The focus is then shifted to the different design optimization of $InGaAs/AlAsSb$ lasers grown on InP substrate. $InAs/AlSb$ lasers grown on $InAs$ substrate are then also described in order to demonstrate emission at the targeted wavelength using different material system and compare laser characteristics to the InP based lasers.

4.2 InP based lasers

The new growth conditions were employed to regrow a set of QCL wafers previously grown using older *MBE* system. $InGaAs/AlAs(Sb)$ QCL design, described in Reference [5], previously emitting at $3.35 - 3.4\ \mu m$ was regrown and characterized. Despite the small defect density ($< 500\ cm^{-2}$) and smooth surface morphology resulting in a very high electrical stability, the measured emission wavelength was blue-shifted by a $\sim 0.3\ \mu m$ compared to the emission spectrum obtained from the same design using older growth conditions. This $\sim 0.3\ \mu m$ wavelength shift, is attributed to the conduction band offset decrease between $InGaAs$ wells and $AlAsSb$ barriers due to reduced interface sharpness caused by the poor previous growth calibration techniques in older *MBE* system. The increase in interface sharpness can be clearly seen in Figure 4.1, where two transmission electron microscopy images of two different growths is presented. Graded interfaces lead to the reduced effective quantum well depth, thus reducing the energy separation between the transition levels in the active region. Figure 4.2 shows wavefunction distribution inside the sharp and graded interfaces of QCL core heterostructure responsible for the wavelength shift.

As a result, the active region design of the subsequent QCL wafers was adjusted to accommodate the observed $0.3\ \mu m$ wavelength shift. The sample $SF0657$ was used as a control reference structure with the original active region design shown in Figure 4.3. This struc-

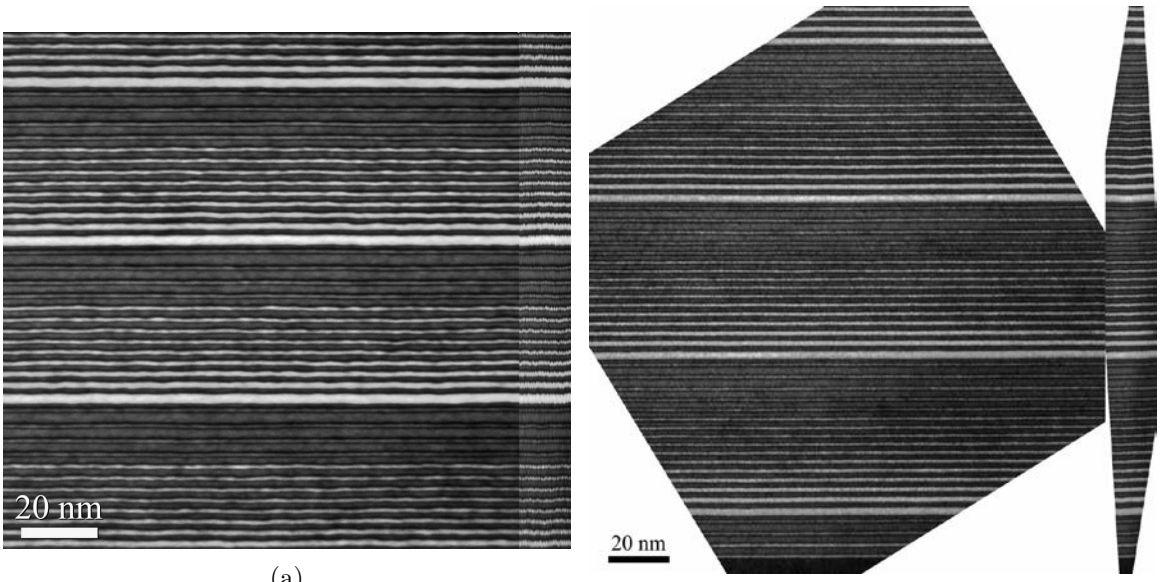

(a) (b)

Figure 4.1: Transmission electron microscopy images of two QCL structures grown after two different calibrations. The interface between two neighboring quantum wells in structure (a) are less defined, causing longer wavelength emission. In contrast, structure (b) has much sharper interfaces, resulting in shorter wavelength emission. The laser emission from the sharp interface devices closely agrees to the designed emission wavelength.

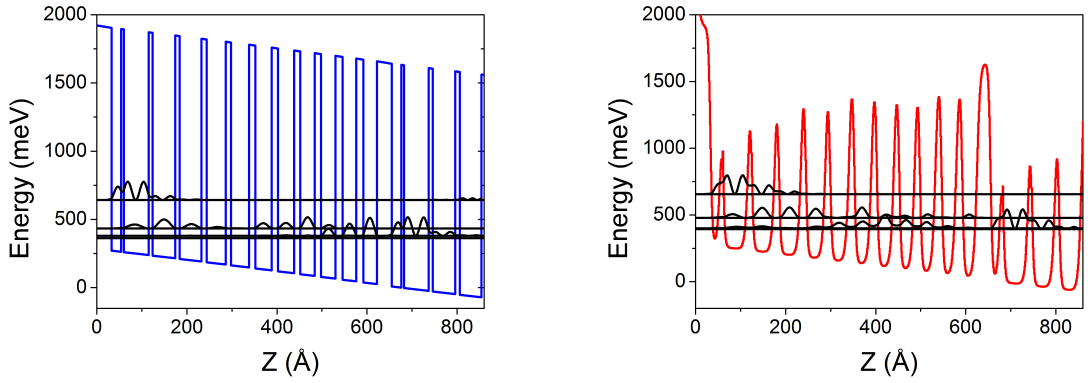

(a) Ideal interface (b) Graded interface

Figure 4.2: Conduction band diagrams of a single QCL core period with ideal (a) and graded (b) interfaces. The energy difference ΔE in a structure with the graded interfaces is smaller than that obtain from ideal interfaces. This reduction correlates with the longer wavelength emission.

ture was previously measured to emit at $\lambda \approx 3.7\ \mu m$ wavelength region. This sample, grown under new growth conditions, should have its emission wavelength reduced to the desired $\lambda \sim 3.35-3.4\ \mu m$ wavelength range due to much sharper QW interfaces achievable with the new *MBE* system

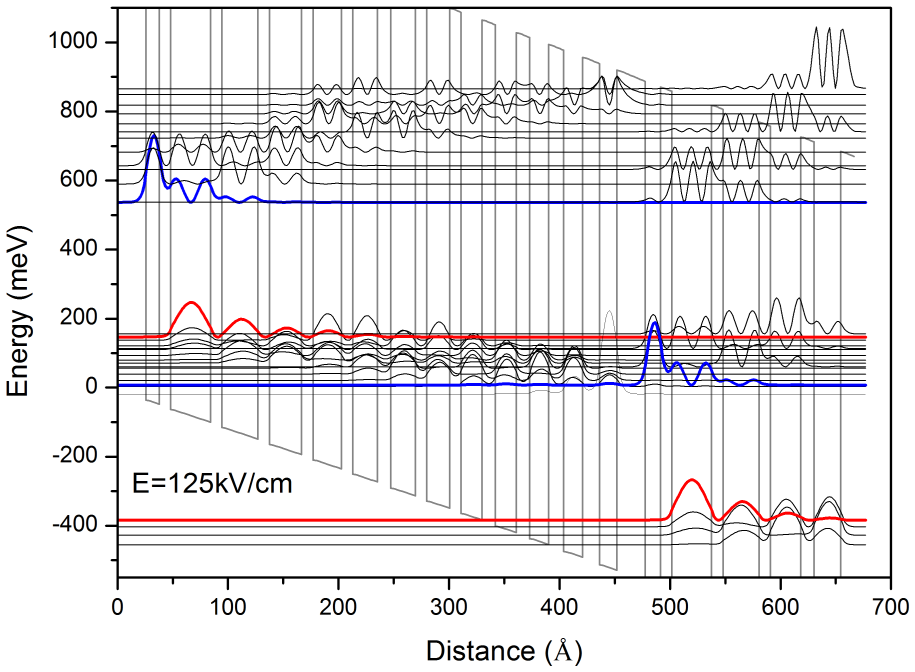

Figure 4.3: Conduction band diagram of the active region of the control reference sample $SF0657$.

The measured emission wavelength of this wafer once again confirmed the $\sim 0.3\ \mu m$ blue-shift, bringing the emission frequency to the targeted wavelength. Despite the improved interface quality and accurate calibration allowing for more predictable wavelength targeting, the performance of newly grown lasers remain inferior to those produced using older growth conditions. The observed laser performance deterioration, such as increased threshold current density, lower emission power and less efficient operation at higher temperatures suggest that sharper interfaces have influenced the alignment of the energy levels, causing less efficient electron flow. As a result, a number of core region changes are made

in order to improve the efficiency and performance of these devices.

4.2.1 Laser design: 1^{st} growth

Sample $SF0657$, emitting at $\lambda \sim 3.35 - 3.4\ \mu m$, was used as a control structure in order to compare all the subsequent core region changes. Eight QCL wafers with modified core designs have been grown. The detailed modifications for different structures are described below.

SF0677

The laser core design of $SF0677$ is based on $SF0657$ with the elevated energy position in the injector designed to improve the energy level alignment and wavefunction overlap between the upper laser level and the injector miniband. The last 4 quantum wells of a full period were grown narrower by 0.5 Å to increase the position of the energy levels by $\sim 10\ meV$. The full design of this structure is described in Appendix A.2.2. The growth of this wafer has been compromised due to poor vacuum inside the *MBE* chamber. Despite the imperfect growth, the fabricated devices were measured and characterized.

SF0678

Sample $SF0678$ is an exact copy of the failed growth run of $SF0677$ sample.

SF0679

The injector design of this structure has been raised even further by narrowing the last 4 quantum wells of a full period by 1 Å compared to the reference sample $SF0657$. Narrow wells elevate the energy level of the injector by $\sim 20\ meV$, potentially improving the level alignment even further.

SF0680

The design of $SF0680$, and all the subsequent structures in this growth batch, was based on $SF0679$ structure. Here, the assumption that narrower wells in the injector will improve the laser efficiency is made. This particular QCL design has increased doping, to observe the effect and characteristics of higher charge density in the bridging region. The doping was increased 4 times to $2.4 \times 10^{18}\ cm^{-3}$, compared to $6 \times 10^{17}\ cm^{-3}$ doping used in the control sample.

SF0681

In contrast to the $SF0680$ structure, this particular design was grown with reduced doping in the injection region. The doping is reduced 4 times to $1.5 \times 10^{17}\ cm^{-3}$.

SF0682

The design of $SF0682$ structure is changed by modifying the length of the injector with the addition of two extra quantum wells. Longer injector increases the energy difference between the injector miniband and the lower laser level, therefore reducing the probability of thermal carrier backfilling.

SF0684

Sample $SF0684$ was designed with narrower injection barrier. The barrier was decreased by $\sim$ 20 % from 26 Å to 22 Å in order to increase injection efficiency by increasing the electron tunneling probability.

SF0685

Similarly to $SF0684$ structure design, this particular sample was grown with all barriers narrowed by 10 % in order to increase the wavefunction coupling between the neighboring energy levels. Thinner barriers across the whole structure increases the quantum tunneling efficiency, hence improving the electron flow inside the active region.

4.2.2 Results

The grown wafers were processed into devices using wet etching to expedite the fabrication process. Lasers were fabricated into 3 mm long and $\sim$ 20 μm wide ridges with as cleaved facets. All devices demonstrated pulsed emission at low temperatures. The measured threshold current versus temperature dependence, wavelength versus temperature dependence and current-voltage characteristics of these devices are shown in Figures 4.4 and 4.5.

Despite the detected light emission from all of the devices at low temperatures, the room temperature operation has been observed with only a handful devices. It can be noticed from Figure 4.4 that the targeted wavelength ($3.35 - 3.4$ μm) is achieved only at temperatures $\sim 200 - 250$ K. Ideally this wavelength should be reached at or near room temperatures, in order for these devices to be used for commercial purposes. The threshold current density at liquid nitrogen temperatures is around 3 kA/cm^2, increasing to 17 kA/cm^2 at room temperature.

The increased injector energy levels ($SF0677/78/79$) did not improve device performance, supposedly bringing two wavefunctions out of the alignment decreasing the overlap between them. All three samples, $SF0677$, $SF0678$ and $SF0679$, demonstrated poorer performance compared to the devices made from the reference structure $SF0657$. The threshold current densities at 240 K are twice as high ($J_{th} \approx 13$ kA/cm^2) compared to the $SF0657$ structure ($J_{th} \approx 6.5$ kA/cm^2). Additionally, neither of these samples oper-

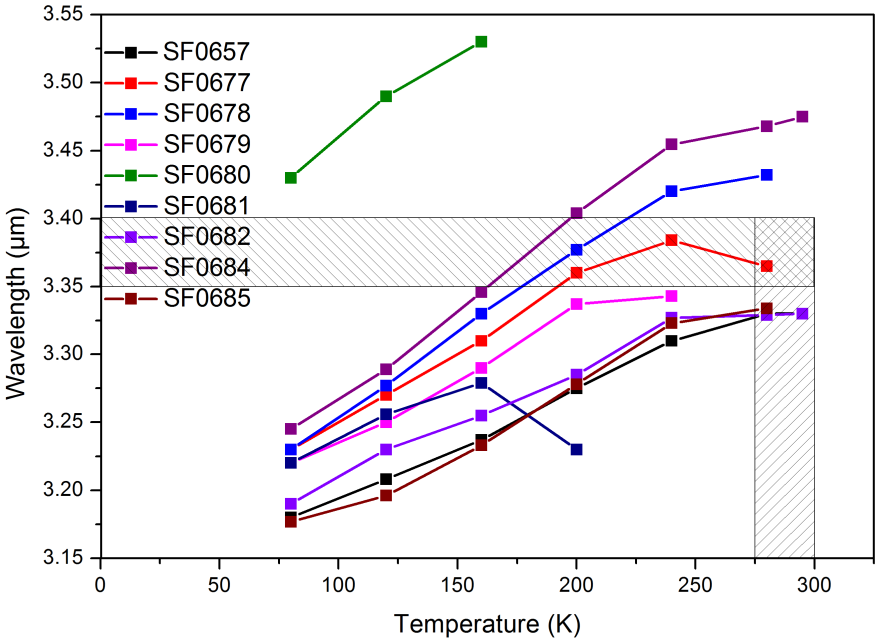

Figure 4.4: Wavelength versus temperature dependence of the fabricated QCL devices

ated at room temperature. The emission wavelength of $SF0677$, despite the failed growth run, stayed in the targeted $\lambda = 3.35 - 3.4\ \mu m$ wavelength region at the $T = 200 - 270\ K$ temperature range.

As shown in Figure 4.5a, the threshold current density of higher doped device ($SF0680$) is about two times higher ($J_{th} = 7\ kA/cm^2$ at $T = 77\ K$) compared to the rest of the devices ($J_{th}^{average} = 3.1\ kA/cm^2$ at $T = 77\ K$). Device is not tested above 160 K due to inaccessibly high currents required to power this laser. The current-voltage characteristics, shown in Figure 4.5b, demonstrate lower voltages and gradual slope associated with lower device resistance at zero bias due to higher free electron density. As expected, the emission wavelength of this device is red shifted due to premature diagonal transitions occurring inside the active region. Energy separation between two laser levels prior to the complete active region alignment is reduced, since the increased carrier concentration triggers shorter

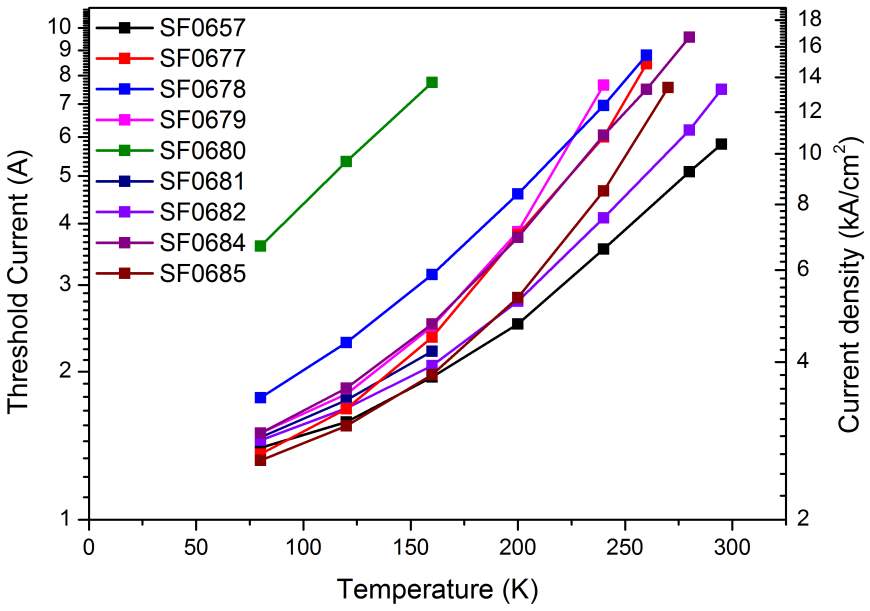

(a) Threshold current versus temperature dependence of the fabricated QCL devices

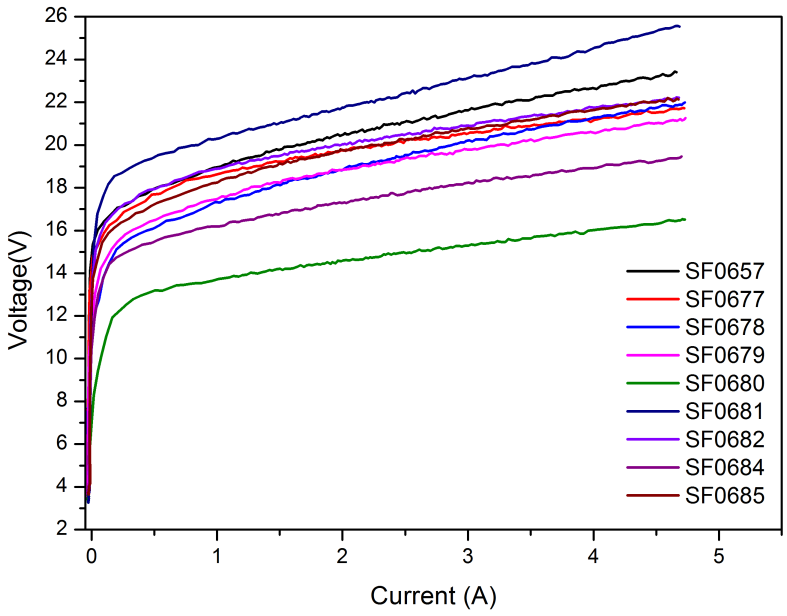

(b) Current-voltage characteristics of the QCL devices at liquid nitrogen (77 K) temperatures.

Figure 4.5

wavelength transitions before the optimal alignment is achieved.

Similarly poor performance has been observed with the structure with lower core region doping ($SF0681$), with no observed emission at temperatures above 200 K. The operational voltage of this structure is much higher, as seen in Figure 4.5b, arising from the lack of free charge carriers inside the injection region. As a result, much earlier roll-over is observed, preventing high temperature operation. The emission wavelength measured from these devices is comparable with the other designs. As expected, the emission wavelength increases as the temperature is raised from $T = 77\ K$ to $T = 160\ K$, due to change in refractive index inside the waveguide, however the observed wavelength starts to decrease as the temperature increases from 160 K to 200 K. This wavelength decrease is associated with the stretched energy transition levels due to laser operation past its roll-over.

Sample $SF0684$, with narrower injection barrier showed room temperature operation with the emission wavelength of $\lambda \sim 3.47\ \mu m$. The overall performance of this sample is comparable to the other devices in this growth batch.

The threshold current density of sample $SF0685$ at low temperatures is similar to the other devices, however, it can be noticed that the increase in J_{th} as the temperature increases is much steeper, indicating low characteristic temperature T_0. Thinner barriers across the whole core region increases tunneling probability of the electrons, possibly allowing some of them to escape into the continuum as the temperature increases, therefore increasing threshold current density at higher temperatures.

4.2.3 Laser design: 2^{nd} growth

Surprisingly, most of the proposed changes brought the overall performance down compared to the control structure $SF0657$. The only improvement was noticed with sample $SF0682$ that demonstrated room temperature operation suggesting that longer injector benefits the laser performance. As a result this particular design was used as a reference for the subsequent QCLs growth run, where further changes have been made:

SF0694

Since the overall performance of $SF0678$ and $SF0679$ structures degraded compared to the reference structure $SF0657$ after the injector energy levels were raised, this structure is designed with the lower energy levels inside the injection region. The last 4 quantum wells are widened by the 0.5 Å in order to decrease the injection energy level by $\sim 10\ meV$.

SF0695

The sample $SF0695$ was designed with multiple changes in order to combine previously observed improvements. This design contains longer injector, achieved by an addition of two extra quantum wells, and thinner $AlAsSb$ barriers for improved wavefunction coupling between the layers. The layered composition of this design is described in Appendix A.2.3

SF0697

This design, similarly to $SF0694$, has been grown with even lower energy levels inside the injector. The last 4 quantum wells of a full period were widened by 1 Å decreasing the energy level by $\sim 20\ meV$. The reduction of the injector energy levels can potentially increase the wavefunction overlap. The layer composition of this design is described in Appendix A.2.4.

SF0698

This particular design focuses on the improvement of characteristic temperature T_0. The extraction section of the injector region is modified by the addition of two extra quantum wells. The addition of these wells distort the continuity of the cascading wavefunction. The addition of these quantum wells introduce a gap in the energy levels between the injector and active region. The position of the energy level in these two wells prevents the

carrier leakage to the continuum at high temperatures, thus increasing its efficiency at high temperatures. The layer composition of this design is described in Appendix A.2.5.

SF0699

The sample $SF0699$ has identical laser core design to $SF0695$ structure with reduced number of cascade periods from 30 down to 25. The period reduction lowers operational voltage and power consumption, at the cost of reduced emission power.

SF0700

Unlike all the previously described designs, this structure is designed to have vertical radiative transition, compared to the diagonal found in all of the previously mentioned structures. This sample was included just to ensure that the wavelength can also be selectively targeted with different transition design. The layer composition of the active region is shown in Appendix A.2.6.

4.2.4 Results

Similarly to the previous batch of grown wafers, the lasers were fabricated into 3 mm long and $\sim$ 20 μm wide wet etched ridges. The threshold current versus temperature dependence and the emission wavelength versus temperature dependence can be compared in Figure 4.6, where the results from both growths are included for comparison purposes.

The devices have very similar emission wavelengths with slight variation caused by the growth non-uniformity. The threshold current values are very similar to those obtained previously, suggesting that small design changes do not increase net gain. It can be noticed that sample $SF0698$ has much more gradual threshold current temperature dependence

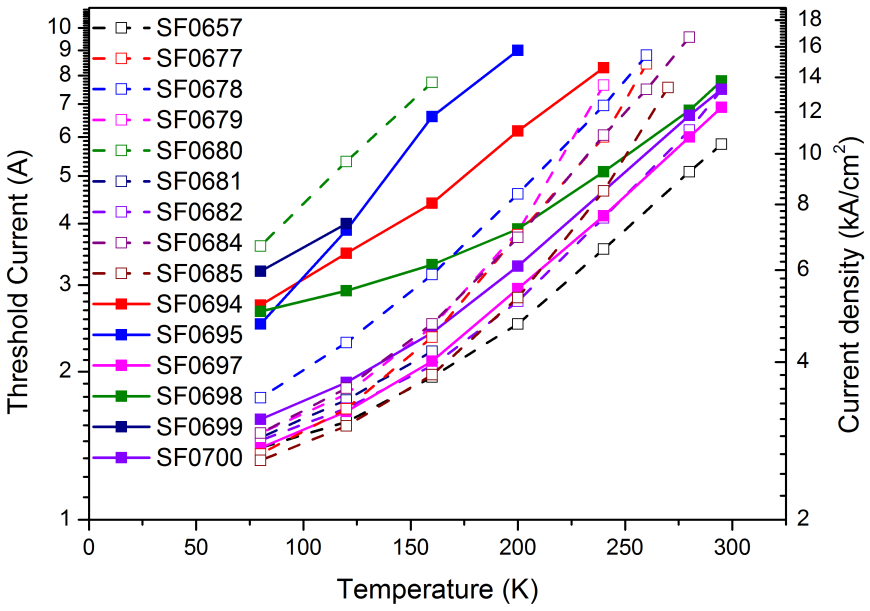

(a) Threshold current versus temperature dependence of fabricated first and second QCL batches

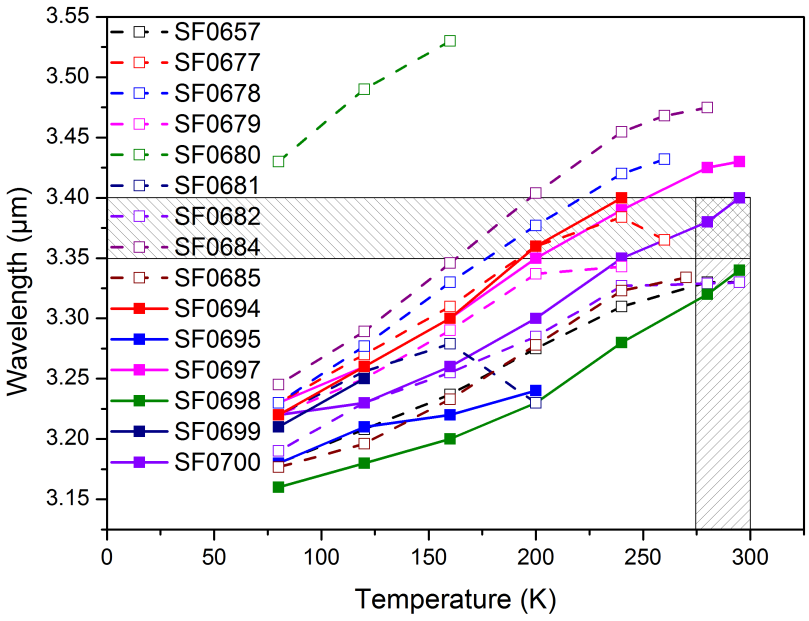

(b) Wavelength versus temperature dependence of fabricated first and second QCL batches

Figure 4.6

curve, compared to the other devices. The gradual threshold current change is characteristic to the devices with high T_0 value. The extra quantum wells introduced into the bridging region of $SF0698$ structure design create a band gap, suppressing electron escape into the continuum at higher temperatures.

It can be noticed in Figure 4.6, that lower injector improved the threshold current density, with observed emission at room temperatures for $SF0697$ sample. Additionally, the comparison between the previously grown samples $SF0678$ and $SF0679$ can be made in order to notice that slightly higher (0.5 Å narrower) and much lower (1 Å wider) injector level increases the performance of the laser compared to the much higher or slightly lower injector levels. The emission wavelength of these structures remained very similar at $\lambda \sim 3.4\ \mu m$.

Unsurprisingly, the sample with lower number of periods ($SF0699$) had no emission above $T = 120\ K$. The optical gain required to sustain the oscillation is too low in the core of the laser with reduced number of active region periods, preventing high temperature operation.

Additionally, much lower measured device resistance ($100s$ of ohms), compared to the typical resistance for the devices at these wavelengths ($100s$ of kilo-ohms) suggest parasitic current leakage bypassing the active region. This leakage can be explained by the metallic defects, shown in Figure 4.7, caused by micro-splashes from Ga cell during material growth. Further investigation revealed that these splashes were originating from the condensed liquid Ga coating on the shutter. The mentioned splashes would form unwanted current channels creating a path for parasitic current leakage.

4.2.5 Laser design: 3^{rd} growth

Further investigation of growth conditions revealed the problem with Ga cell, which has been producing splashes, possibly contaminating the samples responsible for poor performance described above. The cell was changed reducing the density of these defects and

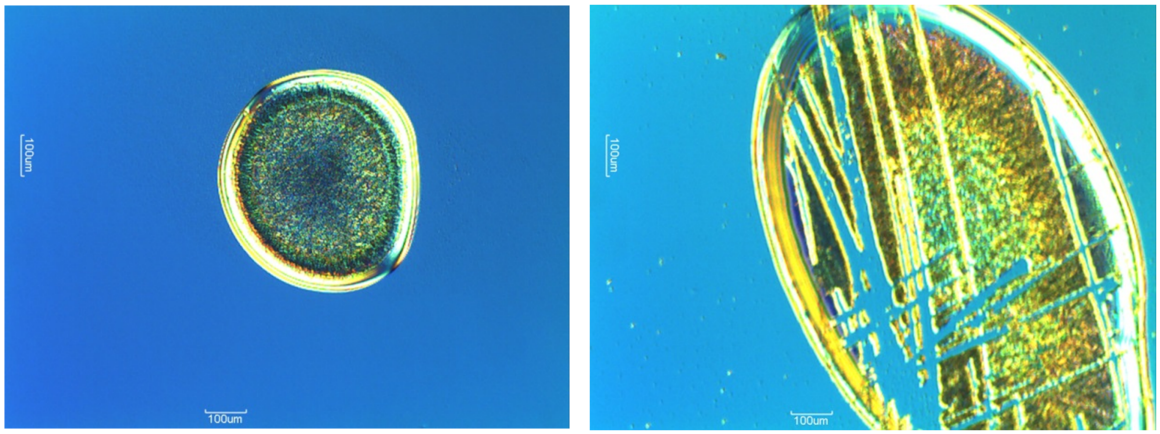

Figure 4.7: Nomarski microscope pictures of metallic defects caused by Ga micro splashes formed on the surface of QCL wafer $SF0657$

a new set of wafers was grown in order to test it. Additional set of five wafers, with the following changes were designed and grown:

SF0721

The design of this wafer is based on $SF0682$ structure. The sample was grown at $30°C$ lower temperature with traveling Sb cracker valve. The antimony valve traveled back to zero position before the growth of $InGaAs$ layers. Sb shutter was also closed during the growth of $InGaAs$ layers further preventing the possibility of contamination.

SF0723

The laser core of $SF0723$ structure is based on $SF0682$ and was also grown at $30°C$ lower temperature but with fixed Sb cracker valve. Fixed Sb cracker valve remains open during the growth time and only Sb shutter interrupts the flux.

SF0732

This design is the exact copy of sample number $SF0682$ grown at standard growth conditions and temperatures.

SF0733

This structure is a copy of $M3767$ [5] QCL structure grown at standard conditions. This structure was previously measured to emit at $\lambda \sim 3.37\ \mu m$ using old growth conditions. The sample is included to confirm if previously observed $\sim 0.3\ \mu m$ wavelength shift still exist.

SF0735

The core design of this structure is based on $SF0682$ heterostructure with the spacer thickness of $0.2\ \mu m$ instead of the usual $1.5\ \mu m$. The spacer thickness is changed in order to test the efficiency of the waveguide confinement as a function of spacer thickness.

4.2.6 Results

Very similar threshold current densities and emission wavelengths, with exception of device number $SF0733$ compared to the previous devices, shown in Figure 4.8, were measured.

Structure $SF0733$ has unmodified design that was not adjusted for the interface grading causing $\sim 0.3\ \mu m$ wavelength shift. As seen from the Figure 4.8, the wavelength of this structure is much shorter with the threshold current densities twice as high at low temperatures compared to the other devices. The emission was only observed at liquid nitrogen temperatures due to inefficient active region alignment under the applied electric field caused from the unchanged structure design. Sample $SF0721$ demonstrated lower

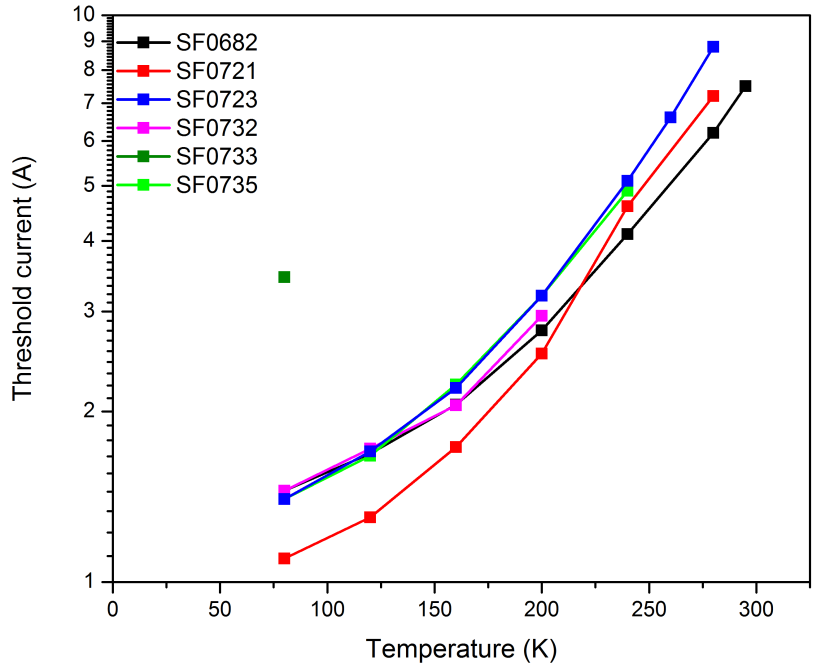

(a) Threshold current temperature dependence of the third fabricated QCL batch

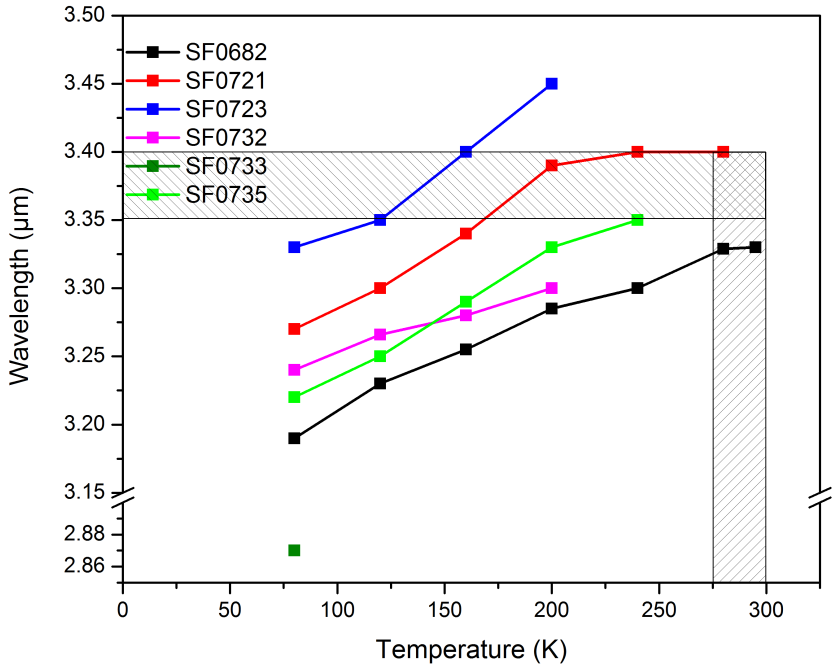

(b) Wavelength versus temperature dependence of the third QCL batch

Figure 4.8

threshold current density at low temperatures compared to the other devices. It is possible that the wafer quality was influenced by the reduced contamination due to fully closed Sb cracker valve during $InGaAs$ layers growth. However, the J_{th} becomes comparable to the other devices at higher temperatures. This behavior can be associated with the lower layer thickness uniformity from period to period due to the backlash in Sb cracker valve mechanism. Despite low T_0, the devices, made from this wafer, demonstrated room temperature operation at the targeted wavelength region.

Although the new growth conditions result in sharper quantum well production and much better structure reproducibility, the grown quantum cascade lasers still have large threshold current densities. It has been shown that the growth temperature change and minor design optimization played very small role on device performance. The samples grown at lower temperatures with traveling Sb cracker valve show some improvement with the emission at the targeted wavelength at room temperature. This suggest that contamination still can be a major cause in achieving high purity structures.

4.3 InAs based lasers

As described in Section 1.4.6 the emission wavelength can be engineered using different material systems through band engineering technique. In order to target previously mentioned $3.35 - 3.4\ \mu m$ wavelength region, $InGaAs/AlAsSb$ material system is substituted with $InAs/AlSb$.

Device, grown on $InAs$ substrate typically has its waveguide made out of the same semiconductor composition as its substrate - $InAs$. The composition of this waveguide allows it to be formed inside the MBE reactor chamber during the same growth run, as opposed to the waveguides based on InP. The waveguides based on InP are usually grown inside the $MOVPE$ reactor, creating the possibility of oxidation and contamination during the transfer of the sample between two reactors. Also, single reactor growth reduces epitaxy

time, and in turn the testing feedback time. $InAs/AlSb$ material system is less sensitive to the As/Sb ratio due to almost perfectly matched lattice constant to $InAs$ substrate. This particular material system also has lower electron effective mass in QWs, potentially allowing higher achievable gain.

Despite these advantages, the efficiency of high temperature and CW operation for short wavelength QCLs based on $InAs$ material system is still very low. The main problems reducing short wavelength performance arise from the interband absorption in the superlattice spacers and the free carrier absorption in the claddings. Additionally, the vertical heat transfer from the hot core region is inefficient, due to the multi-layer composition of the active region and spacers. The MBE growth of short wavelength QCLs is also complicated by the absence of common atoms at the interfaces, straining the possible $AlAs$ and $InSb$ bonds.

The active region of $InAs/AlSb$ heterostructure targeting the emission wavelength of $3.35 - 3.40\ \mu m$ is shown in Figure 4.9. The laser core is made of 25 periods with the exact layer composition described in Appendix A.2.7. The wave confinement was achieved through plasmon-enhanced waveguide. The $InAs$ spacers were replaced with a short period $InAs/AlSb$ superlattice developed by Devenson *et al.* [1] due to the dominating interband absorption in $InAs$ at wavelengths below $3.5\ \mu m$.

The fabricated QCL devices from this wafer demonstrated pulsed emission at room temperature at $\lambda \sim 3.35 - 3.37\ \mu m$ with the threshold current densities of $\sim 8\ kA/cm^2$. A small percentage of arsenic (~ 15 %) has been added to the $AlSb$ barriers in lower cladding superlattice in order to avoid material relaxation. The barriers of the lower cladding superlattice are not sensitive to the interface roughness as its main purpose is to separate the laser core from highly absorbing upper cladding.

In order to improve device performance, a set of $InAs/AlSb$ QCL wafers with $InAs/Al(As)Sb$ lower cladding superlattice was grown utilizing different growth conditions.

The first wafer, $SF0861$, was used as a control structure in order to determine the ac-

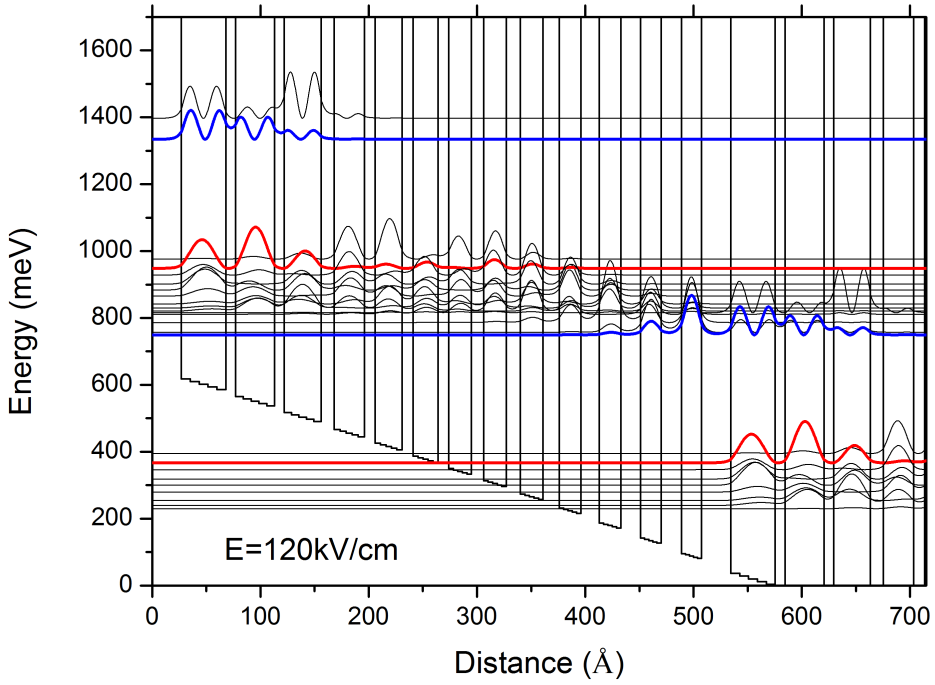

Figure 4.9: Energy band diagram of the $InAs/AlSb$ QCL designed for emission at 3.35 – 3.40 μm wavelength ($SF0780$).

tual emission wavelength and required lattice adjustments in order to target the specific wavelength. Subsequent devices, namely $SF0869$ and $SF0870$, were adjusted for $\lambda \sim 3.37$ μm emission according to the growth rates extracted from the sample $SF0861$. Sample $SF0870$ was grown with In source temperature decreased by $1°C$ to target slightly shorter wavelength. Temperature reduction, decreases the well thickness inside the active region, slightly reducing the emission wavelength.

SF0861

This wafer design was based on the $SF0780$ sample heterostructure shown in Figure 4.9. $InAs/AlAs_{0.15}Sb_{0.85}$ heterostructure was grown with the reversed polarity (reversed layer sequence).

SF0869

The design of this structure is similar to $SF0861$ but grown at $10°C$ lower temperature and 2^{nd} cladding grown at $5°C$ higher temperature. The structure was also grown with the reversed polarity, unlike typical $InGaAs/AlAs(Sb)$ material structures.

SF0870

The last wafer of this batch was based on the same $SF0861$ active region design grown at $10°C$ lower temperature and $15°C$ higher temperature for the 2^{nd} cladding. The cell temperature was decreased by $1°C$ to slightly decrease the emission wavelength. Devices retained reversed polarity compared to the usual systems.

4.4 Results

All fabricated devices demonstrated pulsed emission at room temperature. The threshold current densities of these devices were in $\sim 8-9\ kA/cm^2$ range. The summary of these devices is shown in the table below.

Wafer no.	Emission wavelength at RT (μm)	Ridge width/length (μm)	J_{th} (kA/cm^2)	Pulsed power (mW)	Operating Voltage (V)
SF0780	3.35-3.37	5-20 / 2000	~ 8.0	> 50	15.5
SF0861	3.42	11 / 2000	~ 9.1	> 50	< 17
SF0869	3.45	11 / 2000	~ 8.2	> 50	< 17
SF0870	3.35-3.37	11 / 2000	~ 9.1	> 50	< 17

Some of the devices had HR coating applied to one of the facets in order to minimize the

mirror losses, reducing the threshold current density to $\sim 7\ kA/cm^2$. Samples $SF0780$ and $SF0870$ demonstrate emission at the targeted wavelength ($3.35 - 3.37\ \mu m$) at room temperature with the threshold current densities comparable to the devices grown on InP substrate. The other two samples ($SF0861$ and $SF0869$) have the emission frequency very close to the targeted wavelength.

4.5 Conclusion

The improved growth conditions and more precise calibration influenced the grown material quality, producing sharper, better defined interfaces as seen in Figure 4.1. The reproducible growth allowed for specific wavelength selection by adjusting previously used designs. QCL wafers grown with older designs, under new growth conditions demonstrated shorter wavelength emission, suggesting that previous growth conditions distorted the quantum well sharpness at the interfaces. Improved *MBE* calibration allows for precise wavelength control, opening the possibility to optimize laser design and performance.

A number of changes, made to the laser core design, did not show a major performance improvement. Some improvement has been observed with the traveling *Sb* cracker valve, suggesting that chamber contamination influences the laser performance much stronger than the changes made to the core region design.

An alternative $InAs/AlSb$ material system has been used to demonstrate excellent wavelength selectivity. The material system is less sensitive to layer composition as it uses only binary compounds and it also does not require *MOVPE* cladding overgrowth, reducing the chance of cross-contamination. This particular material system can deliver short wavelength mid-infrared emission above room temperature [6] in both, standalone [7] and external cavity systems [8], potentially allowing the integration of laser based spectroscopy with this material system.

References

[1] J. Devenson, D. Barate, O. Cathabard, R. Teissier, and A. N. Baranov. Very short wavelength ($\lambda = 3.1 - 3.3\,\mu m$) quantum cascade lasers. *Appl. Phys. Lett.*, 89:191115, 2006.

[2] Q.K. Yang, C. Manz, W. Bronner, K. Kohler, and J. Wagner. Room-temperature short-wavelength ($\lambda \sim 3.7 - 3.9\ \mu m$) $GaInAs/AlAsSb$ quantum-cascade lasers. *Appl. Phys. Lett.*, 88:121127, 2006.

[3] I. Vurgaftman, J.R. Meyer, and L.R. Ram-Mohan. Band parameters for $III - V$ compound semiconductors and their alloys. *Journal of Applied Physics*, 89:5815, 2001.

[4] D. G. Revin, J. W. Cockburn, M.J. Steer, R. J. Airey, M. Hopkinson, A. B. Krysa, L. R. Wilson, and S. Menzel. $InGaAs/AlAsSb/InP$ quantum cascade lasers operating at wavelengths close to $3\,\mu m$. *Appl. Phys. Lett.*, 90:021108, 2007.

[5] J. P. Commin, D. G. Revin, S. Y. Zhang, A. B. Krysa, K. Kennedy, and J. W. Cockburn. High peak power $\lambda \sim 3.3$ and $3.5\,\mu m$ InGaAs/AlAs(Sb) quantum cascade lasers operating up to 400 K. *Appl. Phys. Lett.*, 97:031108, 2010.

[6] P. Laffaille, J.C. Moreno, R. Teissier, M. Bahriz, and A.N. Baranov. High temperature operation of short wavelength $InAs$-based quantum cascade lasers. *AIP Advances*, 2 (2):022119, 2012.

[7] A.N. Baranov and R. Teissier. Quantum Cascade Lasers in the $InAs/AlSb$ Material System. *IEEE Journal of Selected Topics in Quantum Electronics*, 21(6):85–96, 2015.

[8] T. Kruczek, K.A. Fedorova, G.S. Sokolovskii, R. Teissier, A.N. Baranov, and E.U. Rafailov. InAs/AlSb widely tunable external cavity quantum cascade laser around 3.2 μm. *Applied Physics Letters*, 102(1):011124, 2013.

Chapter 5

Quantum Cascade Laser with Unilateral Grating

5.1 Introduction

Single mode operation, high output powers and wide tuning range are the main requirements for lasers used in spectroscopic applications. A number of important hydrocarbons, such as CH_2, CH_4, C_2H_2 and many others, as shown in Figure 5.1, absorb light in the mid-infrared region, especially in the $3-4\,\mu m$ spectral window. Tunable laser absorption spectroscopy technique (TLAS) is used to determine the concentration and origin of the gaseous substances and also to resolve the temperature, pressure, velocity and mass flux of the gas under observation. This technique creates demand for suitable light sources emitting at these wavelengths.

However, the availability of such light sources still remains limited due to its uniqueness and high fabrication cost associated with the manufacturing techniques. While $GaSb$ type-I laser diodes [1] and highly promising interband cascade lasers [2] are the alternatives capable of the mid-infrared light emission, quantum cascade lasers are still more preferable

candidates due to their higher output powers [3], wide operating temperature range [4] and broad wavelength selection [5, 6]. However, the complexity of the single mode design for a wide range of target wavelengths, that is imperative for the gas spectroscopy, quite often results in low device yield, resulting from additional fabrication steps that can cause waveguide imperfections leading to multimode emission or single mode emission at the wrong wavelength. Simplification of processing steps is a move towards minimizing the potential fabrication errors, which play very important role in determining device yield, especially at the early stage of the device development.

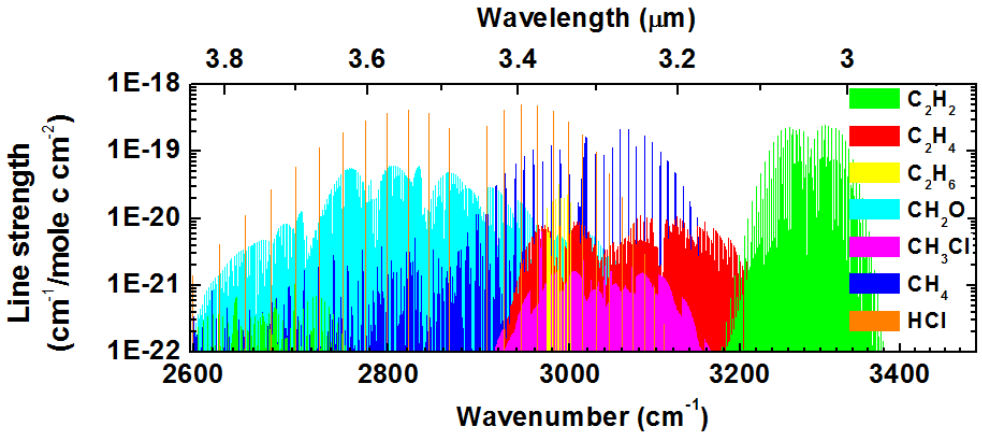

Figure 5.1: Light absorption at various wavelengths by the atmospheric gases, taken from HITRAN database [7].

There is a number of methods for achieving single mode operation in QCLs, including the use of an external cavity [8], that will be described in more details in Chapter 6, distributed Bragg reflector mirrors [9] or distributed feedback (DFB) grating [10]. Since the first demonstration of DFB QCL in 1997 [11] with metalised surface grating, operating at room temperature with the threshold current density of $J_{th} = 7 - 9\ kA/cm^2$ and peak optical powers above 100 mW, various types of DFB gratings have been tried, with the maximum reported continuous wave emission power of 2.4 W at room temperature with $J_{th} = 1.6\ kA/cm^2$ [12].

DFB lasers have a different feedback mechanism from that of Fabry-Perot type lasers.

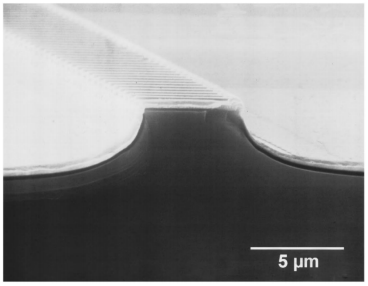

(a) Surface DFB grating

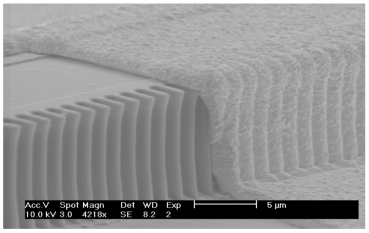

(b) Lateral DFB grating

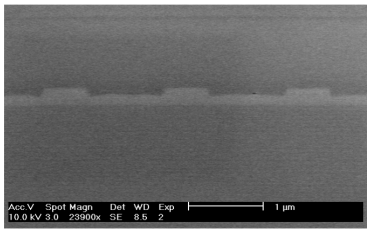

(c) Buried DFB grating

Figure 5.2: Three most common types of DFB grating etched into the QCL waveguide. a) The first DFB QCL with first order surface grating with the grating period of 850 nm [11]. b) Lateral grating with the grating period of 1.58 μm [13]. c) Buried DFB grating placed between the top cladding and active region of the QCL [14]

They all rely on the refractive index fluctuations inside the waveguide caused by the grating. There are three main types of the distributed feedback gratings that are fabricated most often - buried, surface and lateral grating, all shown in Figure 5.2.

The lateral grating (Figure 5.2b) has several advantages over other types of gratings. For example, in contrast with the buried grating (Figure 5.2c), the lateral one involves fewer processing stages and does not require an additional overgrowth step that is both time consuming and may introduce potential defects. The surface gratings (Figure 5.2a) do not require overgrowing too, however, it is much more challenging to control the coupling due to weak mode penetration into the top cladding layer for the short wavelength QCLs. The fabrication of the unilateral grating on one side of the ridge, reduces the possibility of making an error in fabrication even further.

The aim of this chapter is to design and fabricate DFB laser with the targeted emission wavelength in a spectroscopically important mid-infrared region. The fabricated lasers, described in this chapter, have their emission locked at $\lambda \sim 3.6\,\mu m$, suitable for formaldehyde (CH_2O) detection, and $\lambda = 3.37\ \mu m$, often used for butane (C_4H_{10}) detection. This chapter describes the design and fabrication of a DFB laser with an unconventional third order unilateral grating. The fabrication challenges, performed calculations, that were aimed to target specific wavelengths, and measured results are also described.

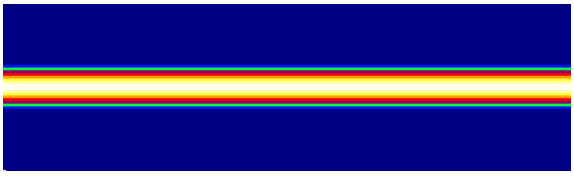

(a) Forward traveling wave in a FP cavity with a lossless waveguide

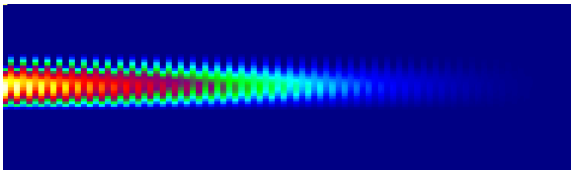

(b) Wave reflections in a DFB laser waveguide caused by the grating

Figure 5.3: Wave propagation in a computer modeled FP (a) and DFB (b) cavities. In a FP cavity the intensity is transmitted with no losses (assuming lossless waveguide), while the waveguide with a DFB grating reflects some of the wave back, reducing the simulated light transmission. FP and DFB waveguides are 10 μm and 10 $\mu m + 2$ μm wide respectively. The color map shows normalized wave intensity inside the waveguide with white color representing unperturbed wave propagation ($W = W_0 = 1$).

5.2 Working principles of distributed feedback

Unlike the Fabry-Perot lasers where the light feedback is achieved from the wave reflection from the side mirrors, the distributed feedback lasers use a periodic grating that provides selective feedback and mode generation.

The grating can select the wavelength of incident light through phenomena recognized and analyzed by Bragg [15]. As shown by the waveguide simulation in Figure 5.3, the incident wave at the left facet of the lossless waveguide travels towards the right facet unperturbed if no grating is present (Figure 5.3a). However, periodic corrugations create a waveguide with the alternating effective refractive indexes (n_{eff}) causing partial reflections as the wave propagates (Figure 5.3b). The reflected wave returns to the left facet partially reflecting again until some of it reaches the point of incidence (left mirror). Upon the arrival to the left mirror the wave is reflected and interferes with the oscillating wave either constructively or destructively, depending on the wavelength. If the oscillating wave is near or at the corresponding Bragg wavelength (λ_B) it interacts constructively providing the required feedback for the lasing to occur. Alternatively, if the wave is away from λ_B, the interference is destructive consequently suppressing the laser emission at that frequency.

Since a Bragg grating amplifies some frequencies and suppress the others it is sensible to combine Fabry-Perot laser cavity with embedded grating creating wavelength selection and selective feedback.

5.2.1 Grating calculation

The etched gratings usually have very small features, much smaller than the laser ridge itself (see Figure 5.2). These features are proportional to the emission wavelength. While it is a common practice to manufacture first order gratings for the far-infrared and terahertz lasers, this task becomes more challenging for devices emitting in the short wavelength mid-infrared spectral region. The typical size of such grating for the wavelength range $3\,\mu m < \lambda < 4\,\mu m$ is in the order of $\sim 250 - 300\,nm$. Features of this size are too small to be defined using ordinary photolithographic techniques, thus it has to be fabricated using either e-beam [16] or holographic lithography [17], increasing the fabrication time of such devices and the ability to integrate this process into a high volume industrial process. Devices made with second order grating typically cause surface emission, proving more difficult to harness emitted light with the existing detection setups here at Sheffield. Additionally, in order to maximize the coupling coefficient, the grating *mark:space* ratio has to divert from 50 % mark, causing some of the fabricated features comparable in size to those required by first order grating, preventing the use of optical lithography. By contrast, in a third order grating [14] the size of these features is increased to $750 - 900\,nm$ allowing them to be defined using conventional UV contact photolithography [18]. However, the downside of using a higher order grating is the reduction of the coupling coefficient κ, that defines how strongly the optical mode is coupled to the grating [19].

For a first order grating, the coupling coefficient is defined in Equation 2.38, where κ is the measure of strength of the backward Bragg scattering and so is the amount of feedback per unit length (cm^{-1}).

For the optimum laser performance the κL product, where L is the length of the optical

cavity must be equal to unity [19]. However, for the real devices it was determined that the lasers have a lower threshold, better slope efficiency and higher optical powers if $\kappa L = 2-3$ [20, 21]. In practice this means that the fabricated lasers require higher coupling coefficient or smaller cavities than predicted, in order to achieve better performance. However, a very small cavity does not provide enough gain for amplified light to overcome the losses resulting in no emission. Alternatively, very big κ will over-couple the laser and therefore reduce its performance.

In order for the Bragg wavelength to interfere constructively with itself, the grating has to be periodic, with the period equal to one half of the designed wavelength as shown in Equation 2.35. It is clear that the size of grating period Λ, scales linearly with the grating order m, making it easier to be fabricated for higher order gratings.

An additional benefit of using third order grating is increased wavelength control, compared to the lower order gratings. As seen from Equation 2.35 the wavelength selectivity is proportional to the grating period Λ and inversely proportional to the order of the grating m. As a result, the wavelength shift, for the third order grating, is one third of that obtained using first order grating. This allows the factor of 3 increase in wavelength selectivity, providing tighter wavelength distribution. The fabrication of third order grating is much simpler technique than the fabrication of sampled gratings, where fine wavelength selection is also possible [22].

5.3 Computer modeling and sample fabrication

This section describes analytical and computational calculations to determine the grating period Λ required to target $\lambda = 3.58\ \mu m$ wavelength often used for sensitive formaldehyde detection. This hydrocarbon is highly toxic and corrosive making it very dangerous for people working with this gas or producing it. The formaldehyde may cause headaches and minor eye and airway irritation at levels bellow the odor threshold (0.83 *ppm* [23, 24])

and is considered to be immediate danger to life or health at concentration of 20 *ppm* [25]. As a result, suitable light sources are required to be used inside the laser based detection systems for sensitive gas detection, such as those produced by the collaborating partner *Sensor Sense* in Netherlands [26]. The sample fabrication is described in Section 5.3.2, where the wafer, with the emission wavelength centered at $3.5 - 3.7\ \mu m$, is being used.

5.3.1 Computer modeling

Prior to the device fabrication the waveguide was modeled using a photonics CAD tool - Fimmwave [27]. The software is capable of simulating the distribution of the optical mode inside a passive waveguide. The layers of the simulated waveguide are defined through characteristic parameters, such as the material's refractive index (n) and the losses (α).

The visual representation of the calculated first mode inside the waveguide structure is shown in Figure 5.4. The software also generates two important values that are used for analytical computations determining optimum conditions - confinement factor Γ and the effective refractive index n_{eff}. Confinement factor Γ specifies the fraction of the optical mode confined inside the core region of the waveguide. Effective refractive index n_{eff} is the average refractive index experienced by the optical mode inside the waveguide as a result of the different material layers inside the core region. Two main calculations, used for the grating dimension determination, are described in the sections below.

Calculation of the grating period Λ

The grating period plays a crucial role in the wavelength selection. As described in Section 5.2.1, the analytical calculation for the grating period Λ can be estimated using Equation 2.35, where the effective refractive index of the waveguide n_{eff} is obtained from the computer model. The effective refractive index for the laser cavity used for this sample

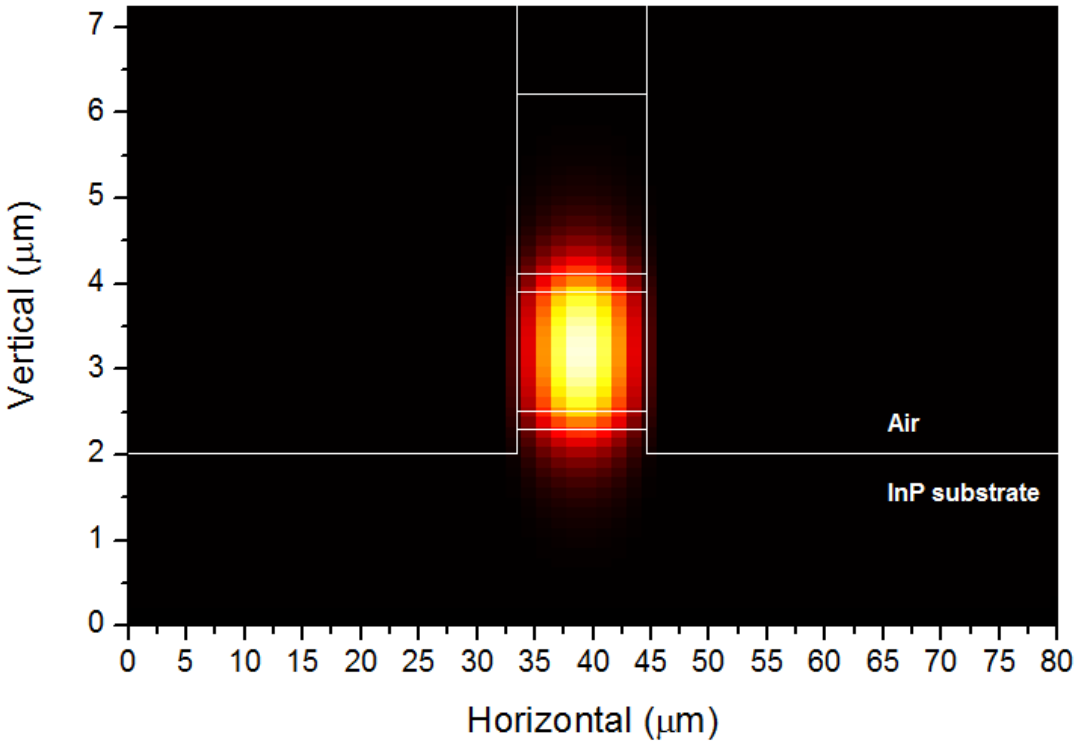

Figure 5.4: Computer generated model of the laser waveguide with the calculated mode intensity inside the ridge. The calculations were performed for emission wavelength in air of $\lambda \sim 3.6\ \mu m$. The composition of layers from the bottom up: InP substrate, $InGaAs$ spacer ($N_d \sim 1 \times 10^{17}\ cm^{-3}$), followed by the laser core region, $InGaAs$ spacer level ($N_d \sim 1 \times 10^{17}\ cm^{-3}$), InP cladding ($N_d \sim 3 - 4 \times 10^{17}\ cm^{-3}$), InP cladding ($N_d \sim 8 \times 10^{18}\ cm^{-3}$), where N_d is doping concentration. The laser waveguide is surrounded with air, with the mode confinement factor of $\Gamma = 0.656$.

fabrication is $n_{eff} = 3.2$, as described in Reference [28]. As a result, the grating period of $\Lambda = 1.678\,\mu m$ is calculated to create selective feedback for the Bragg wavelength of $\lambda_B = 3.57\,\mu m$.

Alternatively, the grating period can be calculated with the 3D waveguide model that simulates wave propagation for a specified corrugated waveguide. The Figure 5.5, plots the wave propagation at a given wavelength as a function of grating period. The lossless waveguide assumption ($\alpha = 0$) allows the observation of the perfect transmission ($T = 100\%$) throughout the waveguide at certain periods and a clear reduction in transmission

for the period equal to $1.68\,\mu m$. The transmission reduction occurs due to some of the wave being reflected back, as described in Section 5.2. Both analytical and computational results closely agree with each other with a negligible difference. This difference can be ignored especially considering that the error during fabrication can be as high as $\sim 0.01\,\mu m$ causing a wavelength variance in the range of $\Delta\lambda = \pm 0.02\ \mu m$.

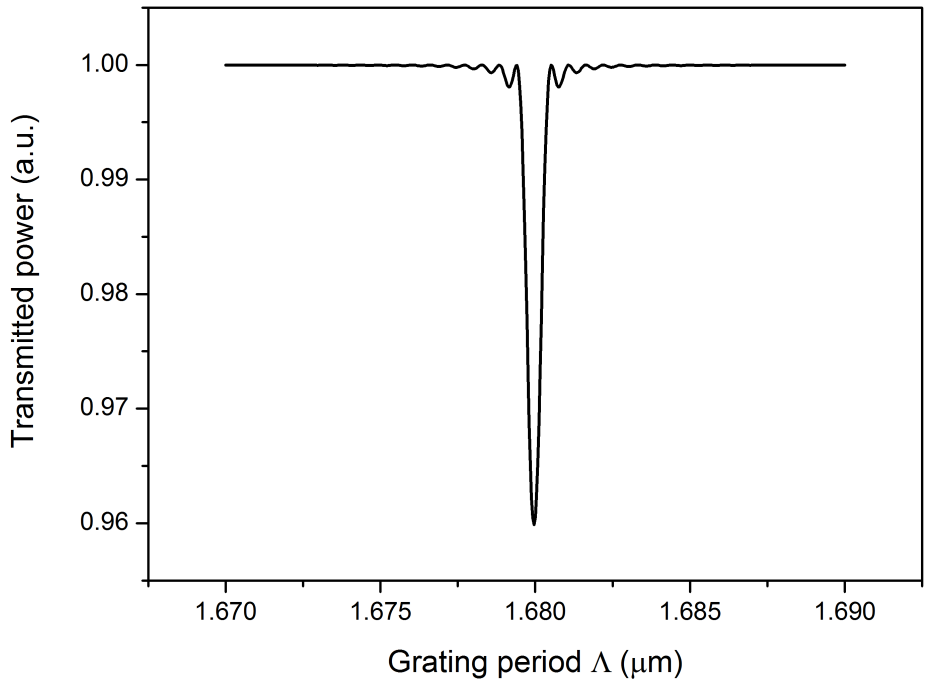

Figure 5.5: Propagating light intensity in the DFB waveguide as a function of varying grating period. The transmission reduction at $\Lambda = 1.680\ \mu m$ corresponds to the grating period required to provoke feedback at $\lambda_B = 3.58\,\mu m$.

Determination of the required device dimensions

The dimensions of the grating as well as the length of the DFB cavity can influence the strength of the feedback received by the device. Smaller cavities tend to have less gain material resulting in weaker wave coupling, while larger cavities might become overcoupled. As a result, the amount of coupling has to be precise for efficient light generation. As

mentioned in previous section, the product κL should be between $2-3$ to achieve the best quantum cascade laser performance [20, 21].

The coupling coefficient is expressed in Equation 5.1.

$$\kappa = \frac{2\Delta n\Gamma}{m\lambda_B} \times f_{red} \tag{5.1}$$

where f_{red} accounts for the variation of the *mark:space* ratio, the ratio of the grating's peak and its period (peak+groove), and is expressed as:

$$f_{red} = sin(\pi\Lambda_1/\Lambda) \tag{5.2}$$

here Γ is the mode confinement factor obtained from the computational model and typically is in a $0.64-0.66$ range, m is the grating order and Λ_1/Λ is grating's the *mark:space* ratio. Δn was found by $\Delta n = n_1 - n_2$, where n_1 and n_2 are the effective refractive indexes of two waveguide segments representing the ridge and grating regions, as shown in Figure 5.6. The effective refractive index was obtained for each segment and used to obtain Δn. For example, $5\,\mu m$ waveguide ridge with $1\,\mu m$ deep double sided lateral grating will be modeled as two different segments - 5 μm and 7 μm wide. Two effective waveguide indexes will be used to calculate Δn, by simply subtracting one from another ($\Delta n = n_{7\mu m} - n_{5\mu m}$).

Once κ is obtained, the length of the laser ridge L can be adjusted in accordance to $\kappa L = 2-3$. The same computational technique can be applied for the single-sided grating. But this time the waveguide will be split into 5 μm and 6 μm wide segments to obtain the $5\,\mu m$ wide ridge with $1\,\mu m$ unilateral grating. One can notice that coupling coefficient κ for $1\,\mu m$ deep double sided grating will be the same as for $2\,\mu m$ deep unilateral grating for the same ridge width.

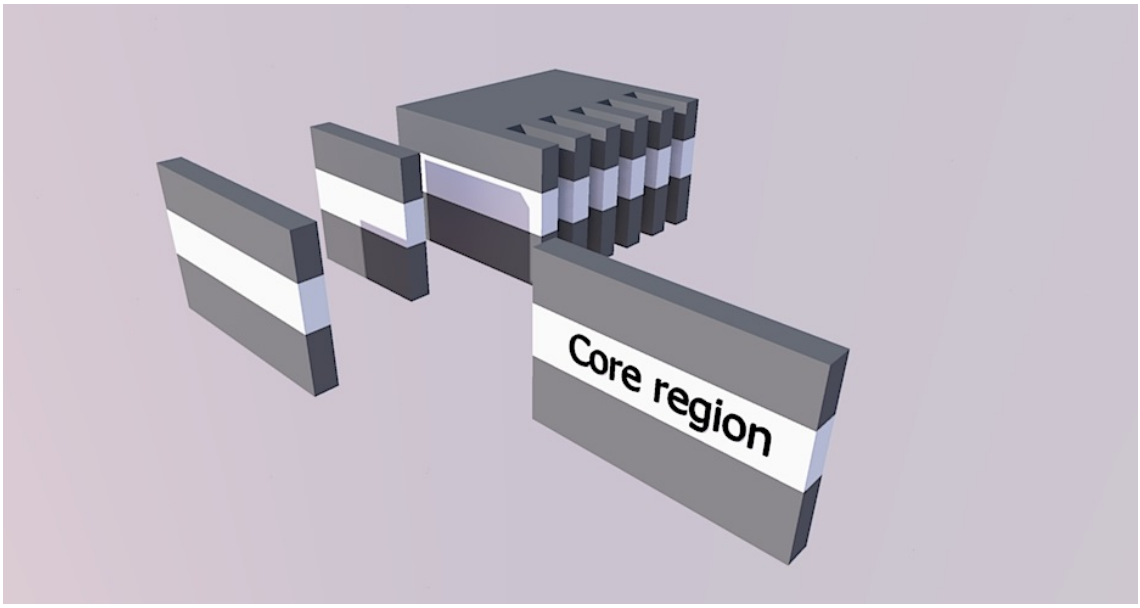

Figure 5.6: Unilateral grating splits into individual segments. Δn is calculated by subtracting the effective refractive index of one segment from another, such as $\Delta n = n_1 - n_2$

5.3.2 Sample fabrication

One of the advantages of making the lateral grating is the simplicity in its fabrication. The processing stages and techniques are the same used for simple ridge definition described in Section 3.3. The main difference between the simple ridge definition and the ridge with the integrated unilateral grating occurs at photolithographic stage of ridge definition and etching.

In general, the resolution of photolithography is expressed in terms of exposure wavelength and numerical aperture (NA) [29], as a result, the achievable exposure resolution is described by

$$Resolution = \xi \frac{\lambda}{NA} \tag{5.3}$$

where the constant ξ is highly dependent on the process being used and typically can have values ranging from 0.5 to 0.8 for a less stringent process. The numerical apertures

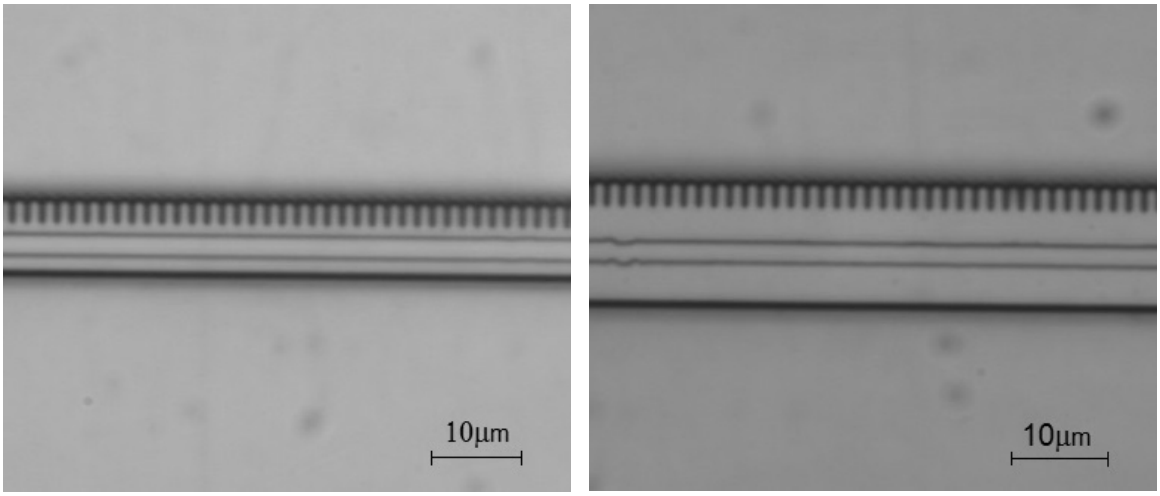

Figure 5.7: An optical image of two, 5 μm and 10 μm wide, fully processed ridges with 2.5 μm wide unilateral grating. The grating pitch is $L = 1.68$ μm.

of commonly used systems range from about 0.5 to 0.6, therefore the maximum resolution that can be achieved using photolithograpic technique is comparable to the exposure wavelength being used. Mask aligner Suss MJB300 has 300 nm wavelength, which is ~ 3 times smaller than the smallest feature of the grating (840 nm).

While grating patterning is easier and cheaper due to the size of the grating and availability of the optical lithography, the main challenge comes from the ability to transfer the pattern onto the semiconductor, *i.e.* etching. Different etching techniques will produce different results, influencing the topography of the substrate. Etching processes can be classed into two categories depending on its dominant mechanisms - *wet* chemical etching and *dry* plasma chemical etching. Pure chemical etching, due to its nature, is isotropic type of etching (Figure 5.8). The chemical reaction with the material is usually the same in all directions, producing undercut and non-vertical sidewalls. Chemical etching can produce vertical walls if over-etched. The rate to the side of the substrate will remain the same producing vertical side walls with much higher opening than the patterning mask. As a result, *wet* etching cannot be used for deep and narrow features, such as those required for unilateral grating definition.

Plasma etching, on the other hand, due to its etching mechanism involving highly energetic

ions in a low pressure atmosphere, has a mean free path that is many times larger than the etching features resulting in etching at right angles, hence anisotropic material removal [30]. In order to form $\sim 5\ \mu m$ deep and 840 nm wide opening with parallel walls the semiconductor etch recipe, consisting of argon (Ar) and silicon tetrachloride ($SiCl_4$) gases, has been used. The close inspection of the formed ridge revealed that etchant penetration to the valleys between the peaks of formed diffraction grating is very poor, resulting in weak mode coupling producing multi-mode laser emission. As a consequence, the etching recipe has been changed to 7 standard cubic centimeters per minute ($sccm$) chlorine flow and 20 $sccm$ argon flow. The RF power was increased from 220 W to 280 W to increase physical etching and gas penetration to the grating valleys. The ICP power was reduced from 1000 W to 500 W to decrease the plasma density inside the processing chamber. Decreased plasma density inside the ICP chamber reduces the chemical etch rate, creating smoother wall surface.

The chlorine based etching process has 2.5 times slower etching rate (400 nm/min for Cl based recipe compared to 1000 nm/min for $SiCl_4$ based recipe) allowing the definition of deep vertical features and exhibits good penetration properties into the narrow areas of the sample. Two images, taken with an optical microscope, of the etched ridge are shown in Figure 5.7. The shown ridges are insulated with a SiO_2 film and contact windows etched.

The grown QCL wafer was designed to have lasing gain centered at $3.5 - 3.7\,\mu m$ at room temperature with a strain compensated $In_{0.7}Ga_{0.3}As/AlAs(Sb)$ laser core design similar to the one described in Reference [28]. $In_{0.53}Ga_{0.47}As$ spacer layers of 200 nm were grown around $\sim 1.32\,\mu m$ thick laser core by MBE on a low doped ($3 - 5 \times 10^{17}\,cm^{-3}$) n-type InP substrate. The upper cladding consisted of InP grown in metal-organic vapour phase epitaxy reactor. The details of the growth and the upper cladding layers can be found in Reference [31]. All devices, targeting 3.58 μm wavelength, were made with $\Lambda = 1.68\ \mu m$ period grating with the lateral depth ranging from 1 μm to 5 μm.

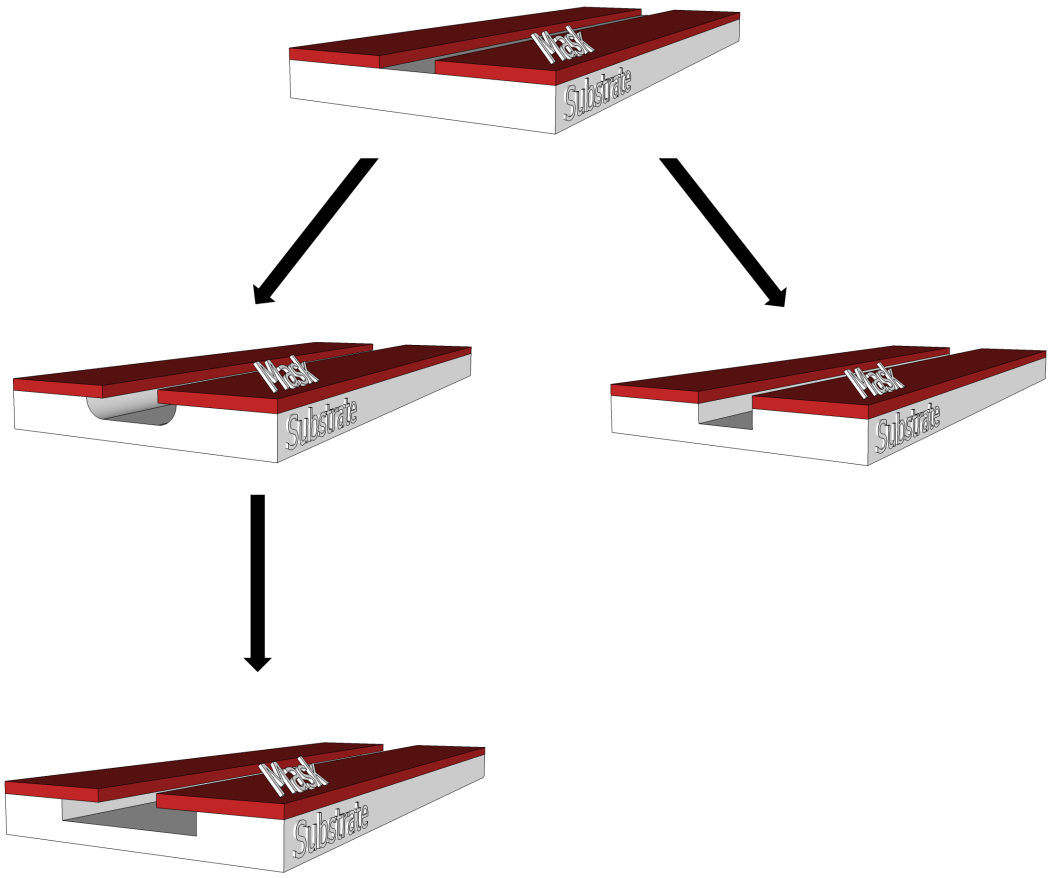

Figure 5.8: Representation of isotropic and anisotropic etching types. Left: Isotropic etch has same rate of etching in both directions - horizontal and vertical, creating arched undercut underneath the mask. If the process is selective the horizontal etch will stop, while vertical etch will form nearly vertical walls. Right: Anisotropic etching vertical component is almost negligible creating a perfect vertical walls.

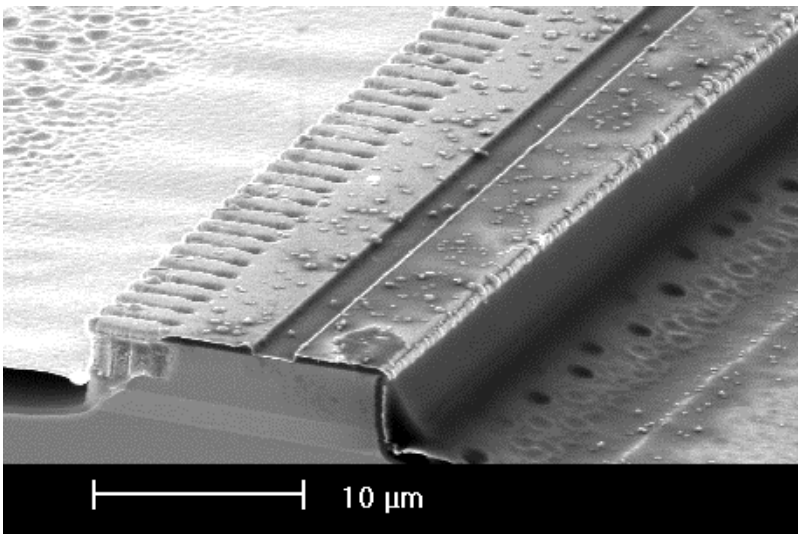

Figure 5.9: Scanning Electron Microscopy image of a fully processed quantum cascade laser ridge with single-sided lateral grating ($10\,\mu m$ wide plain ridge with $3\,\mu m$ wide grating on one side) before deposition of electroplated gold. (The spots on the surface of the laser ridge and around are the results of the residues from SiO_2 hard mask and photoresist.)

5.4 Device characterization

Due to possible mismatch between the actual and calculated effective refractive indexes used in the computational model, lasers were processed into 10 μm and 5 μm wide ridges with three different grating depths ranging from 1 to $5\,\mu m$ and cleaved into 2, 3 and $4\,mm$ long chips. Such variation in the ridge size also helps to compensate for unpredictable fluctuations in coupling coefficient and effective refractive index due to under-etched grating. The longer, 4 mm chips were chosen to maximize the output power, by maximizing the length of the gain region. The scanning electron microscope image of the QCL ridge with unilateral grating is shown in Figure 5.9. It can be noticed that the grating valleys contain some of the active region that wasn't removed during the etch. This extra under-etched material can influence the coupling coefficient and is accounted for by the variation in the device dimensions. The contamination spots seen around the ridge are the result of not properly removed photo-resist after the photo-lithographic stage.

The experimental results showed that the shortest ($2\,mm$) and longest ($4\,mm$) devices have

single mode yield less than 1 % regardless of the width of the ridge and grating, while $3\,mm$ long lasers demonstrate much higher yield ($\sim$ 8 %), especially for the $10\,\mu m$ wide ridges ($\sim$ 20 %). In this chapter, we present laser characteristics for $10+2\,\mu m$ wide ($10\,\mu m$ wide plain ridge + $2\,\mu m$ unilateral grating on the side) and $3\,mm$ long devices.

5.4.1 Results

As shown in Figure 5.10, the typical $10 + 2\,\mu m$ wide device operates in the single mode regime at room temperature with a side mode suppression ratio (SMSR) of $\sim$ 30 dB. The emission wavelength of $\lambda = 3.58\,\mu m$ is in very good agreement with that predicted by the computational model. The effective refractive index of the laser core derived from the observed emission wavelength ($n_{eff} = 3.196$) appears to be almost identical to that used in the model ($n_{eff} = 3.2$).

The full width at half maximum (FWHM) of the single mode emission line for the QCL driven by a 50 ns current pulse is $0.8\,cm^{-1}$. The FWHM still remains high at $0.4\,cm^{-1}$ even if the current pulse width is reduced to $25\,ns$. The origin of this line broadening lies in the large temperature fluctuations as the core region of the device gets heated during the pulse [32]. The emission spectra for different temperatures showing multi- and single-mode lasing are presented in Figure 5.11. For the temperature range $100K$ to $270K$ only multi-mode operation is observed. The average emission line shift rate for Fabry-Perot type lasing is $\Delta\nu/\Delta T \sim -1.3\ cm^{-1}/K$. At temperatures above 280K, as shown in Figure 5.12, the feedback produced by the unilateral grating overlaps with the laser gain, forcing the single mode emission and slowing down the wavelength shift rate to $\Delta\nu/\Delta T \sim -0.2\ cm^{-1}/K$. The device remains in single mode up to 420K, with the wavelength increasing from $\lambda = 3.576$ to $3.61\,\mu m$ as the temperature increases from $280K$ to $420K$. This tuning rate is 6 times lower than that for Fabry-Perot type multi-mode operation but much higher than the typical ($\sim -0.08\,cm^{-1}/K$) value obtained for single mode quantum cascade lasers at longer wavelengths [33]. The faster wavelength shift

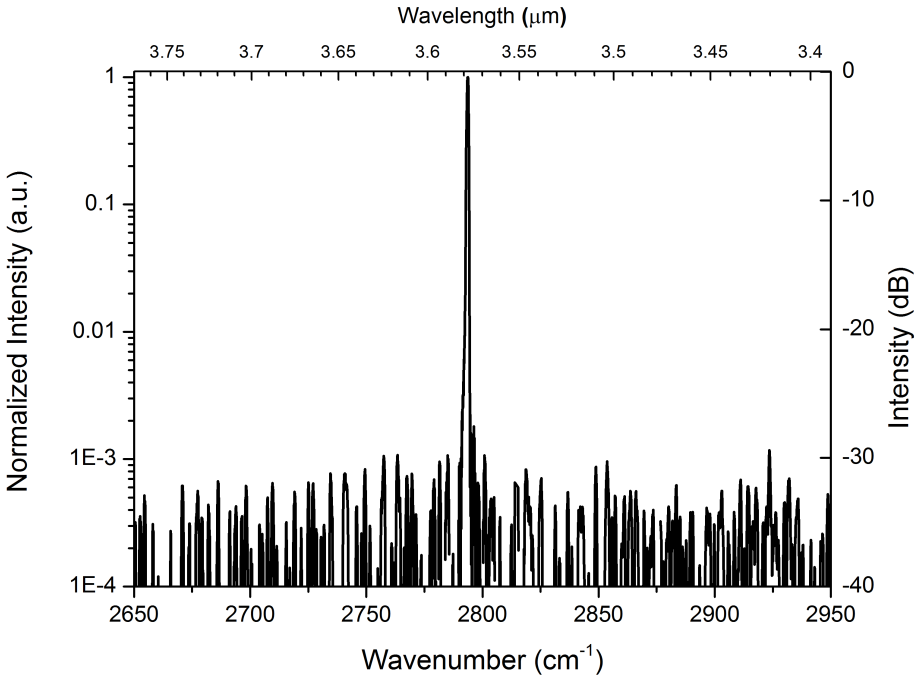

Figure 5.10: Emission spectrum of 3 mm long and $10+2\,\mu m$ wide laser ridge at 20% above its threshold current at room temperature (273K). SMSR of $\sim$ 30 dB is observed.

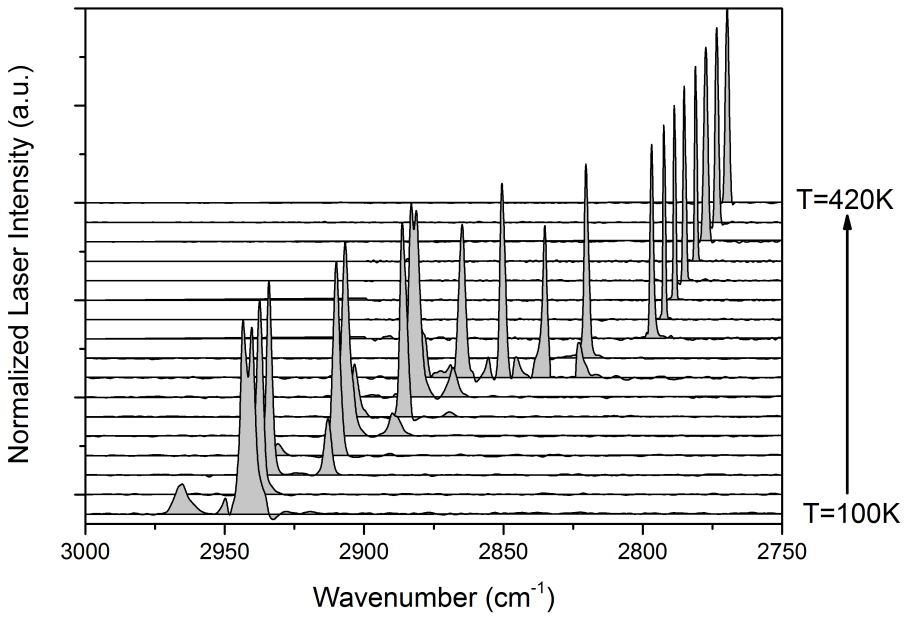

Figure 5.11: Spectrum shift with the temperature from 100K to 420K with an incremental step between neighboring spectra of 20K. The single mode emission is observed at temperatures above 280K. The spectra are vertically shifted for clarity.

makes these short wavelength QCLs very attractive for spectroscopic applications, since it spans over a wider spectral range for the same temperature change ΔT. As a result, much wider gas absorption features can be covered, compared to the single mode emission obtained with the first order grating.

The typical threshold current density of the single mode device increases from $4.3\,kA/cm^2$ at room temperature to $11\,kA/cm^2$ at 420K. At temperatures higher than $\sim 350\,K$ the laser emits exclusively in single mode regime over the whole measured current range. However, at the temperatures lower than 350K single mode emission is only observed up to $7.3\,kA/cm^2$ at room temperature and up to $\sim 11\,kA/cm^2$ at 350K. The single mode emission exhibits maximum peak power of 1.0 W over whole temperature range up to 350K switching to multi-mode regime at higher powers, as shown in Figure 5.13.

The presented lasers with unilateral grating show very similar characteristics (the threshold current and optical power) to other QCLs operating at similar wavelengths [16, 17] but manufactured with more challenging first order double sided or surface gratings. The simpler processing of DFB lasers with single-sided lateral grating makes them more desirable alternatives for short wavelength single mode generation.

5.5 Unilateral grating for 3.37 μm wavelength generation

As mentioned at the beginning of this chapter, hydrocarbons play an important role in industrial processes. Methane (CH_4), ethane (C_2H_6) and butane (C_4H_{10}) are typically closely monitored in industrial and medical applications [34]. The laser emission wavelength of $\lambda \sim 3.37\ \mu m$ is commonly used for butane detection due to the highly absorbent ro-vibrational modes in this spectral region. This section describes the process used to target $\lambda = 3.37\ \mu m$ wavelength with the unilateral grating.

In order to produce emission at $\lambda = 3.37\ \mu m$, the active region of the grown material is designed to have gain width centered at $\lambda \sim 3.3 - 3.5\ \mu m$. Three QCL wafers, $M4054$,

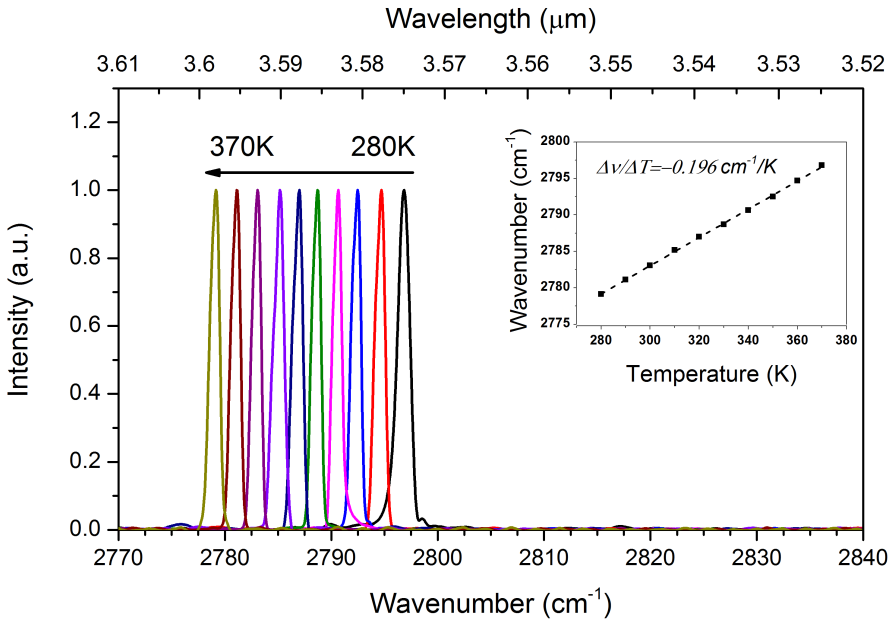

Figure 5.12: Single mode emission observed above 280 K shifts with temperature. The inset shows the tuning rate of the single mode lasing.

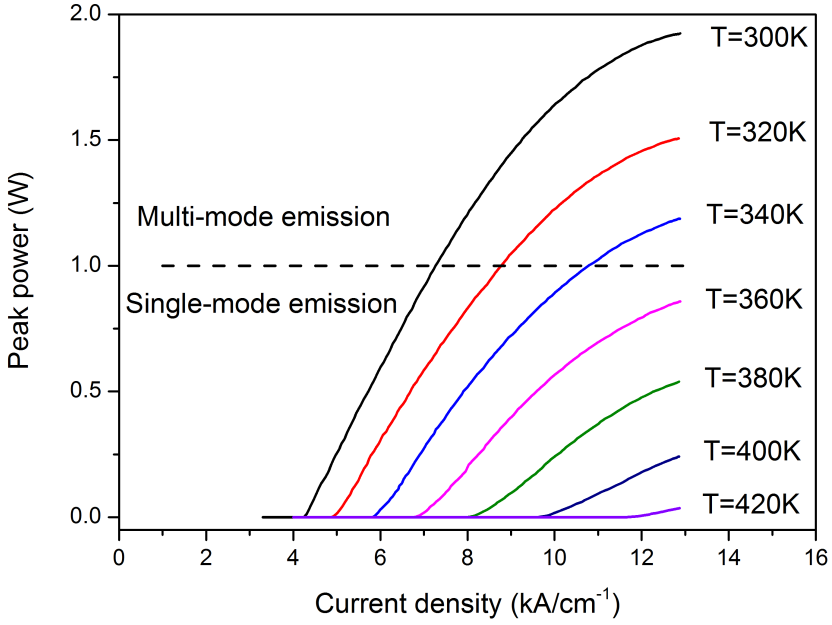

Figure 5.13: Light-current characteristics for the output powers measured from the single facet of a $10 + 2\,\mu m$ wide laser ridge at different operating temperatures.

$M4066$ and $M4071$ were grown using *MBE* with the designed emission wavelength around $\lambda \sim 3.3 - 3.5\ \mu m$ at room temperature. The layer sequence of the $M4054$ design is shown in Appendix A.1. The active region designs of $M4066$ and $M4071$ samples were primarily based on the $M4054$ design with small modifications. Sample $M4066$ had a longer injector with increased number of QWs in the bridging region and sample $M4071$ was designed with tilted injector, with raised injector energy levels aiming to improve electron transfer into the upper laser level.

These wafers were processed into standard ridge waveguides using wet chemical etching, as opposed to plasma etching, for initial testing and characterization in order to determine its performance and potential to be used for specified wavelength generation. The spectra and Current-Voltage (IV) characteristics are shown in Figure 5.14 and Figure 5.15.

As seen from the figures above, neither of the materials has its measured emission centered at the targeted $\lambda = 3.37\ \mu m$ wavelength. The actual emission wavelength can differ from the designed frequency, due to many reasons, including not fully optimized design of the structure, causing the laser emission at neighboring wavelengths or the variation in the designed and the actual epitaxial growth of layers. However, sample number M4066 is emitting the closest to the targeted frequency, with the measured emission wavelength at room temperature of $\lambda \sim 3.27 - 3.33\ \mu m$, depending on the ridge width. The ridge width, as seen from Figure 5.14, plays a role in the emission wavelength. The emission frequency shifts with the different ridge width due to slightly different effective refractive index n_{eff} as well as the different operating temperatures of the device at the threshold. The wider ridges require more current to reach the emission threshold, resulting in a hotter active region responsible for the observed wavelength variation. The gain width of similar structures is typically $\sim 400\ cm^{-1}$ wide [35], providing enough coverage to target 3.37 μm wavelength emission. The DFB grating should contribute enough feedback to force the laser emission at this frequency. Moreover, Figure 5.15 shows that the devices from $M4066$ material require a smaller amount of voltage to align its laser levels, therefore producing

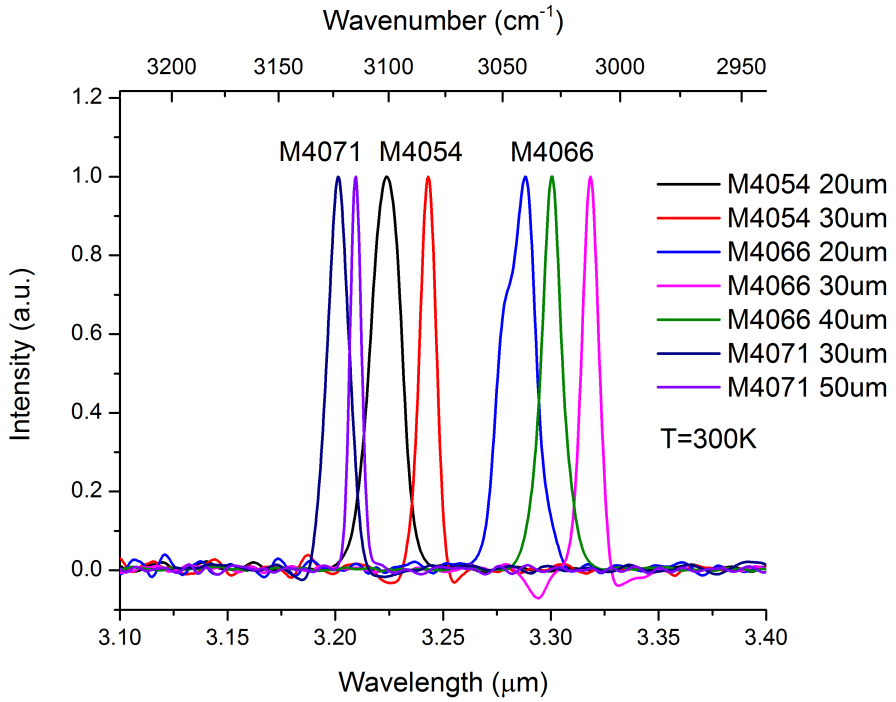

Figure 5.14: Emission spectra from three different wafers. Different width of the ridges were used to demonstrate the wavelength variation between the 3 mm long devices as a result of refractive index dependence on the ridge width.

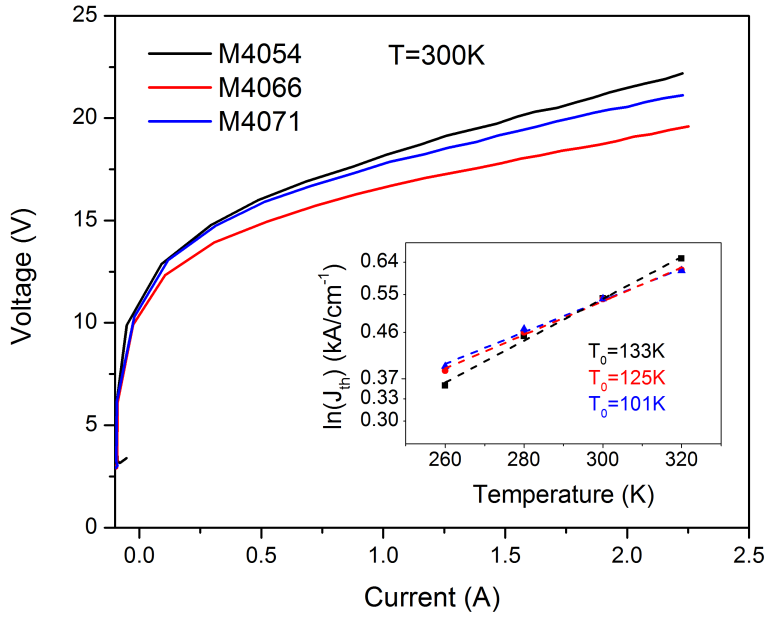

Figure 5.15: IV characteristics of three different wafers. The inset shows threshold current density dependency on the temperature. T_0 extracted from this graph is also included.

less heat compared to the devices requiring higher operational voltages, assuming the I_{th} remains the same or lower.

A simulation process, similar to the one described in Section 5.3.1 was adapted to calculate the required grating period for the material system based on $M4066$ sample design, targeting $\lambda = 3.37\ \mu m$.

Five different grating periods were used in order to compensate for the possible calculation, mask manufacturing and fabrication errors. The mask manufacturers [36] guarantee the tolerances of the requested features to not exceed 200 nm, while the fabrication errors, occurring due to over-etch or over-exposure can be in the region of 10 nm, potentially giving the maximum wavelength variation of $\Delta\lambda_B = 0.448\ \mu m$. The variation can also influence the single mode device yield. The mask consisted of five different unilateral gratings with the grating periods of $\Lambda = 1.54\ \mu m$, $\Lambda = 1.56\ \mu m$, $\Lambda = 1.58\ \mu m$, $\Lambda = 1.60\ \mu m$, and $\Lambda = 1.62\ \mu m$. The ridge widths of 5, 10 and 15 μm were used to obtain wider emission wavelength distribution due to the slightly different effective refractive index n_{eff} for different ridge widths. The lateral depth of the unilateral grating was locked at 1.5 μm.

5.5.1 Results

Figure 5.16 shows the emission spectra obtained from devices with different grating periods. As expected, the single mode emission distribution is equidistant and is in agreement with the corresponding period of the diffraction grating. The equidistant distribution of the frequencies demonstrates the possibility of the very accurate targeting of the specific wavelengths using the third order grating. The emission wavelength of λ =3.38 μm (2959 cm^{-1}) at room temperature is the closest to the targeted wavelength of λ =3.37 μm (2967 cm^{-1}). The emission frequency can slightly be tuned by lowering the temperature of the laser chip.

The calculated wavelength emission shift rate for 5 μm wide laser device with the grating

period of $\Lambda = 1.54$, extracted from Figure 5.17, is $\Delta\nu/\Delta T \sim 0.19\ cm^{-1}/K$. Similarly, the shift rate for 15 μm device is $\Delta\nu/\Delta T \sim 0.17\ cm^{-1}/K$. The results are very similar to the obtained wavelength shift rate of the single mode device emitting at $\lambda \sim 3.58\ \mu m$, described in Section 5.4.1. By analyzing Figure 5.16, it can be noticed that the proposed wavelength of $\lambda = 3.37\ \mu m$ can be reached with the devices with diffraction grating period of $\Lambda = 1.60\ \mu m$ at $T \sim 230\ K$ or with $\Lambda = 1.58\ \mu m$ at $T \sim 450\ K$.

It can be noticed that single mode emission at $\lambda = 3.27\ \mu m$ (3055 cm^{-1}) consists of two peaks spaced $\sim 52\ cm^{-1}$ apart. The second peak (3003 cm^{-1}) appears when the distributed feedback grating is forcing the laser emission further away from the frequencies overlapping with the gain maximum. Figure 5.17 demonstrates mode switching from single-mode to multi-mode emission, similar to that shown in Figure 5.11, where feedback provided by the grating at higher temperatures is too weak to initiate light generation further away from its optical gain. Once the temperature is reduced, the gain curve shifts towards shorter wavelengths, overlapping with the feedback from the grating thus producing single mode emission. More stable single mode emission can be achieved with a QCL material with the gain centered at the targeted wavelength allowing wider temperature variation.

5.6 Conclusion

In conclusion, the importance of single mode generation and its wide frequency tuning requirement has been discussed. The successful wavelength selection for different wavelength regions has been described and demonstrated.

The novel single mode $\lambda \sim 3.58\ \mu m$ $In_{0.7}Ga_{0.3}As/AlAs(Sb)$ QC laser with 3^{rd} order, single-sided lateral grating has been successfully realized for the first time. The fabrication of single sided grating requires fewer fabrication steps, therefore reducing the number of potential defects introduced during device processing. SMSR of $\sim$ 30 dB and peak power

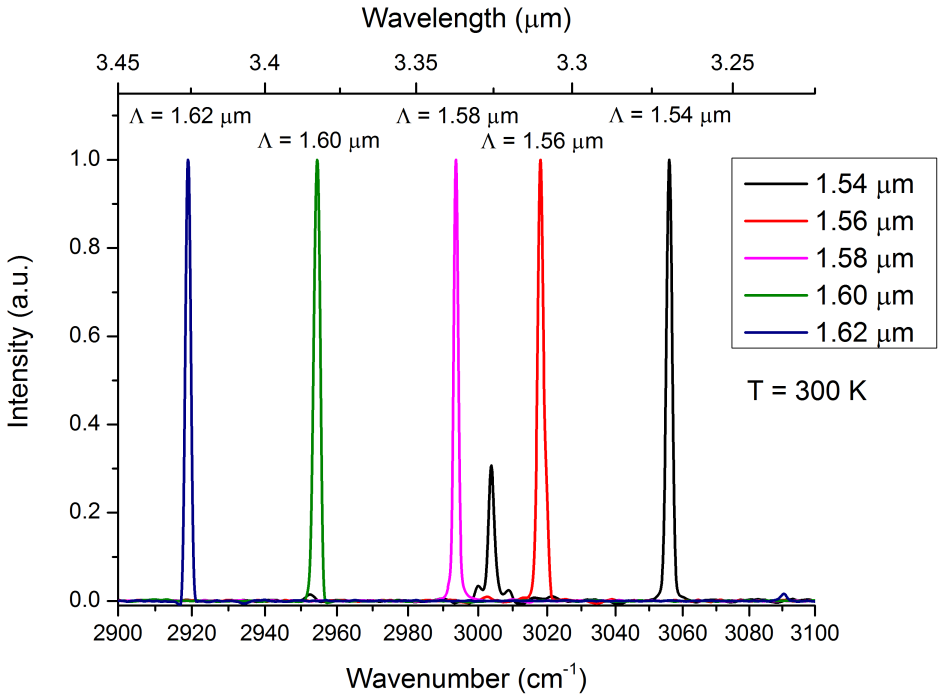

Figure 5.16: The distribution of single mode emission from the devices with different grating period. The grating period of $\Lambda = 1.60$ produces emission closest to $\lambda = 3.37\ \mu m$. The emission at $\lambda \approx 3.27\ \mu m$ ($3055\ cm^{-1}$) has low single mode suppression due to forced emission placed further away from the gain maximum of the structure.

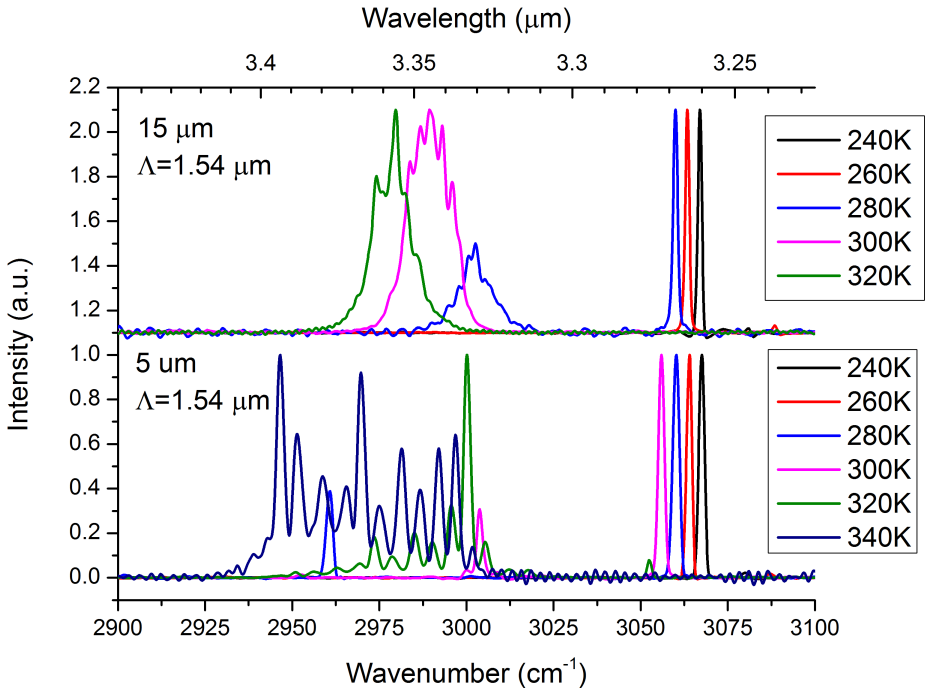

Figure 5.17: The switching behavior between single-mode and multi-mode emission arising due to gain shift as the temperature changes. The single mode emission is observed at lower temperatures, when the gain curve covers shorter wavelengths. Increase in temperature shifts the gain towards the longer wavelengths, producing multi mode emission.

of up to $1.0W$ were observed at room temperature. Single mode operation was obtained in the $280K - 420K$ temperature range, making it accessible for room and high temperature use.

Wavelength selectivity targeting $\lambda = 3.37\ \mu m$ utilizing third order unilateral grating has also been demonstrated. The equidistant emission wavelength distribution for different grating periods demonstrates the ability of selective wavelength generation with much better accuracy than that achieved with the first order gratings [33] due to reduced wavelength sensitivity as a function of grating pitch for higher order gratings. Fine wavelength selectivity utilizing temperature adjustment in order to target specific gas compounds were also discussed and demonstrated.

Most of the fabricated devices described in this chapter revert to the generation of a broad spectrum, characteristic to lasers with Fabry-Pérot cavities, if the feedback from the grating is centered at different frequency than the gain of the QCL material. While calculations, mask manufacturing and fabrication errors have to be taken into account, the targeted wavelengths can be selected with the help of temperature tuning, as demonstrated in this chapter. Additionally, an adjusted active region design allowing laser emission around the targeted wavelength would improve the quality of the single mode generation and provide wider wavelength selection centered around its gain maximum.

References

[1] G. Belenky, L. Shterengas, G.Kipshidze, and T. Hosoda. Type-I diode lasers for spectral region above $3\,\mu m$. *IEEE J. of Sel. Top. in Quant. Electr.*, 17:1426 – 1434, 2011.

[2] C. S. Kim, M. Kim, J. Abell, W. W. Bewley, C. D. Merritt, C.L. Canedy, I. Vurgaftman, and J.R. Meyer. Mid-infrared distributed-feedback interband cascade lasers with continuous-wave single-mode emission to 80^oC. *Appl. Phys. Lett.*, 101:061104–061104–3, 2012.

[3] B. Gökden, Y. Bai, N. Bandyopadhyay, S. Slivken, and M. Razeghi. Broad area photonic crystal distributed feedback quantum cascade lasers emitting 34 W at $\lambda \sim 4.36\,\mu m$. *Applied Physics Letters*, 97(13):131112, 2010.

[4] S. Slivken, N. Bandyopadhyay, S. Tsao, S. Nida, Y. Bai, Q. Y. Lu, and M. Razeghi. Sampled grating, distributed feedback quantum cascade lasers with broad tunability and continuous operation at room temperature. *Appl. Phys. Lett*, 100:261112, 2012.

[5] J. Devenson, O. Cathabard, R. Teissier, and A. N. Baranov. $InAs/AlSb$ quantum cascade lasers emitting at $2.75 - 2.97\ \mu m$. *Appl. Phys. Lett.*, 91:251102, 2007.

[6] H. Luo, S. R. Laframboise, Z. R. Wasilewski, G. C. Aers, H. C. Liu, and J. C. Cao. Terahertz quantum-cascade lasers based on a three-well active module. *Applied Physics Letters*, 90(4):041112, 2007.

[7] L.S. Rothman, I.E. Gordon, A. Barbe, D.Chris Benner, P.F. Bernath, M. Birk, V. Boudon, L.R. Brown, A. Campargue, J.P. Champion, K. Chance, L.H. Coudert, V. Dana, V.M. Devi, S. Fally, J.M. Flaud, R.R. Gamache, A. Goldman, D. Jacquemart, I. Kleiner, N. Lacome, W.J. Lafferty, J.Y. Mandin, S.T. Massie, S.N. Mikhailenko, C.E. Miller, N. Moazzen-Ahmadi, O.V. Naumenko, A.V. Nikitin, J. Orphal, V.I. Perevalov, A. Perrin, A. Predoi-Cross, C.P. Rinsland, M. Rotger,

M. Simeckova, M.A.H. Smith, K. Sung, S.A. Tashkun, J. Tennyson, R.A. Toth, A.C. Vandaele, and J. Vander Auwera. The hitran 2008 molecular spectroscopic database. *Journal of Quantitative Spectroscopy & Radiative Transfer*, 110:533572, 2009.

[8] A. Hugi, R. Terazzi, Y. Bonetti, A. Wittmann, M. Fischer, M. Beck, J. Faist, and E. Gini. External cavity quantum cascade laser tunable from 7.6 to 11.4 μm. *Applied Physics Letters*, 95(6):061103, 2009.

[9] J. Semmel, L. Nähle, S. Höfling, and A. Forchel. Edge emitting quantum cascade microlasers on InP with deeply etched one-dimensional photonic crystals. *Applied Physics Letters*, 91(7):071104, 2007.

[10] S. Golka, C. Pflügl, W. Schrenk, and G. Strasser. Quantum cascade lasers with lateral double-sided distributed feedback grating. *Applied Physics Letters*, 86(11): 111103, 2005.

[11] J. Faist, C. Gmachl, F. Capasso, C Sirtori, D. L. Sivco, J. N. Baillargeon, and Alfred Y. Cho. Distributed feedback quantum cascade lasers. *Appl. Phys. Lett.*, 70: 2670, 1997.

[12] Q.Y. Lu, Y. Bai, N. Bandyopadhyay, S. Slivken, and M. Razeghi. 2.4 W room temperature continuous wave operation of distributed feedback quantum cascade lasers. *Applied Physics Letters*, 98(18), 2011.

[13] K. Kennedy, A.B. Krysa, J.S. Roberts, K.M. Groom, R.A. Hogg, D.G. Revin, L.R. Wilson, and J.W. Cockburn. High performance InP-based quantum cascade distributed feedback lasers with deeply etched lateral gratings. *Appl. Phys. Lett.*, 89: 201117, 2006.

[14] J. P. Commin, K. Kennedy, D. G. Revin, S. Y. Zhang, A. B. Krysa, and J. W. Cockburn. $\lambda \sim 3.36\,\mu m$ room temperature InGaAs/AlAs(Sb) quantum cascade lasers with third order distributed feedback grating. *Appl. Phys. Lett.*, 97:111113, 2010.

[15] W.H. Bragg and W.L. Bragg. The reflection of x-rays by crystals. *Proc R. Soc. Lond.*, 88:428–438, 1913.

[16] T. J. Slight, G. Tandoi, D. G. Revin, A. McKee, S. Y. Zhang, W. Meredith, J. W. Cockburn, and C. N. Ironside. $\lambda \sim 3.35\,\mu m$ distributed-feedback quantum-cascade lasers with high-aspect-ratio lateral grating. *IEEE Phot. Tech. Lett.*, 23:7, 2011.

[17] O. Cathabard, R. Teissier, J. Devenson, and A. N. Baranov. InAs-based distributed feedback quantum cascade lasers. *Electronics Letters*, 45:1028 – 1030, 2009.

[18] L.P. Ghislain, V.B. Elings andK.B. Crozier andS.R. Manalis, S.C. Minne, K. Wilder, G.S. Kino, and C.F. Quate. Near-field photolithography with a solid immersion lens. *Applied Physics Letters*, 74(4):501–503, 1999.

[19] H. Kogelnik and C. Shank. Coupled-wave theory of distributed feedback lasers. *J. Appl. Phys.*, 43:2327, 1972.

[20] J. Faist, F. Capasso, C. Sirtori, D. L. Sivco, J. N. Baillargeon, A. L. Hutchinson, Sung-Nee G. Chu, and A. Y. Cho. High power mid-infrared ($\lambda \sim 5$ μm) quantum cascade lasers operating above room temperature. *Appl. Phys. Lett.*, 68:3680, 1996.

[21] C. Sirtori, J. Faist, F. Capasso, D. L. Sivco, A. L. Hutchinson, S. G. Chu, and A. Y. Cho. Continuous wave operation of mid-infrared (7.4 - 8.6 μm) quantum cascade lasers up to 110 K temperature. *Appl. Phys. Lett.*, 68:1745, 1996.

[22] M. Kamp, J. Hofmann, A. Forchel, F. Schafer, and J.P. Reithmaier. Low-threshold high-quantum-efficiency laterally gain-coupled $InGaAs/AlGaAs$ distributed feedback lasers. *Applied Physics Letters*, 74(4):483–485, 1999.

[23] J.D. Ingle and S.R Crouch. Health and environmental effects profile for formaldehyde. *EPA/600/x-85/362. Environmental Criteria and Assessment Office, Office of Health and Environmental Assessment, Office of Research and Development*, 1998.

[24] J.E. Amoore and E. Hautala. dor as an aid to chemical safety: Odor thresholds

compared with threshold limit values and volatilities for 214 industrial chemicals in air and water dilution. *Journal of Applied Toxicology*, 3:272–290, 1983.

[25] National Institute for Occupational Safety and Health (NIOSH). Pocket guide to chemical hazards. *U.S. Department of Health and Human Services, Public Health Service, Centers for Disease Control and Prevention*, 1997.

[26] SensorSense B.V. Gas analyzers. URL `http://www.sensor-sense.nl/products/gas-analyzers`.

[27] Photon Design Ltd. FIMMWAVE. URL `http://www.photond.com/products/fimmwave.htm`.

[28] J. P. Commin, D. G. Revin, S. Y. Zhang, A. B. Krysa, K. Kennedy, and J. W. Cockburn. High peak power $\lambda \sim 3.3$ and $3.5\,\mu m$ InGaAs/AlAs(Sb) quantum cascade lasers operating up to 400 K. *Appl. Phys. Lett.*, 97:031108, 2010.

[29] L.R. Harriott. Limits of lithography. *Proceedings of the IEEE*, 89(3, SI):366–374, 2001.

[30] D.M. Manos and D.L. Flamm. *Plasma Etching: An Introduction*. Elsevier, 1989.

[31] S. Y. Zhang, D. G. Revin, J. W. Cockburn, K. Kennedy, A. B. Krysa, and M. Hopkinson. $\lambda \sim 3.1\,\mu m$ room temperature $InGaAs/AlAsSb/InP$ quantum cascade lasers. *Appl. Phys. Lett.*, 94:031106, 2009.

[32] R.A. Linke. Transient chirping in single-frequency lasers: lightwave systems consequences. *Electronics Letters*, 20(11):472–474, 1984.

[33] R. P. Green, L. R. Wilson, E. A. Zibik, D. G. Revin, J. W. Cockburn, C. Pflugl, W. Shrenk, G. Strasser, A. B. Krysa, J. S. Roberts, C. M. Tey, and A. G. Cullis. High-performance distributed feedback quantum cascade lasers grown by metalorganic vapor phase epitaxy. *Appl. Phys. Lett.*, 85:5529, 2004.

[34] C.M.F. Kneepkens, G. Lepage, and C.C. Roy. The potential of the hydrocarbon

breath test as a measure of lipid-peroxidation. *Free Radical Biology and Medicine*, 17 (6):609, 1994.

[35] Q.K. Yang, C. Manz, W. Bronner, K. Kohler, and J. Wagner. Room-temperature intersubband emission from $GaInAs - AlAsSb$ quantum cascade structure. *Electronics Letters*, 40(21):1339–1340, OCT 14 2004.

[36] Compugraphics Inc. Compugraphics incorporated. URL `http://www.compugraphics-photomasks.com/`.

Chapter 6

External Cavity Wavelength Modulation Based on Fabry-Pérot Reflector

6.1 Introduction

Most of the ultra-sensitive gas detection systems that are used in the mid-infrared wavelength region still heavily rely on tunable and, most importantly, single mode quantum cascade laser devices. There are a number of ways achieving single mode emission in these semiconductor lasers, with the main two being the distributed feedback grating approach described in Chapter 5, where single mode emission is achieved with the unilateral diffraction grating, and the external cavity (EC) setups, one of which is described in this chapter. The former method locks the laser emission wavelength to the particular frequency during the manufacturing process, preventing wide frequency tunability once devices are fabricated [1]. Fine wavelength adjustments are achieved through temperature tuning, since the temperature affects the effective refractive index of the particular mode inside the laser cavity, shifting the frequency as the index changes. This limits the scanning range to

$\sim 10\ cm^{-1}$ for temperature tuning and only $\sim 1\ cm^{-1}$ for current tuning, where only the laser core is heated. These numbers lie way below the maximum tuning range that can potentially be achieved by QC lasers characterized by the gain width of over 400 cm^{-1} [2, 3]. Distributed feedback lasers provide wavelength stability and easier mechanical arrangement, especially important in field setups, at the cost of lengthy and costly production process required for targeting a specific wavelength that cannot be altered once the laser is manufactured.

The external cavity setup is more versatile for frequency tuning and is a post-fabrication technique, meaning it can provide single mode emission from the devices that were not designed to have single mode emission in the first place. The most commonly used technique to filter unwanted frequencies and provide selective feedback to the cavity employs diffraction gratings [4–8]. The most common configurations are Littrow and Littman-Metcalf [9] configurations that are shown in Figure 6.1. In the Littrow setup the tuning is achieved through the rotation of the diffraction grating, while the Littman-Metcalf configuration utilizes a rotating mirror and the wavelength selectivity is typically stronger since the beam is interacting with the grating twice. The Littrow configuration, on the other hand, maximizes back-coupling into the cavity and is more commonly used in spectroscopic setups.

A number of drawbacks limit the minimum size of such system, since the longitudinal modes of the short external cavity become more widely spaced apart reducing wavelength selectivity. Larger systems allow better wavelength selectivity, however this introduces bulkiness, thus reducing its practical use in mobile applications. External cavity setups can suffer from wide emission linewidth reducing the sensitivity and detection accuracy in spectroscopic applications. Rotating grating setups also limit wavelength tuning speeds due to the need for mechanical grating movement, through friction and equipment inertia.

In this chapter a novel approach for selective wavelength production in external cavity

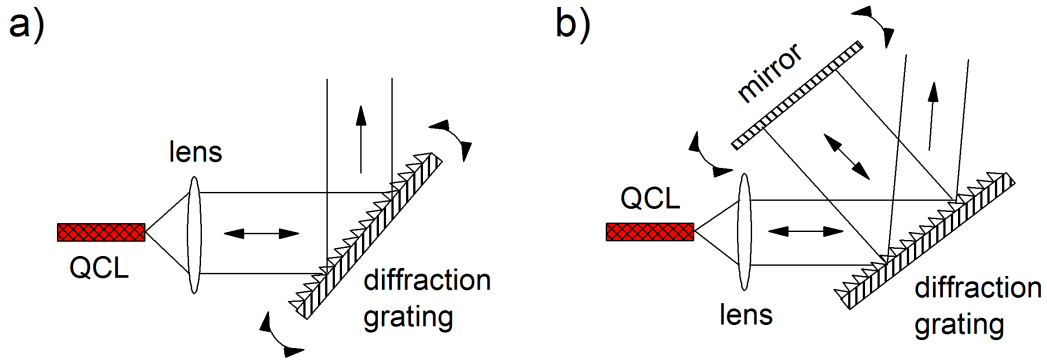

Figure 6.1: a) In Littrow external cavity configuration the 1^{st} order reflection is fed back to the laser while the 0^{th} order is out-coupled. The wavelength tuning is achieved by the rotation of the diffraction grating b) In Littman-Metcalf configuration the first order is directed to the mirror and the wavelength tuning is achieved by the rotation of this mirror.

setups is described. The wavelength selection is achieved through the feedback from the Fabry-Pérot (FP) reflector shown in Figure 6.2, without the need for a diffraction grating. The chapter describes the parameters required to produce the FP reflector with the selective feedback for single mode production. The experimental setup for broad spectra generation through the rapid wavelength scan is also described.

6.2 Fabry-Pérot reflector

The proposed Fabry-Pérot reflector, shown in Figure 6.2, consists of two parallel optical flats closely placed next to each other creating an air-filled FP resonator. Both mirrors are fitted onto mirror holders to provide additional degrees of freedom for the coarse adjustments. The back (primary) mirror is a standard silver coated mirror with $95-97\%$ reflectance at $2-20$ μm wavelength region. The front semi-transparent FP mirror is made of CaF_2 plate. A semi-transparent coating is applied to provide partial reflectance. The secondary semi-transparent mirror is fitted onto the piezoelectric actuators stack for the fine adjustment of the gap (Δd) between the mirrors providing tunable width of the reflector cavity.

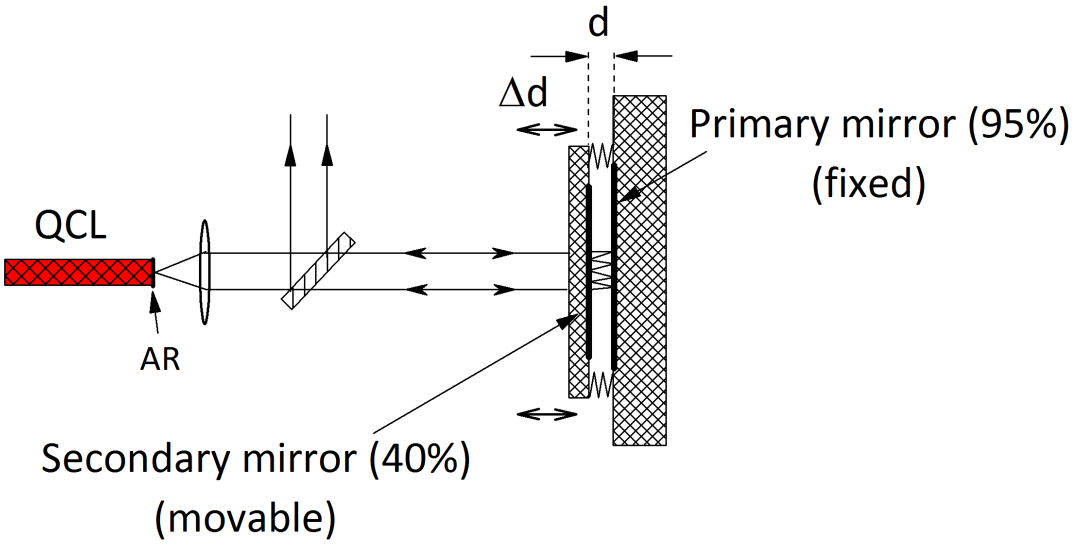

Figure 6.2: Schematic diagram of the Fabry-Pérot reflector. The collimated light from the anti-reflection (AR) coated light source (QCL) bounces back and forth between two closely spaced mirrors to create an interference pattern. This pattern can be used to provide selective feedback to the system. The distance between mirrors is adjustable with piezo-electrical actuators.

The laser beam passing through the first mirror undergoes multiple reflections inside the reflector to produce an interference pattern. The complete interference pattern, created by the FP resonator, is used to provide selective wavelength feedback to the external cavity system.

6.2.1 Theoretical analysis of the Fabry-Pérot reflector

A Fabry-Pérot resonator exhibits certain properties that will be described in this section. These properties can be adjusted to suit a specific design of the system. The analytical approach to the FP reflector is based on the light transmission through the FP etalon. The general equation for wave transmission through two semi-transparent mirrors [10] is given by Equation 6.1.

$$T = \frac{1}{1 + Fsin^2(\theta)} \tag{6.1}$$

The light transmission is dependent on two variables - the contrast factor F and the phase change θ. The contrast factor is linked to the reflectance of two mirrors and is described by Equation 6.2 for two mirrors with equal reflectance R.

$$F = \frac{4R}{(1-R)^2} \tag{6.2}$$

For a standing wave to exist between two mirrors the following phase change condition must hold [11],

$$e^{-2i\theta} = 1 \tag{6.3}$$

where the phase change θ is defined as,

$$\theta = \frac{2\pi nd}{\lambda} cos(\varphi) \tag{6.4}$$

and n is the refractive index, d is the separation between two mirrors, λ is the free space wavelength and φ is the angle of incidence. Assuming the angle of incidence is 0^o, Equation 6.3 holds when

$$2\left(\frac{2\pi nd}{\lambda}\right) = 2\pi m \tag{6.5}$$

where m is the interference order inside the Fabry-Pérot etalon. Equation 6.5 can be rewritten in terms of frequency (f_m)

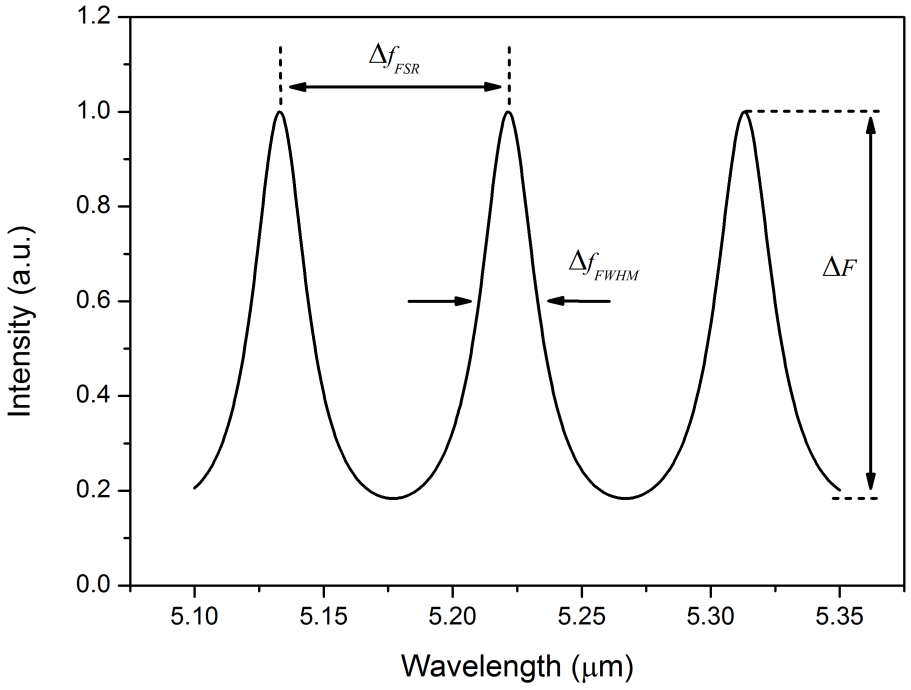

Figure 6.3: Transmission of a Fabry-Pérot etalon indicating Free Spectral Range (FSR), Minimum Resolvable Bandwidth (FWHM) and Contrast Factor as a function of different resonance modes.

$$m = \frac{2nd}{c} f_m \tag{6.6}$$

The typical interference pattern obtained from solving Equation 6.1 inside the etalon is shown in Figure 6.3. The transmission pattern is dependent on the material and the physical dimensions of the etalon. The material influences the interference pattern, through different refractive index in different materials. The distance between two successive peaks is smaller in the etalon made out of CaF_2 compared to the similar etalon filled with an air gap. The main properties characterizing any given etalon, namely *Free Spectral Range*, *Minimum Resolvable Bandwidth*, *Finesse* and *Contrast Factor* are described in more detail in the sections below.

6.2.2 Free spectral range

The free spectral range (FSR) describes the separation between two successive resonant modes inside the Fabry-Pérot cavity.

Considering two successive resonant modes m and $m+1$ inside the resonator, we get:

$$m = \frac{2nd}{c} f_m \tag{6.7}$$

and

$$m + 1 = \frac{2nd}{c} f_{m+1} \tag{6.8}$$

The free spectral range is defined as $\Delta F_{FSR} = f_m - f_{m=1}$, therefore subtracting one from another leads to

$$1 = \frac{2nd}{c}(f_{m+1} - f_m) = \frac{2nd}{c}\Delta f_{FSR} \tag{6.9}$$

thus the free spectral range can be defined as

$$\Delta f_{FSR} = \frac{c}{2nd} \tag{6.10}$$

The FSR and the wavelength are related through the relationship below

$$\frac{\Delta f_{FSR}}{f} = \frac{\Delta \lambda_{FSR}}{\lambda} \tag{6.11}$$

leading to the following expression for FSR in terms of wavelength:

$$\Delta\lambda_{FSR} = \frac{\lambda^2}{2nd} \tag{6.12}$$

It can be seen from Equation 6.10 that the FSR is inversely proportional to the mirror separation. This equation becomes very useful to estimate the mirror separation required in order to produce free spectral range larger or equal to the gain bandwidth of the QCL.

6.2.3 Minimum resolvable bandwidth

The minimum resolvable bandwidth, also known as *fringe width* or the *resolution bandwidth*, is the full width at half maximum (Δf_{FWHM}) of the resonant peak inside the Fabry-Pérot etalon. Narrow Δf_{FWHM} ensures spectrally narrow feedback, eliminating wide peak generation. Peaks with narrow FWHM are also very desirable in spectroscopy, where the emission peak must have narrower linewidth than the absorption features of the targeted analyte. The bandwidth is inversely proportional to the reflectance of the mirrors.

6.2.4 Finesse

The finesse is another important property of Fabry-Pérot interferometer. This property, conceptually, describes the number of interacting beams between two mirrors. The higher the number, the sharper the produced interference pattern. The finesse is defined as a ratio of the free spectral range to the minimum resolvable bandwidth, *i.e.*

$$F_r = \frac{\Delta f_{FSR}}{\Delta f_{FWHM}} \tag{6.13}$$

The finesse is also affected by the reflectance of the mirrors of the system. Higher reflectivity will trap more light between mirrors producing a more complete interference pattern,

hence higher mirror reflectivity leading to higher finesse. This relationship is defined in Reference [12] as

$$F_r = \frac{\pi\sqrt{R}}{1-R} \tag{6.14}$$

The finesse is also affected by mirror surface quality, temperature variations and optical losses associated with the etalon material. Figure 6.4 demonstrates two transmission patterns calculated for different mirror reflectivities. Higher mirror reflectivity produces sharper, better defined linewidth. Different FSR values for two mirrors were chosen to demonstrate the effect of wavelength selection as a function of mirror separation d.

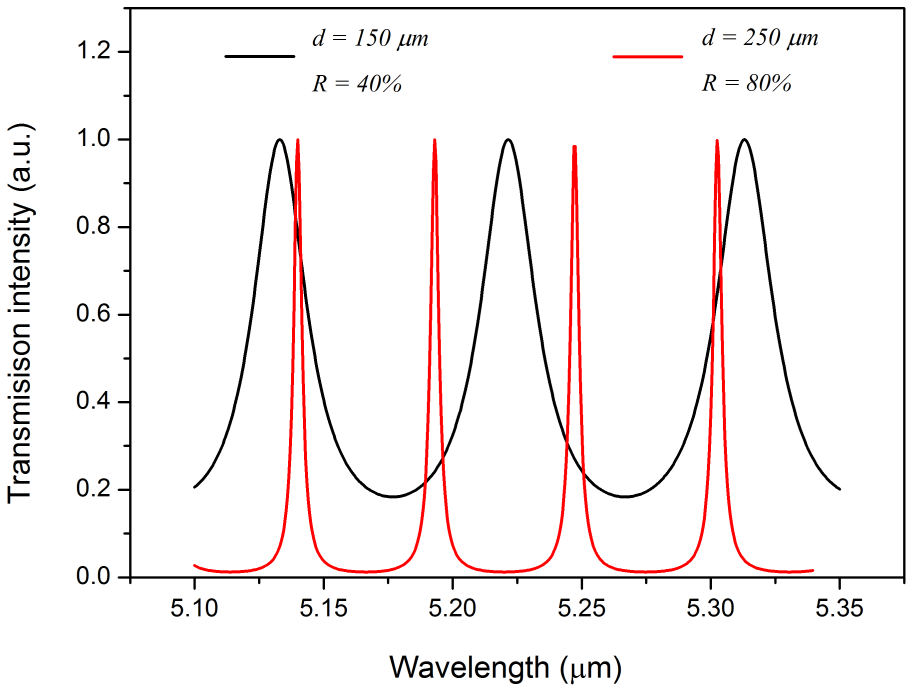

Figure 6.4: Transmission intensity and sharpness variation as a function of different finesse values ($F_r = 3.1$ (black) and $F_r = 14.0$ (red)).

6.2.5 Contrast factor

Just like the free spectral range that defines the maximum frequency difference between two successive peaks, the contrast factor describes the amplitude between the maximum and minimum transmission values. Mathematically this can be described as

$$F = \frac{T_{max}}{T_{min}} \tag{6.15}$$

where T is the transmitted intensity through the etalon. Just like the finesse, the contrast factor is proportional to the reflectance of the Fabry-Pérot mirrors and is described in Equation 6.16 below.

$$F = \frac{(1+R)^2}{(1-R)^2} \approx \frac{4R}{(1-R)^2} \tag{6.16}$$

Equation 6.10 indicates that the contrast factor and the finesse are closely related. As a result it is possible to define one through the other. The relation between these two properties is shown in Equation 6.17.

$$F = 1 + \left(\frac{2F_r}{\pi}\right)^2 \tag{6.17}$$

This also demonstrates that the finesse F_r, is quadratically proportional to the contrast factor, F ($F \propto F_r^2$).

6.3 FP reflector with plain secondary mirror

The experimental setup, shown in Figure 6.2, has been built in order to investigate the intensity and selectivity of the feedback received from the Fabry-Pérot reflector. Two quantum cascade lasers were used for the measurements. The first laser, based on a $InGaAs/InAlAs$ strain compensated heterostructure grown by $MOVPE$ in Sheffield, was indium soldered on a copper submount for better heat dissipation. The laser operates at room temperature at $\lambda \sim 5.30 - 5.40\ \mu m$ and was driven in pulsed mode with duty cycles up to 50%. The laser has a high reflectivity coating (SiO_2/Au) on the back facet and an anti-reflective coating (*"Helia Photonics"*) on its front facet. The second QCL was introduced after the performance deterioration of the first laser, that occurred due to a damaged front facet. The second QCL was obtained from *"Alpes Lasers"* with a similar emission wavelength of $\sim 5.2\ \mu m$. Both facets were covered with anti-reflective coatings. The laser operates in both pulsed and CW regime. The laser beam is collimated using a high (0.56) numerical aperture AR coated molded chalcogenide glass aspheric lens with focal length of 4 mm. The beam is directed onto the Fabry-Pérot reflector at right angles as described in Section 6.2. The light is out-coupled using a CaF_2 plate AR coated on one side and placed between the light source and FP reflector.

The secondary mirror plays an important role in the Fabry-Pérot reflector design. Its reflectivity directly affects finesse, as described in Section 6.2.4. The physical dimensions, such as mirror mass and its diameter ($\varnothing$), have to be taken into account as well, since it has to be capable of rapid response to the mechanical modulation. Inertia of large object reduces the scanning amplitude at higher frequencies, reducing the effective responsiveness of such system. Additionally, the air trapped between two plates at small distances causes resistance to motion, damping high frequency modulation.

The choice of a secondary mirror material is another important factor that has to be taken into account in a FP reflector design. In order to minimize absorption losses by the secondary mirror, it has to be made out of the transparent material for the mid-infrared

wavelengths. The alignment of the FP reflector system is also simplified if the transparency of the chosen material extends to the visible spectral range.

6.3.1 Secondary mirror characteristics

Two flat mirrors of thickness 0.5 mm and 2 mm have been considered for the experiment. The mirrors are made out of CaF_2 with a diameter of 25.4 mm. Both mirror plates were coated with thin film of germanium to create partial reflectivity of $\sim$ 40 %. The other side of the plate was AR coated to prevent internal interference between the two mirror facets. Both, AR and partially transparent coatings were prepared by *"Helia Photonics"*. Figure 6.5 shows reflection as a function of wavelength for the anti-reflective and partially reflective coatings. The wide frequency range is chosen to accommodate a potentially wide wavelength tuning range.

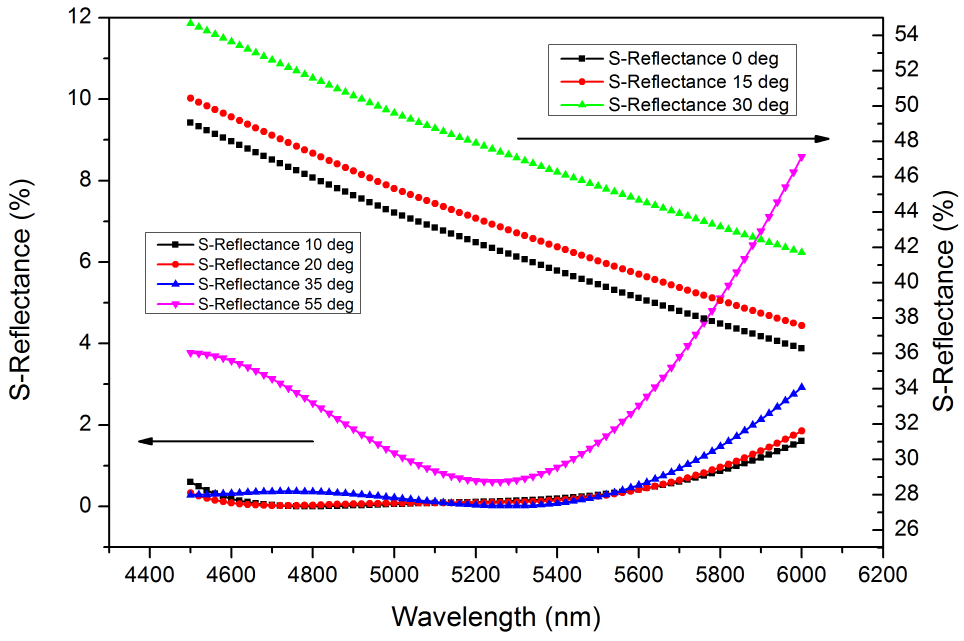

Figure 6.5: The calculated reflectivity of anti-reflective and partially reflective coatings (by *"Helia Photonics"*) as a function of wavelength.

6.3.2 FP reflector alignment

The parallelism between the primary and secondary mirrors is very important in order to form a strong interference pattern. The two mirrors have to be separated by a distance no larger than 100 μm in order to create free spectral range of $\sim 50\ cm^{-1}$ for $\lambda = 5.2\ \mu m$ wavelength. Since the germanium coating is not transparent at visible frequencies, optical alignment utilizing visible light could not be performed. Two alternative techniques were utilized to achieve the desired parallelism.

The first technique relied on putting two mirrors close together and then performing fine adjustment under the optical microscope until two mirrors were parallel. This method has a large error margin due to its subjectivity. The second technique is based on the spatial position of a reflected red laser spot before and after the secondary mirror is introduced. A red laser beam is reflected from the primary mirror onto a distant marked location. Then, the secondary mirror is put in the position closely spaced from the primary mirror. It is then adjusted according to the red laser reflection in order to place the red spot into the same marked location. Due to relatively large distances between the reflector and the marked location, compared to the distance between the mirrors (d), the laser reflection lands on the same spot only when the two mirrors are parallel to each other.

The quality of the parallelism and the distance between the two mirrors is then assessed by reflecting a broadband infrared (IR) light source from the aligned reflector into the FTIR spectrometer and measuring the distance between two successive interference peaks (FSR) in the observed spectra. This distance corresponds to the free spectral range of the etalon described in Section 6.2.2 and is a more important indicator of a correctly displaced mirror than the actual numerical value of the mirror separation. The free spectral range of such a reflector has to be greater than half of the gain width of the laser in order to produce single mode generation. For the single mode emission across the whole gain spectrum, the free spectral range should be greater or equal to the whole gain width of the laser. Large mirror separation harbors multiple modes, separated by the free spectral

range, compromising the required single mode production.

6.3.3 Results

The aligned Fabry-Pérot reflector was tested for the quality of alignment, with the contrast factor being the main indicator of good parallelism between the two mirrors. Typical contrast factor of the system usually did not exceed 20 % and is comparable to the contrast factor of the light transmission observed through the uncoated CaF_2 plate. As mentioned previously, large separation produces a free spectral range much smaller than the width of the gain of the QC laser. The spectrum, obtained with the mirror separation of $\sim 550\ \mu m$ is shown in Figure 6.6a where multiple peaks inside the QCL gain are amplified .

Reduction of the mirror separation d increases the free spectral range of the reflector, providing feedback to a single wavelength inside the gain spectrum of the laser. Fine wavelength selection is performed by applying voltage to the piezoelectric actuators. Applied voltage contracts these actuators, reducing the gap between two mirrors, thus shifting the wavelength. As shown in Figure 6.6b, the multiple emission modes, separated by the free spectral range of the aligned FP reflector, are tuned. Since the FSR is smaller than the gain width of the laser, multiple longitudinal cavity modes are excited. Multi-mode emission is observed across the whole gain spectrum width of $\sim 40\ cm^{-1}$. It can be noticed that emission at the center of the gain is stronger than the emission at the edges.

Further reduction of mirror separation increases the free spectral range, producing fewer interference peaks, allowing only single mode emission when the neighboring peaks lie outside or near the edge of the gain bandwidth. Emission spectra with the mirror separation of 130 μm producing a free spectral range of 38 cm^{-1} is shown in Figure 6.7a. The wavelength selection, achieved through the fine voltage change across the piezoelectric actuators, is possible throughout the whole free spectral range, producing two peaks when two amplified modes fall inside the gain spectrum. The dashed line outlines the wide emission spectrum measured with the flat mirror placed instead of the Fabry-Pérot

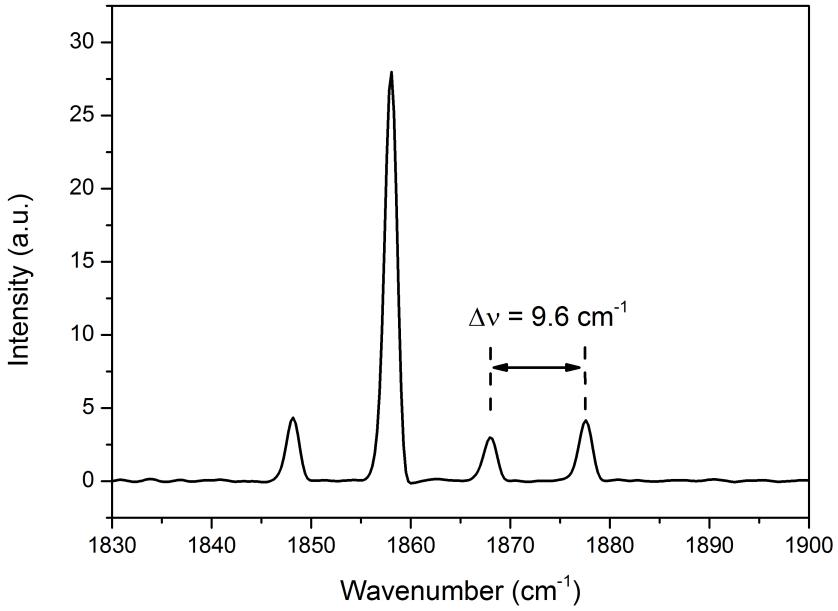

(a) Multi-peak generation as a result of large mirror separation, producing small FSR.

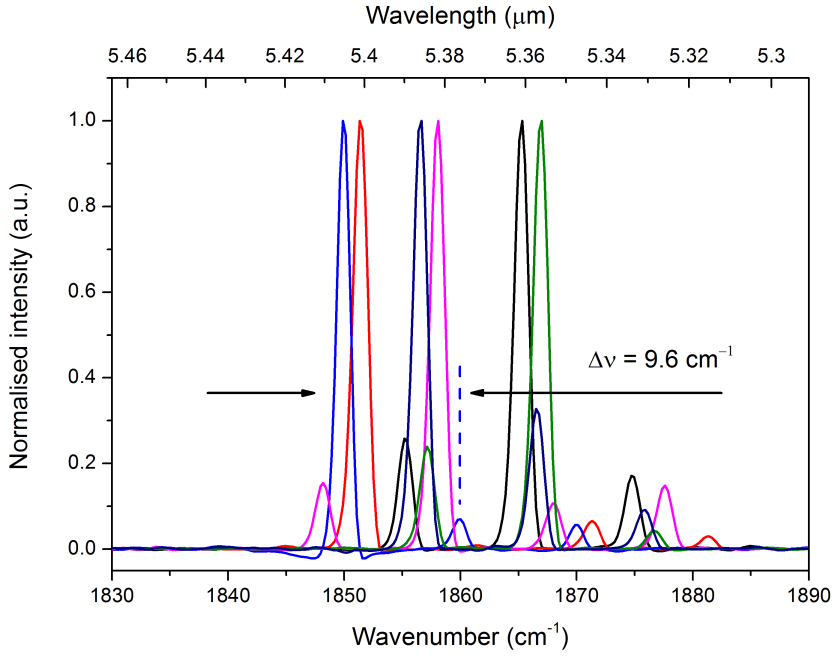

(b) Two peak emission and wavelength shifting as a result of large mirror separation. Different colors represent emission collection at different piezoelectric actuators distance.

Figure 6.6: Large separation between mirrors generate free spectral range smaller than the gain width of the device, producing multi-peak emission (a). The wavelength can still be tuned (b) creating competition between two or more peaks.

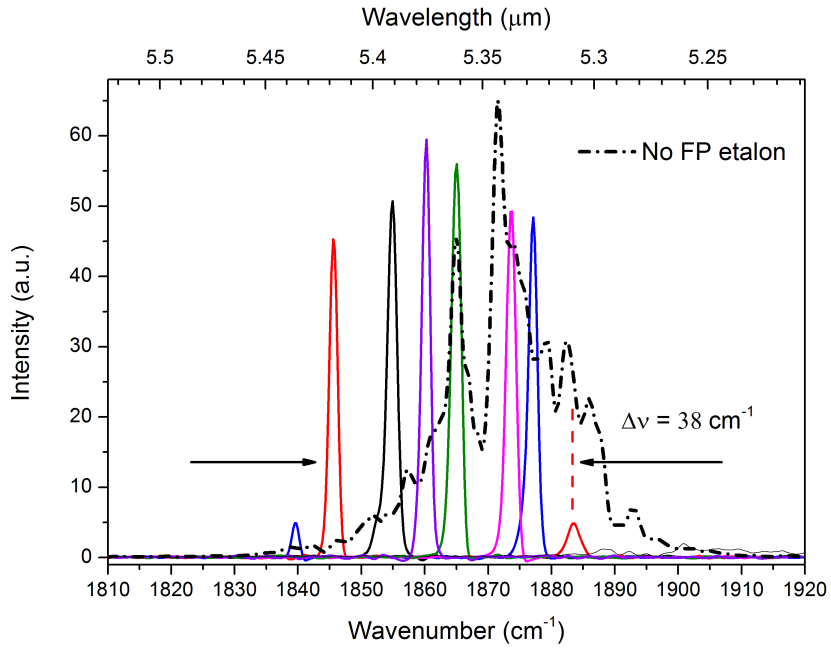

(a) Single mode production across the most of the gain width. Two peaks are visible when two interference peaks fall onto the edge of the gain width. Dashed line shows spectra without FP reflector.

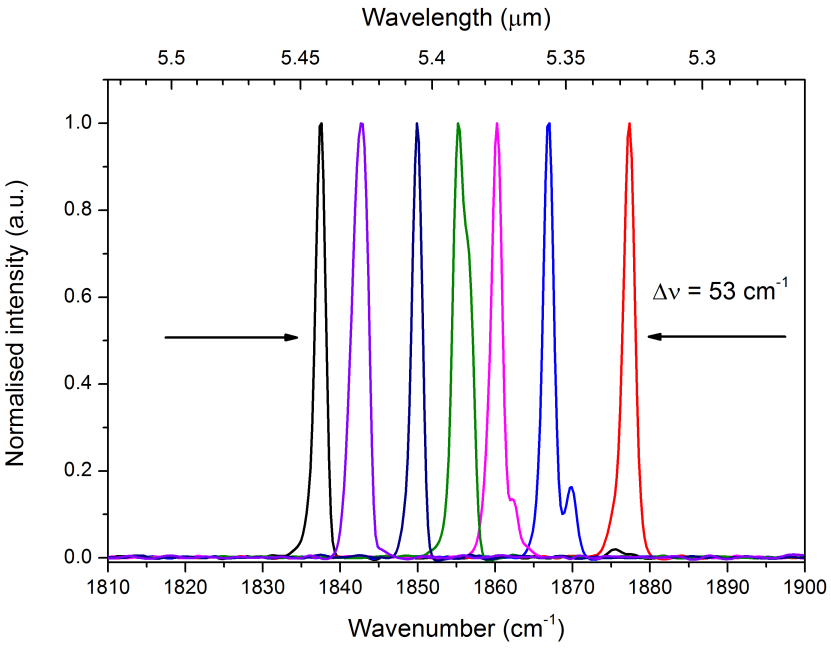

(b) Single mode emission is achieved across the whole gain width. The FWHM and sharpness of these peaks are compromised due to imperfect alignment techniques, producing not parallel mirrors.

Figure 6.7: Decreased mirror separation yields wider wavelength coverage throughout the whole gain width.

reflector, eliminating any particular mode selection.

A mirror separation of 95 μm produces a free spectral range of 53 cm^{-1}, enabling full single mode tunability throughout the whole gain spectrum, as shown in Figure 6.7b. Closer inspection reveals that the integrity of the single peak is slightly compromised. The emission peaks have large FWHM and < 10 dB side mode suppression ratio. This occurs due to the increased mirror alignment sensitivity at short separation distances. Small displacement, at short separation distances, causes large relative perturbation in the parallelism of the two mirrors, having much bigger effect on the quality of the produced fringes, that the same displacement at larger mirror separation. The previously described alignment methods are not reliable at small mirror separation distances and require additional random mirror adjustments in order to generate single mode emission. Additionally, it was noticed that produced emission wavelengths take discrete values separated by the ~ 6.9 cm^{-1}, with no emission between them. The generated single mode emission remains stationary for a small mirror separation change (Δd) before jumping to the next fixed value. This behavior is captured in Figure 6.8, where wavelength intensity fixed at certain frequency decreases before making a transition to the neighboring frequency.

A quick free spectral range conversion into the separation distance revealed that this discrete mode generation is caused by the Fabry-Pérot interference between some two parallel CaF_2 plates spaced exactly 0.5 mm apart. This suggests that either of the two CaF_2 plates used in our system, one to outcouple the light beam to the spectrometer and one acting as a secondary mirror, causes these additional interference patterns, affecting the integrity of continuous wavelength tuning.

Both CaF_2 plates were anti-reflection coated to prevent this sort of behavior. However, there are a few possible reasons explaining the observed phenomenon. Firstly, the anti-reflection coating, as seen in Figure 6.5, is wavelength and angle dependent. The reflectivity increases as the wavelength drifts away from its center value (5200 cm^{-1}) or the designed angle ($10° - 35°$). In the setup, the secondary mirror is perpendicular to the

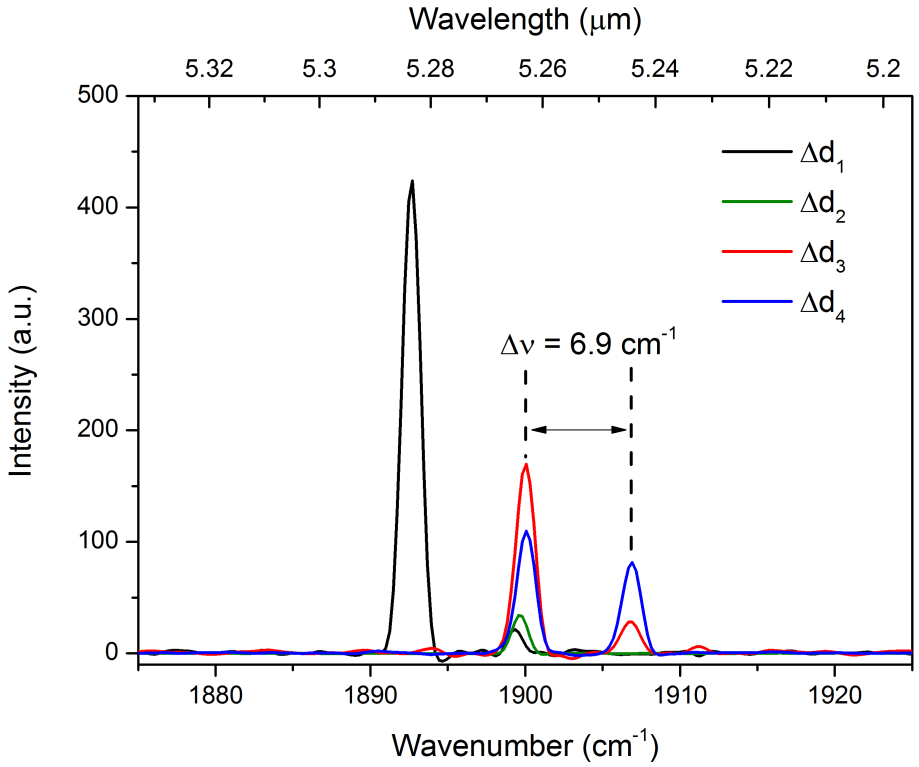

Figure 6.8: Emission spectra are fixed to discrete values. Changing mirror separation forces wavelength shift, however modes can only take certain frequencies, reducing its intensity before making the transition to the neighboring frequency separated by 6.9 cm^{-1}.

beam, making the coating less efficient, possibly creating additional interference patterns. Further investigation shows that the light is still reflected from the AR coated facet, trapping the light inside the optical plate, as shown in Figure 6.9, where 2 mm thick Ge/AR coated CaF_2 plate is tested. The 2 mm thick CaF_2 plate has the same AR coating as 0.5 mm thick plate, and therefore can be used to demonstrate the effectiveness of the AR coating. The periodic oscillations inside the optical plate occur at the angles equal to 90°, while the light transmission at 15° and 45° produce no interference patterns. The free spectral range of these periodic oscillations is $\sim 1.7\ cm^{-1}$ corresponding to the 2 mm thick CaF_2 plate. The optical plate, used to deflect part of the signal towards the spectrometer, does not suffer from this problem since it is placed at an angle ($\sim 45°$), as shown in Figure 6.2, thus producing no interference fringes.

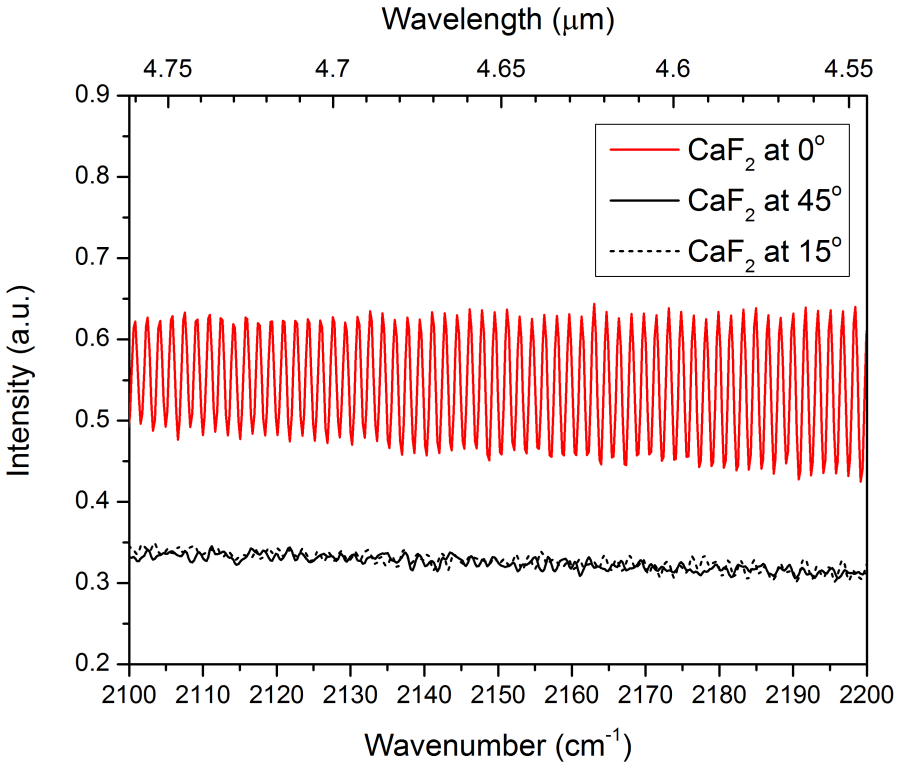

Figure 6.9: Interference pattern is still created in the anti-reflection coated 2 mm thick CaF_2 plate at the perpendicular light incidence angle (0°). The oscillations are suppressed at sharp angles (15° and 45°).

6.3.4 Triangular external cavity setup

In order to suppress interference fringes inside the secondary mirror with the existing anti-reflective coating, the external cavity setup where the incident beam falls under an angle has been built. The schematic diagram of the setup is shown in Figure 6.10.

The experimental setup consists of a quantum cascade laser with $InGaAs/AlInAs$ heterostructure, obtained from *"Alpes lasers"*. Both facets have anti-reflection coatings. The gain bandwidth of this laser is measured to be $\sim 120\ cm^{-1}$. The plate of the secondary mirror and the outcoupling plate were swapped for the 2 mm thick plate.

The collimated beam from the quantum cascade laser is reflected from the Fabry-Pérot reflector at an angle and directed to the external mirror creating a triangular external

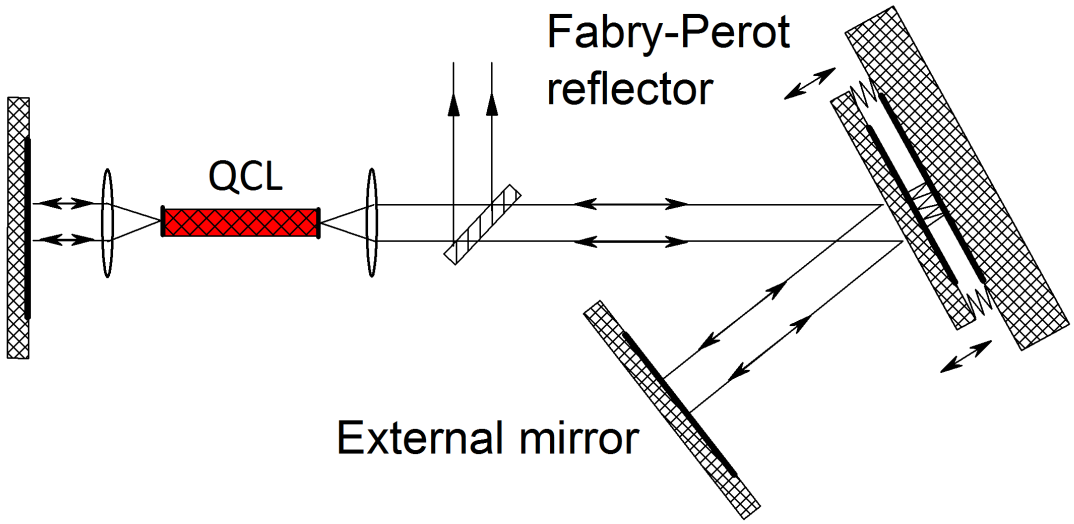

Figure 6.10: Schematic diagram of the angled external cavity setup. The collimated light is directed to the Fabry-Pérot reflector at an angle in order to avoid interference generation inside the secondary mirror. The beam is then reflected onto an external mirror ($95-97\%$ reflectance) and sent back to the external cavity. Both QCL facets have anti-reflection coating. The back facet receives feedback from another external mirror.

cavity. Efficient interference between the two mirrors inside the FP reflector occurs only if the diameter of the beam is much larger than the separation distance between two mirrors. The beam is measured to be $\sim 5\ mm$ in diameter and is much larger than the mirror separation ($< 100\ \mu m$), allowing large incident angles to be used. The reflection angle is measured to be around 15° and is sufficient to suppress the interference inside the secondary mirror, as shown in Figure 6.9.

The separation between two mirrors is set at around $70\ \mu m$ in order to produce a free spectral range of $\sim 70\ cm^{-1}$. The FSR of $\sim 70\ cm^{-1}$ is sufficient to produce one single mode across the whole gain spectrum. A manual voltage scan with a step size of $0.25\ V$ was applied to the piezoelectric actuators in the range of $0-17\ V$. The two piezo electric actuators consist of multiple piezoelectric chips stacked face-to-face and bonded using epoxy and glass beads. Each actuator is made out of four smaller actuators with free stroke displacement of $\sim 2.8\ \mu m$. The stack of four actuators contracts by $\sim 11.2\ \mu m$ at

an applied voltage of 75 V. The displacement Δd, required to move the interference peak across its whole free spectral range for $\lambda = 5.2\ \mu m$ wavelength can be calculated using Equation 6.7 and 6.8. Rearranging for d, we get:

$$d_{in} = \frac{mc}{2nf_m} \tag{6.18}$$

and

$$d_{fin} = \frac{(m+1)c}{2nf_{m+1}} \tag{6.19}$$

where d_{in} and d_{fin} are the initial and final mirror separation values. The difference required to move the peak across the whole spectral region is $\Delta d_{FSR} = d_{fin} - d_{in}$. Therefore we get:

$$\Delta d_{FSR} = \frac{(m+1)c}{2nf_{m+1}} - \frac{mc}{2nf_m} \tag{6.20}$$

after the complete sweep, f_m and f_{m+1} become equal ($f_m = f_{m+1}$) thus:

$$\Delta d_{FSR} = \frac{c}{2nf_m} \tag{6.21}$$

Equation 6.21 can be used to determine the required separation difference in order to move the constructive peak through the whole free spectral range. It can be noticed that the separation is frequency dependent and as a result, Δd_{FSR} for $\lambda \sim 5.2\ \mu m$ is equal to $\sim 2.6\ \mu m$.

Therefore, the voltage V_{FSR}, applied to the piezoelectric actuators, required to produce this displacement is found by:

$$V_{FSR} = \frac{\Delta d_{FSR} V_{tot}}{d_{tot}} \tag{6.22}$$

where V_{tot} is the maximum voltage producing full free stroke displacement d_{tot} of the piezo stacks. As a result, $\Delta V = 17V$ is required in order to displace piezoelectric actuators by $\sim 2.6\ \mu m$, yielding the wavelength change corresponding to the free spectral range for $\lambda = 5.2\ \mu m$.

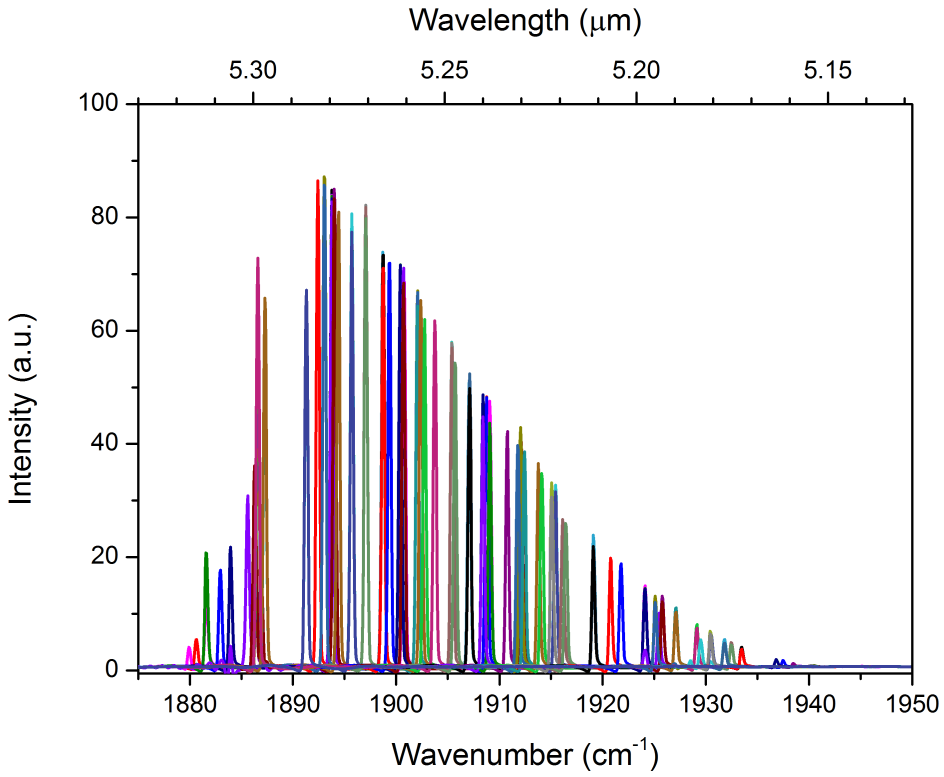

Figure 6.11: Semi-continuous wavelength tuning across the whole gain width. The wavelength tuning still suffers from periodic jumps preventing complete coverage of all frequencies. The wider gaps correspond to the water absorption lines in the atmosphere.

The obtained emission, shown in Figure 6.11, is much more controlled with the sharp single mode emission across the whole free spectral range provided by the FP reflector. Closer inspection shows that the tuning is still not continuous, occupying discrete wavelength values separated by $\sim 1.7\ cm^{-1}$. Wider gaps between some emission lines correspond to water absorption lines in the atmosphere, preventing laser operation at those wavelengths.

It also can be observed, that the laser emits at the same frequencies for multiple mirror separations. This is potentially caused by the imperfect alignment of the system or by the fact that the interference, caused by the additional Fabry-Pérot etalon, such as 2 mm thick CaF_2 plate, is still embedded into the system.

Despite this semi-continuous wavelength selection, it is still possible to control the emission frequency with the accuracy of $\sim$ 1.7 cm^{-1}, covering $\sim$ 60 cm^{-1} spectral range. The discrete wavelength emission can be utilized in some spectroscopic applications, where molecules with wide absorption bands are being detected, such as freon [13].

6.4 FP reflector with wedged secondary mirror

As described in the previous section, the semi-continuous wavelength selection is compromised by the discrete wavelength jumps preventing complete spectral coverage throughout the whole region covered by the laser gain. The observed free spectral range of $\sim 1.7\ cm^{-1}$ corresponds to the interference pattern produced by the parallel plates spaced $\sim 3\ mm$ apart in air or $\sim 2\ mm$ apart in CaF_2 material. The system contains two $2mm$ thick CaF_2 plates - one acting as a beam out-coupler and the other one acting as a secondary mirror. Even though it was demonstrated in Figure 6.9 that these internal oscillations should be suppressed by making the angle of incidence not equal to zero, there is a possibility that some of the effect still remains. In order to improve the selectivity of the FP reflector design, both parallel plates were exchanged with wedged plates.

The wedged CaF_2 plate was chosen to suppress internal Fabry-Pérot modes arising due to high parallelism between two flats of a standard plate. The wedged plate has $\varnothing = 25.4\ mm$ diameter and is 1.5 mm thick with $20 - 40$ arc minutes wedge angle. Figure 6.12 shows a comparison of the transmitted signal through different optical flats, where a broadband light source is transmitted through two different plates to observe internal oscillations. The background signal, bypassing the plates, is used as a reference.

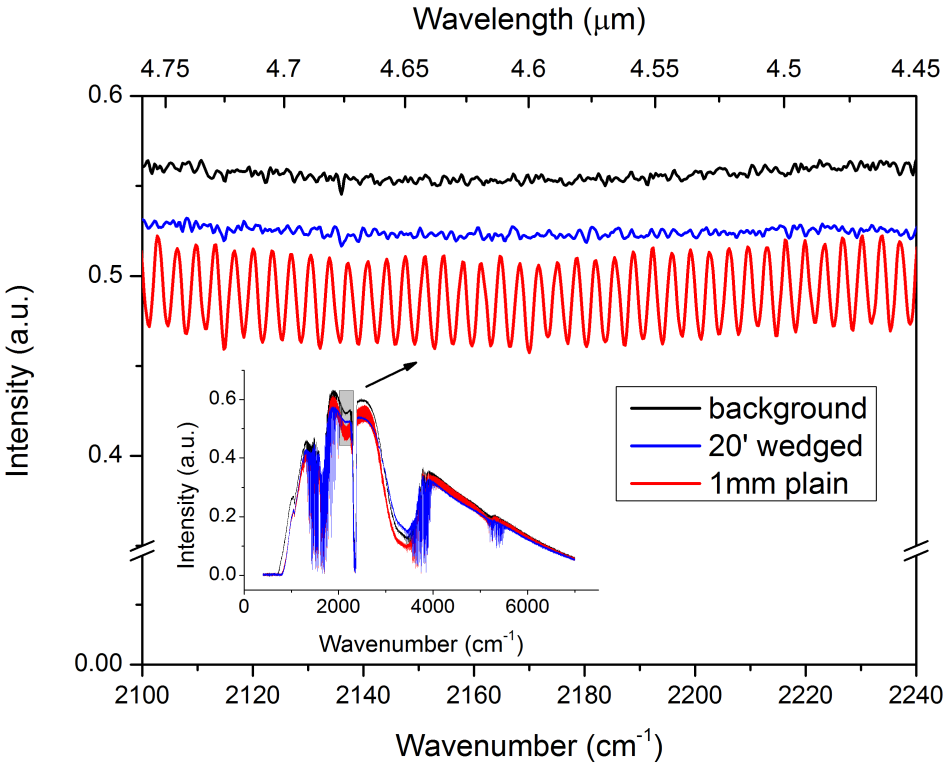

Figure 6.12: A comparison of light transmission through the flat and wedged plates. The flat, uncoated plate produces previously described interference fringes compromising cavity feedback. Wedged plate has transmission comparable to the background signal. Intensity reduction corresponds to ~ 4 % reflection due to refractive index mismatch at the CaF_2 and air interface. The inset shows the full broadband reflection from the "globar" source.

The light transmission through the parallel plate produces interference fringes that can be seen in Figures 6.12 (red). The transmission through the wedged mirror (blue) has no FP fringes, and its signal shape is similar to the background (black) signal. The ~ 4 μm wavelength region is chosen due to absence of absorption features from the atmospheric gases, producing unperturbed transmission spectra.

The demonstrated transmission through the wedged mirror has lower intensity compared to the background signal shown in Figure 6.12. This intensity reduction arises from the partial light reflection due to index mismatch at the CaF_2 and air interface.

6.4.1 Thin film deposition

The reflectivity of a secondary mirror, controlled through the thin film deposition, was chosen to fall into $\sim 40-50$ % range. Smaller reflectivity decreases the contrast ratio and finesse of the interference pattern, compromising sharp single mode generation. Higher than 50 % mirror reflectivity increases the sharpness of the produced interference, but reduces the transmission of visible light hampering the alignment utilizing the *HeNe* laser. The AR coating is not needed, since the interference suppression is achieved through the wedged shape of the plate.

The proposed $40-50$ % reflectivity can be achieved through thin film deposition creating partially reflective surface. The created reflectivity can be controlled by adjusting the thickness and the type of deposited material. Two types of material were considered - a semiconductor and a metal. Semiconductors create reflectivity through the refractive index mismatch and have good adhesion properties. The downside of using semiconductors is the position of their bandgap in the near IR at room temperature. As a result, the visible frequencies are absorbed making the system much more difficult to align (see Section 6.3.2). Thin metal layers, on the other hand, can be semi transparent to both - visible and mid-IR frequencies, has excellent adhesion properties and can be deposited in a controlled fashion through thermal evaporation or sputtering.

As the first step, 10×10 mm^2 square cover glass was used for the calibration of the metal deposition. Titanium was chosen over other metals due to its price, availability and good adhesion properties. Five pieces of cover glass were placed into sputtering system across the submount, equidistantly spaced from each other. The sputtering gun, located at the far end of the submount, creates a thickness gradient of the deposited metal as a function of the distance. The resulted thicknesses of deposited film were measured using an ellipsometer and are shown in Figure 6.13a.

The coated glass pieces, placed into the FTIR spectrometer for the broadband light transmission measurements at 0° angle of incidence, were used. The light transmission through

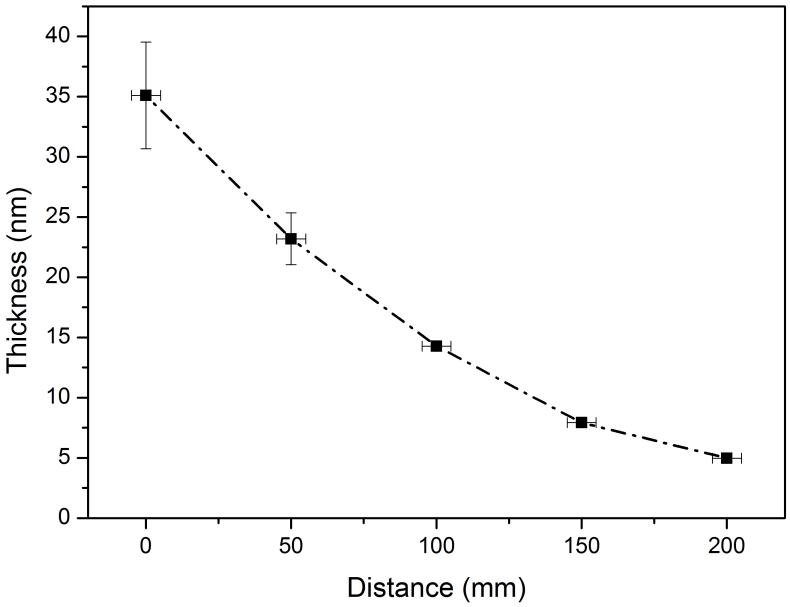

(a) Titanium film thickness vs the distance across the submount.

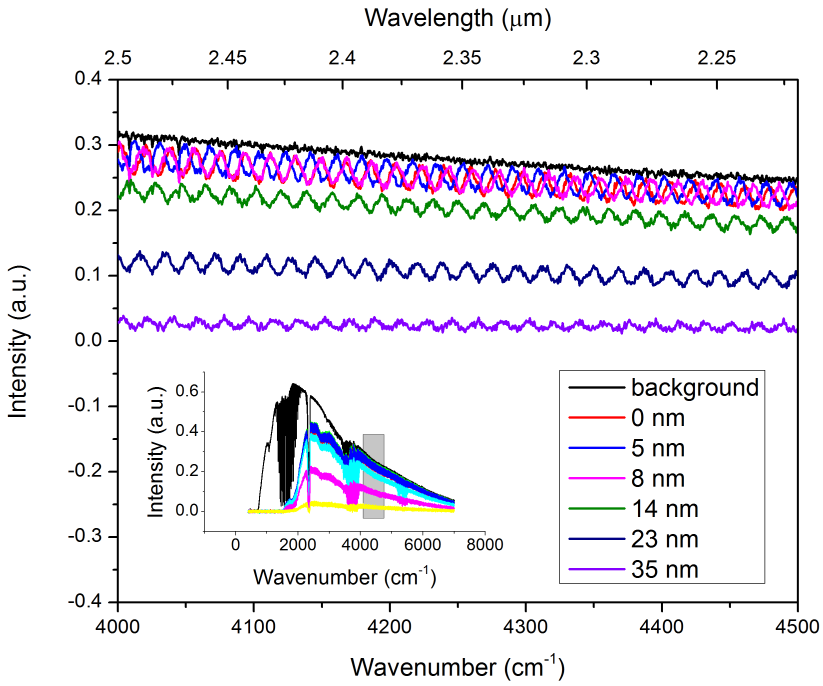

(b) Light transmission intensity decreases with the titanium film thickness.

Figure 6.13: Titanium coating calibration by measuring light transmission as a function of film thickness. The inset in b) shows full broadband spectra obtained from the "*globar*" source.

the glass used for the calibration purposes cuts off below $\sim 2100\ cm^{-1}$ wavenumbers. As a result, the spectral region, shown in Figure 6.13b, is $4000 - 4500\ cm^{-1}$ instead of the usual $2100 - 2200\ cm^{-1}$. From the obtained results it is noticed that the transmitted light intensity is inversely proportional to the thickness of the deposited film. The observed oscillations occur due to internal Fabry-Pérot interference between two parallel cover glass pieces. The free spectral range between two subsequent maxima is $\Delta f_{FSR} \approx 3.5\ cm^{-1}$ corresponding to the $\sim 0.8\ mm$ slide thickness. From this graph it can be estimated, that $\sim 20 - 25\ nm$ of Ti film will yield $\sim 40 - 50$ % reflectivity.

Next, two 25.4 mm in diameter CaF_2 plates - wedged (1.5 mm thick) and parallel (1 mm thick), were each covered with $20 - 25\ nm\ Ti$ layers to produce $40 - 50$ % reflectivity. The measured mid-IR transmission for both plates is shown in Figure 6.14. Since the CaF_2 material is transparent in the mid-IR region, the transmission measurements were performed closer to the 5.2 μm wavelength region. The specific region, showed in Figure 6.14, is chosen due to the lack of atmospheric gas absorption features, producing undistorted transmission curves.

As a result, $\sim 25\ nm$ of deposited titanium reduced the light transmission to 45 % creating $\sim$ 55 % reflectivity. The transmission in Figure 6.14a obtained from the parallel plate contains interference fringes, similar to those observed in other parallel plates. The signal in Figure 6.14b, obtained from wedged plate has no such fringes, signifying that the wedged angle is sufficient to suppress all internal oscillations even at the 0° angle of incidence.

6.4.2 Interferometer alignment

The titanium coating, as opposed to previously used germanium coating, opened up a new alignment possibility - the optical alignment. Unlike germanium, the titanium coating is semi-transparent to visible light. The secondary mirror is roughly positioned close to the primary one under the optical microscope. A red $HeNe$ laser beam is expanded through the set of two lenses and is directed onto the Fabry-Pérot reflector at a small angle

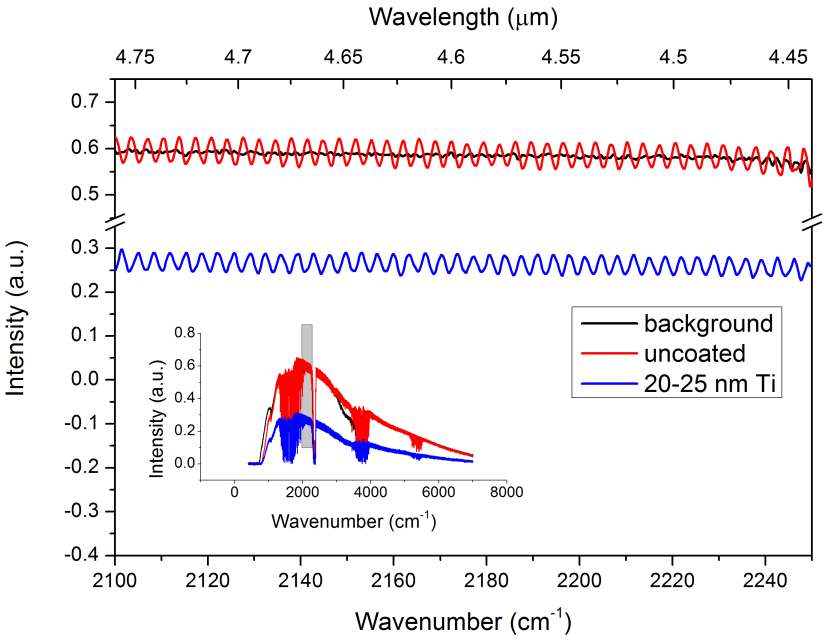

(a) Flat CaF_2 plate

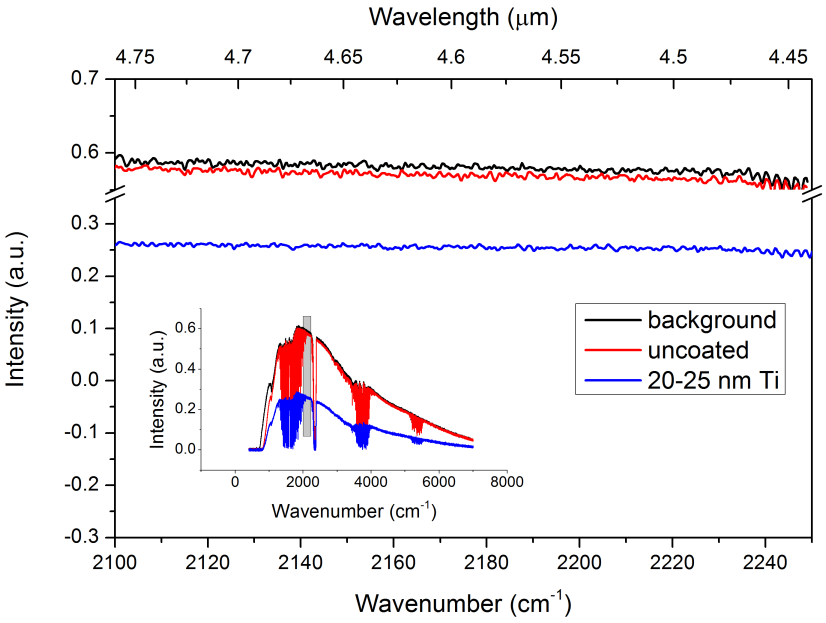

(b) Wedged CaF_2 plate

Figure 6.14: Light transmission intensity before and after 25 nm titanium coat on the flat and wedged plates. The inset shows full broadband spectra obtained from the "*globar*" source.

(< 10°), so that the reflection is created on an external screen. The reflected image takes the appearance of a set of densely spaced parallel lines corresponding to the interference maxima inside the reflector. The mirror adjustments reduce the density of these lines by increasing the distance between them, as the mirror becomes better aligned. Two mirrors are said to be parallel to each other when the sparsely distributed lines disappear from the screen leaving either one interference maximum or one interference minimum displayed on the screen.

As mentioned before, the aligned reflector is then checked for the free spectral range and the alignment quality using the FTIR spectrometer. The typical reflection spectrum using this alignment method is shown in Figure 6.15.

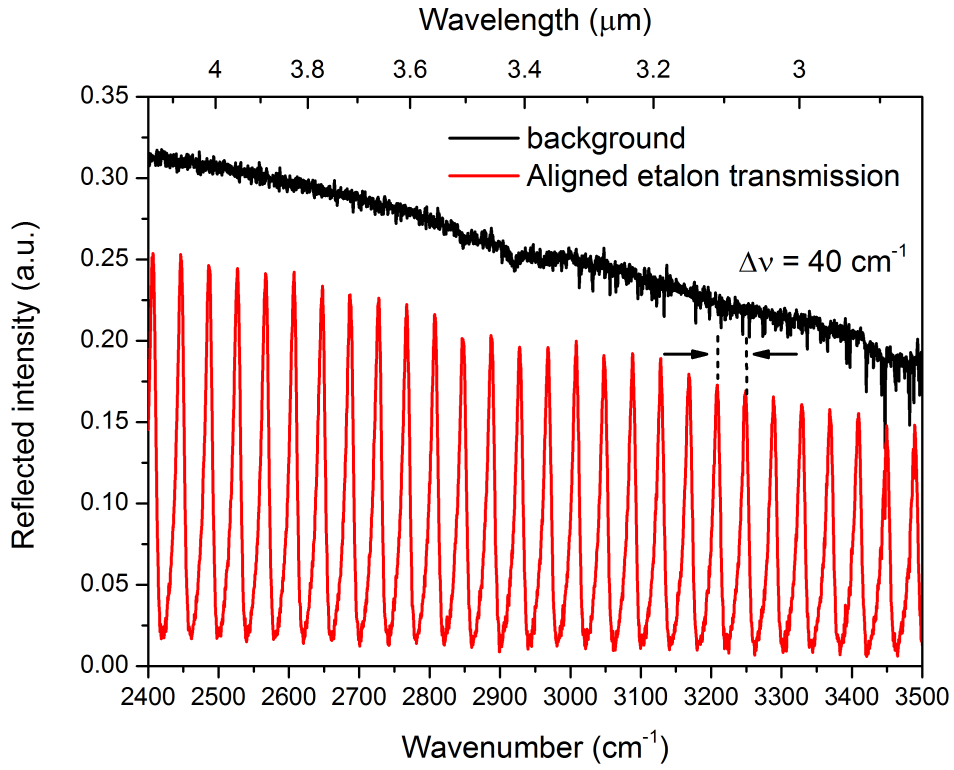

Figure 6.15: Broadband light reflection from the perfectly aligned Fabry-Pérot reflector. The high contrast factor (92%) suggests good mirror parallelism.

It can be noticed that the contrast factor is significantly improved (92%) compared to the one obtained from the reflection spectrum of FP interferometer aligned using the

previously described alignment techniques ($\sim$ 20%). The free spectral range of 40 cm^{-1} corresponds to the mirror separation of $\sim$ 125 μm.

6.4.3 Results

The aligned FP reflector with the wedged secondary mirror coated with Ti film produces sharp, narrow single peak emission. Strong, selective feedback from the reflector allows room temperature, external cavity continuous wave operation. The wide wavelength coverage obtained in CW mode is shown in Figure 6.16.

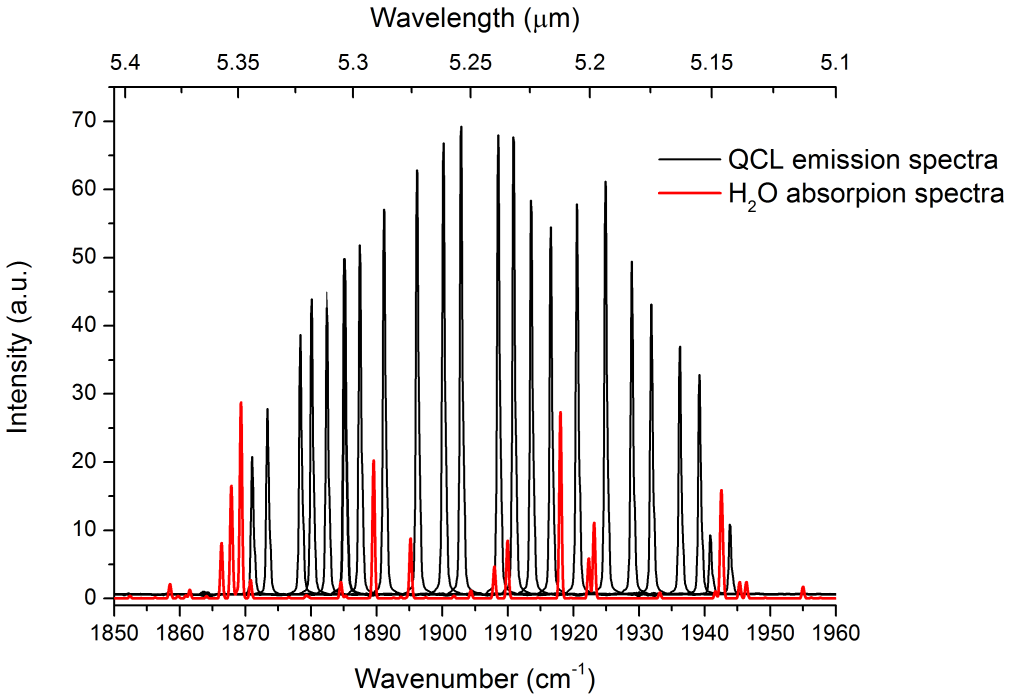

Figure 6.16: Continuous wave single mode emission obtained by changing mirror separation. The FP reflector, covering the whole gain bandwidth. The wider gaps appear either due to the water absorption lines in the atmosphere or the compromised feedback occurring as a result of misaligned mirrors during the movement.

Single peak emission coverage can be achieved across the 80 cm^{-1} wavelength range (1865 – 1945 cm^{-1}) with the mirror separation of $\sim$ 65 μm ($f_{FSR} \approx 77\ cm^{-1}$). The

produced peaks typically have *FWHM* less than 1 cm^{-1} which is much lower than those achieved by the diffraction grating ($\sim$ 2 cm^{-1}). The wavelength selection is much more controlled compared to the previously described results. The emission wavelength demonstrates linear dependence on the voltage applied across the piezoelectric actuators. This allows selective wavelength emission across the whole gain spectrum. However, certain frequencies still cannot be accessed due to the presence of the water absorption lines shown in Figure 6.16 (red). The water absorption at these specific frequencies forces the cavity to jump onto the neighboring cavity modes.

However, not all emission gaps correspond to the presence of the water absorption lines. Some of the frequencies could not be reached despite the absence of the water absorption lines in that spectral region. It is possible that the alignment of two mirrors is compromised during the move. It can occur when two piezo elements move in the different planes, bending the secondary mirror and bringing it out of alignment with respect to the primary one.

6.5 Rapid wavelength modulation via tunable FP reflector

Quantum cascade lasers have become indispensable sources which have improved existing mid-IR technology and enabled the new one in commercial and defense fields. The main advantage of the Fabry-Pérot reflector system is the lack of mechanical components, allowing rapid wavelength scan only limited by the inertia of the secondary mirror and the friction caused from the trapped air between two closely positioned plates.

Wide wavelength tuning and high emission powers can be achieved with diffraction gratings [4–8], however the scanning frequencies in Littrow configuration is limited by the weight of the grating and the friction arising from mechanical movement, restricting the scan to the sub-kHz region. For example, the highest reported tuning rate for the external cavity

QCL is 5 kHz [14]. Higher scanning frequencies would allow noise reduction by increasing the number of scans in a given period of time or would decrease the scanning times.

The angular movement of the mechanical diffraction grating is typically the limiting factor for the rapid wavelength modulation. The unique construction of the Fabry-Pérot reflector eliminates the need for mechanical movement for the continuous wavelength tuning. The secondary mirror, mounted onto the piezoelectric actuator, can only move in line to the propagating beam due to rapid oscillations caused by the actuator. The rigid structure and lack of hinges enable high mirror oscillation frequencies to be achieved.

The wavelength coverage was measured by driving the QCL device in continuous wave mode. The piezoelectric stacks were connected to a function generator that produced a triangular waveform with a 50 % symmetry cycle. This particular symmetry cycle minimizes the abrupt momentum change during the scan and provides linear displacement. The momentum change is much smoother if the sinusoidal mirror modulation is used, however, the mirror displacement is not linear, potentially distorting the spectra. As a result, the sinusoidal mirror modulation is preferred at higher frequencies. The secondary mirror was modulated with a frequency of $100Hz$ and an amplitude of $\Delta V = 10\ V$. The amplitude is limited to 10 V by the function generator output, resulting in the maximum mirror displacement of $\sim 1.5\ \mu m$. The tunable wavelength range, at $\Delta d = 1.5\ \mu m$ mirror displacement depends on the initial mirror separation d. The spectrum collected at 100 Hz and mirror separation $d \approx 65\ \mu m$ is shown in Figure 6.17.

The emission spectrum covers $\sim 60\ cm^{-1}$ spectral range, corresponding to a mirror separation of $d \approx 65\ \mu m$. The dips in the spectra correspond to the light absorption by the gases in the atmosphere, mainly dominated by the water (H_2O) shown in Figure 6.17 in red. The width of the spectral coverage of this system is frequency dependent, due to the non-negligible mass of the secondary mirror and the air resistance between the mirrors. The scanning amplitude of the secondary mirror is reduced when driven at higher frequencies, resulting in reduced spectral coverage width, as seen in Figure 6.19b, where

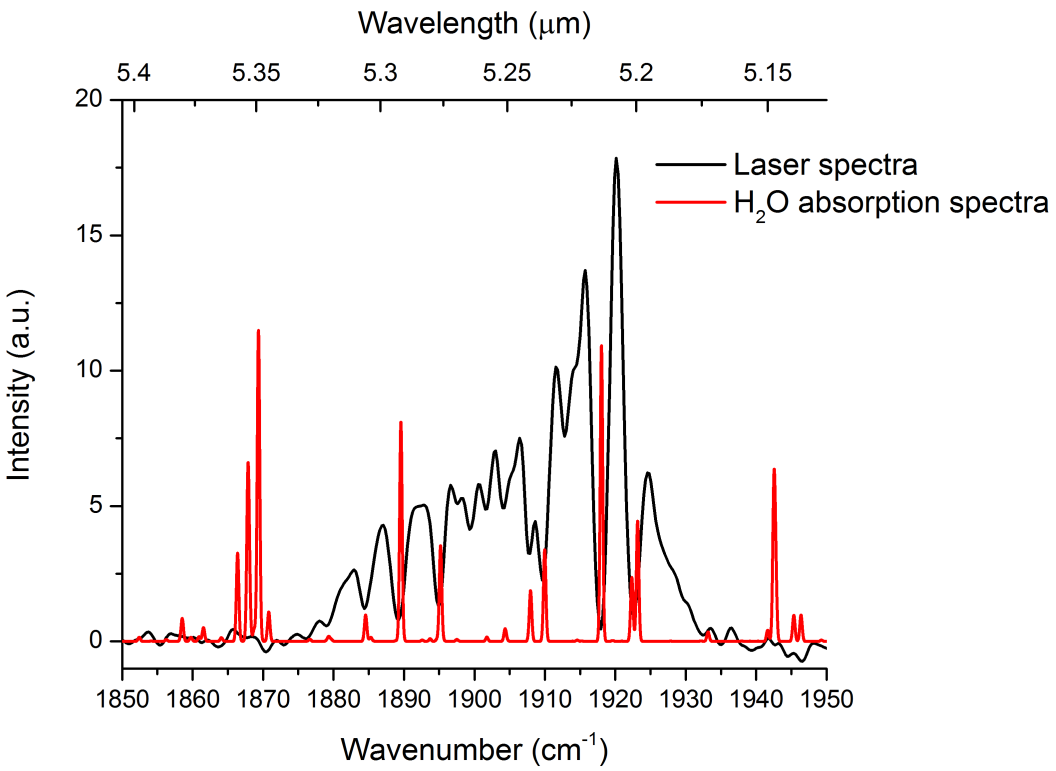

Figure 6.17: Reflected continuous wave emission spectra passed through air from the scanning FP reflector. The secondary mirror was modulated with 50 % symmetrical triangular wave-function at 100 Hz. A lock-in amplifier was used to collect averaged signal with averaging time of 200 ms. The 2 % water concentration absorption lines are also included to demonstrate the dips in the laser emission spectra.

the spectral coverage is reduced from 60 cm^{-1} to 20 cm^{-1} with the increase of scanning frequency from 100 Hz to 1000 Hz. It is possible that the weight of the attached secondary mirror restricts the oscillating motion of the piezoelectric stack, thus reducing the width of the emission spectra. Another possible reason for decreased scanning amplitude is attributed to the restricted air movement between two plates. The air movement between the plates becomes restricted at small separation distance as the mirror modulation frequency increases. While the weight of a such optical plate is typically less than 1 g, combined with the large surface area and air friction, produced during the rapid movement, the amplitude reduction during the scan becomes large enough to be noticed, as shown in Figure 6.19b.

The wavelength coverage with the fixed amplitude d is a function of the mirror separation. The wavelength scanning width is larger for smaller mirror separation d, compared to the larger separation, when the mirror scanning amplitude Δd is kept the same. This is demonstrated in Figure 6.18, where the scanning wavelength width is narrower for larger mirror separation, hence smaller free spectral range. The scanning amplitude is kept constant at $\Delta d \approx 1.5\ \mu m$, corresponding to the displacement required to cover the partial free spectral range.

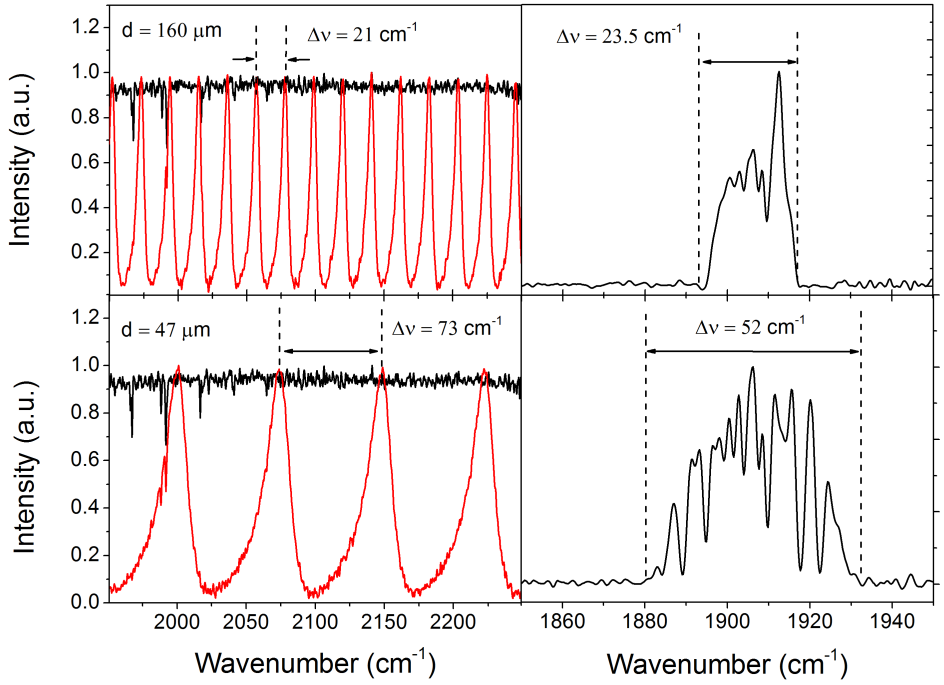

Figure 6.18: Demonstration of the achieved maximum free spectral range as a function of initial mirror separation d with the fixed scanning amplitude $\Delta d = 1.5\ \mu m$. Top graph shows the maximum achieved free spectral range of $\Delta\nu = 23.5\ cm^{-1}$ at mirror separation $d = 160\ \mu m$. The bottom graph shows much wider free spectral range of $\Delta\nu = 52\ cm^{-1}$ with the reduced mirror separation of $d = 47\ \mu m$. The light reflection from the aligned FP reflector is shown in red, the reflection from the plain mirror is shown in black.

Figure 6.19a shows the maximum wavenumber coverage as a function of driving frequency for a given separation. The benefit of quicker scans can outweigh the benefit of having

wider spectra coverage, especially where only narrow absorption features are considered. Sharp absorption lines, such as those produced by NO molecules in a 5 μm spectral range, are typically less than 1 cm^{-1} wide at atmospheric pressure requiring total wavelength change of ~ 1 cm^{-1}. This can be easily achieved with mirror scanning frequencies as high as 5 kHz, where ~ 5 cm^{-1} are covered.

Wide spectral coverage and rapid scan times can be achieved by bringing two mirrors closer together increasing the free spectral range of the FP reflector. Increased free spectral range requires smaller mirror displacement in order to cover the same wavelength range. The oscillations with smaller oscillating amplitudes are less susceptible to the modulation frequency increase, allowing wide spectrum coverage at higher frequencies.

6.6 Conclusion

The system described in this chapter demonstrated tunable single mode emission with the side mode suppression ratio of over 20 dB. It thus shows a lot of potential as an alternative method for single mode generation in an external cavity setup. A diffraction grating currently provides the most popular mean of wavelength selection in EC systems. While producing strong feedback and wide wavelength coverage it is limited to slow scan rates as discussed in this chapter. Furthermore, the intensity of the 1^{st} order mode, typically used as a feedback mechanism in Littrow external cavity setups, is in the region of $80 - 85\%$ compared to the estimated feedback of the Fabry-Pérot reflector of $> 90\%$, only limited by the losses on the mirrors. The Fabry-Pérot reflector demonstrates wide wavelength tuning, strong feedback and rapid wavelength scanning potential.

The current design of the Fabry-Pérot reflector described in this chapter, does not solve the mode-hop problem typically characteristic of EC setups [7]. Due to the large cavity length, the separation between two successive longitudinal cavity modes is too small compared to the width of signature features of the trace gas absorption lines. Additional piezoelectric

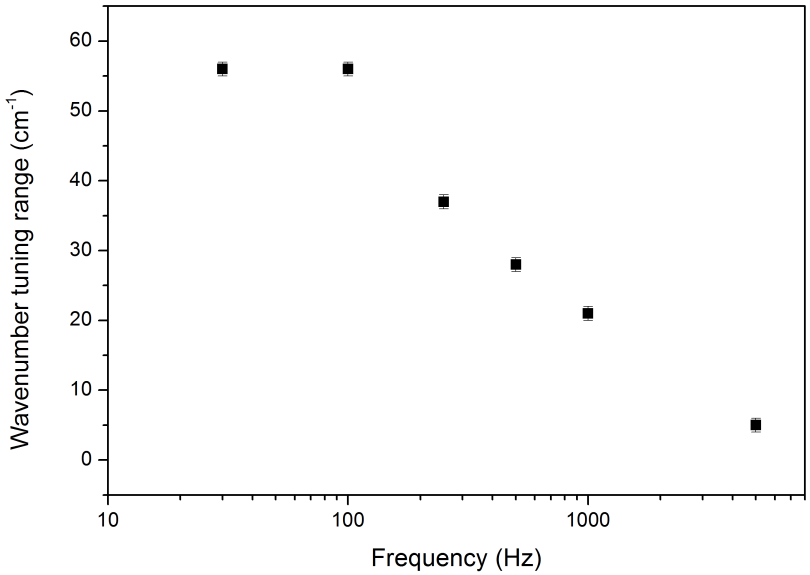

(a) Covered wavelength range as a function of scanning frequency.

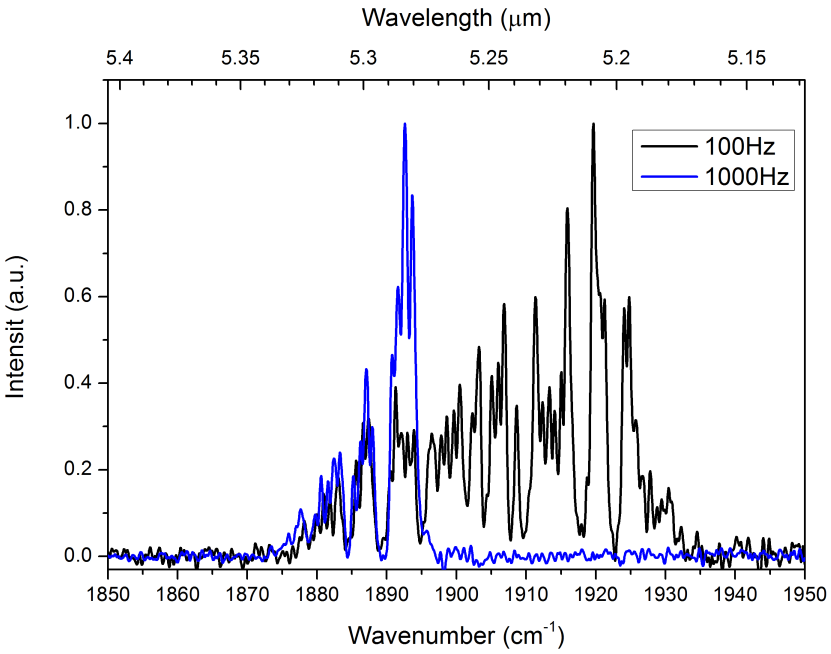

(b) Two different spectral widths at two different scanning frequencies in air. the observed dips in the spectra correspond to the water vapor in the atmosphere.

Figure 6.19: Wavelength scanning range is frequency dependent. This dependency can arise either from the finite mass of the secondary mirror or the air trapped between two parallel plates. As a result, the actual scanning amplitude Δd is smaller than expected. This can be seen in graph a) where the wavelength tuning range (as a result of decreasing Δd) is decreasing with higher mirror scanning frequency.

actuators can be used to adjust cavity length, by changing the position of the primary mirror, to sustain continuous wavelength selection.

Rapid mirror scanning allows broad spectra generation and opens up new possibilities in spectroscopy as well as providing new powerful techniques in optical coherence tomography, cytology, histology and pathology [15, 16]. Presently the wavelength tuning speed is one of the main limitations for quantum cascade lasers to be used in Fourier transform imaging microscopes [17]. The results presented in this chapter bring this realization one step closer.

References

[1] D. Vaitiekus, D.G. Revin, K.L. Kennedy, S.Y.Y. Zhang, and J.W. Cockburn. Quantum cascade laser with unilateral grating. *Photonics Technology Letters*, 24(23): 2112–2114, 2012.

[2] H. Li, S. Katz, G. Boehm, and M.C. Amann. Broad gain injectorless quantum-cascade lasers with low threshold emitting around 8.6 μm. In G.H. Duan, editor, *Optoelectronic Materials and Devices VI*, volume 8308 of *Proceedings of SPIE*, 2011.

[3] A. Hugi, R. Terazzi, Y. Bonetti, A. Wittmann, M. Fischer, M. Beck, J. Faist, and E. Gini. External cavity quantum cascade laser tunable from 7.6 to 11.4 μm. *Applied Physics Letters*, 95(6):061103, 2009.

[4] G.P. Luo, C. Peng, H Q. Le, S.S. Pei, W.Y. Hwang andd B. Ishaug, J. Um, J. N. Baillargeon, and C.H. Lin. Grating-tuned external-cavity quantum cascade semiconductor lasers. *Appl. Phys. Lett*, 78:2834, 2001.

[5] R. Maulini, M. Beck, J. Faist, and E. Gini. Broadband tuning of external cavity bound-to-continuum quantum cascade lasers. *Appl. Phys. Lett*, 84:1659, 2004.

[6] R. Maulini, D.A. Yarekha, J.M. Bulliard, M. Giovannini, and J. Faist. Continuous-wave operation of a broadly tunable thermoelectrically cooled external cavity quantum cascade laser. *Opt. Lett*, 30:2584, 2005.

[7] G. Wysocki, R.F. Curl, F.K. Tittel, R. Maulini, J.M. Bulliard, and J. Faist. Widely tunable mode-hop free external cavity quantum cascade laser for high resolution spectroscopic applications. *Appl. Phys. B*, 81:769, 2005.

[8] I. Dunayevskiy, A. Tsekoun, M. Prasanna, R. Go, and C. K. N. Patel. High-sensitivity detection of triacetone triperoxide (TATP) and its precursor acetone. *Appl. Opt.*, 46: 6397, 2007.

[9] M.G. Littman and H.J. Metcalf. Spectrally narrow pulsed dye laser without beam expander. *Applied Optics*, 17(14):2224–2227, 1978.

[10] S.G. Lipson, H. Lipson, and D.S. Tannhauser. *Optical Physics (3^{rd} edition)*. London: Cambridge U.P., 1995.

[11] G. Keiser. *Optical Fiber Communications*. McGraw-Hill, 2000.

[12] B.E.A. Saleh and M.C. Teich. *Fundamentals of Photonics*. John Willey & Sons Inc, 1991.

[13] A. Lyakh, R. Barron-Jimenez, I. Dunayevskiy, R. Go, C. Kumar, and N. Patel. External cavity quantum cascade lasers with ultra rapid acousto-optic tuning. *Applied Physics Letters*, 106:141101, 2015.

[14] T. Tsai and G. Wysocki. External-cavity quantum cascade lasers with fast wavelength scanning. *Appl. Phys. B*, 100:243, 2010.

[15] D. Huang, E.A. Swanson, C.P. Lin, J.S. Schuman, W.G. Stinson, W. Chang, Mr.R. Hee, T. Flotte, K. Gregory, C.A. Puliafito, and J.G. Fujimoto. Optical coherence tomography. *Science*, 254(5035):1178–1181, 1991.

[16] Ryan P. McNabb, Dilraj S. Grewal, Rajvi Mehta, Stefanie G. Schuman, Joseph A. Izatt, Tamer H. Mahmoud, Glenn J. Jaffe, Prithvi Mruthyunjaya, and Anthony N. Kuo. Wide field of view swept-source optical coherence tomography for peripheral retinal disease. *British Journal of Ophthalmology*, 2016.

[17] David T.D. Childs, Richard A. Hogg, Dmitry G. Revin, Ihtseham Ur Rehman, John W. Cockburn, and Stephen J. Matcher. Sensitivity Advantage of QCL Tunable-Laser MidInfrared Spectroscopy Over FTIR Spectroscopy. *Applied Spectroscopy Reviews*, 50(10):822–839, 2015.

Chapter 7

Quantum Cascade Lasers in Gas Sensing Setups

7.1 Introduction

Sensitive gas detection and quantification are of a great importance in the environmental research [1–6], atmosphere chemistry studies [1], physics [1, 2, 6–9], biology [2, 5], biomedical studies [2, 5, 6, 8–15] and military applications [16, 17]. Laser based spectroscopic detection allows for very accurate, up to pptv (parts per trillion by volume = $1 : 10^{12}$) detection level and quick measurements while giving the benefit of mobile systems and allowing on-field analysis.

Laser based spectroscopy is safe, fast and reliable to compete with the currently available gas detection techniques, making it suitable for clinical studies involving the analysis of volatile organic compounds. Many companies, including the collaborating industry partners *Sensor Sense* and *MSquared*, develop and produce mobile laser based detection systems available for wide range of gas detection in addition to those described in this thesis. The currently available, non-laser based spectroscopic systems, including chemi-

luminescence [13, 18], gas chromatography [19], electronic nose [13, 20, 21] and proton transfer reaction based mass spectrometry (PTR-MS) [19] have their own advantages and disadvantages, whether it is sensitivity, robustness, lengthy measurements, selectivity or the price limiting any one of these systems to dominate the market. For example, the system based on a mass spectrometry can demonstrate high sensitivity and selectivity, but it is bulky and expensive [19]. The laser spectroscopy, on the other hand, is leading in some of these areas providing high spectral power due to its narrow linewidth. Typically, continuous wave lasers can generate linewidth much narrower than the absorption linewidth of the measured gas. Selectivity is also a strong feature of a laser based spectroscopy making it easier to distinguish specific analyte amongst the complex gas mixture. It is also a non-intrusive technique offering remote sensing possibilities.

This chapter starts with the introduction of different laser based spectroscopic techniques. The focus of this chapter then shifts to the description of the experimental setups for methane (CH_4) and nitric oxide (NO) detection. Section 7.3 describes simple direct absorption technique used with the short wavelength QCL developed at the University of Sheffield. The lasers emitting at $\sim 3.3\ \mu m$ are used to target one of the strongest absorption bands of the methane. Section 7.4 describes the laser spectroscopy technique used to determine exact emission wavelength of the $5.3-5.4\ \mu m$ QCL device, also designed and grown at the University of Sheffield, through the nitric oxide absorption bands. The potential of the sensitive absorption measurements at the *Q-branch* is also discussed. All experimental measurements were performed at the Radboud University in Nijmegen, Netherlands with the quantum cascade laser devices designed, grown and fabricated in the University of Sheffield as part of the collaboration of a *Quantatec* project [22].

7.2 Gas absorption in mid-infrared region

The principle of laser spectroscopy is based on the laser light being absorbed at the frequencies corresponding to the spectral absorption lines of the specific gases. These absorption

lines originate from the electronic, rotational or vibrational states of the molecules. The electronic state transitions are much more energetic compared to the other two, and therefore can be detected using visible or near UV wavelengths. The rotational and vibrational states, also being referred to as ro-vibrational states or transitions, can be probed using near and mid-infrared light sources, due to much lower transition energies. The transitions occurring in mid-infrared region, however, are much stronger allowing much lower detection limits. The reduction of the intensity of the transmitted light through the gas can be described using Beer-Lambert law:

$$T(\nu) = T_0(\nu) \cdot e^{-\sigma \cdot \rho_N \cdot l} \tag{7.1}$$

where $T_0(\nu)$ is the light transmission through non-absorbent media, as a function of the light frequency ν; l is the absorption path length; ρ_N - number density of absorbing molecules and σ is the absorption cross-section of the absorbing species expressed in cm^2 units. The absorption coefficient $\alpha(\nu)$ is expressed as:

$$\alpha(\nu) = \sigma \cdot \rho_N \tag{7.2}$$

In the linear optics regime the absorption coefficient doesn't depend on the transmitted light intensity. This approximation fails at higher optical powers, where linear optics regime becomes invalid [23].

7.2.1 Direct absorption spectroscopy

Direct absorption spectroscopy is the simplest and the most fundamental gas detection technique. It is based on the light absorption inside the cell filled with an absorbent gas (analyte) according to Beer-Lambert law, described in Equation 7.1. The modulated laser emission is absorbed by the analyte at the specific wavelengths, corresponding to

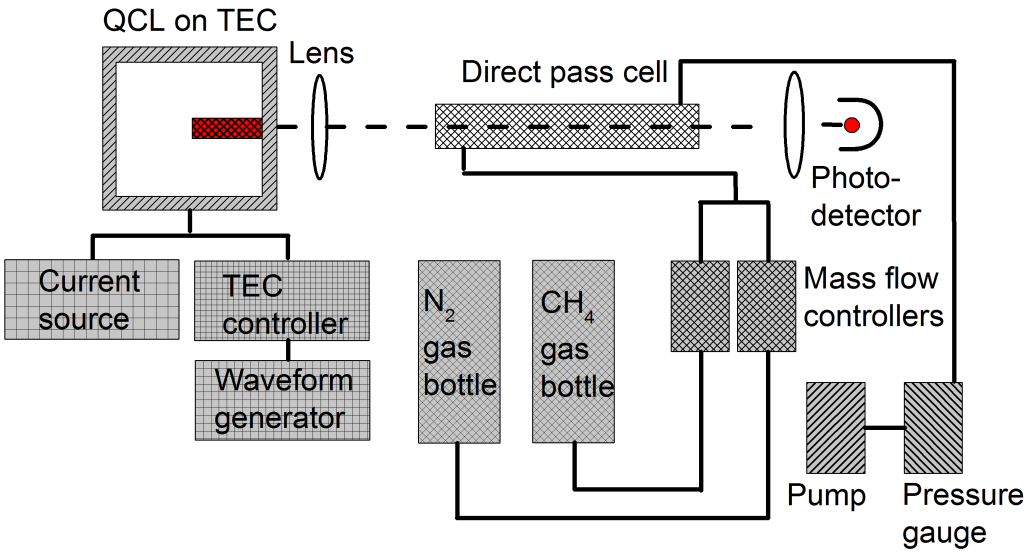

Figure 7.1: Schematic diagram of the direct absorption technique. The modulated laser scans its wavelength through a set of frequencies that are either transmitted or absorbed inside the gas cell. The signal is then recorded with the photodetector and displayed as absorption signal for further analysis.

its ro-vibrational or electronic modes. The wavelength modulation in the semiconductor lasers is typically achieved through the temperature control. The temperature variation of the typical semiconductor laser base allows up to 100 cm^{-1} wavenumber tuning, but the process is slow, usually not exceeding $\sim 0.3\ cm^{-1}/s$. Adjusting the temperature of the laser core, via additional current injection to the active region, on the other hand, is much faster process capable of achieving the wavelength tuning rates up to $\sim 10^4\ cm^{-1}/s$, but with a limiting wavenumber ranges of only $1-2\ cm^{-1}$. The schematic diagram of the direct absorption spectroscopy technique and experimental setup used for methane detection is shown in Figure 7.1.

The temperature modulated laser wavelength, transmitted through the absorbent medium,

is recorded and compared to the laser transmission intensity through the background medium (*i.e.* the gas cell filled with nitrogen gas). The biggest advantage of a direct absorption technique is its ability to provide absolute quantitative description of the gas mixture [24].

Due to the simplicity of this technique the sensitivity is often limited to an absorbance of $\sim 10^{-3}\ Hz^{-1/2}$ [25]. This is mainly limited due to a small change in signal intensity ($\Delta T = T_0 - T$) compared to the noise level of the background signal. However, it has been demonstrated that it is possible to achieve sensitivities much closer to the theoretical shot noise level with absorbance of $\sim 10^{-6}\ Hz^{-1/2}$ [26, 27]. Noise reduction, increase of absorption path length or gas probing at stronger transitions would contribute to the detection limit improvement. The noise levels can be reduced with the help of modulation techniques, the path length increase is achievable with external cavities, such as multi-pass cells, and the stronger absorption lines are located in the mid-infrared spectral region.

7.2.2 Wavelength modulation spectroscopy

The wavelength modulation spectroscopy (WMS) is an example of a more sensitive laser spectroscopy technique. As mentioned previously, the noise is a limiting factor in the direct absorption spectroscopy. WMS overcomes this issue by making use of the fact that the noise, also known as $1/f$ noise, reduces with increasing frequency. The improvement with this technique is achieved by encoding and demodulating the signal at higher frequencies where noise level is much smaller. As a result, the typical detection limit can be improved to $\sim 10^{-5}\ Hz^{-1/2}$ sensitivity detection range.

The schematic diagram of the wavelength modulation spectroscopy setup is shown in Figure 7.2. The laser output is modulated with frequency f around the center of its emission frequency ν_c with a certain modulation amplitude. The modulated signal is passed through a cell filled with analyte and the output signal is being detected using

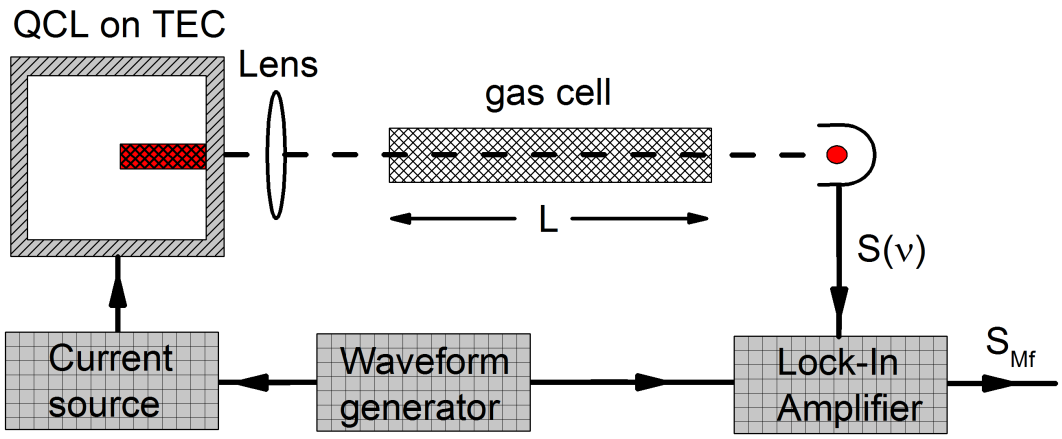

Figure 7.2: Experimental setup of typical wavelength modulation spectroscopy. Function generator provides the modulation signal that is directed to the laser housing (consisting of QCL chip, temperature controller and laser driver) as well as lock-in amplifier. The laser output is directed through the absorption cell into a photodetector. Then the signal $S(\nu)$ is fed into the lock-in amplifier where the output of 1^{st} harmonic constitutes of the WMAS signal (S_f). Reprinted from Reference [28].

suitable photo-detector. The signal is then directed to the lock-in amplifier for 1^{st} harmonic extraction at a detection frequency f. The bandwidth is given by the inverse of the integration time τ.

The output power of a typical semiconductor laser can be modulated by the additional current injection to its active region, raising the core temperature of the laser locally. Sinusoidal modulation of the injection current $I_{ic}(t)$ can be expressed as:

$$I_{ic}(t) = I_c + I_a \cdot cos(2\pi f t) \tag{7.3}$$

where I_c is the offset injection current and I_a is the injection current modulation amplitude. It can be shown that the wavelength modulation process can be expressed in frequency units, with a similarly looking equation [28]:

$$\nu(t) = \nu_c + \nu_a \cdot cos(2\pi ft) \tag{7.4}$$

here ν_c is the laser center emission frequency and ν_a frequency modulation amplitude. The laser intensity transmitted through the cell can then be expressed as a Fourier series expansion. This WMS technique was first applied by Bjorklund [29] using a single mode CW dye laser. Since then, wavelength modulation is mostly used with the diode lasers, due to the ease of current modulation.

7.2.3 Farraday rotation spectroscopy

Faraday rotation spectroscopy (FRS) is often referred to as zero-noise technique. Due to its ability to filter paramagnetic molecules, such as NO and O_2 without the interference from diamagnetic molecules, such as CO_2 and H_2O, makes it very competitive technique allowing quantitative and selective gas detection. The strongest absorption bands of NO lies in the mid-infrared spectrum, at around $5.2-5.4\mu m$ wavelength region. H_2O and CO_2 are also present at this spectral range and can often interfere with the signal, especially when biologically important organic samples are being measured, such as those obtained from human breath or generated by plants.

The Faraday rotation spectroscopy experiment was first described in 1980 [30]. The simple FRS setup consists of a cell with two polarized windows at each end. The AC magnetic modulation field is applied parallel to the laser beam direction. The absorption lines of paramagnetic species (such as NO) inside the cell split, in the simplest case, into two lines due to Zeeman splitting. The linearly polarized incident light is equivalent to a beam composed of two circularly polarized components with equal amplitude, zero phase shift but opposite signs. The split Zeeman lines absorb either left-hand or right-hand circularly polarized light, causing different light propagation velocities for the different polarized components. After the beam interacts with paramagnetic analyte the two components

propagate at different velocities yielding a phase shift between them at the output. The measured rotational angle is proportional to the concentration of the specimen according to:

$$\theta_F = (n^+ - n^-) \cdot B_0 \cdot l \tag{7.5}$$

where $(n^+ - n^-)$ is the difference of refractive indexes between left and right-hand circularly polarized light, B_0 - magnetic field strength and l is the absorption length. As a result, this technique can bring the detection limits close to the theoretical shot-noise levels ($\sim 10^{-8}\ Hz^{-1/2}$)[31].

7.3 Detection of the methane (CH_4) gas using $\lambda \sim 3.3\ \mu m$ QCL

The concentration of methane (CH_4) and nitric oxide (NO) gases in the atmosphere are the primary indicators for the greenhouse effect [32, 33] and, as a result, can be used to efficiently determine the pollution in the atmosphere. Methane has very strong absorption lines with relatively narrow line-widths in the 3.3 μm wavelength region. This wavelength range is in the reach of antimony based short wavelength QCLs produced in our group [34–36].

7.3.1 Motivation and laser design

Pulsed QCLs are less dependent on the efficient active region design, immaculate fabrication and good heat extraction resulting in them being cheaper and more available. High optical power, single mode operation, with good spectral purity and wide tunability, and being affordable are the most important properties required for commercial gas sensing applications. Moreover, pulsed lasers are typically driven with pulse width not exceeding

200 ns, with the duty cycles of $1 - 2$ % with the driving voltages in a range of $10 - 25\ V$ depending on the emission wavelength. The small duty cycle decreases power consumption while still delivering high peak powers. The well designed quantum cascade lasers have wall plug efficiencies in a region of $5 - 10$ % [35, 37], producing sufficient optical outputs for sensitive gas measurements even in a portable systems.

Gas spectroscopy with pulsed lasers can be performed using two different wavelength modulation methods intra- or inter-pulse. Inter-pulse spectroscopy requires short excitation pulses, typically $10 - 20$ ns, to avoid frequency chirping [38], so that the emission wavelength remains unchanged throughout the length of the pulse. The main frequency tuning between the emitting pulses is performed by temperature change. The temperature change of the QCL core can be performed using two different techniques - changing the temperature of the heat-sink, which results in the temperature gradient experienced by the laser or changing the temperature of the laser core. These methods have their own benefits and drawbacks and are described further down in this section. The intra-pulse relies on longer pulses (200+ ns) applied to the laser resulting the chip to heat up providing continuous emission frequency change during the course of the pulse (chirping). While this method does not require additional temperature controllers it still requires efficient heat extraction from the device to ensure that it generates light throughout the whole excitation pulse.

The temperature tuning mentioned in the previous paragraph can be achieved through the temperature change of the whole laser base or just its core. The former process is usually much slower, since it requires extra time to transfer heat from the heat sink, limiting its frequency modulation to the thermo-electric cooler (TEC) response time limit, which is usually not faster than 300 mHz. The temperature change of the laser core is much faster process ($\sim kHz$) and therefore is preferred for rapid scans. Internal temperature of the core is changed by injecting additional current (*Joule heating*) straight to the active region of the laser. The laser core temperature modulation is 1000s times faster, compared to

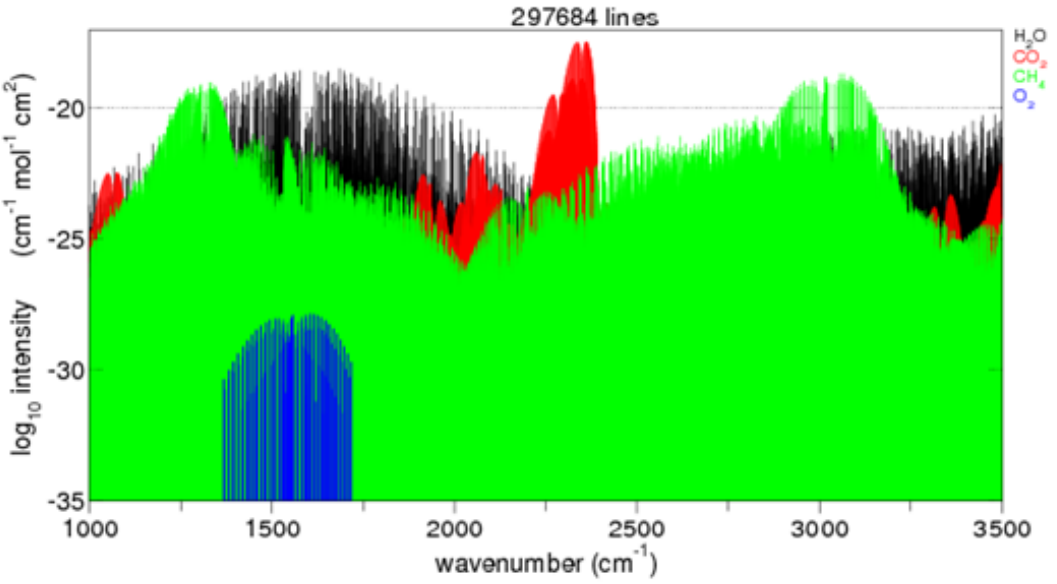

Figure 7.3: Ro-vibrational absorption lines of four common gases in the atmosphere absorbing at mid-infrared spectral region. The data is generated from Spectracalc [39]

the temperature modulation of the laser base.

Regardless of the wavelength scanning technique, the initial temperature adjustment is often needed to bring the laser emission to the vicinity of the particular gas absorbing line. The frequency of interest is determined by the gas absorption spectrum that is associated with its ro-vibrational modes as described in Section 7.2. Typical absorptions spectra in the mid-infrared region for common atmospheric gases are shown in Figure 7.3.

It can be seen that the most sensitive absorbing lines of methane are around $3.2 - 3.4\ \mu m$ wavelength region ($2900 - 3100\ cm^{-1}$), with the strongest absorbing ro-vibrational mode placed at $\sim 3038.5\ cm^{-1}$ as shown in Figure 7.4 [40]. The strongest absorption line is required for achieving very sensitive detection limits (sub-*ppbv*), however, other absorption lines can also be utilized, if less sensitive (few *ppmv*) measurements are sufficient. Less absorbing lines can be more suitable for in-filed measurements, specifically where the intensity drop of the transmitted laser becomes too substantial to be detected with mobile

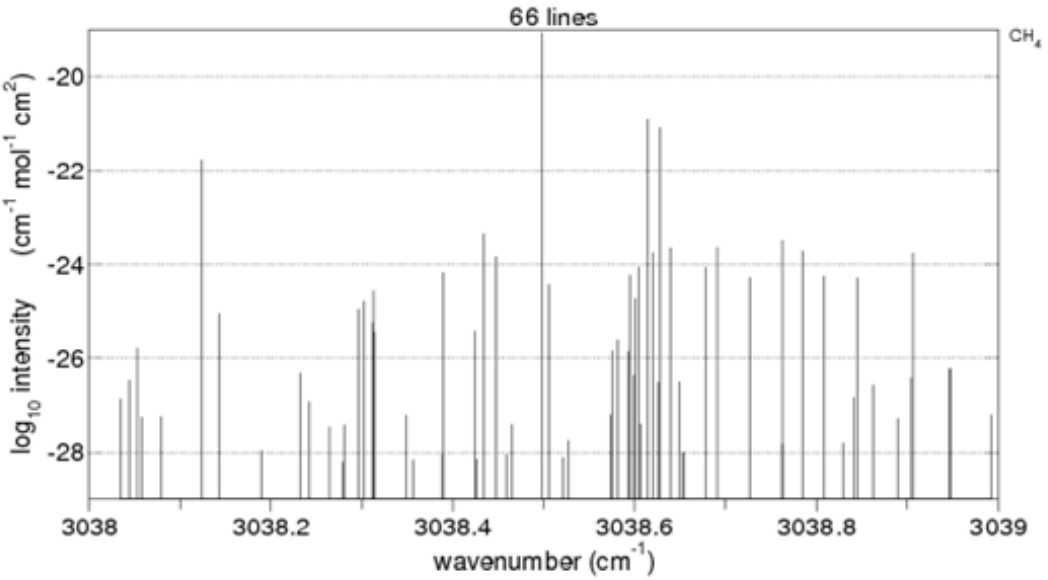

Figure 7.4: Magnified region of simulated methane (CH_4) gas absorption lines in the 3.3 μm emission region.

systems.

A set of suitable QCLs has been fabricated to match the desired wavenumber of 3038 cm^{-1}. The single mode emission was obtained with the selective distributed feedback achieved through the unilateral grating. The design and fabrication of this laser is very similar to the one described in Chapter 5. The single mode emission was obtained at room temperature with the emission wavelength of $\lambda \sim 3.29\ \mu m$ (3039 cm^{-1}). The single mode emission at different temperatures of this laser are summarized in Figure 7.5. The $FWHM$ of this laser is $FWHM = 0.51\ cm^{-1}$ which is much wider than the $FWHM$ of the absorption line of methane at 0.1 bar ($FWHM = 0.021\ cm^{-1}$), however, the line broadening occurs mainly due to intrapulse heating of the core region. Since the wavelength modulation is performed with the help of temperature change, the intrapulse heating, responsible for wavelength broadening, doesn't affect the final results.

The pulsed laser can be tuned to operate at the required wavelength. In this particular case the heat sink had to be kept at the base temperature of $27^o\ C$ (300 K) to emit around

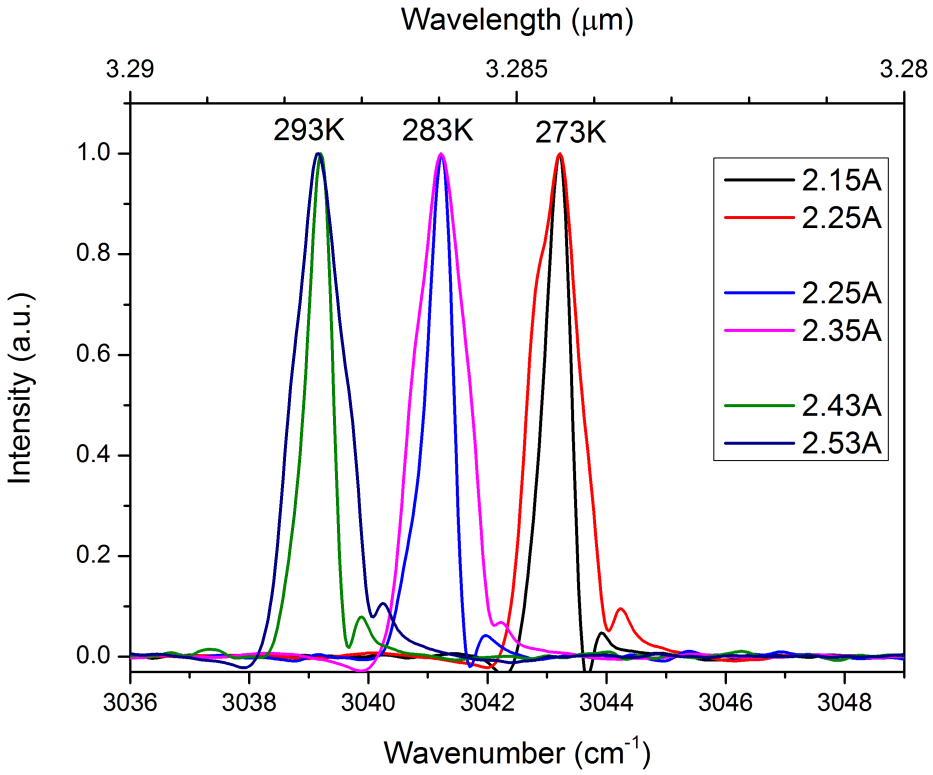

Figure 7.5: Emission spectra of the single mode laser used for CH_4 detection

3038 cm^{-1}.

7.3.2 Pressure dependence

The FWHM of the gas absorption line is pressure dependent. The FWHM of the absorption features increases at higher pressures. The comparison between two calculated methane absorption lines with the same gas concentration at 0.1 and 1 bar is shown in Figure 7.6. The signal measurement obtained at lower pressure is more desired since it reduces the required wavelength scanning amplitude in order to cover the whole absorption line. Sharper features can also be more beneficial when detection of less intense overtones is required. As seen in Figure 7.6, two peaks are observed at 0.1 *bar* (3038.5 cm^{-1} and 3038.6 cm^{-1}) compared to one, much broader peak at 1 *bar* pressure.

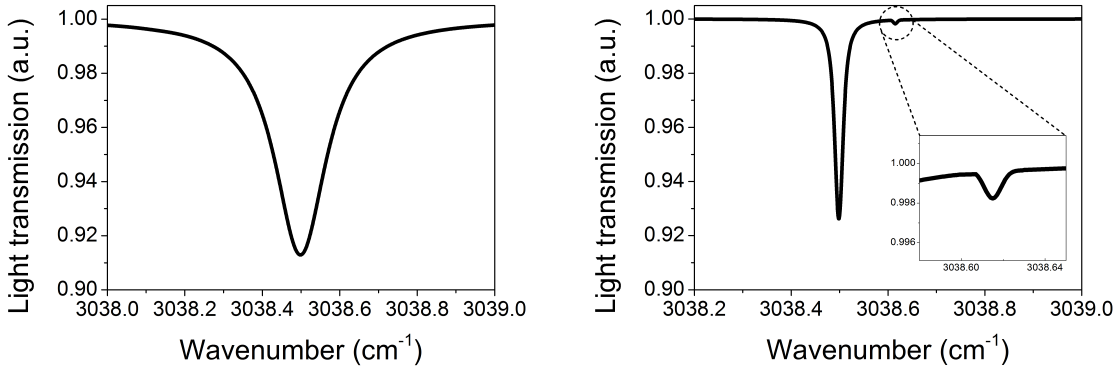

(a) Pressure broadened absorption line at 1 *bar*. (b) Sharper absorption line at 0.1 *bar*.

Figure 7.6: 1% methane (CH_4) absorption line placed at 3038 cm^{-1} region at 1 *bar* (a) and 100 *mbar* (b).

7.3.3 Experimental setup

The experimental setup, shown in Figure 7.1, consists of the QCL mounted onto the temperature controlled semiconductor laser housing with the fitted thermo-electric cooler for the heat sink temperature control. The Peltier cooler is driven with the thermo-electric cooler unit (TCU) equipped with the internal and the external modulation options. The current pulse is created using the pulse generator from *Alpes lasers* with the pulse length of 50 ns and the repetition rate of $\sim$ 10 kHz. The output beam is collimated using *Geltech* aspheric lens. The output light beam is detected using the three stage thermo-electrically cooled *Vigo* photodetector, with the cut-off wavelength of 5 μm, for quick signal detection. The results are displayed on the oscilloscope linked to the computer for digital data analysis.

The first experiment is designed to determine the rate of laser tuning and the required laser base temperature for the wavelength emission at the strongest absorption line of the methane (3038.5 cm^{-1}). The 5 cm long cell filled with high (10 %) methane concentration at 100 $mBar$ pressure. High methane concentration is chosen to enhance the absorbance by the media for demonstration purposes. The laser is temperature tuned from 3035 cm^{-1} up to 3041 cm^{-1} corresponding to the temperature change of $\Delta 30\ K$. The absorption

feature is noticed at 3038.5 cm^{-1} at the laser base temperature of $\sim 306\ K$.

Keeping the base temperature at 306 K the TCU was connected to the frequency generator for periodic temperature scanning. In order to ensure responsive and homogeneous scanning, the modulation of TE cooler is kept at 100 mHz with the temperature scanning amplitude of 2°.

7.3.4 Signal analysis

The light intensity recorded for four different methane concentrations at the pressure of 100 $mBar$ is measured and plotted in Figure 7.7. It can be noticed that the signal intensity, that is not absorbed by one of the methane ro-vibrational modes, in higher concentration mixtures is lower. This can be attributed to the scattering process inside the cell that is proportional to the higher methane concentration. The light passing through the less concentrated specimen have intensities comparable to the background (gas cell filled with nitrogen gas) signal.

For the current setup, the concentrations lower than 1000 $ppmv$ are more difficult to measure with the single scan due to the signal becoming comparable to the noise levels. Signal averaging increases the sensitivity up to 160±60 $ppmv$, as shown in Figure 7.8.

The results on the sensitivity presented here are about four orders of magnitude lower, compared to those published in literature [41]. Firstly, the used direct absorption technique is not the most efficient, but is chosen entirely for the demonstration of principle. The detection limits can be increased through the increase of the effective path length. This is discussed in Section 7.3.6. The reduction in the averaging time is also required, since the signal becomes less reliable during longer scans. Section 7.3.5 discusses the possibility for the averaging time reduction.

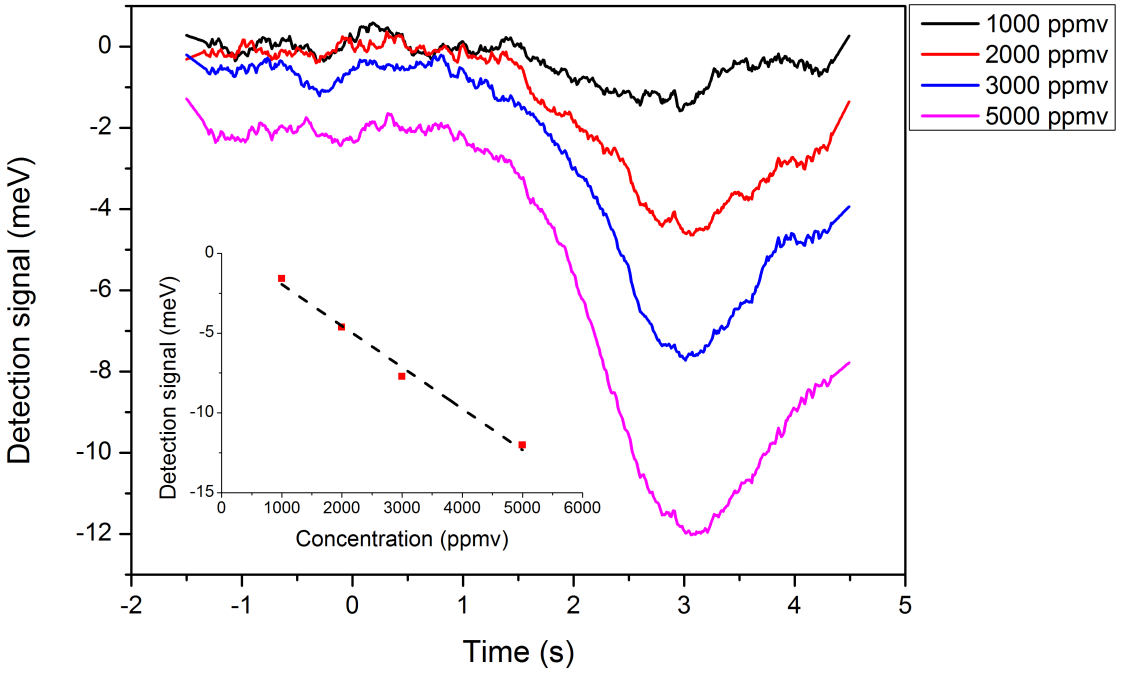

Figure 7.7: Laser light absorption signal passed through the single pass gas cell filled with variable methane CH_4 concentrations. The received signal is subtracted from the background signal (cell filled with nitrogen (N_2)) to account for the background noise. The inset shows the linear signal intensity dependence as a function of analyte concentration. The concentration and pressure inside the cell was controlled by the mass flow controllers and pressure gauge.

7.3.5 Wavelength tuning by current injection scan

The current scan can provide much faster temperature response times due to more localized core heating. The temperature modulation of the base of the laser acts on a much larger area, reducing response time of the laser output. This technique, however, is less destructive to the laser chip, since the thermal expansion is homogeneous throughout the whole chip. The current scan, on the other hand, is based on the sub-threshold current injection straight into the laser core, without the need to heat the rest of the chip thus increasing the response time of the laser. The downside of this modulation technique is reduced lifespan of the laser due to induced thermal stresses [42].

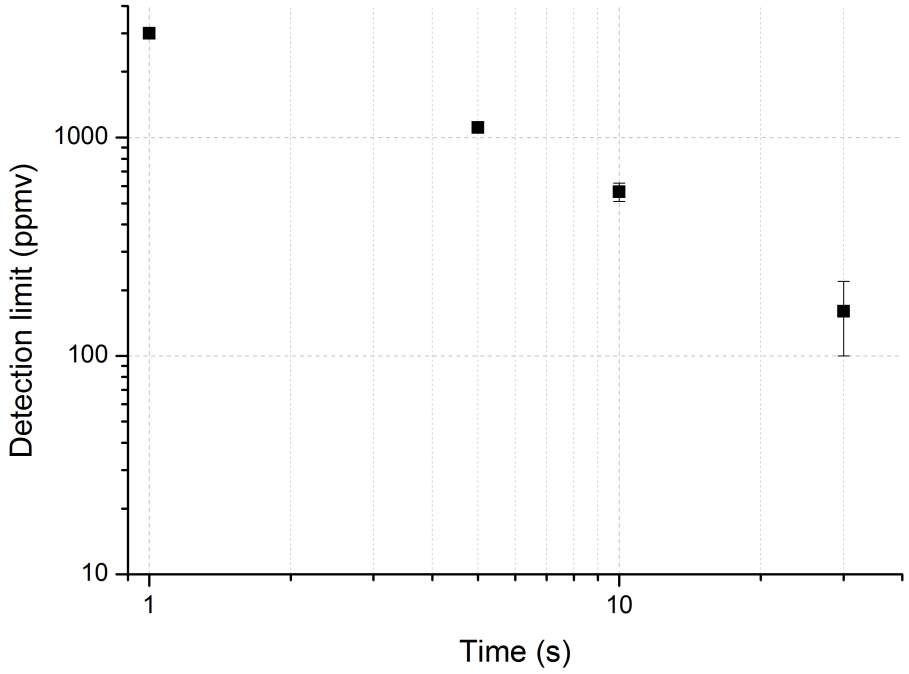

Figure 7.8: Measurable methane concentration levels as a function of the scanning time. 160 ± 60 sensitivity is obtained with 30 seconds averaging time.

The typical current scan can potentially increase the temperature modulation frequencies to the kHz range, with the wavelength tuning range of $\Delta\nu = 0.25\ cm^{-1}$ [43], compared to the *sub-Hz* that is achievable with the temperature scan. The benefit of temperature scan is that it allows for much broader wavelength modulation, typically $\Delta\nu = 20{-}30\ cm^{-1}$, due to the much larger temperature difference [44]. The much quicker wavelength modulation allows for shorter scan times ($\sim 1 - 10\ ms$) resulting in a larger sample size for the same scanning time. Unfortunately, aforementioned lasers have poor thermal conductivity causing the core region to heat up to the point of no light emission even at small current injections. As a result, only heat sink temperature modulation technique could be used for wavelength tuning.

7.3.6 Multi-pass cell

The detection sensitivity is proportional to the absorption path length. Longer paths provide more instances for light interaction with the gas molecules. As mentioned above, the 160 *ppmv* detection limit has been reached using 20 cm long gas cell. This is too high to be considered for any sensitive gas detection applications to be viable, where single digit *ppmv* are typically required [45]. Cells with longer direct transition paths are large and bulky, limiting their mobility.

One way around this problem is to fold the light with the help of multi-pass cells. The multi-pass cell folds the light with the help of astigmatic or spherical mirrors at each end of the cell increasing the effective path length. The cell used in our experiments had an effective path length of 76 m with the base length of only 0.32 m. Two mirrors reflect the light inside the cell up to 238 times before it gets out and is guided to the detector. The mirrors typically have 99.2 % reflectivity at $3 - 10\ \mu m$ wavelength region resulting in only $\sim$ 15 % light transmission at the exit. The more detailed description of the cell can be found in Reference [46].

Due to the large number of reflections, even small mirror losses have big impact on the output light intensity, reducing its power by over 85 %. Another factor contributing to the low output intensity is the asymmetrical beam divergence due to the rectangular laser facets. As a result the laser has low output when driven close to threshold. Increase in driving current often results single mode emission to switch to multi-mode emission making it unusable for spectroscopic applications.

A single mode laser with higher output power can be used to bring the detection limits down to 400 ppbv, by utilizing multi-pass gas cells with effective length of 76 m. High output powers are required in order to detect transmitted power that is partially lost on the mirrors as a result of multiple reflections inside the cell. Combined with the modulation and averaging techniques, described in Sections 7.2.2 and 7.3.5, the sensitivity could be increased even further.

7.4 Nitric oxide (NO) detection

Nitric oxide (NO), found in the atmosphere is an indicator for the air quality in the urban environments worldwide. NO plays very important role in the atmospheric chemistry and significantly contribute to the formation of the photochemical smog and acid rains. It also causes depletion of the stratospheric ozone layer [47, 48]. The typical concentrations of NO in the atmosphere ranges from 20 to 200 $ppbv$, depending on the pollution level and climate [49].

In medicine, medical biology and biochemistry, NO is used as a biomarker. Biological markers or simply biomarkers are the indicators for the current biological state in living organisms. Sensitive detection of the presence or the change in the concentration of such markers may indicate the certain biological abnormalities or tendencies. Nitric oxide molecule, is quite often used as an indicator for airway inflammation in humans [50]. Exhaled NO is a biomarker for asthma and other respiratory diseases [51–53].

There are a number of commercially available sensors used for sensitive NO detection, based on chemiluminescence, electrochemical or laser techniques [11, 54–56]. Chemiluminescence quite often referred to as the "*gold standard*" technique for sensitive NO trace gas detection due to its sensitivity and reproducibility. However, bulkiness and cost, as well as the requirement for technical expertise to operate it limits its applications. Electrochemical sensors are convenient due to their compactness but suffer from lower sensitivity, preventing more precise measurements.

7.4.1 NO absorption bands for FRS

Nitric oxide molecule has well distinguished absorption lines in the 5 μm wavelength region. The presence of H_2O and CO_2 in this region often interfere with the measurements and is tried to be avoided by targeting the spectral areas with minimal absorption features from water and carbon dioxide. As mentioned in Section 7.2.3, NO is paramagnetic molecule

allowing it to be measured using FRS technique without the interference from diamagnetic molecules.

NO ro-vibrational absorption branch that is located at 1875.81 cm^{-1}, also known as *Q-branch*, is of particular interest since it provides the optimum condition for the Faraday rotation spectroscopy. Due to the Zeeman splitting the net effect of the externally applied magnetic field on the given ro-vibrational transition is maximized at *Q-branch*. The *Q-branch* line strength decreases with increasing J value, where J is the rotational quantum number used to describe the splitting of the molecular rotation state resulted from the applied magnetic field. Therefore making $Q_{3/2}(3/2)$ molecular transition at 1875.81 cm^{-1} the best choice for *NO* detection using the *FRS* technique [57]. Figure 7.9 shows *NO* transitions at $5.3 - 5.4$ μm spectral region with the most sensitive *Q-branch* absorption located at 1875.81 cm^{-1}.

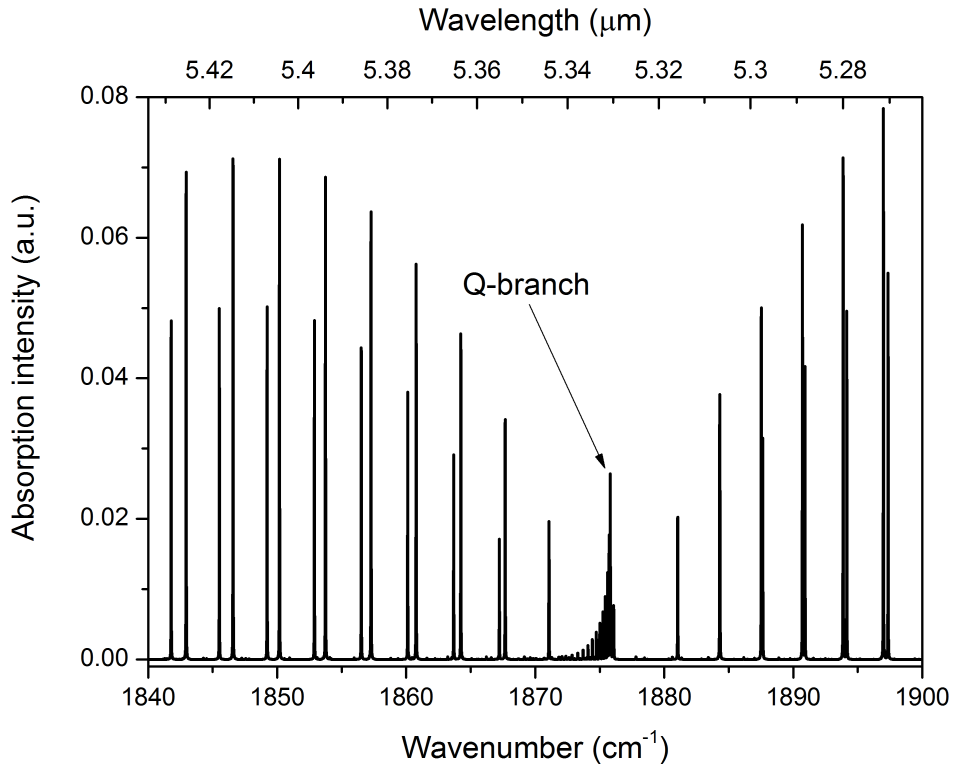

Figure 7.9: *NO* ro-vibrational transitions at 5.3 μm spectral region obtained from HITRAN database.

7.4.2 Experimental setup

Two QC lasers based on $InGaAs/AlInAs$ heterostructure grown on InP substrate with the emission wavenumbers of 1858 and 1868 cm^{-1} at room temperature have been used for the nitric oxide detection. Both lasers were capable of CW operation at RT with the output powers in excess of 50 mW, with the $FWHM = 0.51\ cm^{-1}$ and $FWHM = 0.49\ cm^{-1}$ respectively. The single mode suppression ratio of these lasers were comparable to the previously observed single mode lasers with unilateral grating and is $SMSR = 21\ dB$.

The experimental arrangement of NO detection system is schematically shown in Figure 7.10. The lasers were operated in continuous wave regime at a temperature range from $-37.5°C$ (235.5 K) up to $+40°C$ (313 K) depending on the required emission wavelength.

The collimated QCL beam was directed to 0.32 m long "*Aerodyne Research Inc*" multi-pass cell with the effective path length of 76 m to increase the absorption path length enhancing the interaction time with the analyte. The output signal was guided to the two-staged thermo-electrically cooled "*Vigo*" photodetector. The lasers were current modulated using *"Agilent* 33220*A"* waveform generator producing triangular ramp signal at 1 kHz repetition rate. The current was supplied using "*Newport/ILX Lightwave LDX*-3220*"* precision laser diode current source.

The gas cell was connected to two mass flow controllers, one - to the pure nitrogen and the other - to the NO gas cylinder with the concentration of 100 $ppmv$. The mass controllers could be adjusted to reduce the concentration of NO inside the cell down to 1 $ppmv$ (1 : 99). The pressure was kept at 100 $mBar$ to reduce the linewidth of the absorption features.

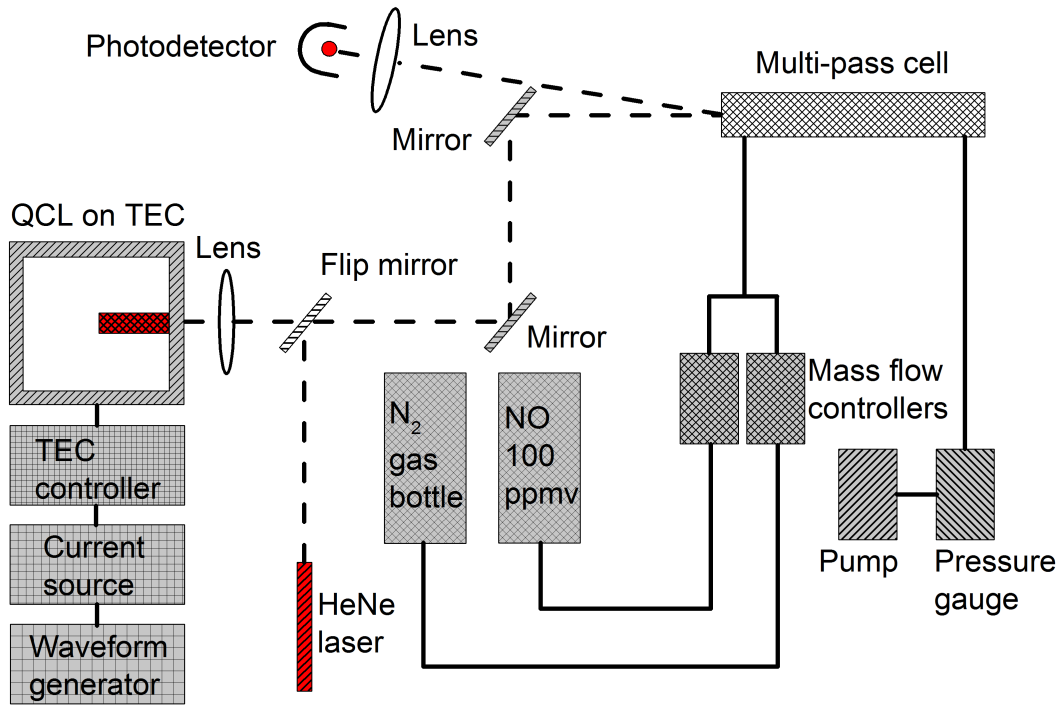

Figure 7.10: Schematic diagram of *NO* direct absorption detection system. The temperature of QCL is regulated by the TEC controller to coarse tune the wavelength. The current source, modulated by the waveform generator, powers the QCL, providing the necessary thermal ramp to scan the wavelength. The beam is focused and diverted through the multi-pass cell towards the detector. The analyte substance, inside the cell, is controlled with the mass flow controllers. The pressure is monitored and controlled using pressure gauge and pump.

7.4.3 Laser wavelength determination and discussion

Two lasers have single mode output at around 1858 and 1868 cm^{-1} wavenumbers at room temperature with the $FWHM = 0.4\ cm^{-1}$ and $SMSR \sim 25\ db$, measured with FTIR spectrometer in Sheffield, prior to taking them to the Radboud University. One of the lasers was used for the direct absorption experiment to resolve its actual emission wavelength in the setup and measure the maximum achievable tuning range in order to determine whether these devices can be used to target specific nitric oxide absorption lines.

The laser was temperature tuned from 260 K ($-13°C$) to 297 K ($24°C$) until the NO absorption bands ranging in the $1856-1872$ cm^{-1} region were detected. Once the absorption signature is discovered, the current modulation was employed to produce sharp, averaged absorption peak. The result of this wavelength scan is shown in Figure 7.11a, where a number of absorption peaks, corresponding to the NO and H_2O gases, are plotted. The water absorption peaks arise from the laser light interaction with the atmosphere on its way to the gas cell. While this path is much shorter than that attained inside the multi-pass cell, the high water concentration in the atmosphere produces peaks with similar strength to that observed by NO absorption.

Figure 7.11b shows ro-vibrational transitions for NO (100 $ppmv$) and H_2O (2 %) obtained from HITRAN database [40]. Two datasets are similar and can be used to determine the existing emission wavelength as a function of temperature. It can be noticed that the measured NO absorption lines correspond to the the actual lines at $1856.5, 1857.3, 1860.1$ and 1860.8 cm^{-1}. The water absorption lines, found in this spectral region between the NO bands are also observed in the experimental measurements. As a result it is determined that the laser operates at the wavelength range of $\lambda \approx 5.372 - 5.386$ μm ($1856.5 - 1861.5$ cm^{-1}) at the temperature range of $T \approx 266 - 296$ K, with the calculated wavenumber change of $\Delta\nu/\Delta T = 0.16$ cm^{-1}/K.

Assuming the wavelength change rate remains linear with the temperature it would require cryogenic temperatures to reach *Q-branch* at 1875.81 cm^{-1} ($T \approx 175$ K). The system would get too complicated to be used in mobile applications. As a result, different laser was interchanged with the emission wavenumber of ~ 1868 cm^{-1} at room temperature. The same wavelength detection was performed and is shown in Figure 7.12.

It can be seen that detected NO modes, correspond to the $1867.2, 1867.6$ and 1871.1 cm^{-1} absorption lines. The absorption bands from the water found in the atmosphere are also present. It was found that the laser emits at $\lambda = 5.355$ μm (1867.2 cm^{-1}) at $T = 285$ K and $\lambda = 5.344$ μm (1871.1 cm^{-1}) at $T = 262$ K. This gives the wavenumber change rate

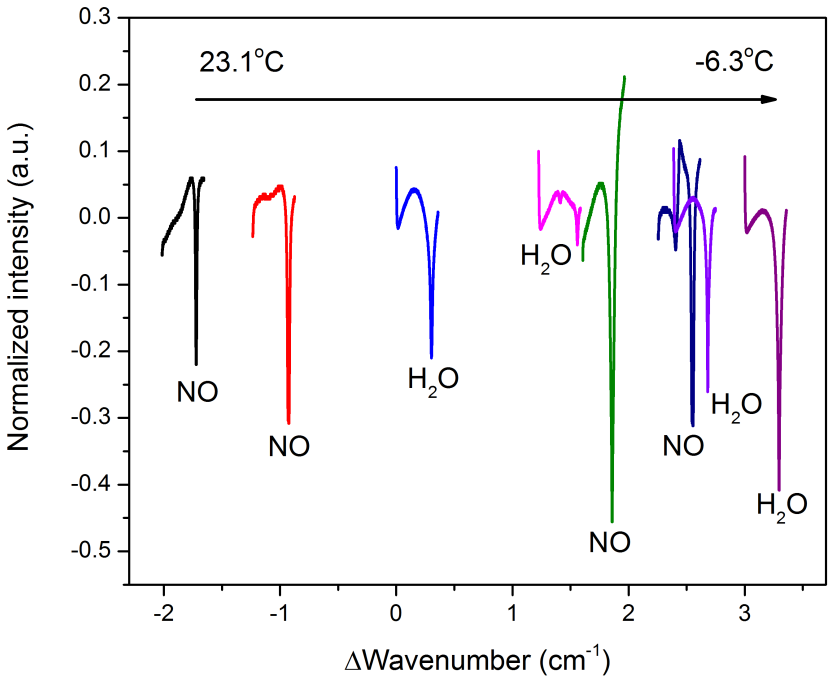

(a) Experimental results of NO and H_2O absorption lines.

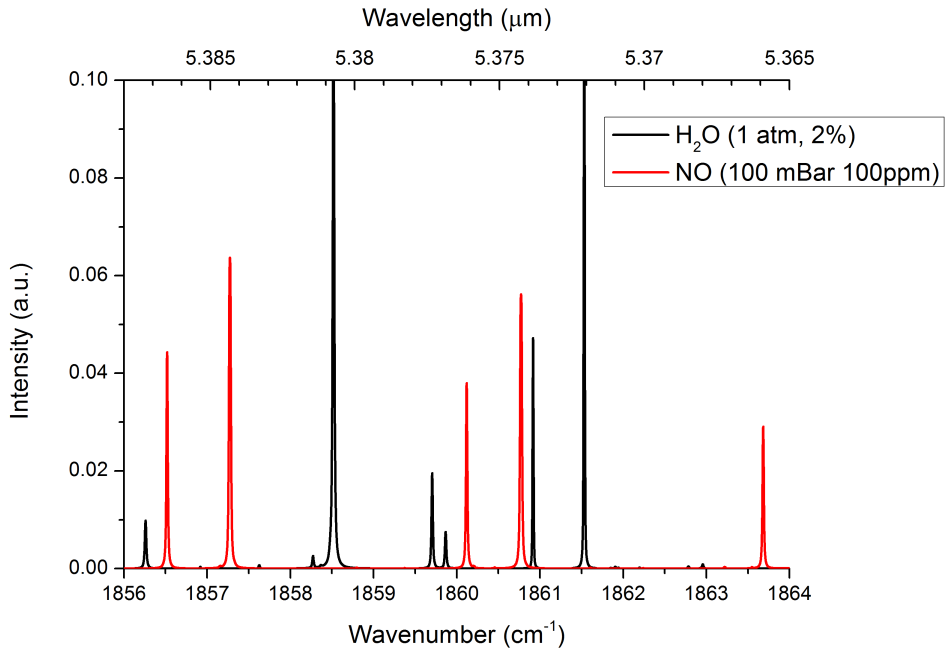

(b) Absorption lines obtained from HITRAN database.

Figure 7.11: Experimental (a) and calculated (b) nitric oxide (NO) and water (H_2O) ro-vibrational transitions in the 5.37 μm mid-IR region

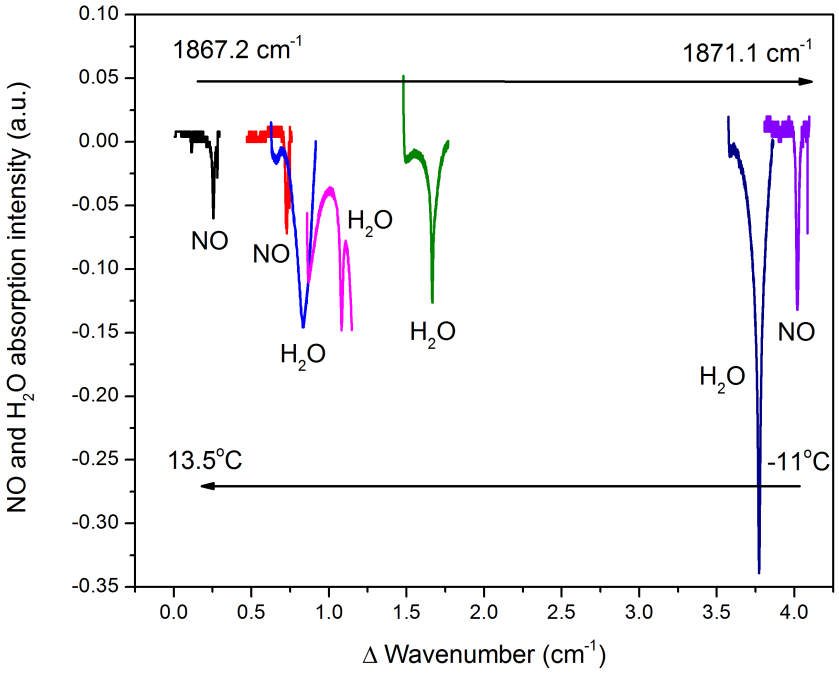

(a) Experimental results of NO and H_2O absorption lines.

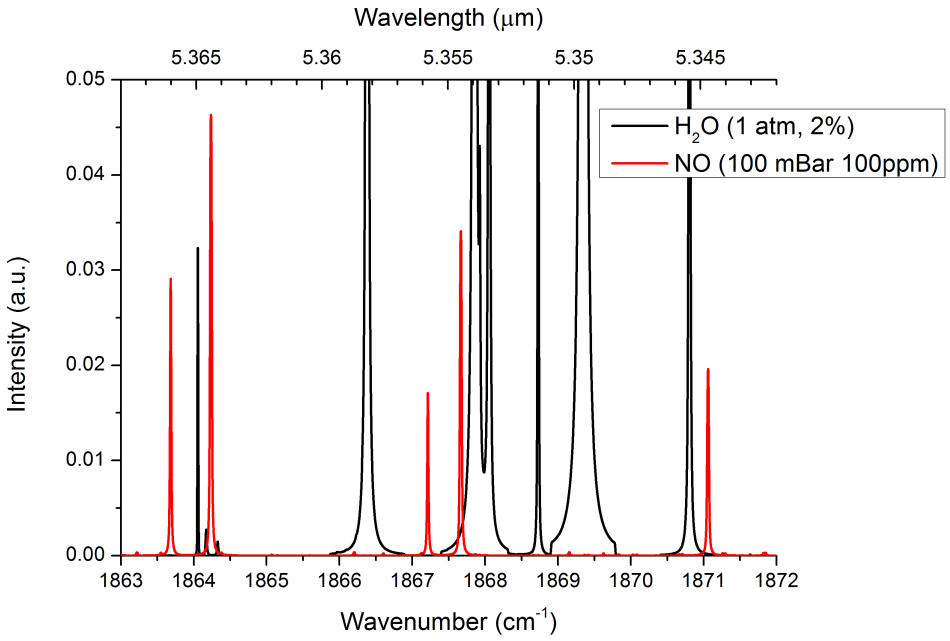

(b) Absorption lines obtained from HITRAN database [40].

Figure 7.12: Experimental (a) and calculated absorption lines in the 5.35 μm mid-IR region.

of $\Delta\nu/\Delta T = 0.16\ cm^{-1}/K$. As a result, the emission at the $\nu = 1875.81$ *Q-branch* is possible at $T \approx 232\ K$, assuming the wavelength change rate remains linear.

Unfortunately, the laser emission at 232 K did not correspond to the expected $\sim 1875\ cm^{-1}$ wavenumber. The observed absorption peaks were used to determine that the laser was emitting near 1871 cm^{-1} region even at low temperatures. It was concluded that the gain shift of the laser is slower than previously predicted. As a result, even lower temperatures are required to move emission frequency to sample the proposed *Q-branch* region. While the current setup could be used for neighboring overtone detection achieving sensitivities as low as 1 *ppmv*, the more sensitive Faraday rotation spectroscopy is required in order to bring the sensitivity level into *ppbv* region [43, 57]

7.5 Summary

The work in this chapter described the techniques and results obtained from targeting specific volatile organic compounds in the mid-infrared spectral region utilizing quantum cascade lasers. Two examples of using Sheffield grown and fabricated quantum cascade lasers for methane (CH_4) and nitric oxide (NO) detection were demonstrated. The low absorption sensitivity is attributed to the suboptimal measuring techniques used to obtain the data. The improvement of the equipment, such as appropriate lenses and mirror coatings, as well as advanced measuring techniques, previously described in this chapter, can potentially increase the sensitivity and decrease the absorption limits to the competitive levels of $sub{-}ppmv$, that are often required for the sensitive gas trace measurements.

Single mode quantum cascade laser with the emission wavelength of $\sim 3039\ cm^{-1}$ has been used to demonstrate the light absorption by the ro-vibrational modes of the methane gas. The simple gas detection system was set up achieving detection limits of 160 *ppmv*. Inefficient thermal extraction of these lasers prevented current modulation limiting the scanning speeds of the system.

Two quantum cascade lasers with the wavelengths around 5.3 μm were used to detect nitric oxide. The observed detection peaks corresponded to the emission wavelengths of $\lambda = 5.39\ \mu m$ (1855 cm^{-1}) and $\lambda = 5.36\ \mu m$ (1865 cm^{-1}) at room temperature with the wavelength tuning range of $\sim \pm 2\ cm^{-1}$, for the range of temperatures achievable by the Peltier cooler. It was possible to observe and measure the concentration of NO up to 1 *ppmv* with the direct absorption technique. The emerged issues preventing the laser emission at the proposed *Q-branch* located at 5.33 μm (1875.81 cm^{-1}) to be identified.

It has been showed that QCLs are reliable and efficient mid-infrared light emitting sources, capable of trace gas detection. The wavelength engineering can be used to target wide range of gases across the mid-infrared region.

References

[1] A.Kosterev, G. Wysocki, Y. Bakhirkin, R. Lewicki S. So, M. Fraser, F. Tittel, and R.F. Curl. Application of quantum cascade lasers to trace gas analysis. *Appl. Phys. B: Lasers Opt.*, 90:165–176, 2008.

[2] S.M. Cristescu, S.T. Persijn, S. te Lintel Hekkert, and F.J.M. Harren. Laser-based systems for trace gas detection in life sciences. *Appl. Phys. B: Lasers Opt.*, 92:343349, 2008.

[3] Craig Stroud, Sasha Madronich, Elliot Atlas, Brian Ridley, Frank Flocke, Andy Weinheimer, Bob Talbot, Alan Fried, Brian Wert, Richard Shetter, Barry Lefer, Mike Coffey, Brian Heikes, and Don Blake. Photochemistry in the arctic free troposphere: no_x budget and the role of odd nitrogen reservoir recycling. *Atmospheric Environment*, 37:33513364, 2003.

[4] A.Kosterev and F. Tittel. Chemical sensors based on quantum cascade lasers. *IEEE J. Quantum Electron,*, 38:582–591, 2002.

[5] T.A. Dueck, R. de Visser, H. Poorter, S. Persijn, A. Gorissen, W. de Visser, A. Schapendonk, J. Verhagen, J. Snel, F.J. Harren, A.K.Y. Ngai, F. Verstappen, H. Bouwmeester, L.A. Voesenek, and A. van der Werf. No evidence for substantial aerobic methane emission by terrestrial plants: a 13c-labelling approach. *New Phytologist*, 175(1):29–35, 2007.

[6] B.J. Orr and Y.B. He. Rapidly swept continuous-wave cavity-ringdown spectroscopy. *Chem. Phys. Lett.*, 512:1–20, 2011.

[7] I. Galli, S. Bartalini, S. Borri, P. Cancio, D. Mazzotti, P. De Natale, and G. Giusfredi. Molecular gas sensing below parts per trillion: Radiocarbon-dioxide optical detection. *Phys. Rev. Lett.*, 107:270802.

[8] F. Adler, M.J. Thorpe, K.C. Cossel, and J. Ye. Cavity-enhanced direct frequency

comb spectroscopy: technology and applications. *Annual Rev. Anal Chem. (Palo Alto Calif)*, 3:175–205, 2010.

[9] D.D. Arslanov, K. Swinkels, S.M. Cristescu, and F.J.M. Harren. Real-time, subsecond, multicomponent breath analysis by optical parametric oscillator based off-axis integrated cavity output spectroscopy. *Optics Express*, 19(24):24078–24089, 2011.

[10] T.H. Risby and S.F. Solga. Current status of clinical breath analysis. *Appl. Phys. B: Lasers Opt.*, 85(2-3):421–426.

[11] T.H. Risby and F.K. Tittel. Current status of midinfrared quantum and interband cascade lasers for clinical breath analysis. *Optical Engineering*, 49(11):111123, 2010.

[12] C. Wang and P. Sahay. Breath analysis using laser spectroscopic techniques: Breath biomarkers, spectral fingerprints, and detection limits. *Sensors*, 9(10):8230–8262, 2009.

[13] J. Mandon, M. Hogman, J.F.M. Merkus, J. van Amsterdam, F.J.M. Harren, and S.M. Cristescu. Exhaled nitric oxide monitoring by quantum cascade laser: comparison with chemiluminescent and electrochemical sensors. *Journal of Biomedical Optics*, 17(1):017003, 2012.

[14] E. Crespo, H. de Ronde, S. Kuijper, A. Pol, A.H.J. Kolk, S.M. Cristescu, R.M. Anhony, and F.J.M. Harren. Potential biomarkers for identification of mycobacterial cultures by proton transfer reaction mass spectrometry analysis. *Rapid Communications in Mass Spectrometry*, 26:679–685, 2012.

[15] L.A.J. Mur, J. Mandon, S.M. Cristescu, F.J.M. Harren, and E. Prats. Methods of nitric oxide detection in plants: A commentary. *Plant Science*, 181(5):509–519, 2011.

[16] F.F. Tian, J. Yu, J.L. Hu, Y. Zhang, M.X. Xie, Y. Liu, X.F. Wang, H.L. Liu, and J. Han. Determination of emulsion explosives with span-80 as emulsifier by gas chromatography-mass spectrometry. *Journal of Chromotography A*, 1218(22): 3521–3528, 2011.

[17] J.R. Castro-Suarez, Y.S. Pollock, and S.P. Hernandez-Rivera. Explosives detection using quantum cascade laser spectroscopy. *Chemical, Biological, Radiological, Nuclear, and Explosives (CBRNE) Sensing XIV*, page 871010, 2013.

[18] A. Artlich, B. Jonsson, M. Bhiladvala, P.A. Lonnqvist, and L.E. Gustafsson. Single breath analysis of endogenous nitric oxide in the newborn. *Biology of Neonate*, 79(1): 21–26, 2001.

[19] B. Buszewski, M. Kesy, T. Ligor, and A. Amann. Human exhaled air analytics: Biomarkers of diseases. *Biomedical Chromotography*, 21(6):553–566, 2007.

[20] V.H. Tran, H.P. Chan, M. Thurston, P. Jackson, C. Lewis, D. Yates, G. Bell, and P.S. Thomas. Breath analysis of lung cancer patients using an electronic nose detection system. *IEEE Sensors Journal*, 10(9):1514–1518, 2010.

[21] A.D. Wilson and M. Baietto. Advances in electronic-nose technologies developed for biomedical applications. *Sensors*, 11(1):1105–1176, 2011.

[22] D. Vaitiekus, D.G. Revin, J.W. Cockburn, J. Mandon, D. Marchenko, F. Harren, N. Hempler, G. Maker, G. Malcolm, and S.L. Hekkert. EU-funded research project - Quantatec. URL `http://www.quantatec.eu/`.

[23] Halina Abramczyk. *Introduction to Laser Spectroscopy.* Elsevier Science, 2005.

[24] A. Fried and D. Richter. *Infrared absorption Spectroscopy, in Analytical Techniques for Atmospheric Measurements.* Blackwell Publishing, 2006.

[25] J.D. Ingle and S.R Crouch. Spectrochemical analysis. *New York: Prentice Hall*, 1998.

[26] B.H Lee, E.C. Wood, M.S. Zahniser, J.B. McManus, D. D.Nelson, S.C. Herndon, G.W. Santoni, S.C. Wofsy, and J.W. Munger. Simultaneous measurements of notrous acid and nitrogen dioxide via absorption spectroscopy using tunable mid-infrared continuous-wave quantum cascade lasers. *Appl. Phys. B: Lasers Opt.*, 102:417–423, 2011.

[27] J.B. McManus, M.S. Zahniser, and D. D.Nelson. Dual quantum cascade laser trace gas instrument with astigmatic herriott cell at high pass number. *Appl. Opt.*, 50: 74–85, 2011.

[28] P. Kluczynski, J. Gustafsson, A.M. Lindberg, and O. Axner. Wavelength modulation absorption spectrometry - an extensive scrutiny of the generation of signals. *Spectrochimica Acta Part B*, 65:1277–1354, 2001.

[29] GC G.C. Bjorklund. Frequency-modulation spectroscopy - new method for measuring weak absorptions and dispersions. *Optics Letters*, 5(1):15–17, 1980.

[30] G. Litfin, C.R. Pollock, R.F. Curl Jr., and F.K. Tittel. Sensitivity enhancement of laser absorption spectroscopy by magnetic rotation effect. *The Journal of Chemical Physics*, 72:6602, 1980.

[31] Y. Wang, M. Nikodem, E. Zhang, F. Cikach, J. Barnes, S. Comhair, R.A. Dweik, C. Kao, and G. Wysocki. Shot-noise limited faraday rotation spectroscopy for detection of nitric oxide isotopes in breath, urine, and blood. *Scientific Reports*, 5:9096, 2015.

[32] IPCC. *Climate Change 2001: The Scientific Basis.* University Press, Cambridge, 2001.

[33] T.J. Blasing and S. Jones. Current greenhouse gas concentrations. *Carbon Dioxide Information Analysis Center (CDIAC)*, 2004.

[34] J. P. Commin, D. G. Revin, S. Y. Zhang, A. B. Krysa, and J. W. Cockburn. High performance, high temperature $\lambda \sim 3.7\,\mu m$ InGaAs/AlAs(Sb) quantum cascade lasers. *Appl. Phys. Lett.*, 95:111113, 2009.

[35] J. P. Commin, D. G. Revin, S. Y. Zhang, A. B. Krysa, K. Kennedy, and J. W. Cockburn. High peak power $\lambda \sim 3.3$ and $3.5\,\mu m$ InGaAs/AlAs(Sb) quantum cascade lasers operating up to 400 K. *Appl. Phys. Lett.*, 97:031108, 2010.

[36] J. P. Commin, K. Kennedy, D. G. Revin, S. Y. Zhang, A. B. Krysa, and J. W. Cockburn. $\lambda \sim 3.36\,\mu m$ room temperature InGaAs/AlAs(Sb) quantum cascade lasers with third order distributed feedback grating. *Appl. Phys. Lett.*, 97:111113, 2010.

[37] D.G. Revin, S. Zhang, J.P. Commin, K. Kennedy, A.B. Krysa, and J.W. Cockburn. High-Peak-Power Room-Temperature $\lambda \sim 3.6\mu m$ $InGaAs/AlAs(Sb)$ Quantum Cascade Lasers. *IEEE Photonics Technology Letters*, 22(11):757–759, 2010.

[38] A. Hangauer, G. Spinner, M. Nikodem, and G. Wysocki. Chirped laser dispersion spectroscopy using a directly modulated quantum cascade laser. *Applied Physics Letters*, 103(19):191107, 2013.

[39] Spectracalc. High resolution spectral modeling, 2015. URL `http://www.spectralcalc.com/info/about.php`.

[40] L.S. Rothman, I.E. Gordon, A. Barbe, D.Chris Benner, P.F. Bernath, M. Birk, V. Boudon, L.R. Brown, A. Campargue, J.P. Champion, K. Chance, L.H. Coudert, V. Dana, V.M. Devi, S. Fally, J.M. Flaud, R.R. Gamache, A. Goldman, D. Jacquemart, I. Kleiner, N. Lacome, W.J. Lafferty, J.Y. Mandin, S.T. Massie, S.N. Mikhailenko, C.E. Miller, N. Moazzen-Ahmadi, O.V. Naumenko, A.V. Nikitin, J. Orphal, V.I. Perevalov, A. Perrin, A. Predoi-Cross, C.P. Rinsland, M. Rotger, M. Simeckova, M.A.H. Smith, K. Sung, S.A. Tashkun, J. Tennyson, R.A. Toth, A.C. Vandaele, and J. Vander Auwera. The hitran 2008 molecular spectroscopic database. *Journal of Quantitative Spectroscopy & Radiative Transfer*, 110:533572, 2009.

[41] Y. Cao, N.P. Sanchez, W. Jiang, R.J. Griffin, F. Xie, L. Hughes, C. Zah, and F.K. Tittel. Simultaneous atmospheric nitrous oxide, methane and water vapor detection with a single continuous wave quantum cascade laser. *Optics Express*, 23(3):2121–2132, 2015.

[42] C.A. Evans, V.D. Jovanovic, D. Indjin, Z. Ikonic, and P. Harrison. Investigation of

thermal effects in quantum-cascade lasers. *IEEE Journal of Quantum Electronics*, 42 (9):859–867, 2006.

[43] D. Marchenko, J. Mandon, S.M. Cristescu, P.J.F.M. Merkus, and F.J.M. Harren. Quantum cascade laser-based sensor for detection of exhaled and biogenic nitric oxide. *Applied Physics B*, 111(3):359–365, 2013.

[44] K. Kennedy, D.G. Revin, J.P. Commin, A.B. Krysa, M.P. Semtsiv, M. Chashnikova, W.T. Masselink, J.W. Cockburn, and R.A. Hogg. Single grating period quantum cascade laser array with broad wavelength tuning range. *Electronics Letters*, 44(22): 1306–1307, 2008.

[45] Z. Bielecki, T. Stacewicz, J. Wojtas, and J. Mikolajczyk. Application of quantum cascade lasers to trace gas detection. *Bulletin of the Polish Academy of Sciences. Technical Sciences*, 63(2), 2015.

[46] J.B. McManus, P.L. Kebabian, and M.S. Zahniser. Astigmatic mirror multipass absorption cells for ion-path-length spectroscopy. *Applied Optics*, 34:3336–3348, 1995.

[47] W. Piver. Global atmospheric changes. *Environ. Health Persp.*, 96:131–137, 1991.

[48] J. Seinfeld and S. Pandis. *Atmospheric Chemistry and Physics: From Air Pollution to Climate Change*. Wiley, New York, 1998.

[49] M. Corradi, A. Pelizzoni, M. Majori, A. Cuomo, E. de Munari, and A. Pesci. Influence of atmospheric nitric oxide concentration on the measurement of nitric oxide in exhaled air. *Thorax*, 53(8):673–676, 1998.

[50] L.E. Gustafsson. Exhaled nitric oxide as a marker in asthma. *The European respiratory journal*, 26:49s–52s, 1998.

[51] A.P. Pietropaoli, I.B. Perillo, A. Torres, P.T. Perkins, L.M. Frasier, M.J. Utell, M.W. Frampton, and R.W. Hyde. Simultaneous measurement of nitric oxide production

by conducting and alveolar airways of humans. *Journal of Applied Physiology*, 87: 1532–1542, 1999.

[52] M. Hogman, N. Drca, C. Ehrstedt, and P. Merilainen. Exhaled nitric oxide partitioned into alveolar, lower airways and nasal contributions. *Respiratory Medicine*, 94:985–991, 2000.

[53] A. Sandrini, D.R. Taylor, P.S. Thomas, and D.H. Yates. Fractional exhaled nitric oxide in asthma: an update. *Respirology*, 15:57–70, 2010.

[54] J.H. Shorter, D.D. Nelson, J.B. McManus, M.S. Zahniser, S.R. Sama, and D.K. Milton. Clinical study of multiple breath biomarkers of asthma and COPD (NO, CO2, CO and N2O) by infrared laser spectroscopy. *Journal of Breath Research*, 5:037108, 2011.

[55] Z. Borrill, D. Clough, N. Truman, J. Morris, S. Langley, and D. Singh. A comparison of exhaled nitric oxide measurements performed using three different analysers. *Respiratory Medicine*, 100:1392–1396, 2006.

[56] K. Namjou, C.B. Roller, T.E. Reich, J.D. Jeffers, G.L. McMillen, P.J. McCann, and M.A. Camp. Determination of exhaled nitric oxide distributions in a diverse sample population using tunable diode laser absorption spectroscopy. *Applied Physics B - Lasers and Optics*, 85:427–435, 2006.

[57] R. Lewicki, J.H. Doty, R.F. Curl, F.K. Tittel, and G. Wysocki. Ultrasensitive detection of nitric oxide at 5.33 μm by using external cavity quantum cascade laser-based Faraday rotation spectroscopy. *Proceedings of the National Academy of Sciences of the United States of America*, 106(31):12587–12592, 2009.

Chapter 8

Conclusion

In conclusion, the work described in this thesis has demonstrated a number of techniques to achieve the reliable light sources required for mid-infrared laser spectroscopy based gas detection applications. The importance of the selective single mode generation in a quantum cascade laser has been discussed throughout the thesis, where two previously unreported methods of achieving single mode generation has been presented.

The first method employs a third order distributed feedback grating fabricated on a single side of the quantum cascade laser ridge. This novel way of achieving selective feedback has proven to be as effective as the alternative methods involving other types of DFB gratings. We have also demonstrated that the third order grating can be used for more sensitive wavelength selection compared to the first order grating.

The second, previously unreported, technique for single mode generation in a QCL device has been discussed in Chapter 6. The Fabry-Pérot reflector is used in conjunction with a quantum cascade laser in an external cavity setup. The laser emission is filtered in the FP reflector and directed back to the laser ridge creating selective feedback that is defined by the Fabry-Pérot interferometry. We have demonstrated wide emission spectra generation, although some frequencies could not be accessed for the reasons discussed in Chapter 6.

Despite this, the continuous wave external cavity operation with the wavelength coverage of 80 cm^{-1} has been reported.

Additionally, a thorough study of QCL active region optimization is given. A number of changes were made to the active region of a QCL device in order to improve the performance. The active region adjustments were made in a way that does not affect the emission wavelength. It has been concluded that surface defects and temperature instabilities play much bigger role in device performance than the small active region adjustments.

Finally, the description of the results obtained for methane (CH_4) and nitric oxide (NO) measurements using laser gas spectroscopy with the Sheffield's single mode lasers is given. Previously described devices were successfully integrated into the gas measuring systems at Radboud University in Nijmegen, Netherlands, and detection of methane and nitric oxide with corresponding concentrations of 160 *ppmv* and 1 *ppmv* respectively have been demonstrated.

Chapter 9

Future Work

The precise wavelength control utilizing unilateral grating (Chapter 5) opens up the possibility for dual wavelength generation [1–3]. Dual wavelength generation could be achieved by the integration of differently pitched grating on the opposite ends of the laser ridge to generate feedback at a different wavelength. Two wavelengths separated by the distance equal to the maximum achievable tuning range produces twice the wavelength coverage compared to that achieved with the single grating. Wider wavelength coverage is beneficial in a laser based spectroscopy systems where there is a need for a multiple closely spaced absorption line measurements.

Another method of generating dual wavelength emission could be achieved by the fabrication of two differently pitched gratings on the opposed ends of the laser ridge. Either dual or single sided grating can be used to explore the feedback strength required to achieve different frequency single mode generation from each end of the laser facet.

Once the single mode emission process is established and optimized, more work is planned for short wavelength QCL active region optimization. Further wafer growth with minimized growth defects is required in order to continue investigation of the active region optimization. Additionally, some work involving fabrication optimization is also planned.

The development of the fabrication process for epilayer-down bonding is needed in order to improve the heat transfer from the core region of the laser. Improved heat transfer reduces threshold current density of the device as well as increasing the operation duty cycle [4]. The overheating core region is the primary reason preventing continuous wave operation in $InGaAs/AlAs(Sb)$ based material system.

Further study, determining the origin of the described spectral gaps in QCL emission obtained using Fabry-Pérot etalon (Chapter 7), is planned. Elimination of these gaps opens up the possibility for the FP reflector in conjunction with quantum cascade laser to be used for sensitive gas spectroscopy, covering much wider gas absorption spectral region than that achieved with DFB lasers.

Finally, the laser integration into gas measuring systems for formaldehyde and butane detection is also planned. These compounds absorb light in the short mid-infrared wavelength region, allowing the integration of Sheffield-made short wavelength QCLs into these systems. The gas measurements and detection system characterization is planned in collaboration with *MSquared* and *SensorSense* gas sensing industrial partners.

References

[1] J. Jagerska, P. Jouy, A. Hugi, B. Tuzson, H. Looser, M. Mangold, M. Beck, L. Emmenegger, and J. Faist. Dual-wavelength quantum cascade laser for trace gas spectroscopy. *Applied Physics Letters*, 105(16), 2014.

[2] J. Jagerska, P. Jouy, B. Tuzson, H. Looser, M. Mangold, P. Soltic, A. Hugi, R. Bronnimann, J. Faist, and L. Emmenegger. Simultaneous measurement of NO and NO_2 by dual-wavelength quantum cascade laser spectroscopy. *Optics express*, 23(2):228881, 2015.

[3] L. Emmenegger, J. Jagerska, R. Bronnimann, J. Faist, P. Jouy, H. Looser, P. Soltic, and B. Tuzson. Multi-Component Trace Gas Spectroscopy Using Dual-Wavelength Quantum Cascade Lasers. *CHIMIA International Journal for Chemistry*, 69(11):708–708, 2015.

[4] C.A. Evans, V.D. Jovanovic, D. Indjin, Z. Ikonic, and P. Harrison. Investigation of thermal effects in quantum-cascade lasers. *IEEE Journal of Quantum Electronics*, 42 (9):859–867, 2006.

Appendix A

Short wavelength QCL Designs

A.1 M4054 laser design for $\lambda \sim 3.3 - 3.5\ \mu m$ emission wavelength

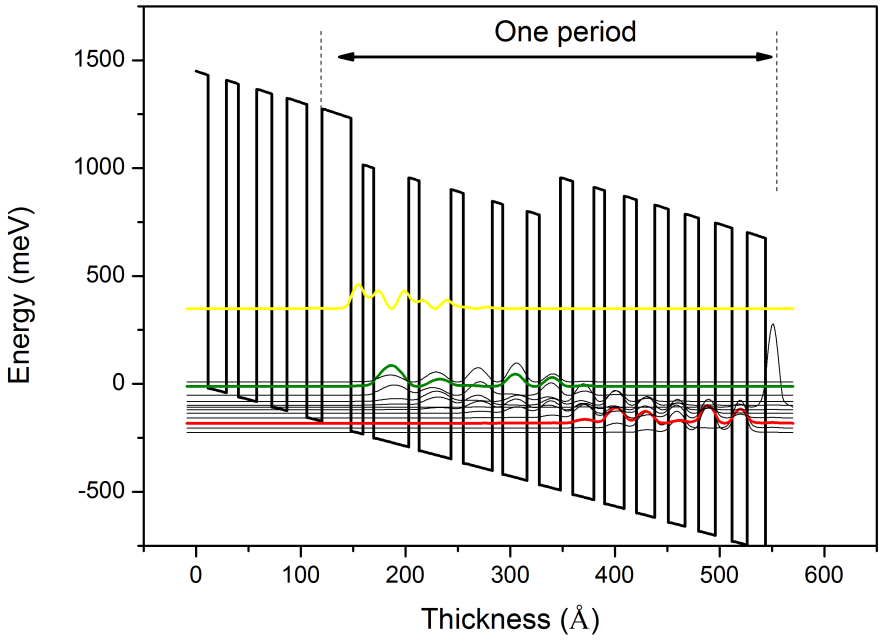

The laser design for $\lambda \sim 3.3 - 3.5\ \mu m$ wavelength emission is shown above. The one period

of the active region consists of the following layers:

27/12/***10***/34/***10***/31/***11***/27/***11***/23/***11***/21/**11**/20/**11**/19/**11**/18/**12**/17/**13**/16/**15**/15/**18**/15

where $AlAsSb$ barriers are in **bold**, $AlAs$ barriers are in bold ***italic*** and $In_{0.7}Ga_{0.3}As$ are in roman. Underlined layers are Si doped to $N_d = 6 \times 10^{17}\ cm^{-3}$. The thicknesses of the above layers are given in angstroms (Å).

The radiative transition occurs between the upper laser energy level (yellow) and the lower energy level (green), with the designed energy difference of $\Delta E = 340.1\ meV$ under the applied electric field of 150 kV/cm.

A.2 MBE grown short wavelength QCL designs

A.2.1 The control QCL design $SF0657$

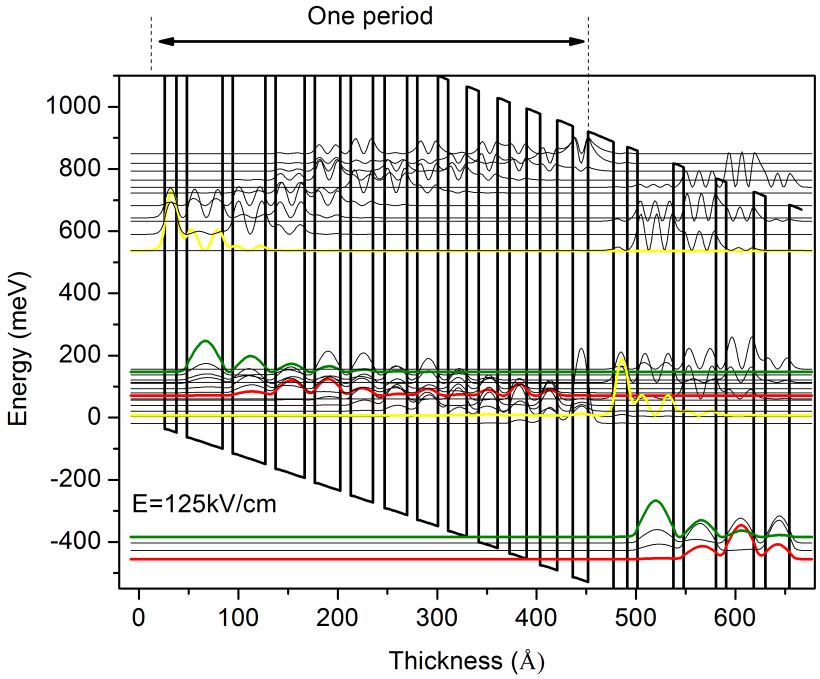

Sample $SF0657$, designed to emit at $\lambda = 3.35 - 3.4\ \mu m$ with the layered sequence of one period shown below.

26/13/***10***/37/***10***/34/***11***/30/***11***/25/***11***/23/**11**/22/**11**/20/**11**/19/**12**/19/**13**/18/**14**/
/17/**16**/17

The design was used as a control structure with all the subsequent adjustments made in reference to this structure. The diagonal radiative transition occurs from the upper laser energy level (yellow) to the lower laser energy level (green). The emission is designed to be at $\lambda = 3.35 - 3.4\ \mu m$ under the applied electric field of $E = 125\ kV/cm$. The $AlAsSb$ barriers are in **bold**, $AlAs$ barriers are in bold ***italic*** and $In_{0.7}Ga_{0.3}As$ are in roman. The thicknesses of the above layers are given in angstroms (Å).

A.2.2 Raised injector design

The layered sequence of the one period of the lowered injector active region design is given below.

26/13/***10***/37/***10***/34/***11***/30/***11***/25/***11***/23/**11**/22/**11**/20/**11**/19/**12**/<u>18.5</u>/**13**/<u>17.5</u>/**14**/
/<u>16.5</u>/**16**/<u>16.5</u>

where widened injection wells, responsible for the injector wavefunction energy reduction, are <u>underlined</u>. The $AlAsSb$ barriers are in **bold**, $AlAs$ barriers are in bold ***italic*** and $In_{0.7}Ga_{0.3}As$ are in roman. The thicknesses of the above layers are given in angstroms (Å).

A.2.3 Longer injector, narrower barriers design

The layered sequence, expressed in angstroms (Å), of the one period of the longer injector and narrower barriers active region design is shown below.
23/13/***10***/37/***10***/34/***10***/30/***10***/25/***10***/23/**10**/22/**10**/<u>21</u>/<u>**10**</u>/<u>20</u>/<u>**10**</u>/20/**10**/19/**11**/18/
/**12**/17/**13**/16/**15**/16

where the additional 4 quantum wells are <u>underlined</u>. The $AlAsSb$ barriers are in **bold**, $AlAs$ barriers are in bold ***italic*** and $In_{0.7}Ga_{0.3}As$ are in roman.

A.2.4 Even more lowered injector design

The layered sequence of the one period of the even more lowered injector active region design is shown below.

26/13/***10***/37/***10***/34/***11***/30/***11***/25/***11***/23/**11**/22/**11**/21/**11**/20/**12**/19/**13**/18/**14**/17/
/**16**/17

where underlined numbers represent the wider wells responsible injection wavefunction energy reduction. The $AlAsSb$ barriers are in **bold**, $AlAs$ barriers are in bold ***italic*** and $In_{0.7}Ga_{0.3}As$ are in roman. The thicknesses of the above layers are given in angstroms (Å).

A.2.5 Laser design to improve T_0

The layered sequence of the one period of the improved T_0 active region design is shown below.

23/13/***10***/37/***10***/34/***10***/30/***10***/24/**8**/20/**8**/20/**9**/21/**10**/22/**10**/21/**10**/20/**10**/19/**10**/
/18/**11**/17/**12**/16.5/**13**/16/**15**/16

Extra 2 quantum wells inside the miniband are underlined. The addition of these two wells break the continuity of the energy level cascade in the upper miniband, suppressing electron escape at higher operational temperatures. The $AlAsSb$ barriers are in **bold**, $AlAs$ barriers are in bold ***italic*** and $In_{0.7}Ga_{0.3}As$ are in roman. The thicknesses of the above layers are given in angstroms (Å).

A.2.6 Vertical transition design

The layered sequence of the vertical transition laser design, expressed in angstroms (Å), is shown below.

23/40/***10***/36/***10***/32/***10***/26/***8***/21/***8***/21/**9**/22/**10**/22/**10**/21/**10**/20/**10**/19/**10**/18/**11**/
/17/**12**/16.5/**13**/16/**15**/16

The wavefunctions of the upper and lower laser energy levels are localized in the same quantum well, providing vertical transition. The $AlAsSb$ barriers are in **bold**, $AlAs$ barriers are in bold ***italic*** and $In_{0.7}Ga_{0.3}As$ are in roman.

A.2.7 *InGaAs* laser design for $\lambda \sim 3.37\ \mu m$

The layered sequence of the active region emitting near $\lambda \sim 3.37\ \mu m$ is shown below.

27/41/**9**/36/**9**/34/**12**/28/**10**/<u>25</u>/**10**/<u>23</u>/**10**/<u>21</u>/**11**/<u>21</u>/**13**/<u>21</u>/**15**/<u>20</u>/**17**/<u>20</u>/**18**/19/**19**/18.

Here the $AlSb$ layers are in **bold** and Te-doped ($N_d = 1 \cdot 10^{17}\ cm^{-3}$) layers are <u>underlined</u>. The thicknesses of the above layers are given in angstroms (Å).